UNIVERSITY COLLEGE LONDON

Faculty of Mathematics and Physical Sciences

Department of Physics & Astronomy

MEASURING MOLECULAR GAS IN GALAXIES WITH APPLICATIONS TO STAR FORMATION EFFICIENCY

Thesis submitted for the Degree of Doctor of Philosophy of the University of London

by

Gioacchino Erminio Accurso

Supervisors:
Dr Amélie Saintonge
Prof Serena Viti

Examiners:
Dr Thomas Greve
Prof Haley Gomez

October 13, 2016

To my grandparents, parents, sister and brother for their perennial love and affection.

I, Gioacchino Erminio Accurso, confirm that the work presented in this thesis is my own. Where information has been derived from other sources, I confirm that this has been indicated in the thesis.

Abstract

The recently established equilibrium model for galaxy evolution gives major importance to the role of gas in regulating galaxy growth; the efficiency of star formation as gas is cycled in and out of galaxies is a central theme in this emergent picture. Low mass galaxies in the local universe, with their low metallicity environments, high gas mass fractions, and low $\frac{L_{\rm CO}}{\rm SFR}$ ratios, make them ideal and interesting candidates to test this model. Several questions remain: How can we accurately trace the total molecular gas in sub-solar metallicity environments where photodissociation of CO occurs? Is there a fundamentally different star formation efficiency in these systems compared to their high mass counterparts? This Thesis answers these questions using a new multiwavelength data set based on the IRAM xCOLD GASS survey, alongside auxiliary [CII] 158um line spectroscopy observations, using PACS on-board Herschel, with a newly built multi-phase ISM Radiative Transfer model and robust statistical methods.

To accurately trace molecular gas in sub-solar metallicity environments we wish to use the [CII] emission line to quantify the CO-dark H_2 gas however, as the [CII] 158μm emission line can arise in all phases of the ISM, being able to disentangle the different ISM contributions is an important yet unresolved problem when undertaking galaxy-wide, integrated [CII] observations. We first present a new multi-phase 3D Radiative Transfer interface that couples STARBURST99, a stellar spectrophotometric code, with the photoionisation and astrochemistry codes MOCASSIN and 3D-PDR. We model entire star forming regions, including the ionised, atomic and molecular phases of the ISM, and apply a Bayesian inference methodology to parametrise how the fraction of the [CII] emission originating from molecular regions, $f_{\rm [CII],mol}$, varies as a function of typical integrated properties of galaxies in the local Universe.

Once this has been achieved we present the first results using xCOLD GASS, a legacy survey of molecular gas in nearby galaxies, now extending down to stellar masses of $10^9 M_\odot$ from its precursor survey COLD GASS. Using the IRAM 30m telescope we measure the CO(1−0) line and, with Herschel PACS observations, measure the [CII] 158μm emission line in a sub-sample of 24 intermediate mass ($9 < \log M_*/M_\odot < 10$) and low metallicity ($0.4 < Z/Z_\odot < 1.0$) galaxies. We provide the first scaling relations for the integrated and molecular region $L_{[\mathrm{CII}]}/L_{\mathrm{CO(1\text{-}0)}}$ ratio as a function of galaxy properties. We connect the $L_{[\mathrm{CII}]}/L_{\mathrm{CO(1\text{-}0)}}$ ratio to the CO-to-H_2 conversion factor and find a multivariate conversion function, which can be used up to z$\sim$2.5. We then apply this to the full xCOLD GASS and PHIBSS1 surveys and investigate molecular gas scaling relations across redshifts, aiming to test the equilibrium model.

Finally we discuss ongoing survey planning and the latest software development for the ongoing JINGLE survey, which aims to simultaneously quantify gas and dust content for a large sample of galaxies. By conducting such a survey we shall be able to investigate how quantities such as the dust temperature, emissivity and dust-to-gas ratio vary systematically across the galaxy population; refining an alternative method to quantify gas masses of galaxies. The first results from JINGLE are presented, demonstrating the potential of the survey and highlighting the work carried out by this author.

Acknowledgements

I would first like to express my sincere gratitude to my supervisor, Dr Amélie Saintonge, for her continuous and overwhelming support during my Ph.D studies, for her patience, motivation, immense knowledge and kindness. For listening to my vast tirades on all things computational, while helping me build a network of wonderful collaborators all around the world, I'm truly grateful. For wonderfully helping me write successful telescope proposals and conference abstracts, enabling me to travel to beautiful parts of the world, I'm truly in your debt. I could not have imagined having a better advisor and mentor for my Ph.D study.

Many thanks go to Prof. Serena Viti for answering all my PDR and astrochemistry questions and making complex ideas sound all too simple. Thanks for guiding me through graduate school, for your wonderful scientific suggestions and for tolerating all my nonsensical questions. A special thanks goes to the amazing Dr Thomas Bisbas for his patience in dealing with my computing issues when using 3D-PDR, and for always being available on Whatsapp/Skype/email. A thanks also goes to Dr Patrick Owen for replying to all my MOCASSIN questions/emails and for all the encouraging conversations and tea breaks. I'd also like to thank Dr Ilse De Looze for answering all my dust related questions throughout our JINGLE work, and for convincing me when it was time to finish work and leave the office.

This work would not have been possible without the help of several collaborators who shared time, knowledge, data, and telescope access. I'd like to thank Prof. Kim-Vy Tran and Dr Jimmy for hosting me while at Texas A&M and giving me a wonderful taste of Texas. Thanks for all the wonderful evenings at Duddley's and food at Antonios. Thank you for allowing me to use the McDonald telescope and for giving me a wonderful taste of

life across the pond. Thanks also goes to the whole Astrophysics group at A&M for their hospitality. I'd also like to thank all the co-authors on the COLD GASS and Herschel [CII] telescope proposals for allowing me to use their data and making the work in this Thesis possible. I'd especially like to thank Prof. Barbara Catinella and Prof. Luca Cortese for their input and advice throughout this project. Thanks goes to Dr Carsten Kramer for being so helpful during my time observing at IRAM and making sure I didn't break the telescope. Finally I'd like to thank Prof Reinhard Genzel and Prof Linda Tacconi for their input, regarding high redshift CO studies, which has helped to strengthen this work.

Thanks to those who have provided me with the resources and funds required to conduct my studies. Thank you to Jon Deacon and Dr Jeremy Yates for the technical support with Archimedes and Phalanx. I also wish to acknowledge the considerable support that I have received from the UK Science and Technologies Facilities Council, without whom this work would not have been possible.

A huge thanks also goes to my fellow PhD students for walking through this journey with me throughout the past three years. A special thanks goes to Teresita for sitting through all my favourite horror movies and Daniela for understanding me so well. Thanks to Guido for being a wonderful younger academic sibling and for spending countless hours with me in Bloomsbury fitness. I blame Davide and Michelle for making me laugh so loudly in the department and over post-seminar drinks. Thanks to Bruno and Danielle for watching tennis with me and for being amazing office mates. Thanks also to Catherine for the hilarity in my final year which kept me sane (or maybe insane?). I have such fond memories of my time with you all and I will never forget your affection and love.

Finally, I would not have made it this far if it hadn't been for my family. Thanks to my grandparents who taught me that with hard work and determination I can achieve anything. Thanks to Mum and Dad for always believing in me and providing for me. You have taught me to never give up on my dreams and to believe in myself. Thanks also to Raffaela for being so smart and allowing me to see the world through the eyes of others and Daniele for always making me laugh.

Contents

List of Figures

List of Tables

Chapter 1

Introduction

When trying to build a framework for galaxy formation and evolution understanding, the process of star formation is a crucial ingredient. One of the first scaling relations detailing the nature of star formation on galactic scales was the empirical Schmidt-Kennicutt law (Schmidt 1959; Kennicutt 1998). It was observed that the star formation rate surface density correlates with the total molecular and atomic gas surface densities as

$$\Sigma_{\rm sfr} \propto (\Sigma_{\rm gas})^n, \text{ with } n \simeq 1.4. \tag{1.1}$$

This pioneering work, connecting the process of star formation to a galaxy's gas content, instigated the numerous endeavours by the scientific community to study, observe and quantify the gas reservoir within galaxies. This has all led to a framework of galaxy evolution where the cycling of gas in and out of galaxies and the efficiency with which this gas fuels star formation are central. The ability to directly measure gas and dust in galaxies at both low and high redshifts has been key in shaping this understanding. This Thesis provides a novel method to quantify molecular gas in galaxies, and then applies it to observational studies of star formation efficiency, at high and low redshift, aiming to test the current theoretical paradigm.

1.1 Background - Galaxy scaling laws

Galaxy evolution involves a wide range of different physical processes operating on stellar to cosmological scales; such processes include the hierarchical growth of structure as

baryons collapse into dark matter filaments, star formation, black hole accretion, and a plethora of feedback processes. Given the complexity in these seemingly chaotic and violent systems, it is surprising that galaxies display simple and tight "scaling laws" between many of their physical properties. Many scaling relations exist in the literature, most notably the well-established relation between a galaxies bulge velocity dispersion and central black hole mass (Magorrian et al. 1998), the circular velocity and luminosity relation for spirals, known as the Tully-Fisher relation (Tully & Fisher 1977), and the relation between the luminosity and the central stellar velocity dispersion of elliptical galaxies known as the Faber-Jackson law (Faber & Jackson 1976). The above are known as dynamical relations and have been around for decades. However, apart from the Schmidt-Kennicutt law in Equation 1.1, only in the past decade have scaling relations concerning the process of star formation and ISM content emerged which involve cold gas; this Thesis will focus on these.

1.1.1 The Main Sequence & Fundamental Mass-Metallicity relation

Over the past decade large imaging and spectroscopic surveys have conducted systematic observations of very large samples of galaxies at optical, ultraviolet (UV) and infrared (IR) wavelengths which have, for example, allowed for precise measurements of stellar masses and star formation rates (SFRs). These measurements show how star-forming galaxies form a tight sequence in the SFR-M_* plane, illustrated in Figure 1.1 (Schiminovich et al. 2007; Elbaz et al. 2007; Noeske et al. 2007; Daddi et al. 2007; Peng et al. 2010). The shape is mostly redshift independent, but the zero-point is shifted to ever higher SFRs as redshift increases. This evolution has been well characterised up to $z \sim 2.5$, as shown in Figure 1.2. Power-law fits to this have been found such that:

$$SFR \sim M_*^a (1+z)^b \tag{1.2}$$

where a ≈ 0.8 and b ≈ 2.5, applicable up to z$\sim$3. Galaxies on the main sequence contribute $\sim$ 90% of the total star formation in the universe (Rodighiero et al. 2011) with high duty cycles, defined as the fraction of its lifetime during which it's actively forming stars (Romano et al. 2014), at $\sim$ 40-70% (Noeske et al. 2007). Furthermore the metallicity and stellar mass of galaxies are tightly correlated (Tremonti et al. 2004; Erb et al. 2006), now known as the mass-metallicity relation, Figure 1.3. Studies have shown that the scatter in this relation is caused by star formation, and is constant across redshifts, championing the Fundamental Mass-Metallicity Relation (FMR) (Mannucci et al. 2010) relation shown

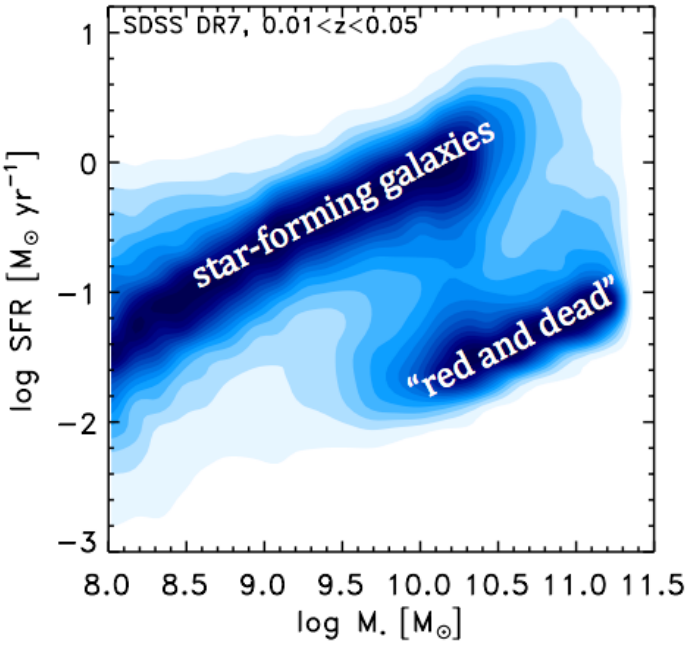

Figure 1.1. The Main Sequence for galaxies, detailing the tight correlation between a galaxy's star formation rate and stellar mass for spiral star-forming galaxies. Elliptical bulge dominated systems lie below, with on average higher stellar masses and lower star formation rates. Figure courtesy of Dr Amélie Saintonge.

in Figure 1.4. Galaxies, except those at z∼3.3, appear to follow the same relation defined by SDSS galaxies. However the FMR is debated as others have suggested that gas content is the third parameter explaining the scatter (Bothwell et al. 2013; Jimmy et al. 2015).

Each of the aforementioned scaling relations have surprisingly low scatter, given the turbulent and complex physical processes underpinning them. The simplicity of these relations hints at an underlying uniformity in galaxy evolution. The very existence and tightness of these relations suggest that galaxies live in a slowly evolving state of equilibrium, downplaying the importance of galaxy mergers in the global star formation budget of the Universe (Robaina et al. 2009; Rodighiero et al. 2011; Kaviraj et al. 2013). Based on these ideas, and inspired by hydrodynamic simulations, Davé et al. (2012) presented an analytic formalism that describes the evolution of the stellar, gas and metal content of galaxies where the ISM plays a crucial role, championing the recently established "equilibrium model" of galaxy evolution, the formalism of which is detailed in Davé et al. (2012); Lilly et al. (2013); Bouché et al. (2010); White & Frenk (1991). Under this framework, star formation in galaxies is controlled by the total available gas reservoir and the inter-

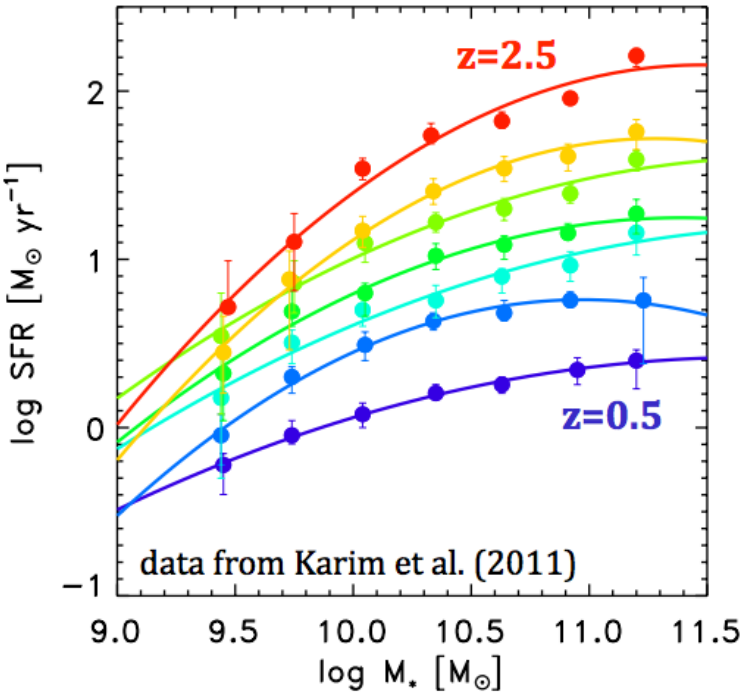

Figure 1.2. The smooth evolution of the main sequence up to $z \sim 2.5$ shown by Karim et al. (2011) where solid points are binned averages and different colours indicate different redshifts.

play of gas inflows and outflows from the circumgalactic medium; ergo galaxies live in a state of equilibrium. What triggers and drives star formation, how the chemical evolution and enrichment of the ISM proceeds, and what causes the growth of galaxies is intricately linked to their total gas content. Being able to quantify and measure gas in the ISM is of the upmost importance to further our understanding of galaxy evolution. A discussion of the main physical processes in this revolutionary theory, based on the formalism in Davé et al. (2012), follows.

1.2 The equilibrium model

Based on intuition gained from hydrodynamic simulations of galaxy formation, the equilibrium model postulates that galaxies are fed primarily by cold ($\sim 10^4$ K) streams connected to filamentary large-scale structure (Kereš et al. 2005; Dekel et al. 2009), outflows are strong and ubiquitous (Springel & Hernquist 2003; Oppenheimer & Davé 2008) and outflowing material commonly returns to galaxies, also known as wind recycling (Oppenheimer et al. 2010). Hence in this framework galaxy evolution is governed by the cycle of

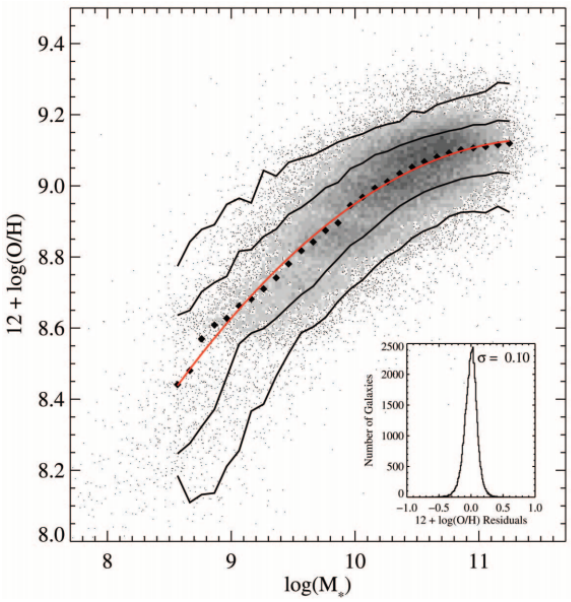

Figure 1.3. Relation between stellar mass, in units of solar masses, and gas-phase oxygen abundance for 53,400 star-forming galaxies in the SDSS; known as the mass-metallicity relation, detailing the tight correlation between a metallicity and stellar mass, regardless of morphology or galaxy type. The large black filled diamonds represent the median in bins of 0.1 dex in mass that include at least 100 data points. The solid lines are the contours that enclose 68% and 95% of the data. The red line shows a polynomial fit to the data. Taken from Brinchmann et al. (2004).

baryons exchanging matter and energy between galaxies, their associated halos, and the surrounding intergalactic gas.

Star forming galaxies are postulated to lie near the *equilibrium condition* such that:

$$\dot{M}_{in} = \dot{M}_{out} + \dot{M}_{*} \tag{1.3}$$

where the terms are the mass inflow rate, mass outflow rate, and star formation rate (SFR), respectively. Defining the mass loading factor $\mu = \dot{M}_{out}/\dot{M}_{*}$, we can rewrite the equilibrium condition as

$$SFR = \dot{M}_{in}/(1+\mu)\,. \tag{1.4}$$

Therefore a galaxy's star formation history is determined by the evolution of $\dot{M}_{in}$ and μ. First let's consider $\dot{M}_{in}$, which can be separated into three terms:

- $\dot{M}_{grav}$ - The baryonic inflow into a galaxy halo which is primarily set by the assumed cosmology. The functional form presented in Dekel et al. (2009) is dependent on M_{halo} and redshift:

$$\dot{M}_{grav} \propto (1+z)^{2.25}. \tag{1.5}$$

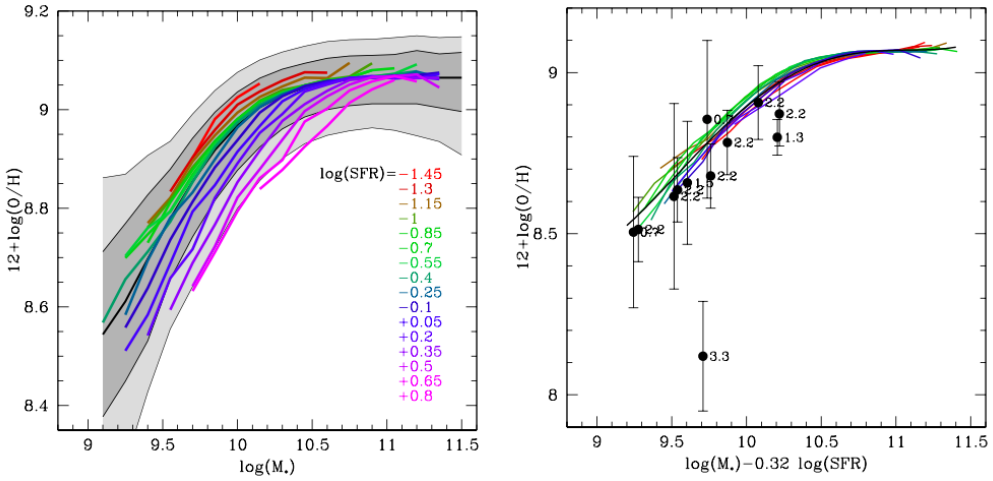

Figure 1.4. Left: The mass-metallicity relation of local SDSS galaxies. The grey-shaded areas contain 64% and 90% of all SDSS galaxies, with the thick central line showing the median relation. The coloured lines show the median star formation rates, as a function of M_*, of SDSS galaxies. **Right:** The Fundamental Mass-Metallicity Relation (FMR) provides an explanation for the scatter found in the mass-metallicity relation, independent of redshift. Coloured lines indicate median star formation rates, as in the left panel, where the x-axis has now changed from stellar mass to a linear combination of stellar mass and SFR which reduces the scatter found in the left plot. The black line shows the polynomial best fit while points are high-redshift galaxies, labelled with their redshifts. Both plots are taken from Mannucci et al. (2010).

- $\dot{M}_{prev}$ - The amount of the gas entering the halo that is prevented from reaching the ISM, and which ends up in the gaseous halo of the galaxy. It can also be regarded as the rate of growth of halo gas.

- $\dot{M}_{recyc}$ - Infalling gas that has previously been ejected in outflows, along with gas returned to the ISM via stellar evolution, which can also be thought of as gas in a galaxy's duty cycle, linked to the recent concept of a galactic fountain (Ceverino et al. 2016).

Expressing $\dot{M}_{in}$ in these terms, we obtain

$$\dot{M}_{in} = \dot{M}_{grav} - \dot{M}_{prev} + \dot{M}_{recyc} \tag{1.6}$$

and then by defining a preventive feedback parameter such that

$$\zeta = 1 - \dot{M}_{prev}/\dot{M}_{grav} \tag{1.7}$$

we obtain

$$\dot{M}_{in} = \zeta \dot{M}_{grav} + \dot{M}_{recyc} \tag{1.8}$$

As mentioned above, $\dot{M}_{grav}$ is determined through cosmology, while ζ is due to feedback processes. There are a number of sources of preventive feedback, each with its own dependence on halo mass and redshift, the products of which comprise the total ζ:

- ζ_{photo} - This represents suppression of inflows owing to photoionisation heating. This operates at low masses, and approaches zero below a photo-suppression mass.
- ζ_{quench} - This is associated with a physical process that quenches star formation in massive halos and prevents cooling flows, related to feedback from supermassive black holes.
- ζ_{grav} - This reflects suppression of inflow by ambient gas heating (shock heating) owing to gravitational structure formation via the formation of virial shocks.
- ζ_{winds} - This is associated with additional heating of surrounding gas provided by energetic input from winds, for example stellar winds. Note that although both ζ_{winds} and μ arise from winds, the former is a preventive feedback parameter, whereas μ is an ejective feedback parameter; the two are not necessarily simply related.

Multiplying these terms together we obtain $\zeta(\mathrm{M}_{halo,z})$, illustrated in Davé et al. (2012). The final term to understand, to gain a complete understanding of $\dot{M}_{in}$, is $\dot{M}_{recyc}$ which is related to the metallicity of the infalling gas, discussed below.

1.2.1 Metallicities

The global metallicity within a galaxy's ISM is given by the enrichment rate, the yield (y) multiplied by the SFR, normalised by the mass inflow rate, $\dot{M}_{in}$. If the inflow has been pre-enriched there is an additional term that depends on $\alpha_Z = \mathrm{Z}_{in}/\mathrm{Z}_{ISM}$, where Z_{in} and Z_{ISM} are the metallicities of the inflowing and ambient ISM gas. Hence,

$$Z_{ISM} = Z_{in} + \frac{y \times SFR}{\dot{M}_{in}}. \tag{1.9}$$

Combining this with equation 1.4 we obtain

$$Z_{ISM} = \frac{y}{1+\mu}\frac{1}{1-\alpha_Z}. \tag{1.10}$$

Hence the mass-metallicity relation and its evolution are established by the mass and redshift dependence of μ and α_Z. In the equilibrium model, μ has a significant mass dependence but little or no redshift dependence, while α_Z has redshift dependence but

very little mass dependence, and is small. This would imply that the shape of the mass-metallicity relation is primarily established by $\mu(M_*)$, while its evolution is driven by α_Z. In this scenario, the shape of the mass-metallicity relation is modulated by the fraction of inflow that forms stars, while its evolution is governed by the enrichment level of in-falling gas.

It is often believed that a galaxy's gravitational potential well governs the shape of the mass-metallicity relation as metals can more easily escape from the shallower potential wells of small galaxies. However, in this paradigm, the net mass outflow rate is the key determinant of the mass-metallicity relation, and the potential well depth is, at most, indirectly implicated.

Metals in the IGM are deposited there by outflows, hence the infalling gas metallicity is a direct measure of $\dot{M}_{recyc}$. Z_{in} is given by the metal mass arriving in the form of recycled winds, divided by the total mass inflow rate, i.e.

$$Z_{in} = Z_{recyc}\frac{\dot{M}_{recyc}}{\dot{M}_{recyc} + \zeta\dot{M}_{grav}}. \tag{1.11}$$

Since galaxies evolve slowly in metallicity (Brooks et al. 2007) and wind recycling times are typically of order a Gyr (Oppenheimer et al. 2010), the galaxy metallicity has probably not evolved strongly from when the gas was ejected to when it is being re-accreted, and hence $\mathrm{Z}_{recyc} \approx \mathrm{Z}_{ISM}$. Substituting this into equation 1.12 gives

$$\dot{M}_{recyc} = \frac{\alpha_Z}{1-\alpha_Z}\zeta\dot{M}_{grav}. \tag{1.12}$$

This relates the mass recycling term in the inflow equation 1.8 to the metallicity infalling into the ISM. In principle α_Z is an observable quantity via absorption or emission measured in the outskirts of galaxies, whereas $\dot{M}_{recyc}$ is not.

1.2.2 The evolution of gas fractions and depletion times.

A galaxys gas fraction is defined here as

$$\begin{aligned} f_{\mathrm{gas}} &= \frac{M_{\mathrm{gas}}}{M_{\mathrm{gas}} + M_*} \\ &= \frac{1}{1 + (t_{\mathrm{dep}}\mathrm{sSFR})^{-1}} \end{aligned} \tag{1.13}$$

where t_{dep} is the gas depletion time, $\frac{M_{gas}}{\mathrm{SFR}}$, and sSFR is the specific star formation rate, $\frac{\mathrm{SFR}}{M_*}$, driven by cosmic inflow. This is intuitive because it splits f_{gas} into a term that

is insensitive to feedback (t_{dep}) and a term that depends strongly on feedback (sSFR). The depletion time measures the timescale over which gas gets converted into stars, the consumption of gas. This is expected to be primarily determined by the star formation law, such as that presented in Equation 1.1. Assuming a Kennicutt- Schmidt law, simulations by Davé et al. (2011a,b) show that t_{dep} is essentially independent of outflows, and scales as

$$t_{dep} \propto t_H M_*^{-0.3} \tag{1.14}$$

where t_H is the Hubble time, giving rise to a weak anti-correlation with M_*. Therefore, bringing this all together, we can say that the evolution of $f_{\rm gas}$ depends on the evolution of t_{dep} and sSFR. The former evolves with t_H, that scales as $(1+z)^{-1.5}$ in the matter dominated regime, while the latter is generally driven by inflows, Equation 1.2, which scales as $(1+z)^{2.25}$ if driven by infall. Combining these, galaxy gas fractions are expected to evolve as $\sim(1+z)^{0.75}$.

Overall, in the equilibrium scenario, galaxy gas fractions represent a competition between supply (sSFR) and consumption (t_{dep}), such that galaxies become less gas-rich with time because the gas supply rate drops faster than the gas consumption rate.

1.2.3 The equilibrium relations

We can substitute equation 1.12 into equation 1.8 to obtain

$$\mathrm{SFR} = \frac{\zeta \dot{M}_{grav}}{(1+\mu)(1-\alpha_Z)} \tag{1.15}$$

This is one of the key equilibrium relations which describes how galaxy star formation rates are governed by accretion and feedback processes. This equation, together with equations 1.10 and 1.13, detail the stellar, gas, and metal content of galaxies across cosmic time.

The equilibrium relations depend on three parameters: μ, ζ, and α_Z, representing ejective feedback (i.e. outflows), preventive feedback, and wind recycling. Additionally, the star formation law governs t_{dep}, while $\dot{M}_{grav}$ is set by cosmology, and α_Z is set by nucleosynthetic processes. Assuming those are well-established, the mass and redshift dependence of μ, ζ, and α_Z govern the evolution of the global SFR, f_{gas}, and Z_{ISM} of galaxies. A pictorial representation of this phenomenological model is shown in Figure 1.5. We now move on from the theoretical underpinnings of the equilibrium model and focus on the observational techniques used to quantify gas in galaxies which have led to the current paradigm.

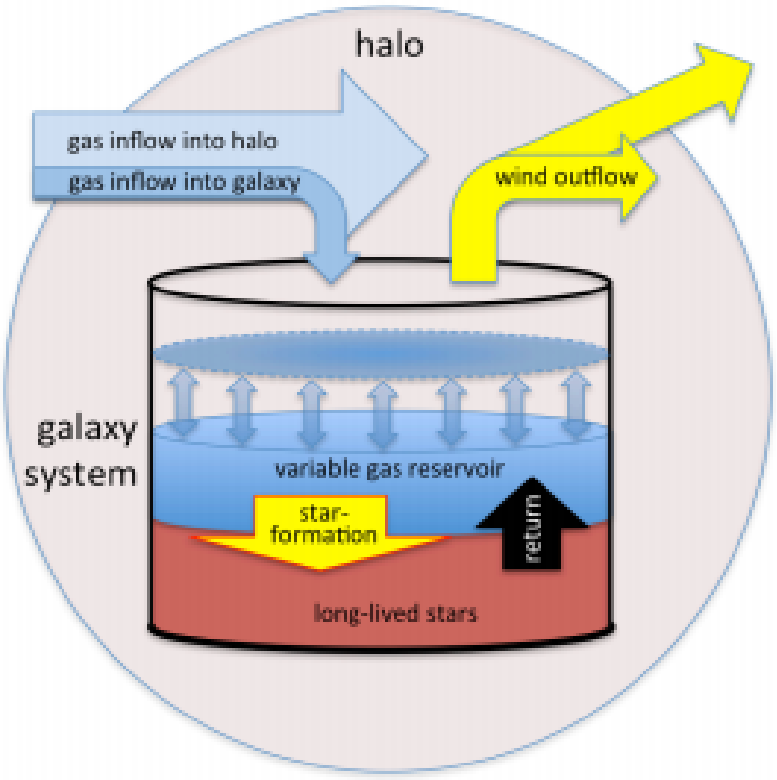

Figure 1.5. A pictorial representation of the equilibrium model, taken from Lilly et al. (2013), showing how inflows and outflows of gas regulate star formation within a galaxy.

1.3 Observational evidence supporting the equilibrium model

The strongest evidence in favour of the equilibrium model comes from molecular gas observations. In the local Universe, with the exception of ULIRGSs, it has now been directly observed that the location of a galaxy on the main sequence is mostly determined by its supply of molecular gas (Saintonge et al. 2016, 2013; Bothwell et al. 2013), with variations in star formation efficiency playing a second order role (Saintonge et al. 2011*b*). High redshift galaxy samples have reached similar conclusions, whether directly using CO data (Genzel et al. 2015; Tacconi et al. 2013) or indirectly using far-infrared photometry to estimate gas masses (Magdis et al. 2012). Outflows of gas, an important element in setting the balance between gas and star formation in the equilibrium model, have now been directly observed in a range of objects (Sturm et al. 2011; Chen et al. 2010).

Detection of CO line emission in normal star-forming galaxies at z>1 (Tacconi et al. 2013, 2010; Daddi et al. 2010) show that the rapid decline in the specific SFR of galaxies since z∼2 can be explained by the measured gas fractions and a slowly varying depletion

timescale, in agreement with the equilibrium model. Further to this, Saintonge et al. (2013) directly probed the cold ISM of normal star forming galaxies, for a sample of 17 lensed galaxies with z $\sim$ 1.4-3.1, finding that the mean gas depletion timescale of main sequence galaxies at z $>$ 2 is measured to be only $\sim$450Myr, a factor of $\sim$1.5 and 5 times shorter than at z = 1 and 0, respectively. The depletion timescale and gas fractions of high redshift normal star-forming galaxies can be explained under the equilibrium model as the gas reservoir of galaxies is the primary driver of the redshift evolution of specific star formation rates. Furthermore high redshift studies using FIR photometry also support the aforementioned conclusions (Genzel et al. 2015), showcasing an alternative method to quantify gas using dust measurements; to be further discussed in section 1.4.4.

1.3.1 The multiwavelength survey era and the need for accurate statistics

It would also be unfair to understate the major role that technological and computational advancements in data acquisition, storage and processing speed have played in ushering in the above paradigm. The recent state of the art surveys now have multiwavelength ancillary data, ranging from the radio to the UV, aiming to characterise and measure multiple physical properties of galaxies across the electromagnetic spectrum. With all this data it is now possible to quantify secondary dependencies on the above scaling relations or to possibly measure divergences away from these; an impossible prospect a decade ago.

All this information requires accurate and robust statistical techniques which can extract signal, measure correlations throughout parameter space and solve optimisation problems when trying to form powerful predictive physical models. This involves using classical statistical techniques, such as Bayesian Statistics, with accurate equation solvers using Monte Carlo Markov Chain methods, with more sophisticated and modern supervised Artificial Intelligence/Machine Learning methods. This Thesis will use a selection of the above with further details provided in the following Chapters.

1.4 How to measure gas in galaxies

Measuring the total gas reservoir involves observing hydrogen, the most abundant element in the universe, in all three of its main ISM phases, namely its ionised, atomic and molecular components. The ionised hydrogen emits light in the visible band as the electrons

recombine with the protons and the neutral atomic and molecular hydrogen emits light in the radio/sub-mm bands of the electromagnetic spectrum. A brief description of the empirical techniques used to quantify gas content arising predominantly from the neutral and molecular phases follows. This Thesis is concerned with quantifying molecular gas, and so emphasis will be placed on that, with only brief discussions regarding neutral gas.

1.4.1 Measuring the atomic gas mass

Neutral hydrogen (HI) atoms are abundant and ubiquitous in low-density regions of the ISM. They are detected using the $\lambda \approx 21$cm (ν_{10}=1420.4 MHz) hyperfine line where two energy levels result from the magnetic interaction between the quantised electron and proton spins (Frosch & Foley 1952). When the relative spins change from parallel to antiparallel, a photon is emitted. The 21cm HI line is an extremely useful tool for **a)** studying gas in the ISM of external galaxies and **b)** tracing the large-scale distribution of galaxies in the universe as HI is detectable in most star-forming galaxies.

If the HI emission from a galaxy is optically thin, then the integrated line flux is proportional to the mass of HI in the galaxy, independent of the unknown HI temperature, as:

$$\frac{M_{\rm HI}}{M_\odot} \approx 2.36 \times 10^5 \left(\frac{D}{\rm Mpc}\right)^2 \left(\frac{S(\nu)}{\rm Jy\ km\ s^{-1}}\right) \tag{1.16}$$

providing the total HI mass of a galaxy. The quantity $S(\nu)$ over the line is called the line flux and is usually expressed in units of Jy km s^{-1}.

1.4.2 Measuring the molecular gas mass

It has been well established that most star formation, in the Milky Way and nearby galaxies, occurs in dense, cold, giant clouds of molecular gas (GMCs) and that most of this molecular gas is in the form of cold H_2; see the recent review by Kennicutt & Evans (2012); Solomon et al. (1987); Young & Scoville (1991); Leroy et al. (2008). Consequently, H_2 plays a central role in the evolution of galaxies. However H_2 lacks a permanent dipole moment, as it is symmetric, resulting in no observable dipolar rotational transitions, hence the cold H_2 is not directly observable.

Astrophysicists resort to using the low-lying rotational transitions from the second most abundant molecule, ^{12}CO, as the molecular gas tracer (see the review by Scoville (2013)). The ground rotational transition of CO has a low excitation temperature, 5.53K,

and a low critical density[1] of 700 cm^{-3}, making it easily excited in cold molecular clouds (Dickman et al. 1986). At a wavelength of 2.6mm the ground state falls within the Earth's atmospheric window allowing it to be easily observed from ground based facilities. Given all this, it has become the workhorse tracer to quantify the total molecular gas reservoir in galaxy evolution studies (Bolatto et al. 2013).

1.4.3 The α_{CO} conversion factor

Although the CO rotational transitions are optically thick in typical conditions, the information on the total molecular gas mass is contained in the width of the line under the assumption that GMCs are virialized and that the line emission is the superposition of a number of such virialized clouds. The correlation between the velocity-integrated line luminosity L'_{CO} in the $1 \rightarrow 0$ transition and the total molecular gas mass is given by the empirical relation (Dickman et al. 1986; Obreschkow & Rawlings 2009).

$$M_{\mathrm{H_2}} = \alpha_{CO(1-0)} L'_{CO(1-0)}. \tag{1.17}$$

Here $M_{H\cdot 2}$ has units of $M_\odot$ and $L'_{CO(1-0)}$ (K km s^{-1} pc^2), the integrated line luminosity, is related to the observed velocity integrated flux density, $I_{CO}\Delta v$ (Jy km s^{-1}), in galaxies following Solomon et al. (1997):

$$L'_{CO(1-0)} = 3.25 \times 10^7 I_{CO} \Delta v \nu_{obs}^{-2} D_L^2 (1+z)^{-3}, \tag{1.18}$$

where the rest frequency, $\nu_{rest} = \nu_{obs}(1+z)$, is in GHz (Solomon et al. 1987) and the luminosity distance, D_L, is in Mpc. Thus α_{CO}, named the CO-to-H_2 factor, can be considered a mass to light ratio. Across observations of the Milky Way and nearby star-forming galaxies, with approximately solar metallicities, the empirical CO(1-0) conversion factors are consistent with a typical value of 4.36 $M_\odot$ (K km s^{-1})$^{-1}$, which includes a 36% correction for Helium gas (Strong & Mattox 1996; Abdo et al. 2010).

1.4.4 An alternative method via dust

While measurements of the mass and properties of the cold gas in the interstellar medium (ISM) are typically obtained via molecular and atomic line spectroscopy, as discussed above, it has been recently shown that far-infrared (FIR)/sub-mm continuum observations

[1]Critical density is defined as the density where the rate of collisional de-excitation is equal to the rate of spontaneous emission. Hence for densities higher than this collision de-excitation dominates and little radiation is emitted, while for densities lower than this the spontaneous decay rate dominates and so there is an emitted photon for each collisional excitation.

of galaxies can also be used to derive total gas masses (Israel 1997; Leroy et al. 2011; Magdis et al. 2011; Eales et al. 2012; Sandstrom et al. 2013; Scoville et al. 2014). First total dust masses are inferred, usually by fitting the far-infrared (FIR) SED with a simple modified black body (Dunne et al. 2000; Vlahakis et al. 2005), and then total gas masses are calculated via the gas-to-dust ratio, of which various metallicity-dependent scalings have emerged (Leroy et al. 2011; Sandstrom et al. 2013).

This method has generated significant interest as it allows for gas masses to be measured for very large samples much more quickly and cheaply than via direct CO and HI measurements; for example, with current astronomical facilities, observing the CO(1-0) transition takes much longer than observing photometric dust continuum emission (Eales et al. 2012). The technique is of particular interest for low-mass and/or high-redshift galaxies with low metallicities, where it is known that CO suffers from photodissociation effects. However, while dust is useful, there are still issues which must be investigated before it can reliably be applied at high redshifts. For example, a simple linear relation between gas-to-dust ratio and metallicity is currently assumed, while there are indications of very large scatter at fixed metallicity (Rémy-Ruyer et al. 2014, 2015; Feldmann 2015), see Figure 1.6, and a possible redshift evolution (Saintonge et al. 2013). Furthermore, questions still linger regarding the usefulness of dust at higher redshifts due to the CMB radiation providing a floor to the dust temperature (da Cunha et al. 2013; Zhang et al. 2016).

However, if these could be addressed, dust provides a fantastic alternative to quantify and measure the total gas contents of galaxies compared to using CO and HI. There is a need for a systematic survey of the dust properties in a variety of galaxies, to benchmark scaling relations with gas contents and stellar, chemical and structural properties. Such work would have major implications for high redshift studies where observers have to look beyond CO(1-0) spectroscopy to quantify the cold ISM.

1.5 Motivation - Testing the equilibrium model

Although substantial evidence has mounted in favour of the equilibrium model, all the above observations have been done for high mass ($>10^{10}$ $M_{\odot}$) and near solar metallicity galaxies. Testing the equilibrium model in the local universe for lower mass and low metallicity galaxies is, so far, uncharted territory; ergo the purpose of this Thesis. Furthermore,

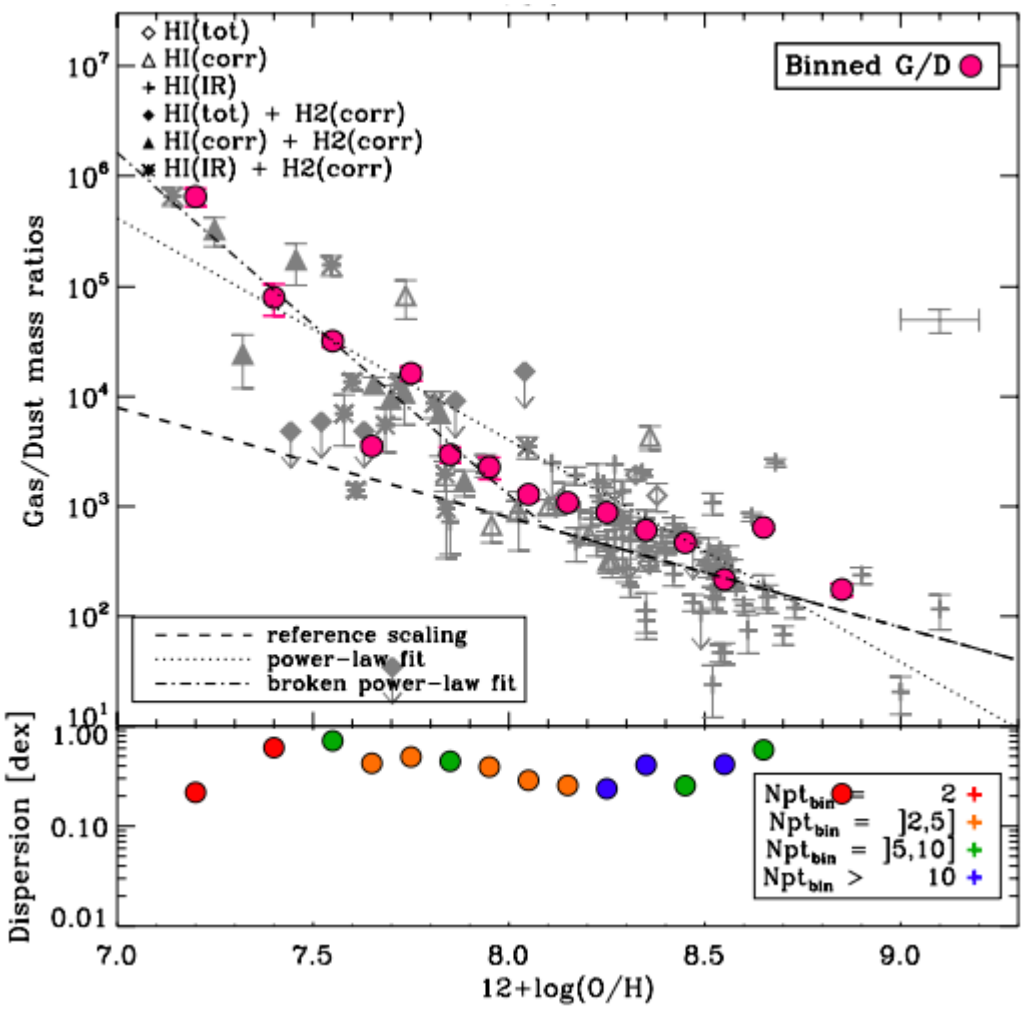

Figure 1.6. The currently observed large scatter of the gas to dust ratio, across a large metallicity range, from Rémy-Ruyer et al. (2014).

at high redshift a constant galactic conversion factor is used to measure molecular gas masses from CO observations; ideally a robust conversion factor should be used. In the local universe, through CO observations, it is clear that there may be a breakdown of the model, see Figure 1.7. Galaxies with stellar mass $< 10^{10}$ $M_{\odot}$ have much lower CO luminosities; ergo their total molecular gas mass, per unit star formation rate, is lower than for their higher mass counterparts. Is this due to a higher star formation efficiency in lower mass galaxies or due to the photodissociation of CO leading to the necessity of higher conversion factors? Such a question can now be solved with the work in this Thesis. Figure 1.7 presents the state of the art in CO observations before the inception of the Thesis. Once a novel conversion function is obtained, in the upcoming Chapters, this Figure will receive an update presented in Figure 5.4.

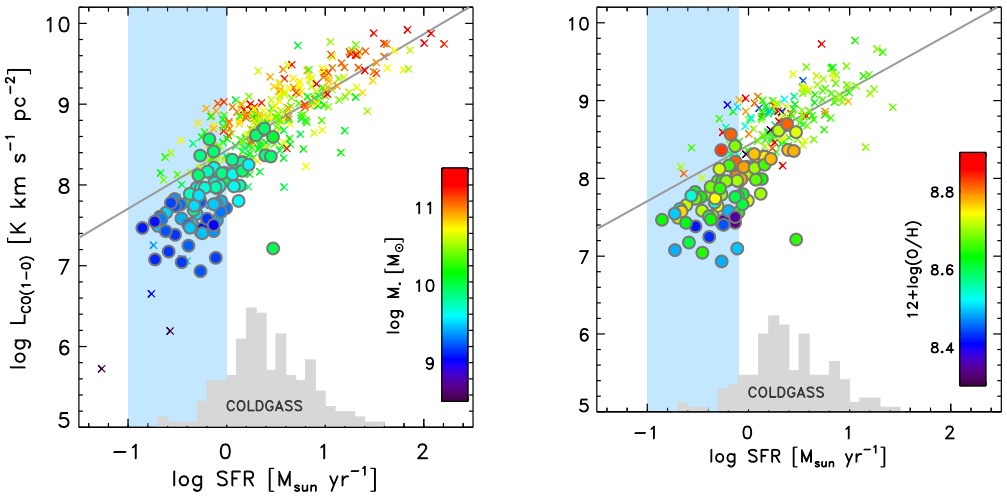

Figure 1.7. Left: A plot of CO(1-0) luminosities, for the full xCOLD GASS sample (to be discussed in Chapter 5), against star formation rate with the colour of each point denoting stellar mass. **Right:** The same as the left plot but now colour denotes metallicity. A slope of one in the above would imply a constant star formation efficiency, defined as the total molecular gas mass per unit star formation rate. Figure courtesy of Dr Amélie Saintonge.

1.5.1 The problem with CO

CO has been difficult to detect in local low mass galaxies and sensitivity has limited CO detections to galaxies with $Z/Z_\odot \geq 0.1$ (Leroy et al. 2009; Schruba et al. 2012; Rémy-Ruyer et al. 2014). Does this mean that these galaxies have low molecular gas reservoirs, or does CO become a poor tracer of the molecular ISM in low metallicity conditions? Indeed there is strong evidence that not all of the H_2 is traced by CO emission; UV radiation from massive stars destroys CO to a cloud depth of a few A_V, which can correspond to a significant fraction of the total gas column in low metallicity clouds (van Dishoeck & Black 1986; Wolfire et al. 2010). While H_2 is self-shielded from this UV radiation, CO relies on dust shielding and therefore, in low metallicity star forming galaxies which have hard radiation fields and lower dust-to-gas mass ratio, CO is easily photodissociated into C^+ and O (Röllig et al. 2006), as illustrated in Figure 1.8.

The regions where molecular hydrogen undergoes a dissociation transition into neutral hydrogen are suitably named photodissociation regions (PDRs[2] hereafter) and it is here that CO is also photodissociated. In this case, the CO flux per fixed hydrogen column

[2]Also known as Photo-Dominated/Photodissociation regions - surfaces of molecular clouds where all the chemical and heating processes are dominated by photochemistry caused by the strong FUV radiation, between $6 - 13.4$ eV. They are also defined as the transition zone between an ionised and dark molecular region, and hence contain neutral and molecular gas.

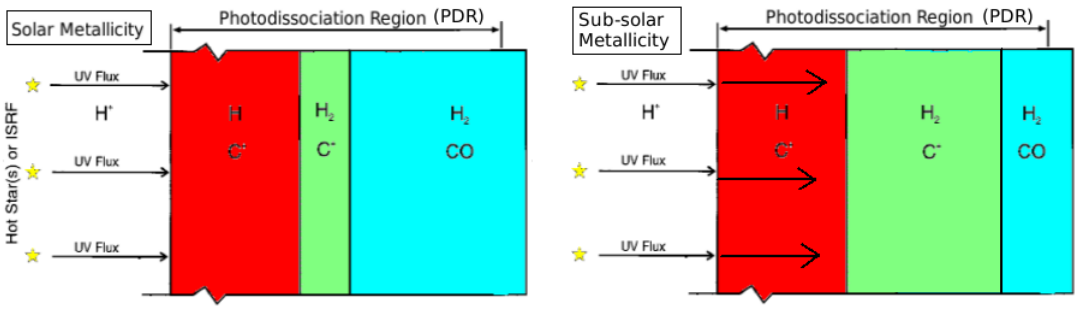

Figure 1.8. Left: The structure of a typical PDR at solar metallicity. UV radiation from young stars impinges onto the surface of the gas leading to the formation of a HII/HI/H_2 layer and a [CII]/[CI]/CO layer. **Right:** As the metallicity decreases the UV radiation penetrates further into the cloud, photodissociating CO, leading to a larger region where [CI] traces the H_2.

is less than in high metallicity environments and, in turn, the Galactic conversion factor globally underestimates the true molecular hydrogen content (Arimoto et al. 1996; Leroy et al. 2011). However, in these low metallicity conditions, it is unknown how much larger the conversion factor should be to account for the H_2 not traced by CO, and how the conversion function varies with galaxy parameters.

A number of studies have attempted to quantify a prescription for the conversion function (Wilson 1995; Israel 1997; Boselli et al. 2002; Israel & Baas 2003; Leroy et al. 2011; Genzel et al. 2012; Schruba et al. 2012; Bolatto et al. 2013; Sandstrom et al. 2013), however the astrophysics community is yet to agree on an accepted prescription and adopt a single method as different assumptions concerning different constant depletion timescales/constant star formation rate efficiencies are usually employed to reach said prescriptions. Furthermore, these aforementioned studies have not built up enough auxiliary data to test secondary dependencies on their conversion functions. Only recently have studies started to use multi-wavelength datasets to test for any extra dependencies (Magnelli et al. 2012), which can explain the scatter found in previous prescriptions (Lee et al. 2015).

1.5.2 Measuring the "dark CO" molecular gas mass

The molecular gas not traced by CO emission is referred to as "dark gas" (Wolfire et al. 2010; Grenier et al. 2005; Smith et al. 2012) and emits brightly in other fine-structure PDR tracers such as [OI] and [CII] due to the photodissociation of CO into ionised carbon and neutral oxygen (Röllig et al. 2006; Poglitsch et al. 1995). By measuring carbon both in its

molecular and ionised form (e.g observing [CII] and CO) in PDRs, alongside a statistically robust sample of galaxies, with a full suite of multi-wavelength observations, is it possible to investigate any secondary dependencies of the conversion function. Such a dataset would allow us to fully parametrise and quantify variations in the conversion function on galaxy properties. This Thesis focuses on using [CII] as a means to quantify this dark molecular gas, and the conversion function.

The [CII] 158μm emission line is one of the strongest coolants of the interstellar medium and can contribute up to a few percent of the total FIR emission from a galaxy (Tielens & Hollenbach 1985). Ionised carbon has a lower ionisation potential, of 11.3 eV, than hydrogen's of 13.6eV (Kaufman et al. 1999; Kauffmann et al. 2003*a*), and the [CII] line lies 92K above the ground state with a critical density for collisions with neutral hydrogen of 3×10^3 cm^{-3} (Kaufman et al. 1999) meaning it emits in PDRs, not traced by CO, and also the ionised and atomic phases of the ISM. It provides a promising tracer to quantify the total dark molecular gas reservoir and was first used in this way in a low metallicity dwarf galaxy (Madden et al. 1997). Ergo measuring [CII] emission from PDRs only, combined with observations of CO (which can only arise in PDRs), can be used **a)** to trace the total molecular reservoir on galaxy wide scales and **b)** to quantify the nature of variations of the conversion function.

1.5.3 The need for accurate radiative transfer modelling

Ionised carbon (C^+) emission is seen to correlate with the total molecular gas mass of galaxies (M_{H_2}), as measured from ^{12}CO emission, and with the total star formation rate inferred from FIR luminosity (de Looze et al. 2011). For these reasons, [CII] is an important and widely used tracer of massive star formation in galaxies at both low and high redshifts (Stacey et al. 2010).

While [CII] originates in good part from PDRs, explaining the correlation with M_{H_2} and SFR, observations have shown that a non-negligible fraction of the emission can originate from the ionised and diffuse atomic gas components where massive star formation does not occur (Heiles et al. 1994; Vasta et al. 2010; Langer et al. 2010; Pineda et al. 2013), as shown in Figure 1.9.

The CO molecule, as a tracer of the cold molecular phase of the ISM, suffers from the opposite problem: in low metallicity environments, the CO molecule can be photo-dissociated by UV radiation while H_2 self-shields and survives, resulting in the presence

of molecular gas that is missed by CO observations. For example, Velusamy et al. (2010) find that $\sim$ 25% of the molecular gas in the Milky Way may be CO-dark in such a way. If it were possible to discern the contribution of the different ISM phases to the total [CII] emission, then the combination of CO and [CII] measurements could increase significantly the accuracy of $M_{\rm H_2}$ calculations (Mookerjea et al. 2016). There is also a new interest in using [CII] as a probe of the ISM in $z > 5$ galaxies, up to the epoch of reionisation; such studies are now made increasingly possible with facilities such as ALMA and NOEMA (e.g. Ota et al. 2014; Riechers et al. 2014; Maiolino et al. 2015). In this context also, disentangling the contributions from the different phases of the ISM is of significant importance, yet this problem remains unsolved.

Solving this problem requires one of two things: either high spatial resolution observations of several FIR lines such as [NII]122,205μm and [OI]63,145μm in addition to [CII], or a self-consistent model of the ISM on galaxy-wide scales, including PDRs, ionised and neutral diffuse regions. Since such detailed observations are only available for a handful of very nearby galaxies, this Thesis focuses on the radiative transfer modelling approach. To computationally solve such a problem one needs to model the different phases of the ISM, in PDRs and ionised regions, on galaxy-wide scales, in a self-consistent unified manner.

1.6 Radiative transfer

An understanding of how the interaction between gas, dust and photons in a galaxy change the chemical and physical state of the ISM is crucial in trying to link gas properties with ongoing star formation. Understanding how molecules form, the precursor to star formation, and how their physical properties can change is of upmost importance in ISM studies. Quantifying the amount of CO photodissociation and carbon production is of particular interest here. Most of the ISM mass is contained in two regions: photodissociation regions (PDRs) and photoionisation regions. These two regions often lie next to each other, as shown above in Figure 1.9, as they represent regions where photons have energies less than and greater than the ionisation potential of hydrogen, respectively. The two are associated with neutral and ionised gas, respectively, where the PDRs include molecular material (mostly H_2 and CO).

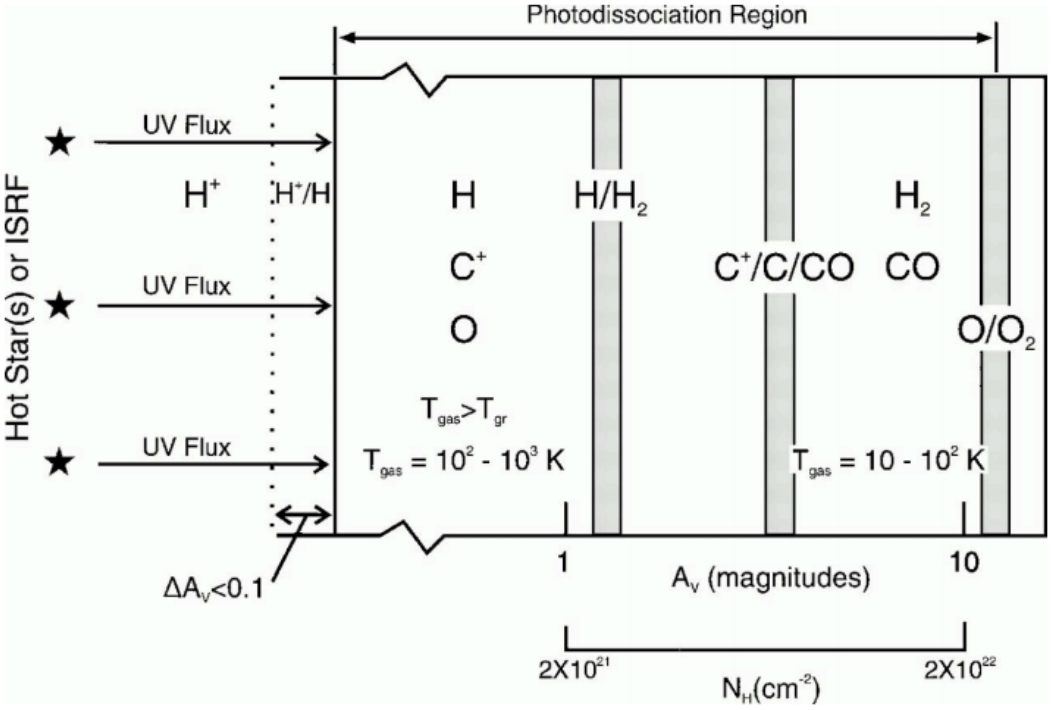

Figure 1.9. A more detailed schematic diagram of a PDR region, illuminated from the left, where UV radiation extends from the predominantly atomic surface region to the point where O_2 is not photodissociated (at $A_v \sim 10$) (Hollenbach et al. 1991). Figure taken from Prof James R. Graham's lecture slides, UC, Berkeley.

1.6.1 The physics of photoionisation (HII) regions

High energy ultraviolet light from stars provide the source of energy that radiates any nearby gas, leading to photoionisation of the gas, and the formation of a HII region/Strömgren Sphere. During this process, where energy is transferred to the cloud, photons with energy greater than the hydrogen ionisation potential, 13.6eV, are absorbed and the excess energy of the photons is converted into kinetic energy of a photoelectron. Electron-electron and electron-ion collisions have energies distributed as a Maxwellian velocity distribution with temperatures in the range 5,000K $<$ T $<$ 20,000K. These photoelectrons also excite the low lying energy levels of ions, such is the case with [CII]. At the typical low densities of ionised regions the probability of collisional de-excitation is smaller than other downward radiation transitions, hence forbidden transitions dominate in emission and absorption, such as the [CII] 158μm emission line. This line is excited via collisions with electrons in photoionisation regions and therefore has a critical density of $\sim 40 - 50$ cm^{-3}, as temperatures in the ionised gas can range anywhere from $\sim$5,000K to $\sim$10,000K (see Table 1.1).

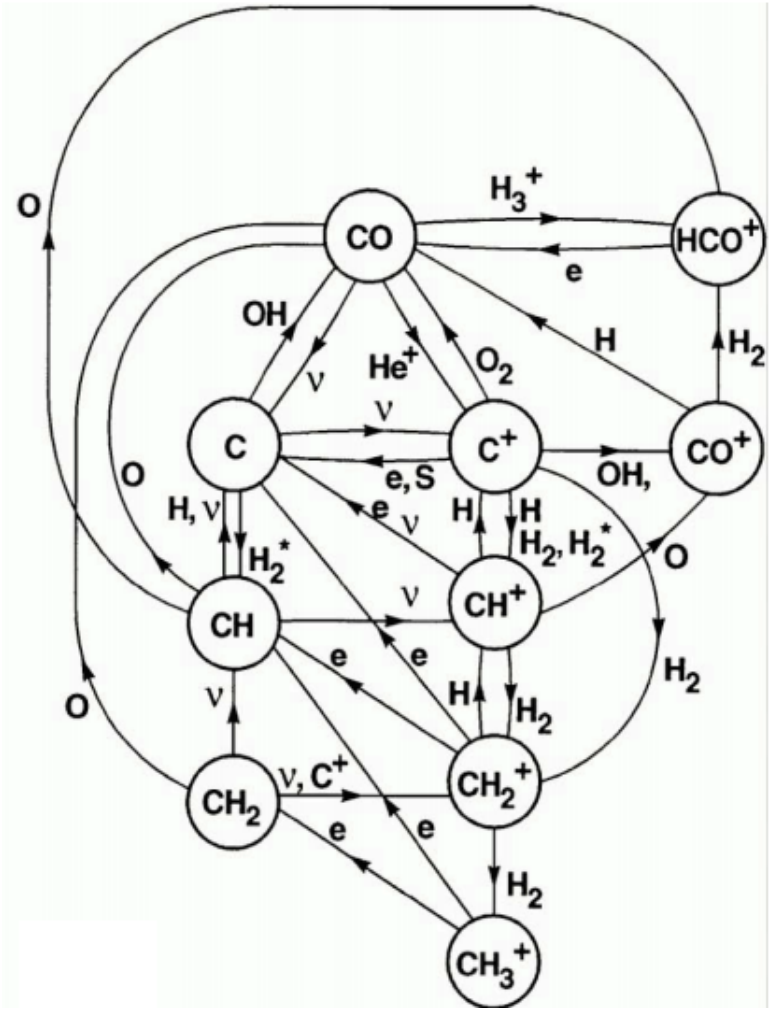

Figure 1.10. The most important reactions in the chemistry of carbon compounds. CO is photodissociated to **(a)** ionised carbon either directly via the reaction with a He^+ free radical or indirectly via reactions with cosmic rays **(b)** neutral carbon directly via reactions with cosmic rays. These reaction routes will be important in Chapter 4 and are taken from Sternberg & Dalgarno (1995).

Table 1.1. Critical Densities for the [CII] 158μm Fine Structure Line (cm^{-3}) for different collision partners from Goldsmith et al. (2012)

Temperature(K)	Electrons	Atomic Hydrogen	Molecular Hydrogen
20	5	3800	7600
100	9	3000	6100
500	16	2400	4800
1000	20	2200	4400
8000	44	1600	3300

Thermal electrons are recaptured by the ions and the degree of ionisation at each point within the HII region is fixed by the equilibrium between photoionisation and recombination. The total radiation field is the sum of the stellar and the diffuse components. The stellar component consists of photons emitted directly by the stars/the local ionising source, whereas the diffuse component is emitted by the gas.

Photoionisation

Photoionisation occurs when, during the interaction of a photon with an atom, the photon transfers its energy to one of the bound electrons, which then escapes leading to the formation of an ion. Any photons with wavelengths shorter than the Lyman limit of $912\mathring{A}$ are sufficiently energetic to ionised hydrogen atoms, leading to the formation of HII regions. The higher the temperature and luminosity of the ionising source, the higher the degree of ionisation in these regions. Hydrogen is the most abundant element in the ISM, however it is possible to find heavier elements in various ionised states (singly, doubly ionised etc). The photoelectrons released in the ionisation process then collide with other ions exciting atoms in the region, which then emit in forbidden spectral lines. As these lines are suppressed by collisional de-excitation at laboratory densities, it is impossible to detect them in the lab, hence they are referred to as forbidden lines.

Approximating the region as a sphere with uniform density, the UV flux, which originated from the nearby star and now permeates through the cloud, decreases with distance from the star due to geometric dilution and absorption along the photon path through the gas. This continues until a radius where the UV energy is less than 13.6eV, the potential energy of hydrogen, and hence photons can no longer ionise the gas. This leads to a transition of hydrogen from its ionised to neutral form; the radius at which this occurs is known as the Strömgren radius. Beyond this, the gas is neutral. We now hit the beginning of the neutral ISM phase, also known as the PDR.

1.6.2 The physics of photodissociation regions (PDRs)

In PDRs, photons have wavelengths longer than the Lyman limit, and so are unable to ionise hydrogen, leading to chemistry driven by photoionisation of heavier elements, photodissociation and photochemistry. The radiative transfer of the FUV photons affects the survival of the two most important molecules, H_2 and CO. There are many physical parameters which affect the conditions within PDRs, but the two most important are the

hydrogen nuclei number density and the strength of the FUV radiation field. The definition of the surface of the PDR is then the point at which the FUV radiation field impinges onto neutral gas (e.g it starts at the transition zone between ionised and neutral gas.) PDRs also contain the transition zone between the neutral and molecular phase of hydrogen and it is this molecular gas which is the precursor for star formation. Therefore, being able to simulate conditions in PDRs to understand the average ISM physical properties and conditions is crucial when trying to test the equilibrium model and constrain variations in the conversion function (discussed above in Section 1.5.1).

Dust grains within PDRs shield the gas from the harsh UV radiation field, allowing temperatures to drop to as low as 10-30K limiting the ionisation of species within, while also providing a surface for the formation of molecular hydrogen. These dense cool cloud regions fragment and collapse to form stars. FUV radiation is also attenuated by dust grains as they absorb and scatter light at visible and UV wavelengths. The attenuation of the FUV flux with distance gives rise to a characteristic depth dependent chemical structure, separated into distinct zones with different gas-phase reactions. Furthermore, as FUV radiation still penetrates into the cloud photo-reactions are important alongside reactions with cosmic ray protons.

The Chemistry of PDRs - H_2 and CO

The formation of H_2 starts with a hydrogen atom being adsorbed onto the surface of a dust grain. The atom collides with the surface and sufficient energy is then dumped into vibrational modes of the grain so that the atom can now stick to the grain via Van der Waals bonds. These hydrogen atoms then quantum-mechanically tunnel among the possible adsorption sites on the grain surface, until they react to form molecular hydrogen. The bond energy of H_2 (4.5 eV) is sufficient to detach the molecule from the grain and release it into the gas phase. The destruction of H_2 is usually driven by UV radiation, since at molecular cloud or even PDR temperatures, collisional dissociation is inefficient. The principal interaction of UV photons with H_2 involves excited electronic states leading to the Lyman and Werner band absorption lines. As one moves into a PDR, the molecular hydrogen becomes self-shielding at column densities $N(H_2)>10\ cm^{-2}$. That is, the radiation in the Lyman and Werner series lines has already been absorbed, so that the FUV radiation that filters into the PDR becomes less efficient (it must excite weaker H_2 lines or operate farther from line centre). The rate of photodissociation is then

suppressed by a self-shielding factor which is inversely proportional to the column density; hence why, as one moves deeper into the PDR, hydrogen gas becomes mostly molecular.

At the beginning of the transition from the HII region to the PDR, carbon is mostly in ionised form owing to its ionisation potential energy being less than hydrogen's, hence it is photoionised by FUV radiation. However, as one goes deeper into the PDR, dust absorbs the FUV photons and some self-shielding of neutral carbon takes place, leading to carbon becoming mainly neutral. The transition to neutral carbon is also characterised by the formation of the molecule CO. This is a tightly bound molecule (bond energy 11 eV) and its formation can be catalysed by a variety of non-radiative molecular reactions starting from O, H_2, and C/C^+. The most important reactions in the chemistry of carbon are schematically shown in Figure 1.10. The photodissociation of CO is caused by the absorption of an FUV photon to an excited electron state, followed by a transition to a repulsive electronic state and hence dissociation. While H_2 can self shield from the FUV radiation field, as discussed above, CO can only shield itself via nearby dust grains. CO can self-shield in the same way as molecular hydrogen, as its photoionisation occurs via line absorption, however the contribution of self-shielding to the total shielding is small; this is because the absorption lines of CO do not become optically thick, hence the column density term is small compared to hydrogen's, because of the low abundance of CO relative to H_2. Molecular hydrogen therefore can effectively shield itself, since its lines become optically thick whereas CO can not. As one moves further into the cloud, fewer H_2 and CO molecules are dissociated by FUV photons.

The HII/HI/H_2 layer

The different ionisation stages of hydrogen and carbon, in a PDR, are schematically shown in Figure 1.9. The penetration of FUV radiation influences the chemistry, giving rise to these distinct zones. At the surface of the PDR, ionised hydrogen rapidly recombines, leading to the formation of a H^+/H layer, whereas molecular hydrogen is rapidly photodissociated, as described above. Therefore the surface layer of the PDR consists mainly of atomic hydrogen while, further into the cloud, the FUV flux begins to attenuate and the formation of H_2 starts to dominate over photodissociation. This leads to the formation of a H/H_2 layer which plays an important role in the PDR chemistry as further reactions are initiated once molecular hydrogen is sufficiently abundant; these additional reactions lead to the formation of other molecular species such as H_2O, O_2 and CO.

The [CII]/[CI]/CO layer

The photoionisation of atomic carbon creates a distinct layer of ionised carbon at the beginning of the PDR. Because of the self-shielding of H_2, the layer of [CII] extends to a greater depth than the HI zone. Moreover, the H_2 shielding actually allows for a layer in which the carbon is ionised while the hydrogen is in molecular form. This region contains the "dark-CO" H_2 gas, as it's traced by [CII], and is of crucial importance for this Thesis. Generally the [CII] zone extends out to $A_v \sim 2$ mag and ionised carbon, in this environment, is very important as it allows for the start of chemical reactions producing carbon bearing free-radicals (Figure 1.10). In the PDR, collisions are predominantly with neutral hydrogen and therefore the [CII] line has a critical density of $\sim 3 \times 10^3$ cm^{-3} in these regions (Table 1.1).

As we venture deeper into the cloud, the abundance of these free radicals decreases, leading to the formation of complex hydrocarbons, and the ionised carbon abundance also decreases. While the FUV radiation penetrates deeper into the cloud and is further attenuated, the C^+ undergoes radiative recombination and charge transfer with atomic sulphur causing the density of neutral carbon to spike up beyond this point, creating a [CII]/[CI] transition zone. At these depths, the UV radiation becomes severely attenuated and ionised carbon can also make the transition from a singly ionised state to molecular state in CO, leading to a coexisting transition zone of [CII]/CO. At greater depths carbon is predominantly in the form of CO and the atomic carbon abundance drops rapidly.

1.6.3 Multi-phase radiative transfer modelling

Although numerical models for the individual components of the ISM are aplenty, codes which can simulate all aforementioned phases of the ISM consistently are not so common. One very successful example is CLOUDY (Ferland et al. 2013), a plasma simulation which models the ionisation, chemical and thermal state of the gas that may be exposed to an external radiation field coming from nearby heating sources such as star clusters. The code works by predicting the spectrum from this non-equilibrium gas and simulating its level populations as well as its ionisation, molecular and thermal states, over a wide range of densities and temperatures. However, CLOUDY is intrinsically a 1D code, and involves assumptions concerning the thermal balance in PDRs. Both of these limitations should be addressed to accurately simulate the entire ISM of star-forming regions and galaxies.

Indeed, it has been shown that results from 1D and 3D simulations vary depending on the specific physical conditions (Ercolano et al. 2012). An example of a successful attempt at building such a 3D, multi-phase radiative transfer code is TORUS-3DPDR (Bisbas et al. 2015*a*), a hydrodynamics and Monte Carlo radiative transfer code. TORUS-3DPDR does not use the complexity of other photoionisation-only codes to calculate particular photoionisation calculations and therefore will not be as accurate.

1.7 This Thesis

In this Thesis a new multi-phase 3D radiative transfer interface is first presented that couples STARBURST99, a stellar spectrophotometric code, with the photoionisation and astrochemistry codes MOCASSIN and 3D-PDR. Entire star forming regions are simulated, including the ionised, atomic and molecular phases of the ISM, followed by a qualitative investigation of parameter space in Chapter 2. This is followed, in Chapter 3, by a Bayesian inference methodology to parametrise how the fraction of [CII] emission originating from molecular regions, $f_{\rm [CII],mol}$, varies as a function of typical integrated properties of galaxies in the local Universe.

Once this has been achieved, in Chapter 4, results using xCOLD GASS, a legacy survey of molecular gas in nearby galaxies, is presented, extending down to stellar masses of $10^9 M_{\odot}$. Using the IRAM 30m telescope the CO(1−0) line and, with Herschel PACS observations, the [CII] 158μm emission line were both measured for a sub-sample of 24 intermediate mass ($9 < \log M_*/M_{\odot} < 10$) and low metallicity ($0.4 < Z/Z_{\odot} < 1.0$) galaxies. The combined observations of carbon, both in its molecular and ionised forms, leads to the provision of the first scaling relations for the integrated and molecular region $L_{\rm [CII]}/L_{\rm CO(1\text{-}0)}$ ratio as a function of galaxy properties. Connecting the $L_{\rm [CII]}/L_{\rm CO(1\text{-}0)}$ ratio to the CO-to-H_2 conversion factor follows where a multivariate conversion function is derived. This relation can be used up to $z \sim 2.5$.

Applying this new conversion function to the full xCOLD GASS and PHIBSS1 surveys, in Chapter 5, leads to the investigation of molecular gas fraction and gas depletion time scaling relations. A discussion on the implications for the equilibrium model follows with commentary on the redshift evolution of depletion time and molecular gas fractions. Finally the new upcoming JINGLE survey is presented, in Chapter 6, which aims to provide an alternative method to quantify the gas content of galaxies. The capabilities of a new

Bayesian tool to fit dust SEDs are also explored. Finally, the summary and conclusions from this work are given in Chapter 7.

Throughout this Thesis a standard flat ΛCDM cosmology with $H_0 = 70$ km s^{-1} Mpc^{-1} and a Chabrier IMF (Chabrier 2003) are used.

Chapter 2

Multi-phase Radiative Transfer modelling of Star Forming Regions

In this chapter, we[1] present a new modelling interface which combines self-consistently state of the art astrochemistry and photoionisation codes: 3D-PDR, a three-dimensional code for treating PDRs and molecular regions, MOCASSIN, a full 3D Monte Carlo photoionisation code, and STARBURST99, a stellar population synthesis code. This integrated code is used to simulate entire star forming regions, including the ionised, neutral and molecular phases of the ISM, with the aim of measuring how the fraction of the total [CII] emission originating from molecular regions, $f_{\rm [CII],mol}$ varies as a function of the physical properties of each star forming region.

2.1 Overview of numerical codes

We here briefly describe each of the codes used within this work. For a more detailed explanation of each individual code see the references detailed in their respective sections.

[1]The pronoun 'we' refers to the group of scientists with whom I have collaborated, to achieve the science results presented throughout this Thesis. This convention will be used throughout this work, unless otherwise stated.

2.1.1 The STARBURST99 code

STARBURST99 (Leitherer et al. 1999, 2010; Vázquez & Leitherer 2005; Conroy 2013), hereafter SB99, is a multi-purpose evolutionary synthesis code which models the spectrophotometric properties of unresolved stellar populations, and makes predictions for various observables, such as spectral energy distributions, supernovae rates, and mass loss rates. The code simulates a population of stars based on an input metallicity and stellar initial mass function (IMF), and evolves them across the Hertzprung-Russell diagram. At each time interval, individual stars are assigned a spectrum based on their masses and evolutionary states, and the integrated spectrum for the population is obtained by summing over these contributions. SB99 can thus provide the relation between the stellar mass (M_*) and luminosity (L_*) of the stellar population at any time interval.

2.1.2 The MOCASSIN code

Photoionisation codes, used to model the HII regions, have likewise been around for several decades now. They typically work by solving the equations of radiative transfer while making assumptions concerning spherical symmetry. The earliest HII region models contained the basic physics of ionisation, recombination of hydrogen and helium, thermal balance, and the emission of photons from the nebula (Flower 1968), with subsequent codes including other important physical processes such as charge exchange and dielectric recombination, and the consideration of a wider range of ions. More recently, three dimensional codes have been developed to handle varying geometries using a Monte-Carlo approach to solve the 3D equations of radiative transport (Wood et al. 2004).

We here use the numerical code MOCASSIN (MOnte CArlo SimulationS of Ionised Nebulae) (Ercolano et al. 2003), a three-dimensional Monte Carlo (MC) radiative transfer code which operates on a non-uniform cartesian grid. It was originally intended as a tool to construct realistic gas models of planetary nebulae, but has since evolved to incorporate dust radiative transfer (Ercolano et al. 2005) and is now used to simulate ionised gas emission on galaxy-wide scales (Karczewski et al. 2013). Photoionization calculations are performed using an iterative Monte Carlo photon energy packet propagating routine, based on the methods presented by Lucy (1999). Photons are emitted from the ionising source in random but isotropic directions, and propagate for a path length, l, determined by a randomly-selected optical depth (Harries & Howarth 1997). An abundance file is

used as an input, providing the chemical abundance of each species, along with an input SED and files specifying the dust properties, opacities, cross-sections etc. Given these, the code self-consistently solves the radiative transfer equations and calculates the gas and dust temperatures, ionisation degree, and the overall emergent SED of the full dust, gas and stars network.

At each grid point the electron number density and chemical abundance are specified and hence the code allows for arbitrary non-uniform three-dimensional geometries, allowing for more precise simulations of non homogenous physical and chemical conditions. The code also allows dust-only, gas-only or dust and gas simulations, with multiple ionising sources and with multiple dust species of arbitrary size. Given these input parameters the code self-consistently solves the radiative transfer equations and calculates the gas and dust temperature, ionisation degree, and the overall emergent SED of the full dust, gas and stars network.

Below we provide a brief overview emphasising the key features of the MC photoionisation techniques.

Monte Carlo Photoionisation

Energy packets are bundles of photons where the total energy, ϵ, remains constant while the number of photons contained in the bundle varies for different frequencies ν. In the model, which requires an input stellar spectrum, the constant energy value ϵ for each photon packet is simply the total energy emitted by the stellar source (e.g the total luminosity, L) during the duration δt of the iteration divided by the total number of photon packets N (which is specified by the user) such that:

$$\epsilon = \frac{L\delta t}{N}. \tag{2.1}$$

From here ensues the Monte Carlo approach: Photons are then emitted from the ionising source in random, but isotropic, directions where they will propagate for a path length, l, determined by a randomly selected optical depth. The length l is determined by the position at which the next event will occur. The possible events which occur are either an interaction with the material (such as a scattering or absorption) after traversing a random optical depth given by:

$$\tau = \ln(1 - \epsilon) \tag{2.2}$$

where ϵ is a randomly selected number between 0 and 1, detailed in Harries & Howarth (1997). If a photon fails to escape a cell after travelling an optical depth τ then the photon

either is absorbed or scattered where the probability of these events are calculated from the absorption and recombination coefficients. Furthermore, once a photon is absorbed an emission event can occur, again calculated from appropriate emission probabilities.

The Monte Carlo approach is successful because, by tracking every photon/energy packet, it easy to determine where in the simulation grid energy is being absorbed. When energy is deposited at a given location the local medium is heated and, whenever this occurs, the new local temperature is calculated and the packet is then re-emitted accordingly. The packets are followed through the region, as they undergo scatterings and absorptions followed by re-emissions, with the temperatures being updated after each event, until the packets reach the edge of the nebula and escape to infinity, hence contributing to the emergent spectrum. Once all the stellar photon packets have escaped, the resulting envelope temperature and the emergent spectrum are correct without the need of any further iterations.

The code tracks all photons, their interactions across the cartesian grid and calculates the energy density at each given cell in the three dimensional space. The energy density dU of a radiation field is given by:

$$dU = \frac{4\pi J_\nu}{c} d\nu \tag{2.3}$$

where J_ν is the specific intensity at a given frequency ν. For a photon packet travelling a length l it therefore contributes a total energy $\epsilon l / c\delta$t and so by summing over all paths the energy density of a given cell of volume V can also be determined as:

$$dU = \frac{\epsilon}{c\delta t} \frac{1}{V} \sum_{d\nu} l. \tag{2.4}$$

This Monte Carlo approximation makes it possible to solve for the ionisation fractions of a given species. The calculations of this are performed iteratively until the temperature and ionisation fractions converge. Please see Ercolano et al. (2003) for further details and references therein.

Thermal Balance and Model Chemisty

An abundance file is used as an input for the code providing the chemical abundance of each species. Files specifying the dust properties, opacities, cross-sections, sizes, different grain species etc are included as input files into the code (there is a folder within the downloadable software containing all the dust files) and hence dust radiative transfer is simultaneously computed along with that of the gas.

The heating and cooling rates are calculated from the summation of trajectories of photon packets through the cell and the ejection of photoelectrons through the cell. The summations of these terms enables the calculations of the heating and cooling rates and the temperature will reach convergence once the heating and cooling rates are balanced. Heating is dominated by photoionisation as photoelectrons are ejected from Hydrogen and Helium with thermal energies of a few eV. Cooling is dominated by electron-ion collisional excitation of metal ions followed by emission of forbidden lines from low-lying fine structure levels.

2.1.3 The 3D-PDR code

Numerical codes treating PDRs have been around for decades and have now grown into complex models capable of solving the thermal balance equations and chemical reactions occurring within these regions (Viti 2013). Some codes have aimed to include all the small scale physics to describe the chemical and thermal processes at work in the gas and grains, while others focus on treating the gas-grain chemistry while approximating other processes. Various codes treating one dimensional PDRs have been developed in the past and only recently three-dimensional codes have emerged which can treat PDRs of an arbitrary density distribution (Bisbas et al. 2012). Furthermore, calculations typically treat the ionised and PDR regions separately (Röllig et al. 2006), which is problematic for emission lines such as [CII] that originate in both these phases of the ISM and can lead to overestimations of line intensities and incorrect interpretations of the physical conditions in the ISM (e.g. hydrogen column density and incident ionisation field).

We here use 3D-PDR code (Bisbas et al. 2012), a three-dimensional astrochemistry code which simulates PDRs of arbitrary density distribution. It solves the chemistry and the thermal balance self-consistently in each computational element of a given cloud and uses the chemical model features of Bell et al. (2006). Like MOCASSIN, the code has been used in various extragalactic applications such as modelling molecular line intensities in NGC 4038 (Bisbas et al. 2014) and neutral carbon mapping (Offner et al. 2014).

Ray-tracing scheme

3D-PDR uses a ray-tracing scheme based on the HEALPIX (Górski et al. 2005) package which calculates properties along a given line of sight. This allows for the quick calculation of a) column densities of species along a particular direction b) the attenuation of the

Draine field[2] in the PDR and c) the propagation of the FIR/submm line emission out of the PDR.

The attenuation of the UV field, χ, at point, p, is evaluated using the equation

$$\chi(p) = \frac{1}{N_l} \sum_{\mathbf{q}=1}^{N_l} \chi_0(\mathbf{q}) e^{-\tau_{UV} A_V(\mathbf{q})} \tag{2.5}$$

where χ_0 is the unattenuated UV field magnitude along the HEALPIX direction $\mathbf{q}$. N_l is the number of HEALPIX rays at level of refinement l while τ_{UV} =3.02 is a factor converting the visual extinction to UV attenuation (Bell et al. 2006), and A_V is the visual extinction along the line of sight $\mathbf{q}$ defined as

$$A_V(\mathbf{q}) = A_{V,o} \int_L^0 n_H dr. \tag{2.6}$$

In the above equation $A_{V,o} = 6.3 \times 10^{-22}$ mag cm^2 and the integration is performed along the line of sight of length L of the column density of hydrogen.

Thermal Balance and Model Chemistry

The chemistry and thermal balance are calculated self-consistently at each depth of the cloud providing chemical abundances, line emissivities and gas temperatures as a function of depth. At each depth the model calculates the attenuation of the FUV field, as described above, before determining the gas temperature at which the total heating and cooling rates are equal; thus reaching a state of thermal balance.

The reaction rates within the chemical network are taken from the UMIST 2012 chemical network database in McElroy et al. (2013). Extinction within the cloud is calculated assuming a grain size of 0.1μm[3], albedo of 0.7 and a mean photon scattering by grains of $g = 0.9$. Emission and fine structure lines are calculated using the escape probability method of de Jong et al. (1980) and non-LTE level populations determined from the collisional rate coefficients explained in Bisbas et al. (2012).

Moreover, for the H_2 and CO photodissociation rates, the code adopts the treatments of Lee et al. (1996) and van Dishoeck & Black (1988). To account for the shielding of CI the code uses the treatment of Kamp & Bertoldi (2000) in order to estimate the

[2]The Draine field is defined as the integral of the SED in the far-UV range between 912 to 2400Å, for photons between $6 < h\nu <$13.6eV, representing Lyman continuum photons and hence the strength of the UV radiation field.

[3]This is a typical value hard-coded into 3D-PDR. Variations of the grain size is not expected to change the results presented here as the total dust emission contributing to the cooling rate depends on the amount of available dust. At a fixed dust mass the size of the grains will not change these results as dust FIR continuum emission, assumed to be optically thin, only depends on the total dust mass.

photoionisation rate of carbon. The rate of molecular hydrogen formation on dust grains is calculated using the treatment of Cazaux & Tielens (2004) while the thermally averaged sticking coefficient of hydrogen atoms on dust grains is taken from Hollenbach & McKee (1979). The dust temperature at each point in the density distribution is calculated using the treatment of Hollenbach et al. (1991) to account for the grain heating due to the incident FUV photons.

2.2 Self-consistent coupling method

To self-consistently couple all three of the above codes it is important to use as many outputs from one model as inputs for subsequent models, ensuring consistency within the full simulation. This coupling technique was first attempted in Vasta (2010) to model carbon and oxygen emission in nearby galaxies. We describe here how each code is numerically coupled to the other models, with a detailed discussion of the specific input parameters and their values presented in Section 2.3. Spherical symmetry is assumed throughout this paper, in all phases of the ISM and for all the simulated 3D clouds. Although MOCASSIN and 3D-PDR are both fully capable of handling non-uniform densities, this will not be used here.

2.2.1 Coupling STARBURST99 to MOCASSIN

A stellar radiation density field, coming from the stellar population within our simulated star forming regions, is created using SB99. From this output SB99 stellar spectrum, the luminosity, temperature and number of ionising photons of the source are calculated; these quantities are then used as input parameters for the 3D photoionisation code MOCASSIN. In this way, the radiation field is coupled with the photoionisation in the HII region. Therefore the stellar SED, luminosity, temperature and the number of ionising photons from the ionising source are the important outputs taken from SB99 used as input parameters into the 3D photoionisation code MOCASSIN.

By assuming blackbody radiation, the temperature and luminosity of the stellar cluster is calculated by the following

$$\mathrm{T_{source}} = \frac{2.90 \times 10^{7} \text{Å K}}{\lambda_{\mathrm{max}}} \tag{2.7}$$

$$\mathrm{L_{source}} = \int_{0}^{\infty} f(\nu) d\nu \tag{2.8}$$

$$\text{Number of Ionising Photons} = \int_0^\infty \frac{f(\nu)}{\nu} d\nu \tag{2.9}$$

where $\lambda_{\max}$ is the wavelength at which the stellar SED peaks, in units of Angstroms and $f(\nu)$ is the frequency dependent flux of the SED.

2.2.2 Coupling MOCASSIN to 3D-PDR

Henney et al. (2005) showed how dynamical processes, such as gas flows and thermal gas pressure, link the HII and PDR regions, which are simulated here by MOCASSIN and 3D-PDR, respectively. The physical properties of the PDR are a consequence of the transport of gas, dust and radiation through the ionised region, while the converse is also true. Other than in the case of a very fortuitous choice of initial conditions, simply matching boundary conditions between quantities such as temperature and density, of the two regions, can lead to discontinuities in the thermal and dynamical pressure across the two ISM phases. Only by physically coupling the two regions is it possible to get an accurate representation of the multi-phase ISM; this modelling philosophy is at the heart of this work as we aim to self-consistently calculate the temperature, ionisation, and density at the face of PDR regions.

The output of the MOCASSIN code is the SED of the ionised gas, dust and stars emerging from the HII region, along with the flux in the most important far infrared fine structure emission lines from the ionised gas, such as [CII]. We calculate the strength of the radiation field, G_0, at the ionisation front between the HII and neutral gas regions by integrating the MOCASSIN SED in the far-UV range between 912 to 2400Å, which corresponds to the classical Draine field definition given by Draine (1978) for photons between $6 < h\nu < 13.6$eV, representing Lyman continuum photons. This value of G_0, once converted to Draine field units (1 Draine = 2.74 erg s^{-1} cm^{-2}), is used as an input into 3D-PDR. We also need to ensure that MOCASSIN only simulates the gas up to the edge of the ionised region and does not leak over into the neutral regions (which 3D-PDR will simulate). To this end, we first calculate the outer radius of the ionised cloud simply by running MOCASSIN to a very large radius, and then inspecting at which radius the ionised Hydrogen abundance is less than 10%, ensuring the end of the ionised region has been reached; this is taken to be the outer radius of the ionised part of the star forming region. The inner radius of the PDR is equal to the outer radius of the ionised region, ensuring that the PDR is adjacent to the ionised region (see Section 2.3.2 for further details).

To ensure that the temperature and density between the two regions are consistent, we further link the HII and PDR regions by assuming constant total pressure at the interface. This pressure originates from internal radiation, from the gas and dust, and the thermodynamic gas pressure. Constant pressure is an approximation to the actual flow which has been assumed by previous authors such as Carral et al. (1994), Abel et al. (2005) and Ferland et al. (2013). Therefore, the pressure equation of state between the two regions is as follows:

$$\begin{aligned} n_{\rm HII}\, k_{\rm b} T^{\rm gas}_{\rm HII} + \frac{\epsilon^{\rm HII}_{\rm gas}\, \sigma_{\rm b} T^{4,\rm gas}_{\rm HII}}{c} + \frac{\epsilon^{\rm HII}_{\rm dust} \sigma_{\rm b} T^{4,\rm dust}_{\rm HII}}{c} \\ = n_{\rm PDR} k_{\rm b} T^{\rm gas}_{\rm PDR} + \frac{\epsilon^{\rm PDR}_{\rm gas} \sigma_{\rm b} T^{4,\rm gas}_{\rm PDR}}{c} + \frac{\epsilon^{\rm PDR}_{\rm dust} \sigma_{\rm b} T^{4,\rm dust}_{\rm PDR}}{c}. \end{aligned} \tag{2.10}$$

where $n_{\rm HII}$ and $n_{\rm PDR}$ are the electron number densities in the HII and PDR region, respectively, $k_{\rm b}$ is the Boltzmann Constant, $\sigma_{\rm b}$ is the Stefan Boltzmann constant, while $\epsilon_{\rm gas}$ and $\epsilon_{\rm dust}$ are the emissivities of the gas and dust species. $T^{\rm gas}_{\rm HII}$ and $T^{\rm dust}_{\rm HII}$ are the gas and dust temperatures at the edge of the HII region, as calculated from the MOCASSIN output. Since $n_{\rm HII}$ is one of the input parameters of our code, the above equation needs to be solved for for $n_{\rm PDR}$, $T^{\rm gas}_{\rm PDR}$ and $T^{\rm dust}_{\rm PDR}$. To do this, we separate the contributions of the dust and gas to the equation of state (Eq. 2.10). The equation of state, solely for the gas, includes:

$$n_{\rm HII}\, k_{\rm b} T^{\rm gas}_{\rm HII} + \frac{\epsilon^{\rm HII}_{\rm gas}\, \sigma_{\rm b} T^{4,\rm gas}_{\rm HII}}{c} = n_{\rm PDR} k_{\rm b} T^{\rm gas}_{\rm PDR} + \frac{\epsilon^{\rm PDR}_{\rm gas} \sigma_{\rm b} T^{4,\rm gas}_{\rm PDR}}{c}. \tag{2.11}$$

Due to the low emissivity of gas we make the approximation that the radiation pressure caused by photons emitted from the gas can be ignored and so this term is set to zero. Therefore, to set the conditions in the PDR, caused by the ionised region, we are left to solve:

$$n_{\rm HII}\, T^{\rm gas}_{\rm HII} = n_{\rm PDR} T^{\rm gas}_{\rm PDR}\,. \tag{2.12}$$

The temperature at the surface of the PDR is dependent on its hydrogen number density, $n_{\rm PDR}$, shown in Figure 2.1, therefore the above equation can be solved using a Newton-Raphson numerical method to provide the value of the hydrogen number density of the PDR given the conditions in the HII region[4], ensuring self-consistency. As the temperature at the surface of the PDR depends on the hydrogen number density, while all other input parameters remain unchanged, we can effectively solve this using a one-dimensional

[4]We iteratively solve Equation 2.12 up to a 1% accuracy level.

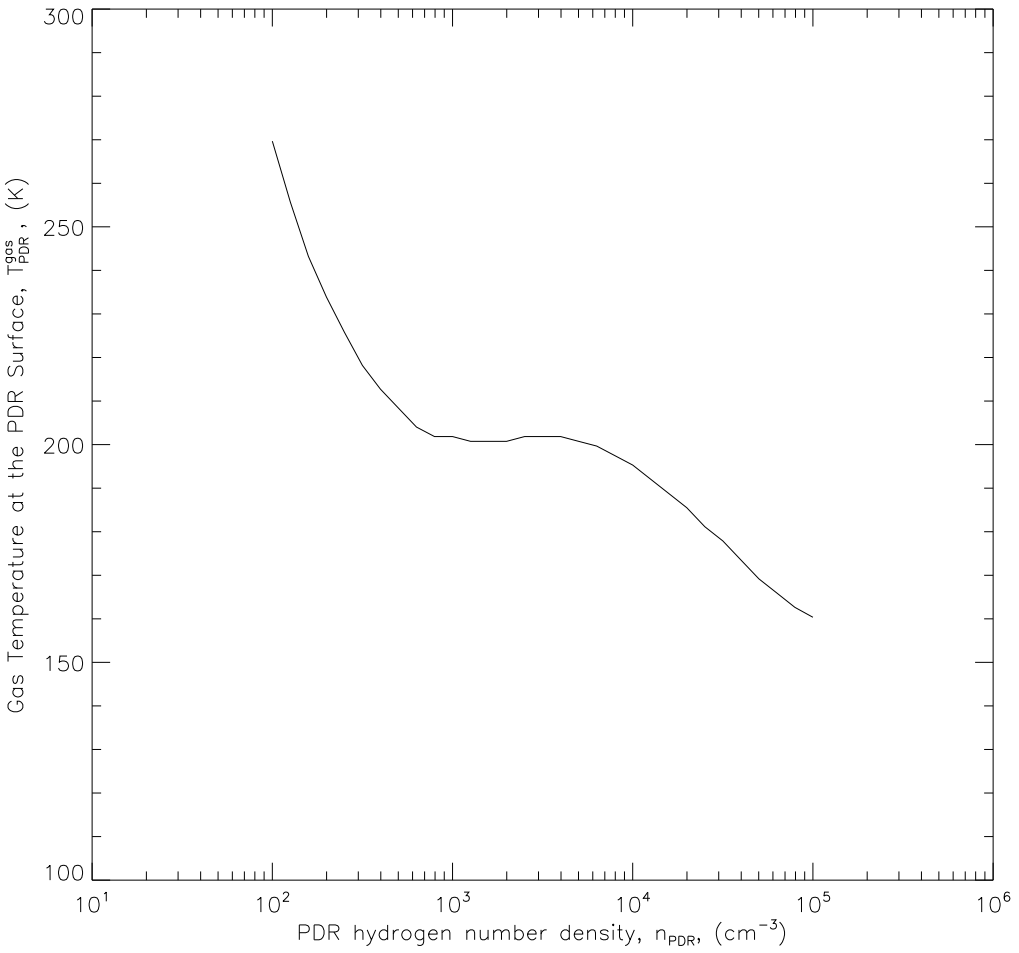

Figure 2.1. We plot how the temperature at the surface of the PDR varies with the hydrogen number density of the PDR, while all other input parameters in 3D-PDR remain unchanged.

Newton-Raphson numerical technique for the hydrogen number density, $n_{\rm PDR}$. The equation of state, solely for the dust, includes:

$$\epsilon^{\rm HII}_{\rm dust} T^{4,\rm dust}_{\rm HII} = \epsilon^{\rm PDR}_{\rm dust} T^{4,\rm dust}_{\rm PDR}. \tag{2.13}$$

Assuming the same dust species are present in both regions, the emissivities cancel out leaving the simple condition for the interface between the two regions

$$T^{\rm dust}_{\rm HII} = T^{\rm dust}_{\rm PDR}. \tag{2.14}$$

This leads to dust temperature continuity between the two regions, and also ensures gas pressure equilibrium.

2.2.3 Updating 3D-PDR for coupling

The previous version of the code (Bisbas et al. 2012), detailed in Section 2.1.3, performed computation at a fixed solar value of metallicity, with a gas to dust ratio also fixed at 10^2. However, for the nature of this work, where gas-phase metallicity will be a variable input parameter, and where MOCASSIN and SB99 can handle variable metallicities, it was necessary to make improvements to the original software package to allow for a varying metallicity parameter across the full coupled model. Here we report an update to the original 3D-PDR in which metallicity can now be varied accordingly.

The grain surface H_2 formation rate of Cazaux & Tielens (2004) is still adopted but now scales linearly with metallicity, by simply multiplying the formulae presented in Bisbas et al. (2012) by metallicity. The dust to gas ratio also scales linearly with metallicity, taking a standard value of 10^{-2} at Solar metallicity, following the prescription by Leroy et al. (2011) given by:

$$\log \delta_{\rm GDR} = 9.4 - 0.85 \times [12 + \log({\rm O/H})] \tag{2.15}$$

which is also consistent with the metallicity prescription used in MOCASSIN. The number density of dust is implicitly dependent on metallicity. For this we employ the prescription by Bell et al. (2006) such that,

$$N_{\rm grain} = 2 \times 10^{-12} \times n_{\rm h} \times \frac{Z}{Z_{\odot}} \tag{2.16}$$

where $n_{\rm h}$ is the electron number density and Z is the gas-phase metallicity. Furthermore, $A_{\rm v,0}$, detailed in Equation 2.6, also scales linearly with metallicity as:

$$A_{\rm v,0} = 6.289 \times 10^{-22} \times \frac{\rm Z}{\rm Z_{\odot}} \, . \tag{2.17}$$

The dust and PAH photoelectric heating also scales with metallicity following the prescription in Leroy et al. (2011).

After these updates to the code it is now possible to vary multiple input parameters to investigate how the ionised carbon contribution from different ISM components varies as a function of star forming region properties. We now report on the input parameters and model parameter space used in this work.

2.3 Model parameter space

The main purpose of this work is to provide a prescription to calculate the fraction of the total integrated [CII] emission of a galaxy emanating from the molecular phase of the ISM,

$f_{[\mathrm{CII}],\mathrm{mol}}$, as a function of typical extragalactic observables such as stellar mass, sSFR and metallicity. Therefore, we are interested in running our self-consistent modelling interface over an input parameter space corresponding to meaningful observables on galaxy wide scales. To this end, parameters which do not correspond to galactic observables shall be kept constant and typical values shall be used and taken from the literature. Before presenting the results of the modelling, we describe in this Section the parameters chosen for the different codes, and the final seven input parameters that are required to run the full coupled model.

2.3.1 Stellar population parameters in STARBURST99

We simulate the total stellar SED as originating from a single ionising source (even though it physically originates from multiple sources) for simplicity and ease. Karczewski et al. (2013) have compared the outputs of MOCASSIN when the ionising flux is produced by a single source or by 100 sources distributed uniformly within a sphere of 0.2 kpc. They find the results to vary only at small radii; outside of the inner radius, the gas effectively sees a point source. As we are here integrating far out of the cloud, this simplifying assumption will not affect our results. The specific SED produced by SB99 depends on assumptions made regarding the star formation history and metallicity of the stellar population. The code allows input stellar metallicities of 0.02, 0.2, 1 or 2.5 $Z_\odot$, and either periods of constant star formation or instantaneous bursts. Although the stellar metallicity is not a variable parameter in this work, it is undoubtedly correlated with the gas-phase metallicity, which will be a variable parameter in our models. Within these constraints, we build the star formation histories of our model galaxies as follows: (1) a first instantaneous burst of star formation at approximately the Hubble time with the total stellar mass produced in this burst given as an input parameter, and a stellar metallicity of $0.02Z_\odot$ as the metal content of the early universe is negligible, (2) a period of quiescence followed by a secondary burst, with the age of this second burst another input parameter, and (3) a period of constant star formation until the present day, with this rate of star formation a third input parameter.

We note that this star formation rate history is overly simplified and may not be realistic of galaxies in the local universe, however, for the purpose of this modelling, we are only interested in the UV part of the spectrum which leads to the ionisation and photodissociation within our simulations. The UV radiation comes from the most recent and youngest period of star formation, i.e phase (3) as seen in Figure 2.2. Our

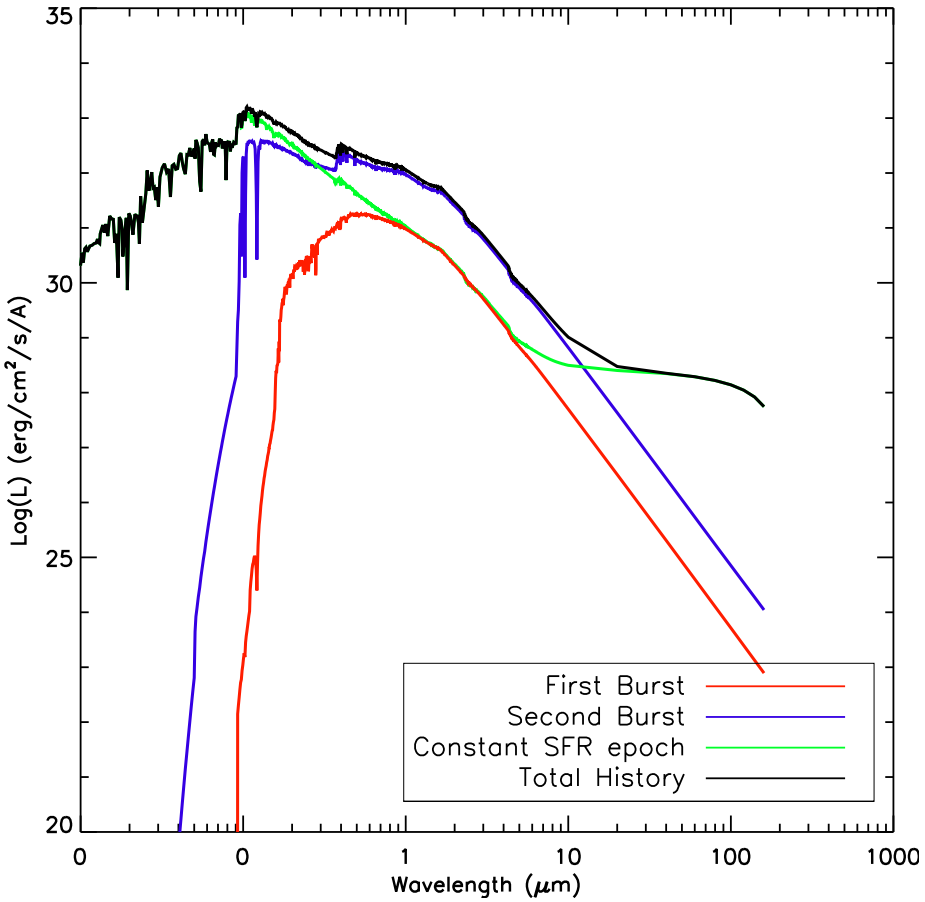

Figure 2.2. Example stellar SEDs from the population of stars created throughout the whole star formation history of our clouds. The instantaneous burst and constant star formation rate epoch both compete to dominate the UV part of the spectrum.

simulations results are therefore only sensitive to the most recent period of star formation, and older epochs are irrelevant, meaning that our choice of the star formation rate history is extraneous.

Due to metal enrichment of the gas from previous supernovae, we set the stellar metallicity of phases (2) and (3) to be the available input parameter greater than the input gas-phase metallicity, e.g for a gas-phase metallicity of $0.65Z_{\odot}$ we would set the stellar metallicity to $1Z_{\odot}$. The mass lost to supernovae and stellar winds in the initial burst is calculated and fed back into the secondary burst, ergo the input stellar mass parameter for phase (2), ensuring that the total stellar mass of the star forming region (one of the input parameters) is successfully produced by the present day. When running SB99, we use the Padova stellar evolution tracks, detailed in Fagotto et al. (1994), with thermally

pulsating AGB stars and Pauldrach and Hiller model atmospheres. Figure 2.2 shows an example of a stellar SED produced by SB99 for such a star formation history, with the contribution of the three different phases also shown separately.

2.3.2 Ionised region parameters in MOCASSIN

The input stellar spectrum, the source luminosity and temperature are all taken from SB99 into MOCASSIN which then calculates the number of ionising photons per second, Q_{phot}. The resolution of the grid, n_{xyz}[5], was chosen to be 15 so as not to be too computationally expensive, while also ensuring no loss of detail via blending across cells. Once all the inputs from SB99 are fed into MOCASSIN we vary the electron number density of the HII region, ranging between typical values from $10^{1.5}$ to 10^{3} cm^{-3}, and the gas-phase metallicity, via the initial abundances provided for in our chemical network, between 0.2-1.1$Z_{\odot}$. All simulations employ 3D spherically symmetric geometry.

With regards to geometry MOCASSIN does not make assumptions concerning a Strömgren sphere and so does not analytically compute a numerical value a priori for the radial distance out to the edge of the HII region (a drawback of the Monte Carlo method); hence a user can input the inner and outer radius of the HII region. We assume that the gas is isotropically and homogeneously surrounding the stars and so we set the inner radius of the ionised gas region to be as close to zero as computationally possible. For computational reasons it can not be set to exactly zero due to infinities arising in SB99 etc [6]. The input parameter for the outer radius of the ionised gas is determined as follows: run MOCASSIN up to a large outer radius and, from the results of this run, calculate the radius at which the ionised hydrogen fraction drops below ten percent (this is the effective Strömgren sphere radius). Then take this calculated radius value and re-run MOCASSIN but now setting the outer radius to this calculated radius. We use MOCASSIN only to simulate the ionised gas, hence the outer radius of the HII region goes up to this calculated effective Strömgren sphere radius. For the purpose of this work hydrodynamical effects such as turbulence, shocks and magnetic fields are ignored in our simulations.

Furthermore, setting appropriate dust properties is crucial due to the important role dust plays in heating the gas via the photoelectric effect, which depends on the dust abundance and varying dust grain sizes. Moreover, the radiative transfer processes are

[5]This term denotes the number of grid points in each of the x, y and z axis.
[6]The R_{inner} parameter is set to 10^{-5} parsec

Table 2.1. Gas-phase elemental abundances used in MOCASSIN and 3D-PDR, relative to total hydrogen number density, at Solar metallicity. All these elements, except Hydrogen and Helium which are primordial in origin, scale linearly with metallicity.

Species	Gas-phase abundance
He/H	0.1
O/H	4.9×10^{-4}
N/H	6.9×10^{-5}
Ne/H	1.1×10^{-4}
S/H	8.1×10^{-6}
Ar/H	1.9×10^{-6}
C/H	3.6×10^{-4}
Si/H	4.8×10^{-6}
Mg/H	4.0×10^{-5}
Fe/H	3.6×10^{-6}

strongly influenced by the characteristics of the grains. We use different grain properties for both HII and PDR regions due to the different physical conditions found in these regions. Within MOCASSIN we use the standard silicate dust properties detailed in Draine & Lee (1984). These grains have a sublimation temperature of 1400K, an average weight, in atomic mass units, of 20.77, a grain mass density of 3.6 g cm^{-3} and a radius of 0.16 μm. Further information regarding the optical emissivity data can be found within the dust data library in the MOCASSIN software package. For the PDR region we use a mixture of silicates + PAHS + graphite, due to the higher column densities, with graphite grains being the dominant dust species. 3D-PDR assumes graphite as a dust component, although this is yet to be observed directly in the ISM (Messenger et al. 1998; Nuth 1985). Carbon rich dust is clearly a major component of dust grains and as such graphite provides an example of this, while recent results suggest that most dust is in the form of amorphous carbon (Jones 2014). Finally, we use a grain mass density of 2.0 g cm^{-3} with a grain radius of 0.16 μm.

2.3.3 Photodissociation region parameters in 3D-PDR

For 3D-PDR, we consider a spherically symmetric shell of uniform density neutral and molecular gas, surrounding the ionised region, where the modelling strategy is shown schematically in Figure 2.3. The inner radius of the PDR region is therefore the outer radius of the ionised region as calculated with MOCASSIN, and the outer radius (and corresponding A_v) is set by the dust mass fraction, M_{dust}/M_*; we integrate out to a radius

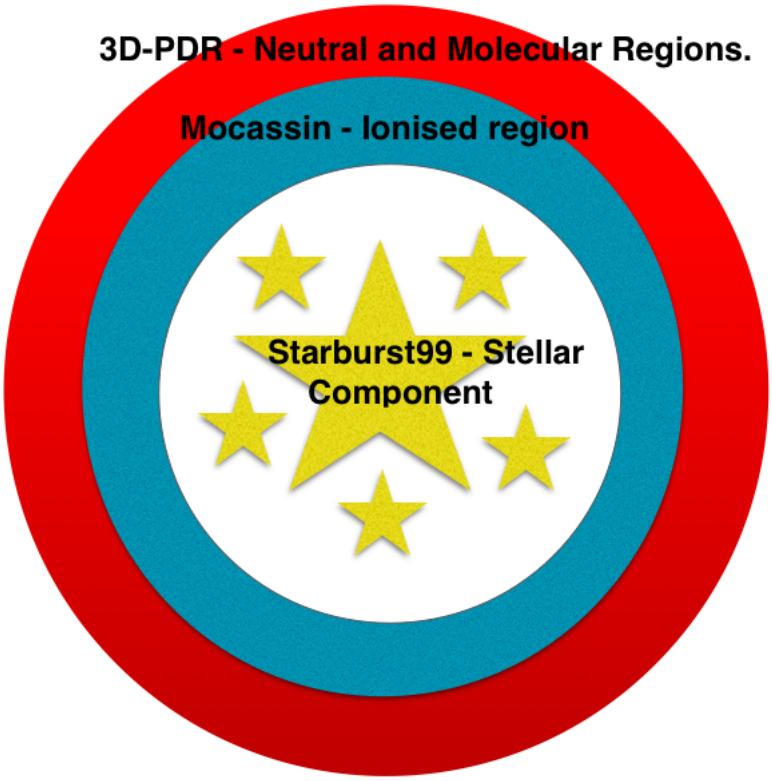

Figure 2.3. Representation of the spherically symmetric modelling geometry employed here, alongside the codes which shall be used to simulate each region.

that is set by the dust mass budget available. We define the molecular region as the region where more than 1% of hydrogen is in molecular form, marking the beginning of the CO-dark phase. Geometrical dilution effects of the UV field are taken into account to obtain accurate 3D results.

We assume a standard turbulent velocity of 1.5 kms^{-1}, while the hydrogen number density is self-consistently calculated (see Section 2.2.2). Therefore, the two input parameters we are free to vary for the PDR regions are the cosmic ray ionisation rate and the dust mass fraction. The gas-phase metallicity is taken to be the same as the value selected for the ionised region. Abundances of all metals scale linearly with metallicity, and Table 2.1 summarises the initial chemical abundances used in both MOCASSIN and in 3D-PDR at Solar metallicity. We use identical chemical abundances between the codes to maintain self-consistency and take the abundances at Solar metallicity from Cormier et al. (2012).

2.3.4 Summary of input parameters

Our objective is to provide a prescription for variations of $f_{[\mathrm{CII}],\mathrm{mol}}$ in galaxy-integrated observations that can be applied to unresolved galaxy-wide observations. Therefore, we use as input parameters quantities that are motivated by galaxy-wide observations, where possible. Choices for all the input parameters of our multi-phase ISM code are justified here and summarised in Table 2.2.

- *Stellar mass* - We let the stellar mass of our simulated star-forming regions vary from 10^2 to 10^4 $\mathrm{M}_\odot$. These values are typical of star-forming regions within the Milky Way (Wright et al. 2010*b*).

- *Age of the secondary burst* - Since our choice of star formation histories is meant to reproduce a broad range of possible integrated population ages, we choose to probe a wide range for the time since the secondary burst, spanning over 1.5 dex from 10^2 - $10^{3.5}$ Myr.

- *Specific star formation rate* - Deep multi-wavelength extragalactic surveys have revealed a tight correlation between SFR and stellar mass for star-forming galaxies (e.g. Noeske et al. 2007; Elbaz et al. 2007; Daddi et al. 2007). This correlation is well-established in the local universe and up to $z \sim 3$ (e.g. Brinchmann et al. 2004; Peng et al. 2010; Reddy et al. 2012). We choose sSFRs in the range of $10^{-11.5} - 10^{-9.5}$ yr^{-1}, typical of main sequence galaxies in the local universe and up to $z < 2$ (Rowlands et al. 2014).

- *Gas-phase metallicity* - We use the mass metallicity relation from Tremonti et al. (2004) to guide this choice, and adopt a metallicity range of 0.2 - $1.1\mathrm{Z}_\odot$ to reproduce conditions in local universe star-forming galaxies with $M_*> 10^9 M_\odot$.

- *Electron number density of the HII region* - We choose to vary the hydrogen number density between $10^{1.5}$ and $10^{3.0}$ cm^{-3} based on the values calculated by Hunt & Hirashita (2009) for extragalactic HII regions.

- *Cosmic Ray Ionisation Rate* (ζ)- In the local universe, this is known to be roughly 10^{-17} s^{-1} - 10^{-16} s^{-1} (Cummings 2015; Dalgarno 2006), but values can be larger by up to three orders of magnitude in galaxies with very large SFRs such as local ULIRGs and high-redshift star-forming galaxies (Papadopoulos 2010). We therefore

Table 2.2. Variable input parameters used in the fully coupled multi-phase code.

Input parameter	Minimum value	Maximum value	Number of Variations	Model
Gas-phase metallicity	$0.20Z_{\odot}$	$1.1Z_{\odot}$	4	MOCASSIN, 3D-PDR, SB99
Stellar mass of the cloud	10^2 $M_{\odot}$	10^4 $M_{\odot}$	3	SB99
Stellar population age	10^2Myr	$10^{3.0}$Myr	3	SB99
HII region electron number density	$10^{1.5}$ cm^{-3}	$10^{3.0}$ cm^{-3}	4	MOCASSIN
Cosmic ray ionisation rate	10^{-17} s^{-1}	10^{-14} s^{-1}	4	3D-PDR
Dust mass fraction	10^{-4}	10^{-2}	5	3D-PDR
Specific star formation rate	$10^{-11.5}$ yr^{-1}	$10^{-9.5}$ yr^{-1}	3	SB99

explore a range of cosmic ray ionisation rates ranging from 10^{-17} to 10^{-14} s^{-1} to allow us to also explore conditions typical of $z \sim 2$ galaxies.

- *Dust Mass Fraction* - We run models with the dust mass fraction (M_{dust}/M_*) varying between 10^{-4} and 10^{-2} based on the scaling relation between dust mass fraction and stellar mass derived from the galaxies in the Herschel Reference Survey (Boselli et al. 2010).

Overall our parameter space means we will simulate 8640 individual star forming regions with a wide range of physical conditions. We now show the trends observed from the modelling which emerge when varying this parameter space using the fully coupled 3D radiative transfer multi-phase interface.

2.4 Numerical Results

Of the total 8640 simulated star forming regions, 8016 clouds fully converged to a solution achieving thermal equilibrium. The main quantity of interest in the context of this study is $f_{[CII],mol}$, the fraction of the total [CII] emission originating from the molecular regions. In Figure 2.4, we plot scaling relations for $f_{[CII],mol}$ as a function of the input parameters of the coupled model. It can be seen that no one input parameter is solely responsible for variations in $f_{[CII],mol}$. The strongest trend is seen with dust mass fraction. This is expected, as this parameter determines the size of each cloud, and therefore how deep into the PDR regions we perform the integration. The higher the dust mass fraction, the further we integrate into the PDR regions leading to an increase in $f_{[CII],mol}$. However, the dispersion is still very high indicating that other parameters do play a role.

A quantitative analysis of the data requires a multi-dimensional hierarchical Bayesian inference method, which will be performed in Section 4.3. For now, we qualitatively explain the physics behind the trends observed in Figure 2.4 and the dependence of $f_{[CII],mol}$ on the input parameters of the model. In Appendix A the full results from the simulations are presented in Table A.1 for clouds with cosmic ray ionisation rates equalling 10^{-17} s^{-1}. The quadratic fits in Figure 2.4, shown by the black dotted lines, are presented solely to visually aid the reader and were obtained via a simple chi-squared fitting technique; a more sophisticated multi-dimensional hierarchical Bayesian inference method will be performed in Section 4.3.

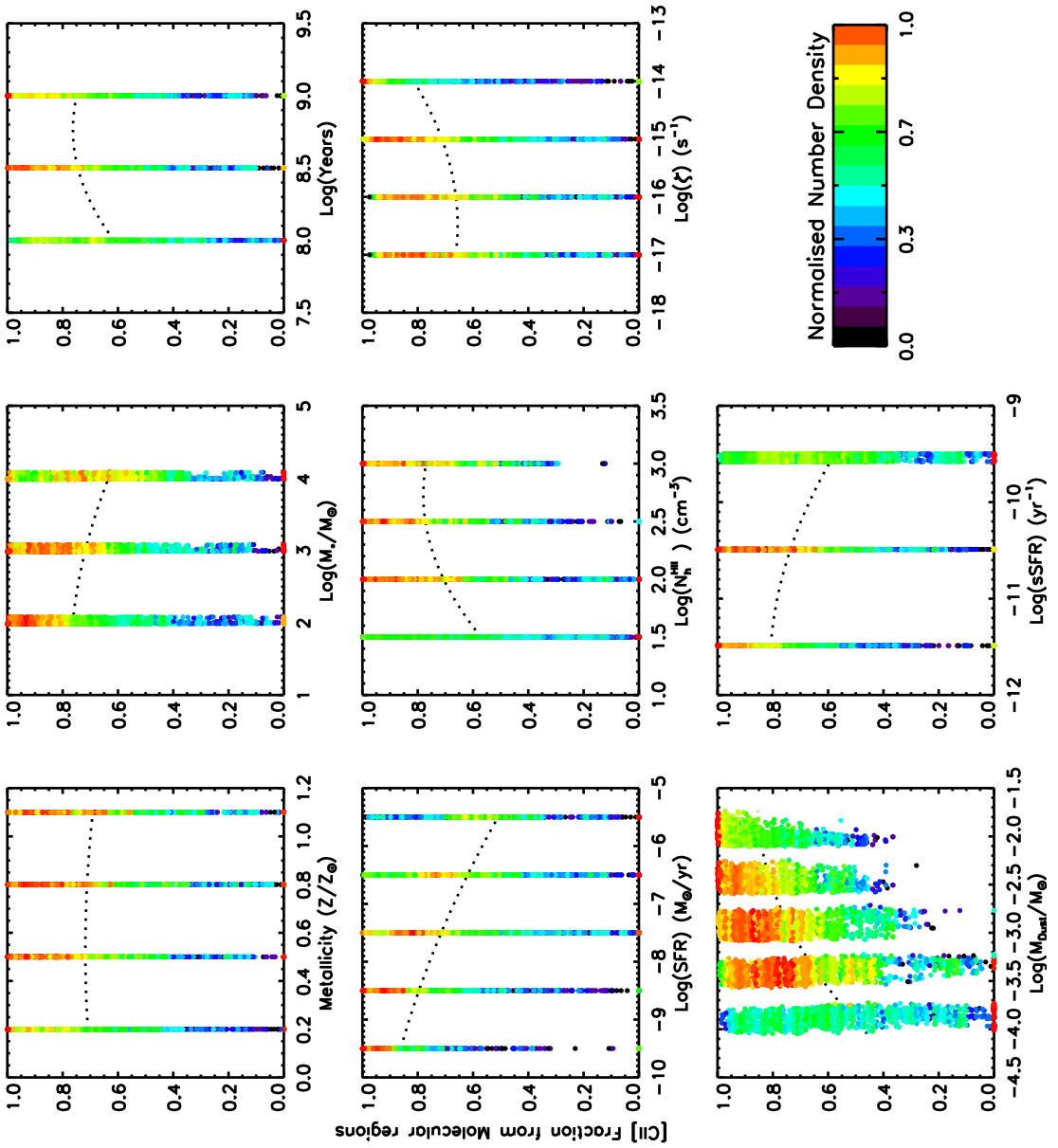

Figure 2.4. Scaling relations for all the simulated clouds which reached thermal equilibrium. Due to the large number of data points we provide a colour coding which indicates the one dimensional normalised number density, within each bin of our parameter space. Red points represent areas within each bin having the highest number of data points. The dotted lines are quadratic fits to the data, aiding visual inspection due to the large number of points in each panel.

2.4.1 Stellar mass and star formation rate

To disentangle the contributions of the different parameters to the variations seen in Figure 2.4, we show in Figure 2.5 how $f_{[\mathrm{CII}],\mathrm{mol}}$ varies as a function of metallicity for three different values of stellar mass. At fixed mass and metallicity, the figure also shows the impact of a varying the dust mass fraction and SFR. In this example, the hydrogen number density, the cosmic ray ionisation rate and the age of the secondary burst of star formation are kept fixed. The figure shows that $f_{[\mathrm{CII}],\mathrm{mol}}$ does not vary significantly with stellar mass. This is as expected because, as the stellar mass decreases, the number of ionising photons also decreases, reducing the overall size of the cloud. However, the relative sizes and densities of the HII to PDR regions will not change. By scaling down the stellar mass at the centre of each cloud we have simply scaled down the size of the cloud while maintaining the same physical structure throughout each cloud.

Figure 2.5 also shows that at fixed stellar mass, metallicity and dust mass fraction, an increase in SFR corresponds to a decrease in $f_{[\mathrm{CII}],\mathrm{mol}}$. This is because, at fixed dust mass, an increase in the star formation rate leads to an increase in the radius of the HII regions as more photoionising UV photons are available. More [CII] will therefore arise from the ionised regions versus the molecular regions, and hence $f_{[\mathrm{CII}],\mathrm{mol}}$ decreases.

2.4.2 Age of secondary burst

The variations caused by the age of the secondary burst are of a similar nature to star formation rate. Star formation histories which involve a younger secondary burst provide more photoionising UV photons. Hence, the younger the age of the secondary burst, the more [CII] will emerge from the HII regions, as the Strömgren sphere radius increases. This can be seen in Figure 2.6, with the mean value of $f_{[\mathrm{CII}],\mathrm{mol}}$ increasing as the age of the secondary burst increases from 0.1 to 0.32 to 1.0 Gyr. This effect is less pronounced than that caused by variations in star formation rate, because the majority of UV photons are produced by the low level star formation happening at the present time rather than by the secondary burst (see Figure 2.2). Interestingly though, the time since the last burst of star formation nonetheless has a detectable effect on $f_{[\mathrm{CII}],\mathrm{mol}}$ variations.

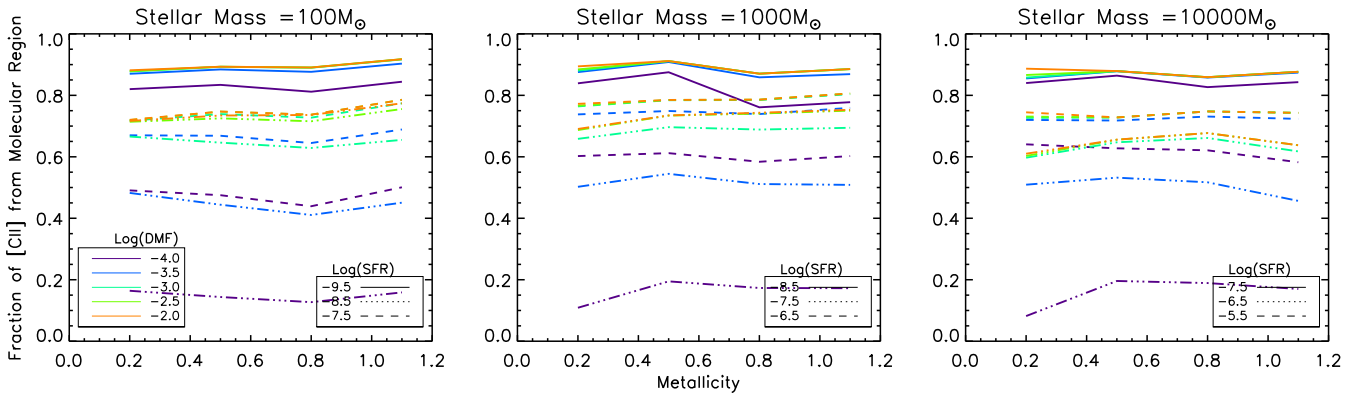

Figure 2.5. Variations of $f_{[\mathrm{CII}],\mathrm{mol}}$ as a function of metallicity for three different stellar mass bins. In each panel the relation is shown for different values of the dust mass fraction (different colours) and SFR (different linestyles). The hydrogen number density, cosmic ray ionisation rate and age of the secondary burst of star formation are kept constant.

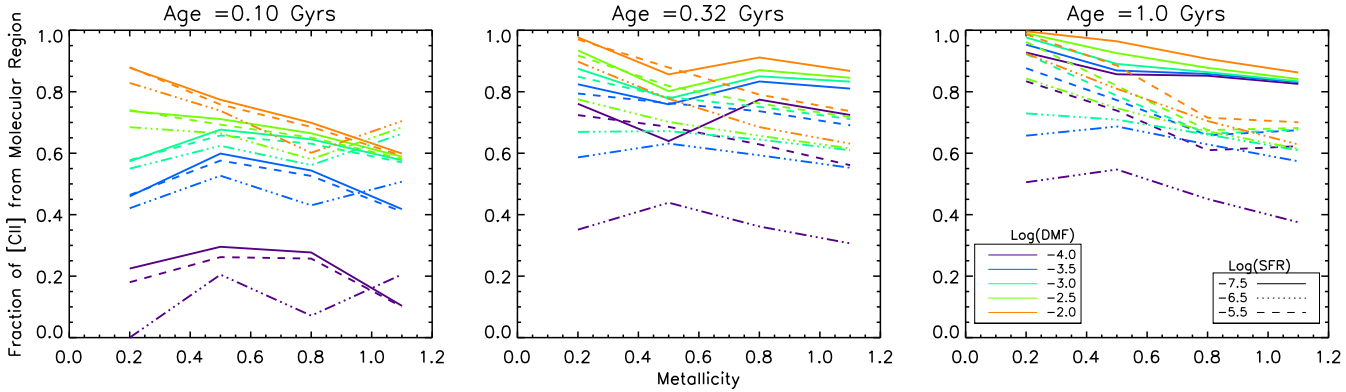

Figure 2.6. Variations of $f_{[\mathrm{CII}],\mathrm{mol}}$ as a function of metallicity for three different ages for the secondary burst of star formation. In each panel the relation is shown for different values of the dust mass fraction (different colours) and SFR (different linestyles). The hydrogen number density, cosmic ray ionisation rate and stellar mass are kept constant.

2.4.3 Gas-phase metallicity

Metallicity is responsible for variations in a more complex manner, with two main effects competing for dominance. To investigate these two processes we refer to Figs. 2.5 and 2.6.

One could naively expect that by decreasing the amount of metals available throughout the whole system, that the abundance of carbon in the ionised, neutral and molecular regions would decrease in equal measure and hence no variations of $f_{[\mathrm{CII}],\mathrm{mol}}$ should be seen because of metallicity (a similar argument to the lack of variation caused by stellar mass). However, within the ionised regions, the cooling rate is a function of metallicity; a decrease in metallicity leads to a lower cooling rate and therefore an increase in the size of the Strömgren sphere. Hence, from this first effect (the cooling rate effect, hereafter), we can expect that by decreasing metallicity there will follow a decrease of $f_{[\mathrm{CII}],\mathrm{mol}}$.

However a second, more dominant effect, is the well-known photodissociation of CO into ionised carbon (the photodissociation effect, hereafter). In low metallicity environments, FUV radiation penetrates further into the clouds leading to an enhanced abundance of ionised carbon in the molecular regions. The photodissociation effect therefore has the opposite effect of increasing $f_{[\mathrm{CII}],\mathrm{mol}}$ as metallicity decreases.

In different parts of parameter space, the cooling rate and the photodissociation effects cancel each other out, leading to negligible variations of $f_{[\mathrm{CII}],\mathrm{mol}}$ as a function of metallicity, as seen in Figs. 2.5 and Figure 2.6. Under other circumstances, the cooling rate or the photodissociation effect dominates, leading to positive or negative slopes in the $f_{[\mathrm{CII}],\mathrm{mol}}$-Z relation, respectively.

2.4.4 Electron number density of the ionised region.

An increase in the density of the ionised region (n_e) leads to no change on the [CII] emission from this region as we've already reached the critical density for collisions with electrons, of $\sim$50cm^{-3} (Goldsmith et al. 2012), which dominate in the HII region. However, due to equilibrium, this leads to an increase in the density of the PDR allowing for an increase in the [CII] emission from the molecular region, and correspondingly, an increase of $f_{[\mathrm{CII}],\mathrm{mol}}$. This continues until we reach the critical density for collisions with hydrogen in the PDR, of $\sim 10^{3.5}$cm^{-3} (Goldsmith et al. 2012), which dominate in the neutral ISM phases, at which point $f_{[\mathrm{CII}],\mathrm{mol}}$ remains roughly constant. We can see these variations caused by

the electron number density in the ionised regions in Figure 2.7. We keep the cosmic ray ionisation rate, stellar mass and age of the secondary burst constant and see that increasing n_e leads to an increase of $f_{[\mathrm{CII}],\mathrm{mol}}$, in all dust mass fraction and star formation rate bins.

The variations caused by density are linked with those of metallicity. In lower density environments, which have larger ionised regions, the metallicity variations are either flat or have a positive gradient implying that the cooling rate effect, detailed above, is more dominant. However, as density increases, the slope of the $f_{[\mathrm{CII}],\mathrm{mol}}$-Z relation changes as the photodissociation effect begins to dominate. Understanding quantitatively how, and when, these effects dominate follows in Section 4.3. We stress that these are qualitative trends which emerge from the data via visual inspection; a more thorough statistically robust treatment will be performed in Section 4.3.

2.4.5 Cosmic ray ionisation rate

The cosmic ray ionisation rate input parameter is used only in the molecular and neutral regions (i.e the PDR) where the heating function increases with the cosmic ray ionisation rate. This creates higher temperatures in the PDR regions, which leads an increase in the [CII] PDR emission, as this line is a major coolant of the gas, leading to an increase in $f_{[\mathrm{CII}],\mathrm{mol}}$. Work done by Bisbas et al. (2015*b*) has shown that [CII] starts to dramatically increase for cosmic ray values greater than 10^{-15} s^{-1}, explaining the trend in Figure 2.4 when going from lower to higher cosmic ray ionisation rates.

2.4.6 Dust mass fraction

As discussed previously, the dust mass fraction effectively controls the total size of our clouds and determines how far into the PDR we integrate up to. In Figure 2.8 we show for two different example clouds how the emissivity and carbonaceous species abundances relative to Hydrogen vary as a function of the radius in the neutral and molecular regions. Under certain conditions 'warm clouds' are simulated such that the temperature of the PDR never reaches 10K, the freeze-out temperature of hydrogen onto dust grains. This occurs for clouds with low PDR densities, high cosmic rays ionisation rates and high gas-phase metallicities. In these warm clouds the emissivity of [CII] always remains larger than that of CO (top left panel). This is because of the warmer conditions, and because the relative abundance of ionised carbon is also always larger than its molecular counterpart

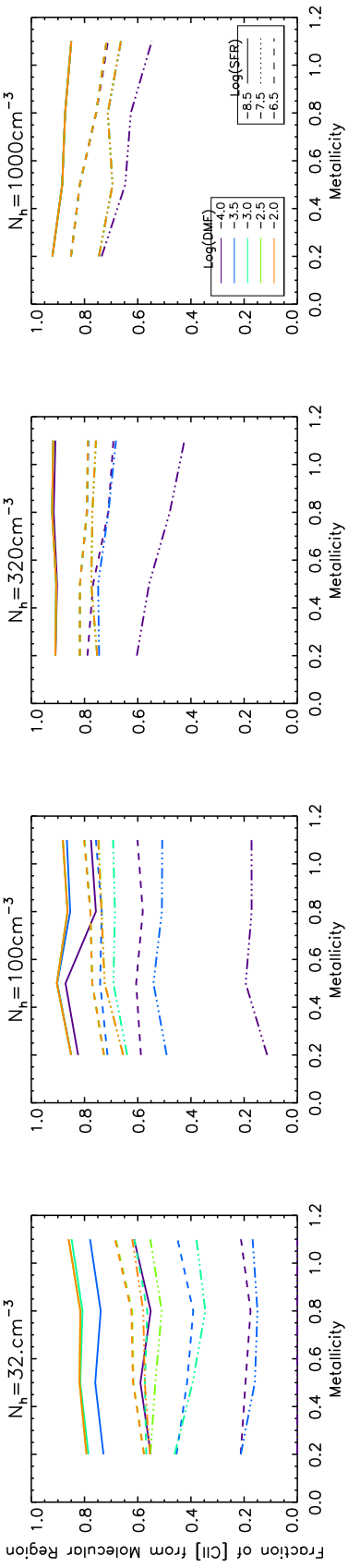

Figure 2.7. Variations of $f_{[\mathrm{CII}],\mathrm{mol}}$ as a function of metallicity for four different density bins. In each panel the relation is shown for different values of the dust mass fraction (different colours) and SFR (different linestyles). The stellar mass, cosmic ray ionisation rate and age of the secondary burst of star formation are kept constant.

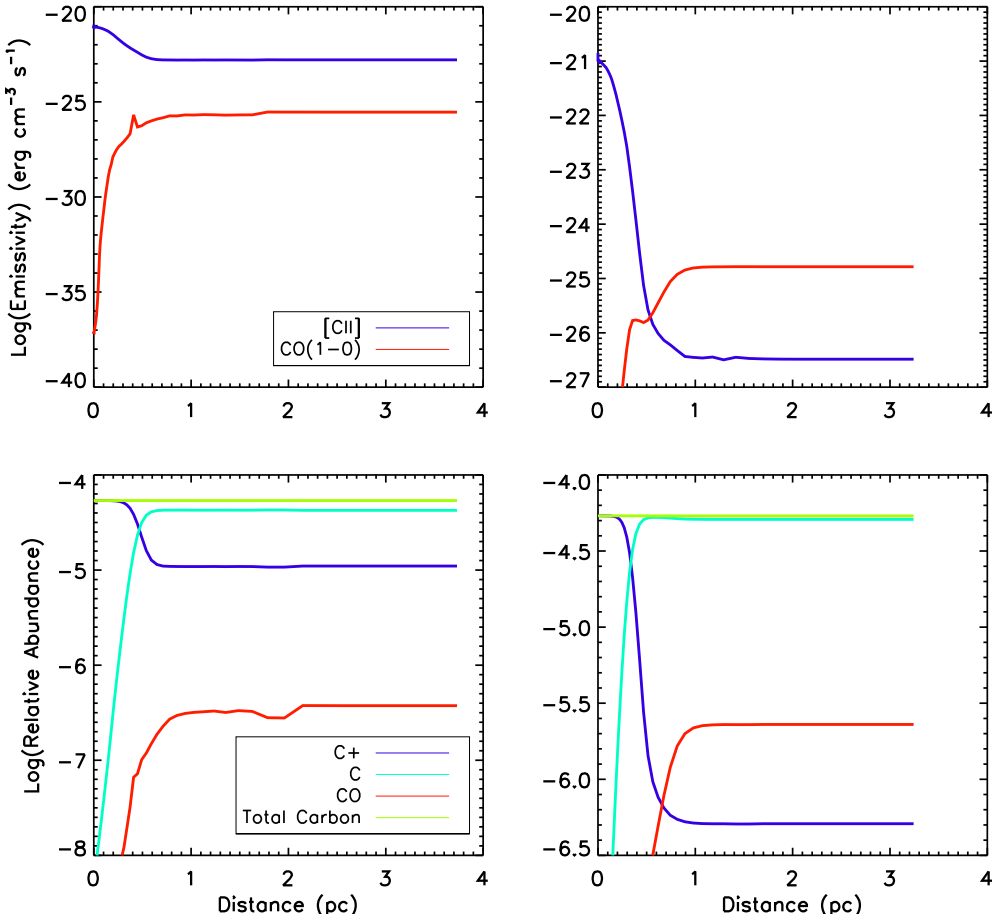

Figure 2.8. Examples of a warm (left) and cold (right) clouds. The top row shows for each example cloud how the emissivity of the different carbon phases varies with radius in the cloud, while the bottom two shows the relative abundance of these species. In warm clouds, even within PDRs, the emission of ionised carbon always remains larger than that of CO(1-0), while in cold clouds the CO(1-0) molecular phase dominates.

(bottom left panel). Therefore, by increasing the dust mass fraction, we are able to retrieve more [CII] the deeper we integrate, and so $f_{[\mathrm{CII}],\mathrm{mol}}$ increases with the dust mass fraction.

However in 'colder' conditions, where the temperature of the PDR eventually reaches 10K, the emissivity of ionised carbon decreases deep into the molecular regions, where molecular emission begins to dominate (top right panel). Therefore, increasing the dust mass fraction (i.e integrating further into the cloud) does not affect the relative emission of [CII]. This can also been seen in the abundance profile (bottom right panel), where the molecular carbon abundance now dominates deep into the clouds. Hence, in cases such as these, increasing the dust mass fraction will only increase $f_{[\mathrm{CII}],\mathrm{mol}}$ up to a point before no more [CII] is obtained and increasing dust mass fraction makes no difference.

We find that 6513, out of our 8016, clouds harbour these 'warmer' conditions with [CII] emission dominating over CO(1-0). The emergence of these two groups of clouds has been physically observed in the Galactic Plane (Langer et al. 2014) where 557/1804 clouds observed there where detected in [CII] with no CO. Our fraction of warm clouds to cold clouds defer to the observations because our parameter space is not representative of the Galactic plane, as explained above. Approximately 31% of the clouds in the Galactic Plane measurements were detected in [CII] with no CO, compared to our value of circa 81%. This is because, within the Galactic Plane, (Langer et al. 2014) would have been targeting dustier, gas rich and hence higher star forming clouds with cosmic ray values closer to the Milky Way value; our simulations encapsulate a much larger parameter space of which the Galactic Plane clouds only lie in a very small part of. Sensitivity issues and statistical issues involving fewer observed sources in the Galactic Plane compared to our number of simulated clouds could also explain the discrepancy.

2.5 Summary & Conclusions

We built a new 3D multi-phase radiative transfer interface through the combination of STARBURST99, MOCASSIN and 3D-PDR, which can simulate all phases of the interstellar medium, from ionised to molecular, where photoionisation and photochemistry dominates. We assume pressure equilibrium between the ionised and neutral phases of the ISM, solving the thermal balance equations between the two regions to ensure self-consistency. This interface was used to simulate a broad family of spherically-symmetric star-forming regions, with the aim of understanding how much of the total [CII] emission originates from the cold molecular ISM under varying conditions, by exploring a large seven dimensional parameter space. We found that:

- *Stellar Mass* - The relative emission of [CII] emerging from the molecular regions does not change going from clouds with low to higher stellar masses, at their centres, and no overall trend is noticeable with stellar mass. This is as expected because, as the stellar mass decreases the number of ionising photons also decreases, therefore reducing the overall size of the cloud. By scaling down the mass of each cloud we have simply scaled down the size of the cloud while maintaining the same structure throughout each cloud.

- *Star Formation Rate* - An increase in star formation leads to a decrease in the [CII] emerging from molecular regions. This is because, at fixed dust mass, an increase in the star formation rate leads to an increase in the radius of the Stromgren sphere and the size of the HII regions as more photoionising UV photons are available. More [CII] will therefore arise from the ionised regions versus the PDR and hence the PDR fraction will decrease.

- *Age of Secondary Burst* - The variations caused by the age of the secondary burst are of a similar nature to star formation rate. Younger ages of the secondary burst produce more [CII] from the HII regions, leading to a decrease in the amount of [CII] emerging from the molecular regions. Star formation histories which involve a younger secondary burst will provide more photoionising UV photons. Hence the younger the age of the secondary burst the more [CII] will emerge from the HII regions, as the Stromgren sphere increases, leading to a decrease in the amount of [CII] emerging from the molecular regions.

- *Gas-phase Metallicity* - In lower density environments a decrease in metallicity leads to a decrease in the fraction of [CII] emitting from molecular regions. However in higher density conditions a decrease in metallicity leads to an increase in the aforementioned quantity due to photodissociation of CO into ionised carbon.

- *Hydrogen Number Density* - The radius of the Stromgren sphere is inversely proportional to the density and, hence, an increase in the density will lead to a contraction in the size of the ionised region causing an increase in the relative contribution of [CII] emission from the molecular regions.

- *Cosmic Ray Ionisation Rate* - The PDR heating function increases with the cosmic ray ionisation rate and so an increase in this leads to an increase in the amount of [CII] emission from the molecular region.

- *Dust Mass Fraction* - In warm clouds, where CO does not dominate deep into the

clouds, an increase in this parameter leads to an increase in the relative fraction of [CII] from the molecular region. However in cold clouds, where CO does dominates deep in the clouds, increasing this parameter does not have an affect once the end of the [CII] emission profile is reached.

We now move onto applying and quantifying the above variations to galaxy wide scales through a Bayesian and Random Forest technique.

Chapter 3

Radiative transfer meets Bayesian statistics: where does a galaxy's [CII] come from?

In this chapter the results from the modelling interface are used to parametrise an analytical expression for how the fraction of the total [CII] emission originating from molecular regions, $f_{[\mathrm{CII}],\mathrm{mol}}$ varies as a function of typical integrated properties of galaxies in the local Universe. A Bayesian Inference technique is used to solve this complex multi-parameter problem, allowing us to derive a series of functions to calculate the contributions of the different phases of the ISM to the total integrated [CII] emission in extragalactic sources.

3.1 Applications to galaxy wide observations

The qualitative discussion in Section 2.4 was sufficient to understand the physics underpinning the variations of $f_{[\mathrm{CII}],\mathrm{mol}}$ between our different simulated star forming regions. In this section, we make the jump from these individual star forming regions to the ISM of entire galaxies. Ideally, we would want to build a model for the ISM of a whole galaxy by appropriately summing up a number of our individual simulated clouds. To do this, we could start from observations of the molecular cloud mass function (e.g. Wright et al. 2010*b*; Wong et al. 2011; Colombo et al. 2014; Gusev et al. 2016), however it is still highly

debated whether there is a universal cloud mass function that is applicable to all galaxies, or whether the properties of clouds depend on other global physical parameters and therefore vary from galaxy to galaxy (see e.g. Hughes et al. 2013). Given this uncertainty and as a first step, we here propose a simpler alternative method to predict how $f_{[\mathrm{CII}],\mathrm{mol}}$ varies as a function of integrated galaxy properties using our simulated clouds. We make the assumption that the physical conditions found in each of our clouds, for a given set of input parameters, can represent the average physical conditions found on galaxy-wide scales for galaxies with similar physical properties. Under this assumption, a whole galaxy can be considered to be built up from an appropriate number of identical star forming regions.

3.1.1 Bayesian inference

From the scaling relations shown in Figure 2.4, we now want (a) to parametrise an analytic prescription for how $f_{[\mathrm{CII}],\mathrm{mol}}$ varies as a function of our model parameters for extragalactic observations on galaxy wide scales, and (b) to determine the minimum number of parameters needed to provide a statistically-robust fit to our data. We therefore use a Bayesian inference method to find the best fit relations and the minimum number of parameters required. Bayesian interference fitting methods have been successfully employed in several, wide-ranging, astrophysical scenarios from the derivation of the extinction law in the Perseus molecular cloud (Foster et al. 2013) and Type Ia supernova light curve analysis (Mandel et al. 2011) to the extragalactic Kennicutt-Schmidt relation (Shetty et al. 2013) and the formation and evolution of Interstellar Ice (Makrymallis & Viti 2014). For a more in depth explanation of the Bayesian regression fitting method we refer the reader to Kelly (2007) and restrict ourselves here to the basic concepts.

Our 3D radiative transfer methodology provides a complete model for how [CII] varies as a function of the seven input parameters of the coupled code. However, the radiative transfer modelling is highly non-linear and complex, so we explore how well a polynomial fit can describe the outputs from the coupled 3D radiative transfer simulation, and determine the optimal number of parameters for this fit. This is done by evaluating the posterior probability of the simulated data, $y_{\mathrm{RT\ Model}}$, given the polynomial fit, denoted y_{QF}. We assume that the measurement uncertainties associated with each of our fits, are normally distributed, therefore $y_{\mathrm{QF,i}}$ is a random variable distributed like:

$$y_{\mathrm{QF,i}} = \mathcal{N}(y_{\mathrm{RT\ Model,\ i}}, \sigma^2_{y_{\mathrm{QF,\ i}}}) \tag{3.1}$$

where $\sigma_{y_{\mathrm{QF,\,i}}}$ is the measurement uncertainty associated with the polynomial fit $y_{\mathrm{QF,\,i}}$ on the i^{th} model which will be an additional parameter which we need to fit. For simplicity, we assume that all $\sigma_{y_{\mathrm{QF,i}}}$ are equal to the same value, $\sigma_{y_{\mathrm{QF}}}$.

Under the assumption of the normal distribution in Equation 3.1, the probability of obtaining a certain polynomial fit, given the output of the numerical modelling, combined with the fitted uncertainties and the weighting factors is:

$$P(y_{\mathrm{QF,i}}|y_{\mathrm{RT\ Model,i}}, \sigma_{y_{\mathrm{QF}}}) = \frac{\sqrt{\mathrm{g}_i}}{\sqrt{2\pi\sigma^2_{y_{\mathrm{QF}}}}} \times \exp\left(-\frac{\mathrm{g}_i(y_{\mathrm{RT\ Model,i}} - y_{\mathrm{QF,i}})^2}{2\sigma^2_{y_{\mathrm{QF}}}}\right). \quad (3.2)$$

where g_i is the dimensionless statistical weighting for each cloud. As described in Section 3.1.3, weights are assigned to each of the simulated clouds to take into account how likely they are to reproduce ISM conditions typical of local galaxies.

The next assumption to make is that all our radiative transfer simulated data points are independent, which is perfectly reasonable as we ran through each point in parameter space regardless of the other parameters. Under this assumption, all the individual probabilities can be multiplied to produce the Likelihood. By taking the log-likelihood the product returns back to a sum so:

$$\mathcal{L} = -\frac{N}{2}\ln(2\pi) - N\ln(\sigma_{y_{\mathrm{QF}}}) - \sum_{i=1}^{N}\left(\frac{\mathrm{g}_i(y_{\mathrm{RT\ Model,i}} - y_{\mathrm{QF,i}})^2}{2\sigma^2_{y_{\mathrm{QF}}}}\right) + \sum_{i=1}^{N}\left(\frac{\ln\,\mathrm{g}_i}{2}\right). \quad (3.3)$$

Maximising this log-likelihood for the polynomial fit parameters and the associated error, $\sigma_{y_{\mathrm{QF}}}$, will provide us with the best fitting analytical expression alongside the one sigma error of the parametrisation.

To compare likelihoods from models with different numbers of free parameters we use two different methodologies. Firstly we employ the Akaike Information Criterion (AIC) (Akaike 1981):

$$\mathrm{AIC} = -2\mathcal{L} + 2p + \frac{2p(p+1)}{N-p-1}\,. \quad (3.4)$$

where p is the number of free parameters and N is the sample size. The best model and the optimal number of free parameters is found by minimising the AIC. We also calculate the Bayesian Information Criterion (BIC) (Schwarz 1978):

$$\mathrm{BIC} = -2\mathcal{L} + p\mathrm{Log}(N), \quad (3.5)$$

and compare the results of both tests to ensure our results are not dependent on the choice of the information criterion used.

3.1.2 Sampling methods and quadratic models

A direct solution for the posterior probability distribution is computationally expensive and so, to efficiently and effectively sample the full parameter space, we use the well tested Python implementation of the affine-invariant ensemble sampler for Markov Chan Monte Carlo (MCMC) called emcee[1] (Goodman & Weare 2010).

Given the saturation effect which may occur when [CII] is mainly emitted from the molecular regions (i.e. when $f_{\rm [CII],mol}$ approaches 1) and the low number of bins in our parameter space, we only fit quadratic polynomials to our data, including all second order cross-terms when multiple parameters are involved e.g for three parameters we would use:

$$\begin{aligned} y_{\rm QF,i} = \alpha_1 + \alpha_2 x_{1,i} + \alpha_3 x_{1,i}^2 + \alpha_4 x_{2,i} + \alpha_5 x_{2,i}^2 + \alpha_6 x_{3,i} \\ + \alpha_7 x_{3,i}^2 + \alpha_8 x_{1,i} x_{2,i} + \alpha_9 x_{1,i} x_{3,i} + \alpha_{10} x_{2,i} x_{3,i}. \end{aligned} \tag{3.6}$$

We also fit for $\sigma_{y_{\rm QF}}$ and therefore have $2(\epsilon+1) + {}^{\epsilon}C_2$ free parameters to constrain, where ϵ is the number of different variables in our fits[2]. This number can range from 1 to 4 as we focus on the four input parameters of the coupled code which are also commonly-available extragalactic observables. These are the gas-phase metallicity, the electron number density of the HII regions, the specific star formation rate and the dust mass fraction.

3.1.3 Statistical weighting calculation

The simulated clouds, which we now assume represent average physical conditions on galaxy wide scales, fill up a very large parameter space representing a large range of possible physical conditions. In which parts of this parameter space do galaxies actually lie? Which simulated clouds therefore represent average physical conditions in local galaxies? To account for this, we calculate a weighting factor for each cloud based on how likely it is to be representative of a local galaxy. To accomplish this we need as statistically complete a sample of galaxies as possible, which also has as many observable parameters of our parameter space.

We therefore make use of the Herschel Reference Survey (Cortese et al. 2012 , HRS hereafter), a K-band selected sample of galaxies located between 15 and 25 Mpc (Boselli et al. 2010) of which a large fraction are located within the Virgo cluster. It is as close to a statistically complete sample of galaxies with measured dust mass fractions, sSFRs,

[1] An example of the code can be found at http://dan.iel.fm/emcee/current/.
[2] This applies when ϵ is greater or equal to two. For one variable we have four free parameters.

electron number densities and metallicities known to this author. We retrieve dust masses, stellar masses and star formation rates from HRS catalogs (Boselli et al. 2015; Cortese et al. 2014; Boselli et al. 2013) using the online data tables from *Vizier*. From these we can directly infer for 215/323 HRS galaxies two of the input parameters of our coupled model: dust mass fractions and specific star formation rates. Another input parameter, the electron number densities in the ionised regions, is calculated from the [SII] line intensity ratio (taken from Boselli et al. (2015) using *Vizier*) $R = [\mathrm{SII}]\lambda6716/\lambda6731$ using the prescription of Sanders et al. (2016):

$$n_e = \sqrt{T_e}\left(\frac{1.4498 - R}{0.1595R - 0.0688}\right). \tag{3.7}$$

where T_e is the electron temperature and assumed to be a standard 10^4 K, typical for HII regions. Similar temperature assumptions have been made previously in Ho et al. (2014) and Sanders et al. (2016). These electrons densities are equivalent to hydrogen number densities in the HII regions in the range of $10 - 1000$ cm^{-3}. Comparison with the input parameters for the coupled multi-phase code given in Table 2.2 confirms that we have sampled the appropriate ranges to reproduce conditions typical of local galaxies. After this remains 112/323 HRS galaxies which have accurate dust masses, stellar masses, star formation rates and electron number densities which match our modelling parameter space e.g those which have densities greater than $10^{1.5}$ cm^{-3}. The distribution of stellar masses for the 112 HRS galaxies is shown in Figure 3.1.

We bin the HRS data to match the sampling used in the Radiative Transfer modelling (shown in Figure 2.4), i.e for the above three parameters (dust mass fractions, sSFR and n_e) we bin the 112 HRS galaxies into 60 bins (5×4×3). It is possible to include metallicity in the binning, from Boselli et al. (2013) using *Vizier*, however, this would restrict and reduce the sample size further. If we did include metallicity our sample would now shrink to 69 objects[3] and we would now have 120 bins meaning that our weighting function would be comb-like leading to erroneous results as the number of bins exceed the sample size. A variant of the Freedman & Diaconis rule (Freedman & Diaconis 1981) states that the number of bins must be less than the sample size, hence why we do not include metallicity into the weighting. We use the Python N-dimensional histogram routine, *histogramdd*, to calculate the normalised weighting for each of our simulated clouds.

From here on, we limit our sample to clouds with cosmic ray ionisation rates equal

[3]Unfortunately not all the galaxies have [OIII], H_α, H_β and [NII] measurements on the *Vizier* database.

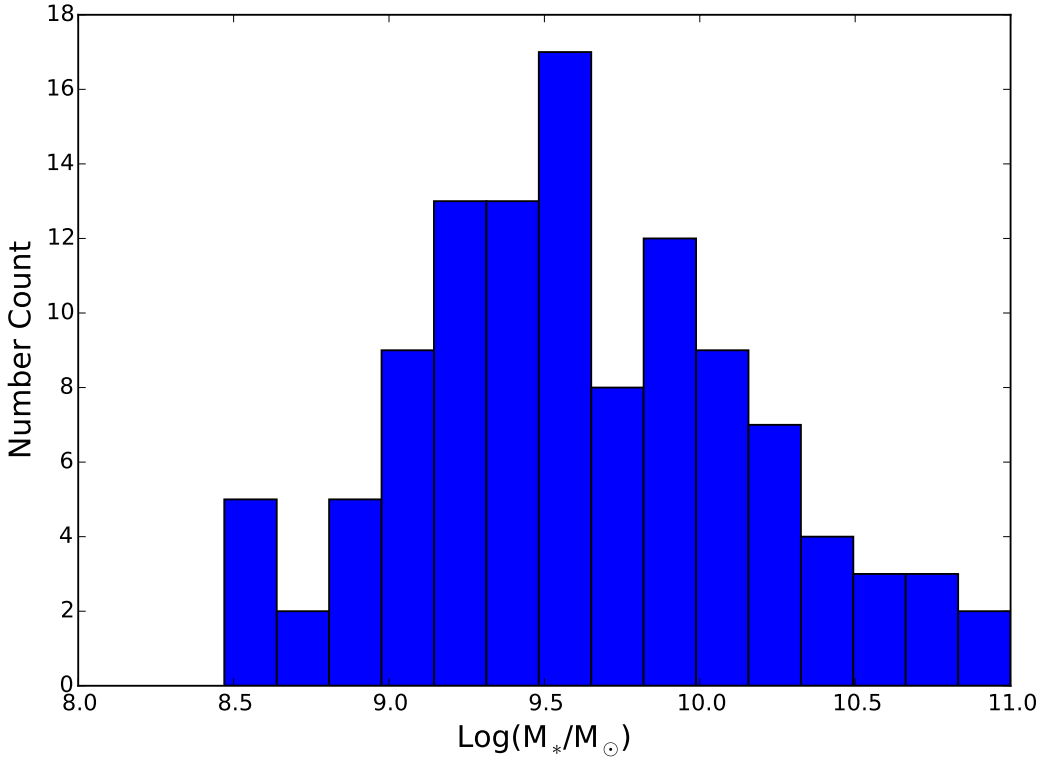

Figure 3.1. The distribution of stellar masses for the 112 HRS galaxies.

to the average Milky Way value (10^{-17} s^{-1}), as it is unlikely to vary much away from this value for any of the HRS galaxies, which are local normal star-forming and quiescent galaxies. Higher cosmic ray rates ($\sim 10^3$x Milky Way value) are found in ULIRGs and galaxies with more enhanced star formation (Kelly et al. 2015), hence we keep this fixed at the average Milky Way value for now. Even though the HRS sample does not have measured cosmic ray ionisation rates, based on their position in the SFR-M_* plane, and the fact that they are local galaxies, we can be sure that they all have a value approximately equal to that of the average Milky Way cosmic ray ionisation rate. Therefore we set to 0 the statistical weight of any cloud simulated with a cosmic ray ionisation rate higher than that of the Milky Way.

We also present in Section 3.3.1 the results if we limit our sample to clouds with cosmic ray ionisation rates equal to ten times the average Milky Way value (10^{-16} s^{-1}). We find identical results when using the two different cosmic ray ionisation rates; using the average Milky Way value (10^{-17} s^{-1}) does not affect our results for local universe galaxies.

3.1.4 Statistical results

Using the Bayesian formalism and statistical weights described above, we fit the simulated values of $f_{[\mathrm{CII}],\mathrm{mol}}$ as a function of the four key observables (density, dust mass fraction, sSFR and metallicity), allowing the number of these parameters used in any one fit to vary between 1 and 4. As the number of free parameters increases, the quality of the fit improves as shown by both the AIC and BIC (Figure 3.2).

We hereby present several novel prescriptions for the fraction of [CII] emission emerging from molecular regions on galaxy wide scales simply involving dust mass fraction, HII region electron number density, specific star formation rate and metallicity. The full analytical prescription, according to the AIC and BIC is one involving all four galaxy parameters, namely:

$$\begin{aligned} f_{[\mathrm{CII}],\mathrm{mol}} = -4.405 + 0.133\frac{Z}{Z_\odot} - 0.172\frac{Z}{Z_\odot}^2 + 1.448\rho - 0.206\rho^2 + 0.814\phi - 0.050\phi^2 - 0.818\psi \\ -0.032\psi^2 - 0.063\frac{Z}{Z_\odot}\rho + 0.003\frac{Z}{Z_\odot}\phi - 0.027\frac{Z}{Z_\odot}\psi - 0.222\rho\phi + 0.098\rho\psi + 0.050\phi\psi\,. \end{aligned} \tag{3.8}$$

where $\frac{Z}{Z_\odot}$ is the metallicity, $\rho = \log n_e$, $\phi = \log \frac{M_{dust}}{M_*}$ and $\psi = \log(\mathrm{sSFR})$. The one sigma error derived from the fitting is $\sigma_{f_{[\mathrm{CII}],\mathrm{mol}}} = 0.0597$ (a unit-less quantity as it's a relative fraction). Furthermore, we also present the best three, two and one parameter prescriptions as we understand acquiring all the necessary data to use Equation. 3.8 may be a challenge. The three parameter prescription includes only dust mass fraction, n_e and sSFR:

$$\begin{aligned} f_{[\mathrm{CII}],\mathrm{mol}} = -3.92 + 1.50\rho - 0.209\rho^2 + 0.471\phi - 0.072\phi^2 \\ - 0.628\psi - 0.018\psi^2 - 0.227\rho\phi + 0.106\rho\psi + 0.027\phi\psi\,. \end{aligned} \tag{3.9}$$

The one sigma error in this case is is $\sigma_{f_{[CII],mol}} = 0.061$. The two parameter prescription does away with the dust mass fraction and therefore simplifies as

$$f_{[\mathrm{CII}],\mathrm{mol}} = -5.63 + 1.31\rho - 0.17\rho^2 - 0.87\psi - 0.034\psi^2 + 0.046\psi\rho,. \tag{3.10}$$

with an error of $\sigma_{f_{[CII],mol}} = 0.064$. The best fitting one parameter prescription involves only n_e and has $\sigma_{f_{[CII],mol}} = 0.069$[4]:

$$f_{[\mathrm{CII}],\mathrm{mol}} = -0.556 + 1.087\rho - 0.219\rho^2. \tag{3.11}$$

[4]We stress that the errors quoted here are only the errors in the theoretical determination and do not represent errors in an actual [CII] observation which will be higher than circa 6.9%. For this the user needs to appropriately propagate the errors through when applying to observations.

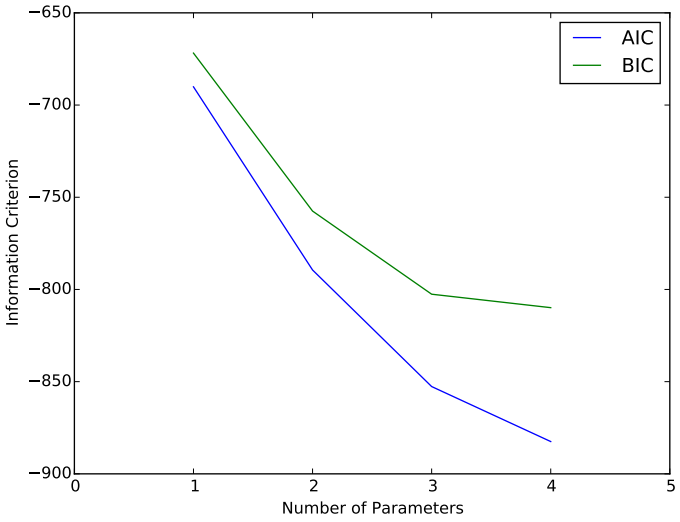

Figure 3.2. We provide a plot for the variation of the Akaike Information Criterion and the Bayesian Information Criteria in blue and green respectively. It can be seen how, although they give different absolute numerical values (due to their different analytic expressions), they reach a minimum at four parameters.

As we will show in the next section, there is also a trend between $f_{[\mathrm{CII}],\mathrm{mol}}$ and sSFR. As this latter quantity is typically more readily available to extragalactic observers than n_e, we also perform this one parameter fit even though it is not formally selected by the AIC and BIC. This alternative one parameter prescription, with an associated error of $\sigma_{f_{[CII],mol}} = 0.072$, is

$$f_{[\mathrm{CII}],\mathrm{mol}} = -6.224 - 1.235\psi - 0.0543\psi^2. \tag{3.12}$$

In the following section, we test and compare these five prescriptions, and then advise on the best relation to use to estimate $f_{[\mathrm{CII}],\mathrm{mol}}$ for individual galaxies in Section 3.2.

We are here arguing that with these four aforementioned quantities one can estimate the relative fraction of [CII] emerging from galaxy wide observations. An important implication of our results regard using [CII] as a star forming tracer. Ideally [CII] should only be used to trace star formation in galaxies where it predominantly arises from molecular regions; hence our prescription is able to predict, and hence provide a quantifiable measure on, whether [CII] can be used as a star forming tracer for global galaxy observations.

3.1.5 Validation of the $f_{[\mathrm{CII}],\mathrm{mol}}$ prescriptions and example applications

Measurement of the [CII] fraction emerging from molecular regions in extragalactic objects are uncommon at best, making validating our prescription for $f_{[\mathrm{CII}],\mathrm{mol}}$ against a large and

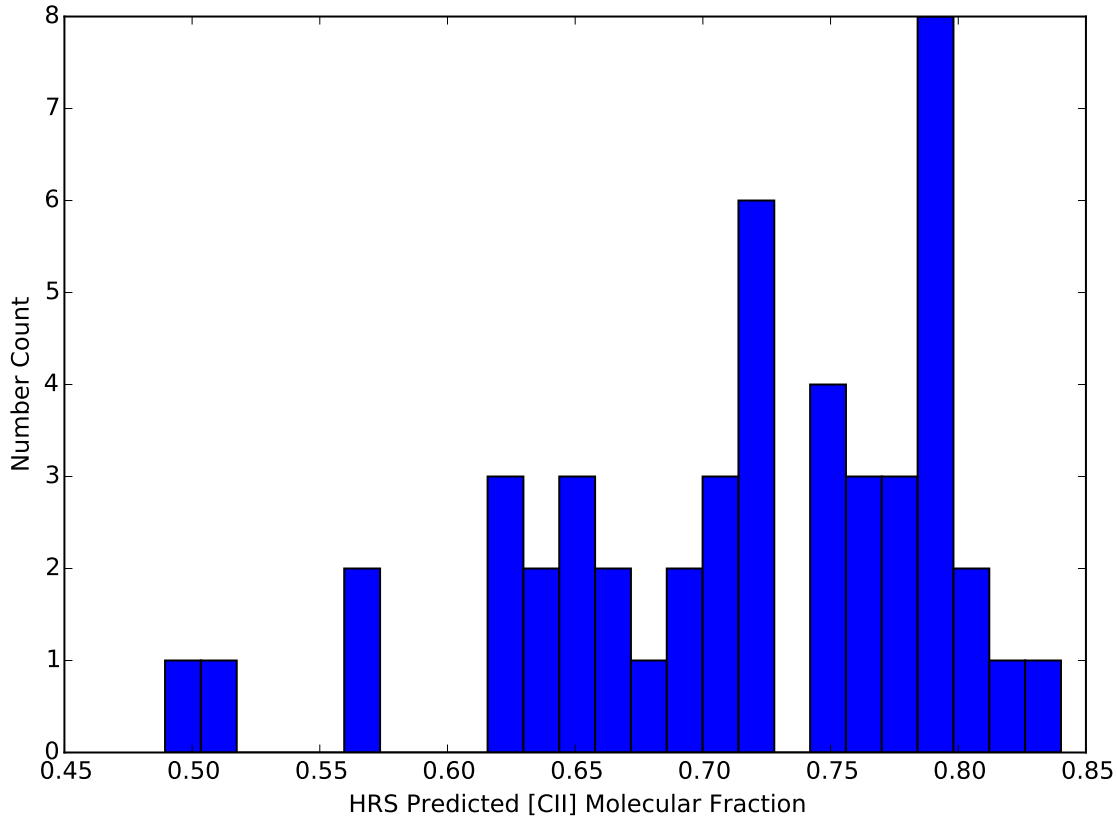

Figure 3.3. By applying our prescription to the HRS sample we find that the majority of the galaxies have 60-80% of their total integrated [CII] emission arising from molecular regions. Due to the completeness of the sample it implies that on galaxy wide scales, in the local universe, 60-80% of a galaxy's [CII] emission will originate from molecular regions.

complete galaxy sample impossible. However, Pineda et al. (2013) measured $f_{[\mathrm{CII}],\mathrm{mol}}$ of 75%[5] across the Milky Way as part of the GOT C^+ survey. Assuming a dust mass for the Milky Way of $10^{7.7}$ $M_\odot$ (Pierce-Price et al. 2000), a star formation rate of 1.65 $M_\odot$ yr^{-1} and a total stellar mass of $10^{10.78}$ $M_\odot$ (Licquia & Newman 2014), a metallicity of $1Z_\odot$ and finally a electron number density of 100 cm^{-3}, Equation 3.8 predicts $f_{[\mathrm{CII}],\mathrm{mol}}$= 75.8±6.0% for the Milky Way. As a comparison, the alternative prescriptions evoking fewer input parameters, Equations 3.12, 3.11, 3.10 and 3.9, predict values of 77.6 ± 6.3%, 74.4 ± 6.9%, 74.4 ± 6.9% and 73.8 ± 6.1%. All are in excellent agreement with Pineda et al. (2013).

Extragalactic observations have accurately measured the fraction of [CII] emerging from *ionised* gas regions, using the [CII]/[NII] 205μm and [NII] 122μm/[NII] 205μm ratios (Oberst et al. 2006). This fraction has been measured to be between 15%-65% in NGC

[5]This is the average value.

891 (Hughes et al. 2015) and 20%-30% in the star forming region BCLMP 302 of M33 (Mookerjea et al. 2011). Our ISM model here is unable to measure exactly the [CII] fraction arising from similar ionised regions; it would have to be modified to produce the emissivity profiles across the ionised and neutral phases to discriminate the origin of [CII] between these two phases of the ISM. We can however provide an upper limit for the fraction of [CII] emerging from the ionised regions as 1-$f_{\rm [CII],mol} \simeq 20-40\%$, in agreement with these observations.

We also apply our prescription to the HRS galaxies which have measurements available for all four physical parameters required for Equation 3.8, and find that the typical value of $f_{\rm [CII],mol}$ for these representative local galaxies is 60-80%, Figure 3.3, in agreement with numerical modelling of Olsen et al. (2015) who find the total [CII] emission to be dominated by molecular gas. Furthermore Figure 3.4 shows how these values of $f_{\rm [CII],mol}$ depend on key parameters. In the model grid (Table 2.2), all the parameters were varied independently, without enforcing any correlations between each of them. However, observations of star-forming regions and local galaxies make it clear that many of these physical properties are highly correlated. The scaling relations of Figure 3.4 therefore implicitly contain these physical correlations, and interestingly show no trend with metallicity and dust mass fraction. Correlations are seen however with sSFR and n_e with explanations similar to those in Sections 2.4.1 and 2.4.4. This is to be contrasted with the scaling relations shown in Figure 2.4 which contained all the simulated clouds, regardless of their likeliness to be representative of local star-forming galaxies. The initial increase in $f_{\rm [CII],mol}$ with n_e occurs as we have already reached the critical density of [CII] in the HII region, hence emission from the HII region saturates while continuing to increase in the PDR region. There is then a plateau of the relation which occurs at $\sim 10^{2.5}$ cm^{-3} because the densities are starting to approach the critical density of [CII] in the PDR regions as shown in Figure 3.5. At these densities the [CII] emission from the PDR also saturates, leading to an overall constant value of $f_{\rm [CII],mol}$.

Finally, we test the consistency of the values of $f_{\rm [CII],mol}$ obtained from Equation 3.8-3.12. The value of $f_{\rm [CII],mol}$ is calculated for the HRS galaxies using all five of these equations. Assuming that the most accurate estimate is given by the four parameter Equation 3.8, the offset between the other sets of measurements and this reference are shown in Figure 3.6. As expected, the dispersion increases as the number of parameters used to calculate $f_{\rm [CII],mol}$ decreases, and the uncertainty on $f_{\rm [CII],mol}$ increases when using

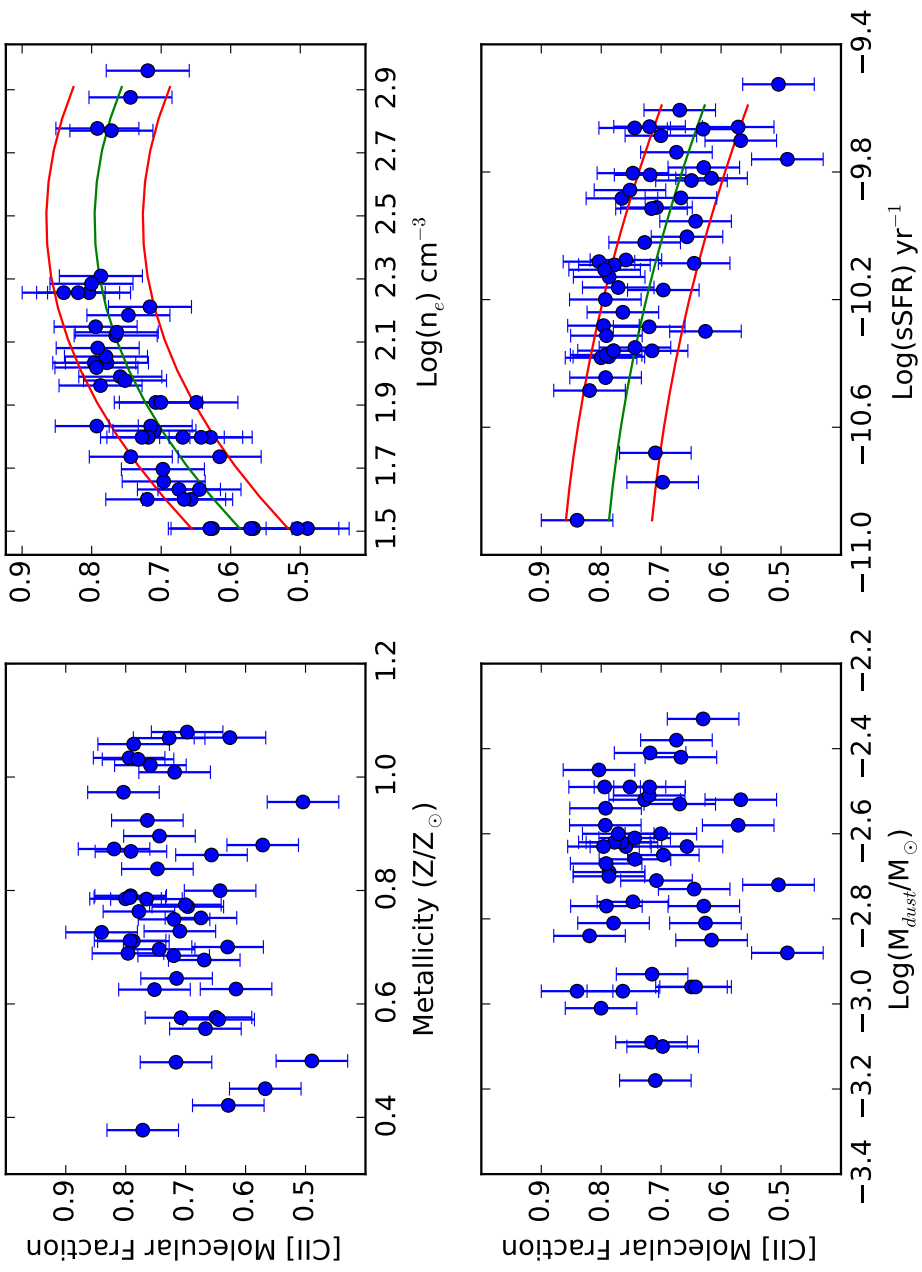

Figure 3.4. Relation between $f_{[\mathrm{CII}],\mathrm{mol}}$ as calculated from Equation 3.8 for galaxies from the HRS sample that have four key integrated properties (metallicity, density, dust mass fraction and sSFR). We also overlay the single prescriptions for density and sSFR, Equations 3.11 and 3.12 respectively, in the upper right and bottom right panels by the green lines. The red lines represent the one sigma errors on both prescriptions. The abrupt cut-off for HRS galaxies with densities less than $10^{1.5}$ cm^{-3} occurs because we under sampled the parameter space in the theoretical modelling, and didn't simulate clouds with densities lower than this value.

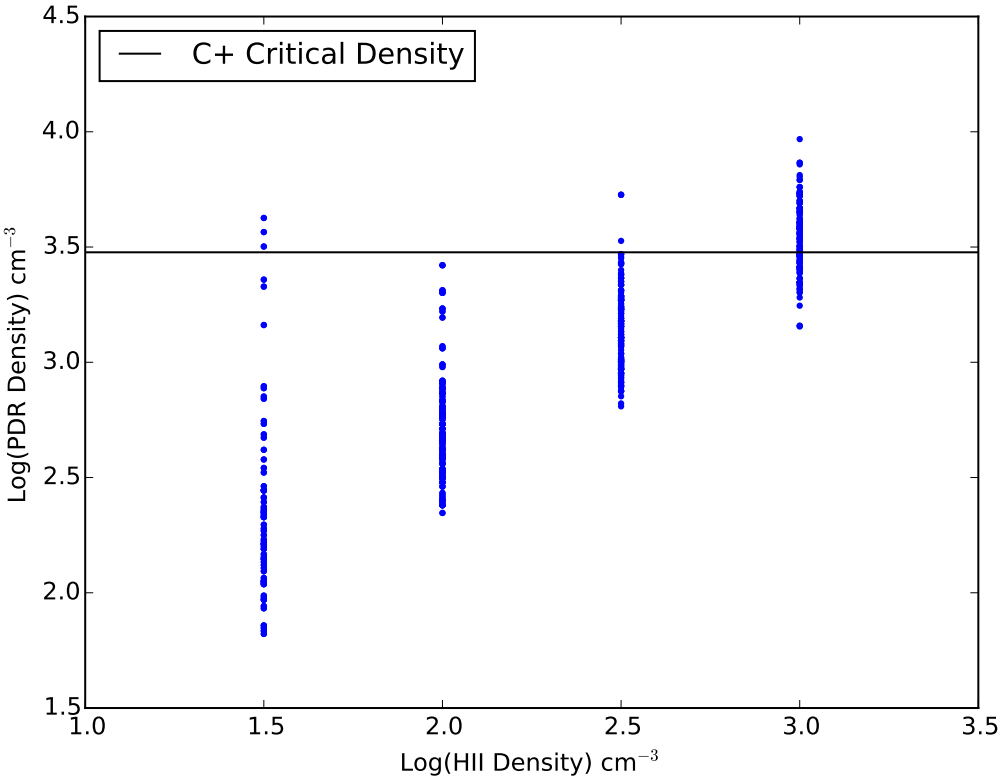

Figure 3.5. We plot the input Hydrogen number density (equivalent to n_e) used in ionised regions against the calculated PDR number densities. As can be seen for a HII density of 10^3 cm^{-3} the PDR density starts to exceed the critical density of [CII].

the one-parameter Equations 3.11 or 3.12 compared to the four-parameter Equation 3.8. This increase in uncertainty is accounted for by the larger $\sigma_{f_{[CII],mol}}$ values of Equations 3.11 and 3.12 versus that of Equation 3.8. We are aware that the dispersion with Equation 3.12 is bimodal and believe this to be a consequence of the binning method used to plot the histogram and details how appropriate a quadratic fit represents the data. To derive the above errors we computed the standard deviation of the measurements and hence, even for partially bimodal distributions, are suitable.

As these relations were derived using the HRS to determine weighting factors, they are mostly applicable over the parameter space probed by the HRS galaxies which can be seen in Figure 3.4. While the full parameter space covered by our simulated clouds was very large (see Tab. 2.2) some regions of this space were ignored via the weighting factors if found to be not representative of physical conditions in local galaxies. Throughout the analysis presented in Section 3.1, a Galactic cosmic ray ionisation rate was used, and so our prescriptions should only be used for low-redshift, normal star-forming galaxies. High-

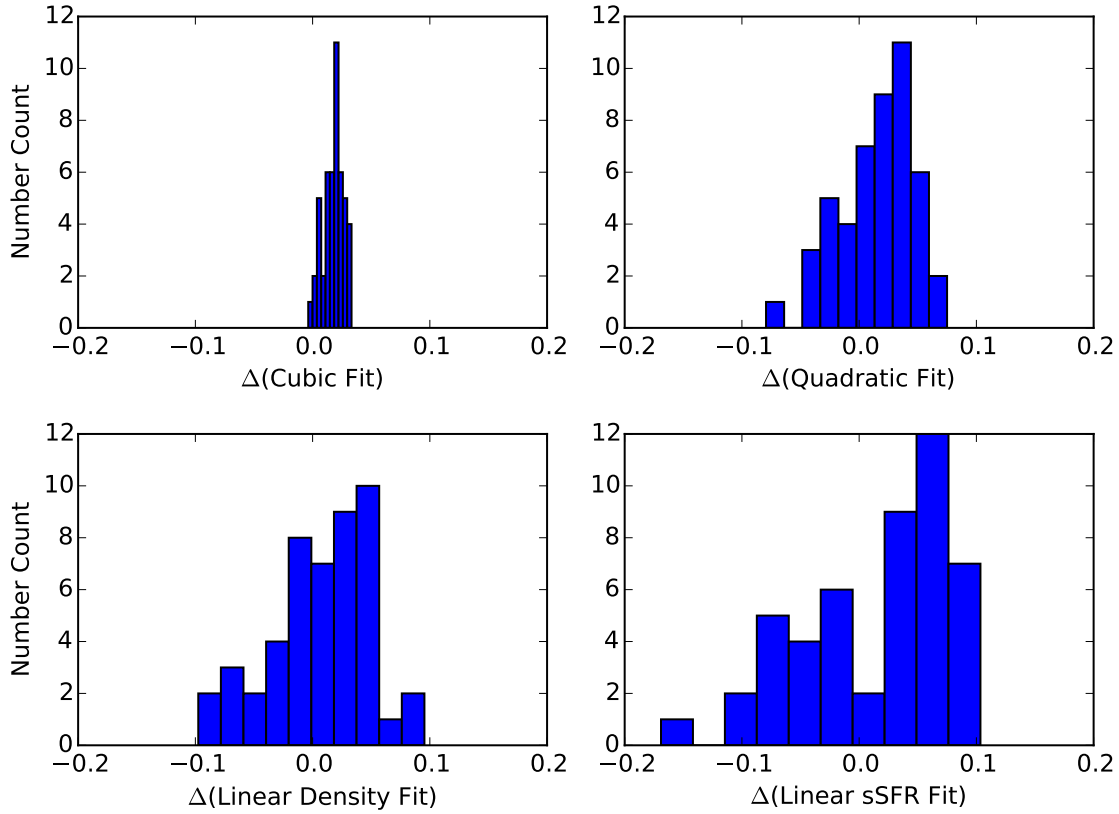

Figure 3.6. Distribution of the offset between the best prediction of $f_{[\mathrm{CII}],\mathrm{mol}}$ from Equation 3.8 for the HRS galaxies, and the values produced by the four alternative prescriptions (Equations. 3.9-3.12).

redshift galaxies, local ULIRGS, and other intensely star forming objects are very likely to have higher cosmic ray ionisation rates (100-1000× the Milky Way value). An analysis of the simulated clouds with high ionisation rates would require a representative sample of galaxies at high redshift, similar to the HRS at $z \sim 0$, which is beyond the scope of this Thesis.

Finally, throughout the modelling presented here, we held constant the N/O abundance ratio which is known to vary as a function of metallicity (Guseva et al. 2011; Pettini et al. 2008). In Section 3.3.3 we explore how variations of this abundance ratio change our results, and find an uncertainty on $f_{[\mathrm{CII}],\mathrm{mol}}$ of less than 3%, less than the reported errors in Equations 3.8-3.12); ergo this does not affect our results or the conclusions of this Thesis.

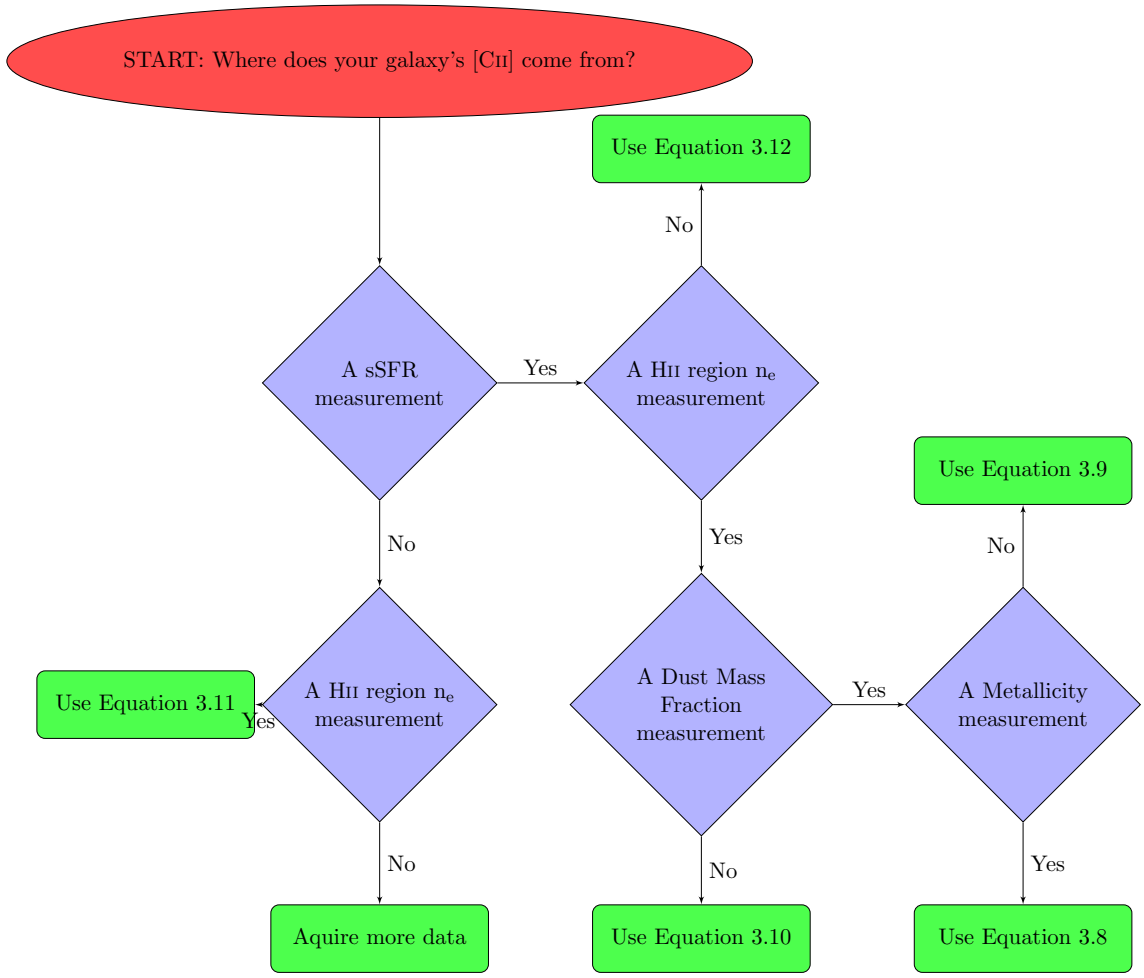

Figure 3.7. We here present a flowchart which can be used to constrain the fraction of [CII] emission from molecular regions from a galaxy. This will help to decide which equation should be used depending on which physical parameters of the galaxy have been observed and, therefore, what data is available for an individual galaxy.

3.2 Where does a galaxy's [CII] come from?

Here we summarise the main prescriptions detailed in this Chapter, and provide a cookbook to help decide which prescription is appropriate for a user's specific needs given their available data. There are five prescriptions (Equations 3.8, 3.9, 3.10, 3.11, 3.12) which accurately quantify the fraction of [CII] emission emerging from molecular regions, however which one should be used? To answer this we present a flowchart in Figure 3.7, which can be used to make this decision. The main decisions lie in determining which physical parameters of the galaxy have been observed and, therefore, what data is available.

3.3 Caveats

As mentioned above, to derive the prescriptions given, we only used clouds with cosmic ray ionisation rates equal to the the average Milky Way value (10^{-17} s^{-1}). We therefore test how the results from above change for cosmic ray ionisation rates equal to ten times the average Milky Way value (10^{-16} s^{-1}). We are also aware that our fitting procedure gives higher weights to galaxies which are more common (statistically probable) in the local universe. We therefore investigate an alternative Machine Learning technique to show that our prescriptions are appropriate and can be used for low weighted objects too. Finally, throughout the modelling presented here, we held constant the N/O abundance ratio which is known to vary as a function of metallicity (Guseva et al. 2011; Pettini et al. 2008). We now explore how variations of this abundance ratio change our results.

3.3.1 Different Cosmic Ray Ionisation Rates

We performed a similar analysis as in Section 4.3 for clouds with a cosmic ray ionisation rate 10x the average Milky Way value (10^{-16} s^{-1}). We find that the same four parameters emerge as necessary to provide the a prescription for $f_{\rm [CII],mol}$. We use this higher cosmic ray ionisation rate and produce identical plots to Figs 3.2, 3.4 and 3.3. We use a weighting of zero for clouds with cosmic ray ionisation rates different to this value.

We show in Fig 3.8 a plot for the AIC and BIC, similar to Figure 3.2, and find three to four parameters are needed, similar to that in Section 4.3. Once we obtained our prescription we applied it to the HRS objects, which have observed values for the four important parameters. We present these results in Figure 3.9 and, qualitatively, it is clear that the results are very similar and almost identical to those shown in Figure. 3.4. Finally we bin the HRS results, similar to Figure 3.3, and again find that, even for clouds with a cosmic ray ionisation rate 10x the average Milky Way value, the majority of the galaxies have 60-80% of their total integrated [CII] emission arising from molecular regions, shown in Figure 3.10.

Overall we claim that, even if a galaxy is thought to have cosmic ray ionisation rates ten times larger than the Milky Way value, our prescriptions detailed in Section 3.1 are still robust and accurate as the cosmic ray ionisation rate value does not affect the results at these levels. Higher redshift objects and ULIRGS will have cosmic ray ionisation rates more than $\sim 10^3$ times that of the Milky Way, and for those cases our prescription, in

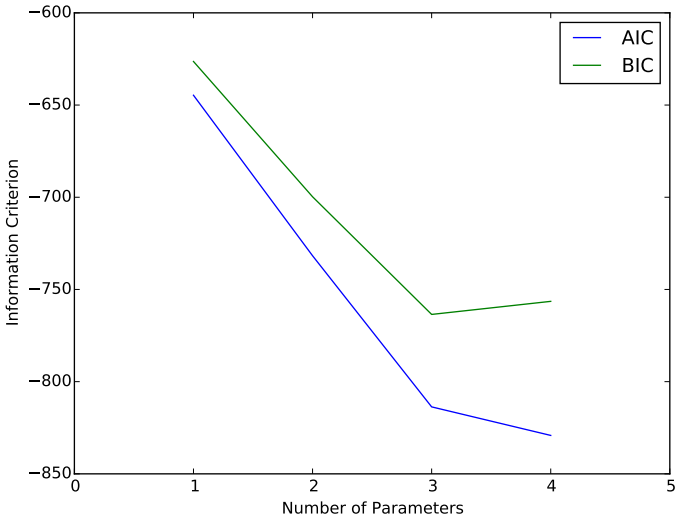

Figure 3.8. We provide a plot for the variation of the Akaike Information Criterion and the Bayesian Information Criteria in blue and green respectively, but now for clouds with a cosmic ray ionisation rate 10x the average Milky Way value. It can be seen how they reach a minimum of three to four necessary parameters, similar to Figure 3.2.

Section 3.1, starts to break down. Furthermore our prescription would not be valid at high redshift because the HRS sample is not representative of galaxies at higher redshifts. Therefore, our prescription is accurate only for low redshift, star forming and quiescent, galaxies regardless of their cosmic ray ionisation rate.

Obtaining a similar prescription for high redshift objects is possible, using the above method, however a statistically complete sample of galaxies at high redshift would be needed to provide the weightings necessary for the Bayesian Inference method. This could be done via a Machine Learning technique to generate a predictive sample of galaxies at high redshift, however this is beyond the scope of this Thesis.

3.3.2 Investigating weighting biases via Machine Learning

The statistical methodology used above may provide a better fit to data points with a higher weighting than those with lower weightings, due to the nature of our likelihood function in Equation 3.3. To overcome this possible issue of weighting biases we employ a Random Forest Machine Learning algorithm which does not include a statistical weighting on each data point.

A Random Forest algorithm is a tree-based classification method that learns how to classify objects into different classes using a training set. It is an ensemble supervised

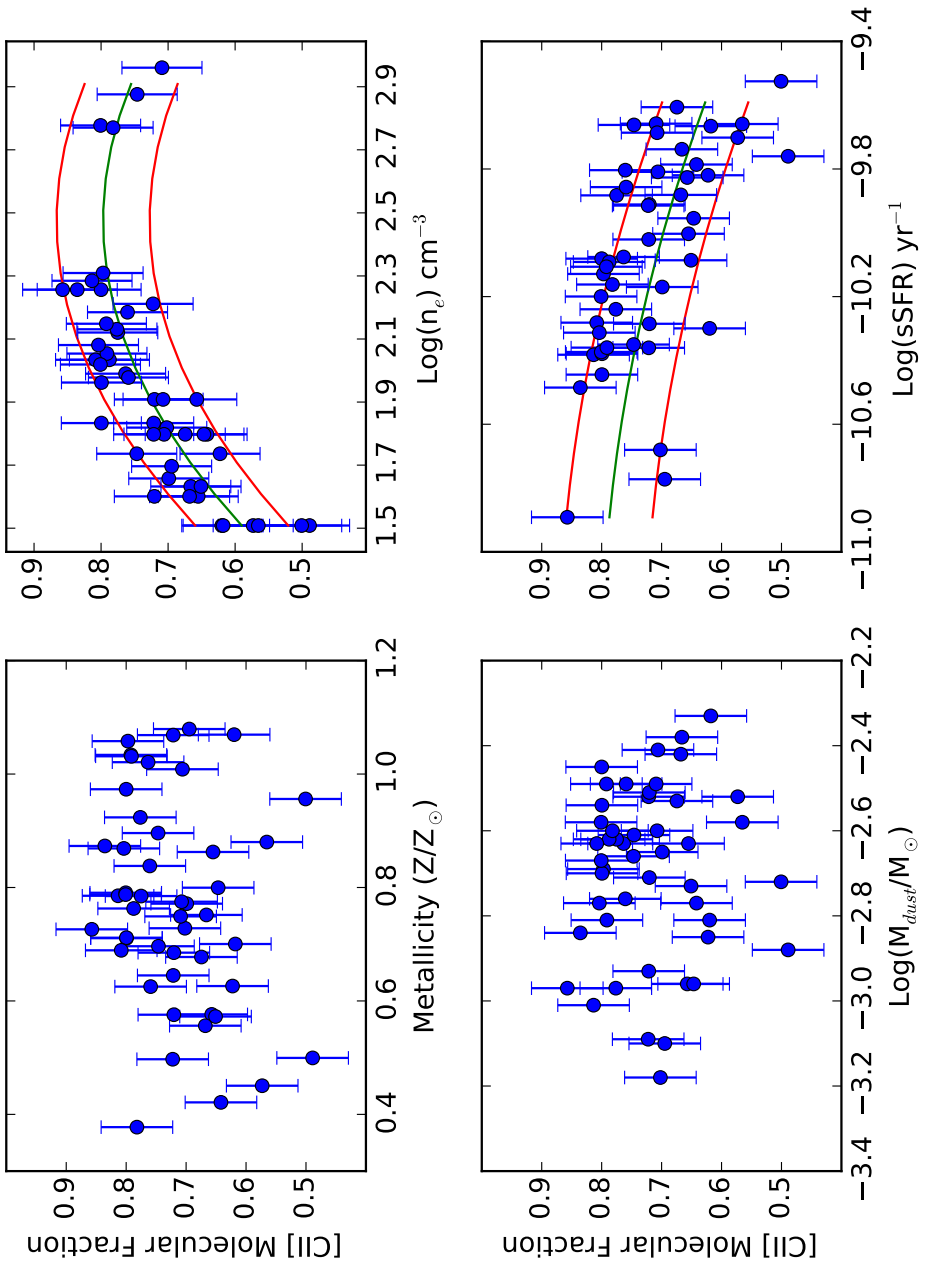

Figure 3.9. Relation between $f_{[\mathrm{CII}],\mathrm{mol}}$ for galaxies from the HRS sample with a cosmic ray ionisation rate 10x the average Milky Way value, a comparable plot to Figure 3.4. The different coloured lines here represent the same as those in Figure 3.4.

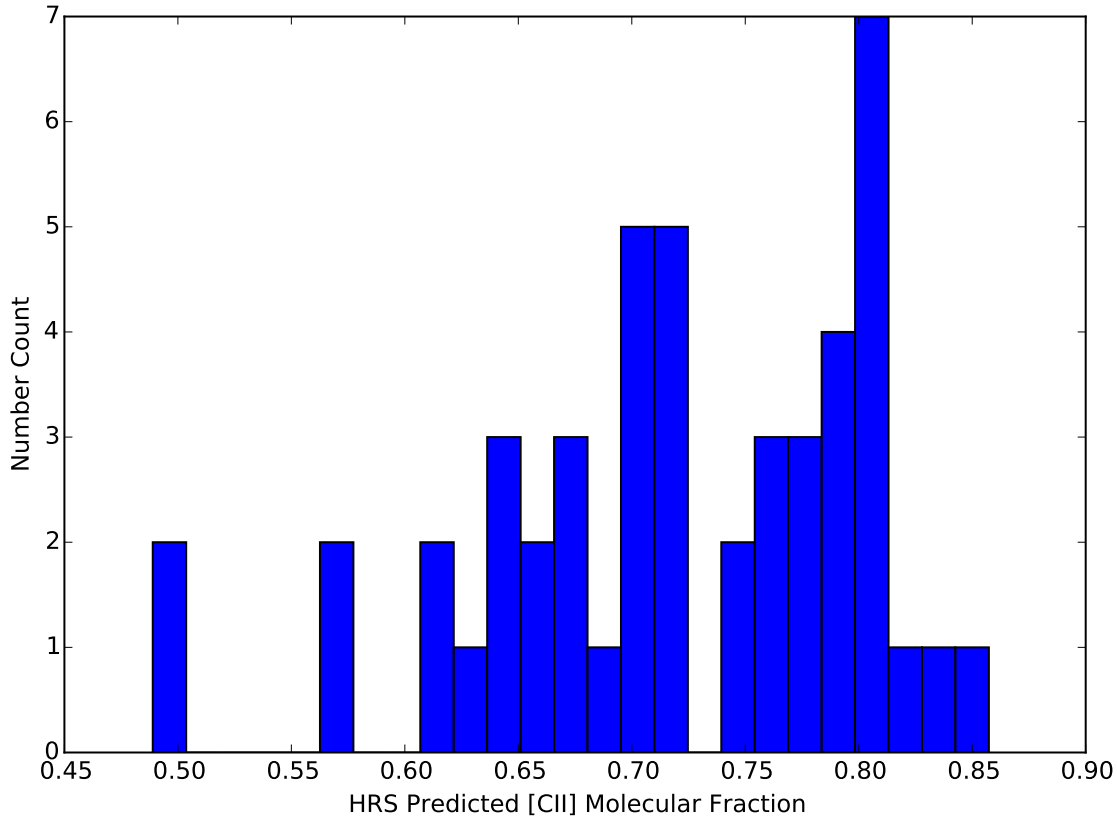

Figure 3.10. From the HRS sample we find that the majority of the galaxies have 60-80% of their total integrated [CII] emission arising from molecular regions, even for a cosmic ray ionisation rate 10x the average Milky Way value, a similar result to that in Figure 3.3.

machine learning classification technique that first assembles a decision tree for a random subsample of a full training set, with known features and classifications. It performs this multiple times (specified by the user) on different subsets, ergo building up a forest of decision trees on many different sub samples of the full training set. It finally combines the results from all the individual tree predictors to provide a tree predictor for the full training set (Breiman 2006). It is one of the most accurate classification algorithms available (Caruana & Niculescu-Mizil 2006) and is extremely fast while handling large quantities of data. The Random Forest algorithm has been used in various astrophysical problems such as the automatic classification of variable stars (Richards et al. 2011), the photometric classification of supernovae (Carliles et al. 2010) and for classifying variable 3XMM sources (Farrell et al. 2015). Technical details regarding the decision tree process are beyond this Thesis, however we refer readers to some of the original work in Quinlan (1986). A brief overview is also given in Carrasco et al. (2015) and Louppe (2014).

For our training set we use the collection of 1728 simulated clouds with a Milky Way like value of cosmic ray ionisation rate and only use the dust mass fraction, specific star formation, metallicity and density as our features to be used for selection and make the classification based on our values of $f_{[\mathrm{CII}],\mathrm{mol}}$ calculated from the Radiative Transfer modelling. We use this collection of 1728 clouds for the training set because we only want to include clouds which have a cosmic ray ionisation rate equal to the Milky Way value, typical of local universe galaxies and, hence, the HRS galaxies. We could use the full suite of simulated clouds for our training set, but then would have needed to include the cosmic ray ionisation rate as an additional feature to select for; these two methods would produce the same results. We use the *scikit-learn* (Pedregosa et al. 2012) Python software package *RandomForestClassifier* to run the algorithm.

We first replicate Figure 3.4 and present a similar plot in 3.11. Using this method, although the results are slightly different numerically, the trends are virtually identical. The one sigma scatter is larger for the random forest method as this is a far less statistically robust method to obtain accurate predictions for the HRS and is also trying to provide a robust fit on the low weighting objects too. This is reassuring and implies that our Bayesian method is robust for galaxies which would receive a low or high weighting based on the HRS.

We are also able to retrieve which features affect the classification most and we plot these results in Figure 3.12. Given the fact that we used the 1728 clouds which have a Milky Way like value of the cosmic ray ionisation rate, we would expect the feature selection to pick out parameters which most affect $f_{[\mathrm{CII}],\mathrm{mol}}$ which are similar to those seen in Figure 2.4; indeed it does, shown in Figure 3.12. We find that dust mass fraction is the parameter most responsible for trends in $f_{[\mathrm{CII}],\mathrm{mol}}$ while the others less so. We find a very similar result to the initial qualitative analysis in Chapter 2 where dust mass fraction, specific star formation rate and metallicity are the main drivers for the variations in $f_{[\mathrm{CII}],\mathrm{mol}}$.

Furthermore, we explicitly measure the difference between the results from the radiative transfer simulation versus the predicted quantities using Equations 3.11, 3.10, 3.9 and 3.8. We plot the results in Figure 3.14 and find that low weighted objects are fit as well as high weighted objects.

Finally, to emphasis that our prescriptions are equally robust for low and high weighted objects we plot the residuals of the simulated $f_{[\mathrm{CII}],\mathrm{mol}}$ value versus the predicted value

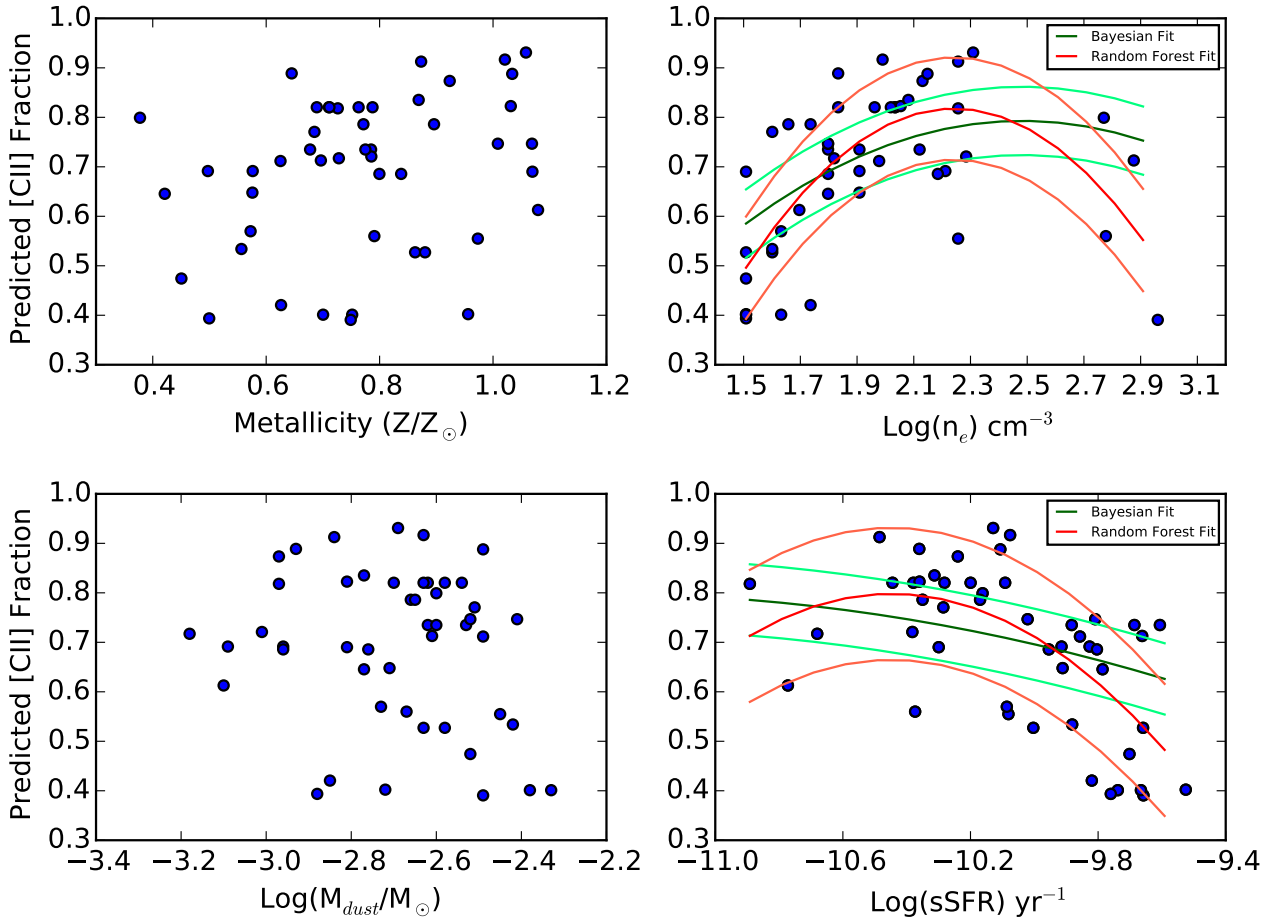

Figure 3.11. Relation between $f_{[\mathrm{CII}],\mathrm{mol}}$ using a Random Forest technique for galaxies from the HRS sample that have four key integrated properties (metallicity, density, dust mass fraction and sSFR). We also overlay the single prescriptions for density and sSFR, Equations 3.11 and 3.12 respectively, in the upper right and bottom right panels by the different shade of green lines; brighter green lines show the one sigma error. The red lines represent quadratic fits to the data.

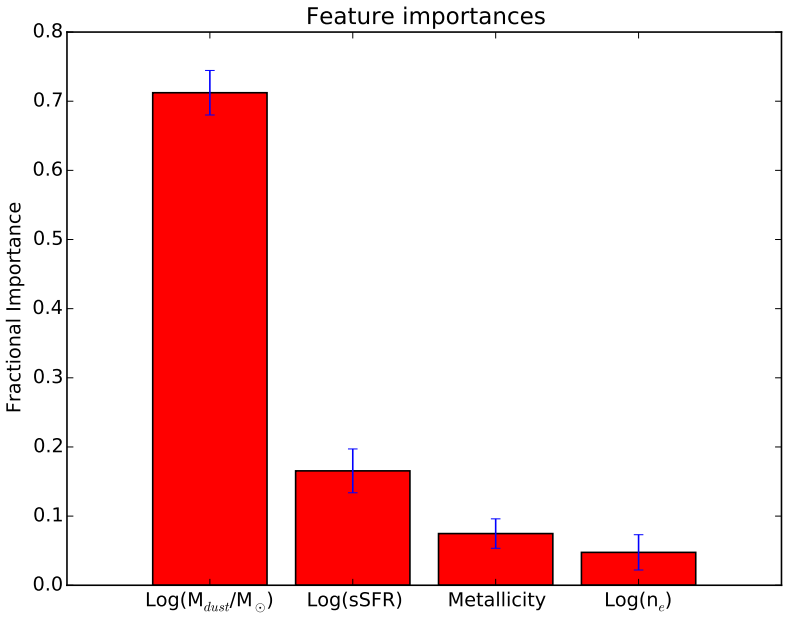

Figure 3.12. Our random forest method also provides information regarding which parameters are most important. These results are similar to the parameters retrieved using the Bayesian method.

using Equation 3.8 and find that the dispersion is independent of weighting.

We can therefore say with confidence that **a)** the Random Forest method has validated the results from our Bayesian approach and **b)** our prescriptions are robust for typical or more rarer/uncommon galaxies at low redshift.

3.3.3 Varying chemical abundances

When varying the metallicity parameter, we scaled all the abundances in Table 2.1 equally, except for hydrogen and helium. This means that the relative abundances between non-hydrogen and helium elements is constant. While this is generally correct, it is not true of the N/O ratio, which varies as a function of metallicity (Guseva et al. 2011; Pettini et al. 2008). When $\log(\mathrm{O/H}) + 12 > 8.2$, nitrogen is a secondary element and the N/O ratio decreases with metallicity. However, when $\log(\mathrm{O/H}) + 12 < 8.2$, nitrogen is a primary element and the N/O ratio is of constant value $10^{-1.5}$. Therefore, by assuming a constant N/O ratio, we have over-supplied the low metallicity clouds with nitrogen, which could lead to an erroneous [CII] emission calculation in the MOCASSIN simulations. Given that nitrogen is a coolant in ionised regions only, this would manifest itself as an underestimation of the [CII] emission from the ionised regions.

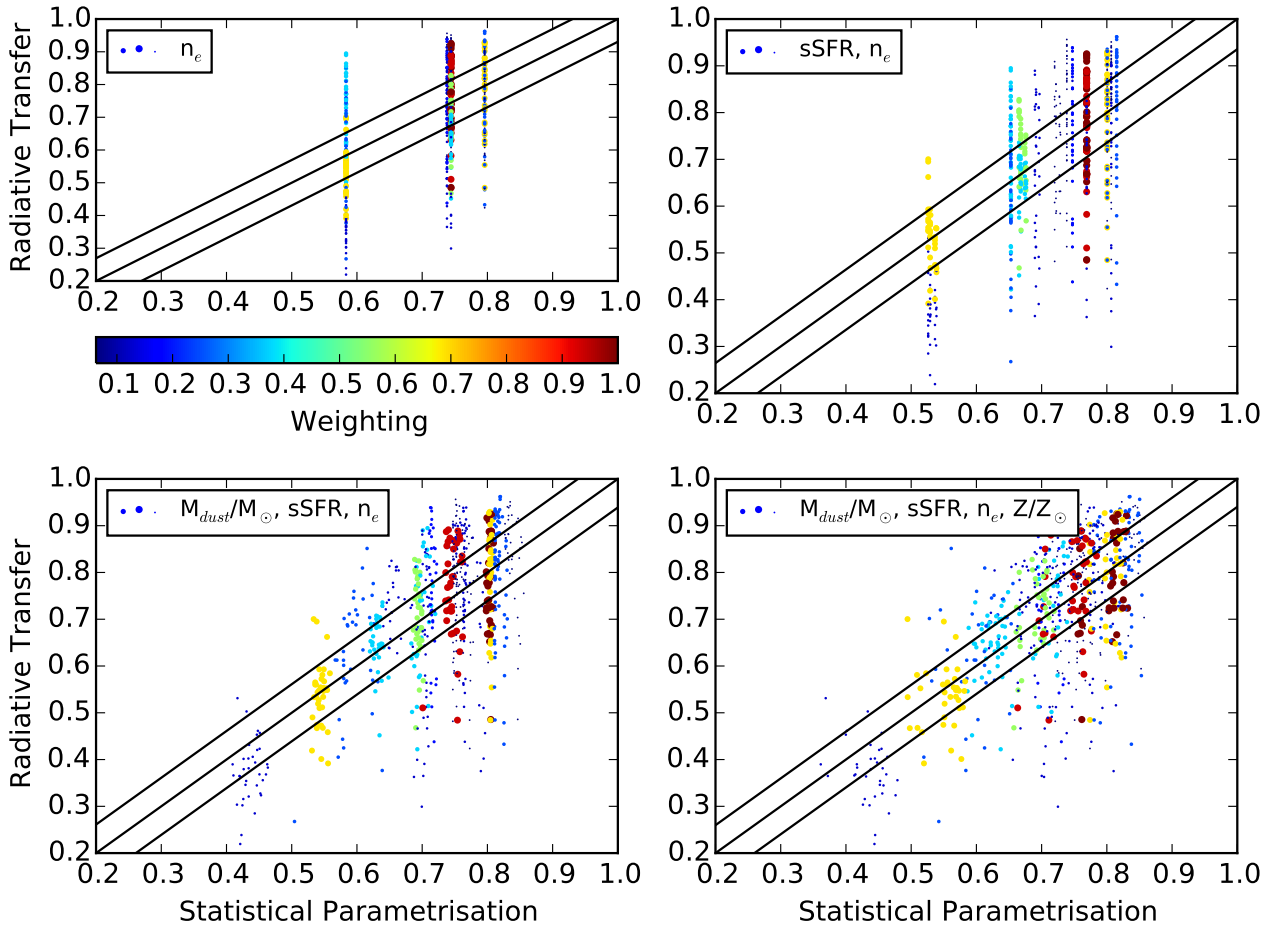

Figure 3.13. We plot results from the radiative transfer simulation versus the predicted quantities using Equations 3.11, 3.10, 3.9 and 3.8 where the colour of each point denotes the weighting it received. The black lines represent the unity relation and the one sigma scatter of the data in each plot.

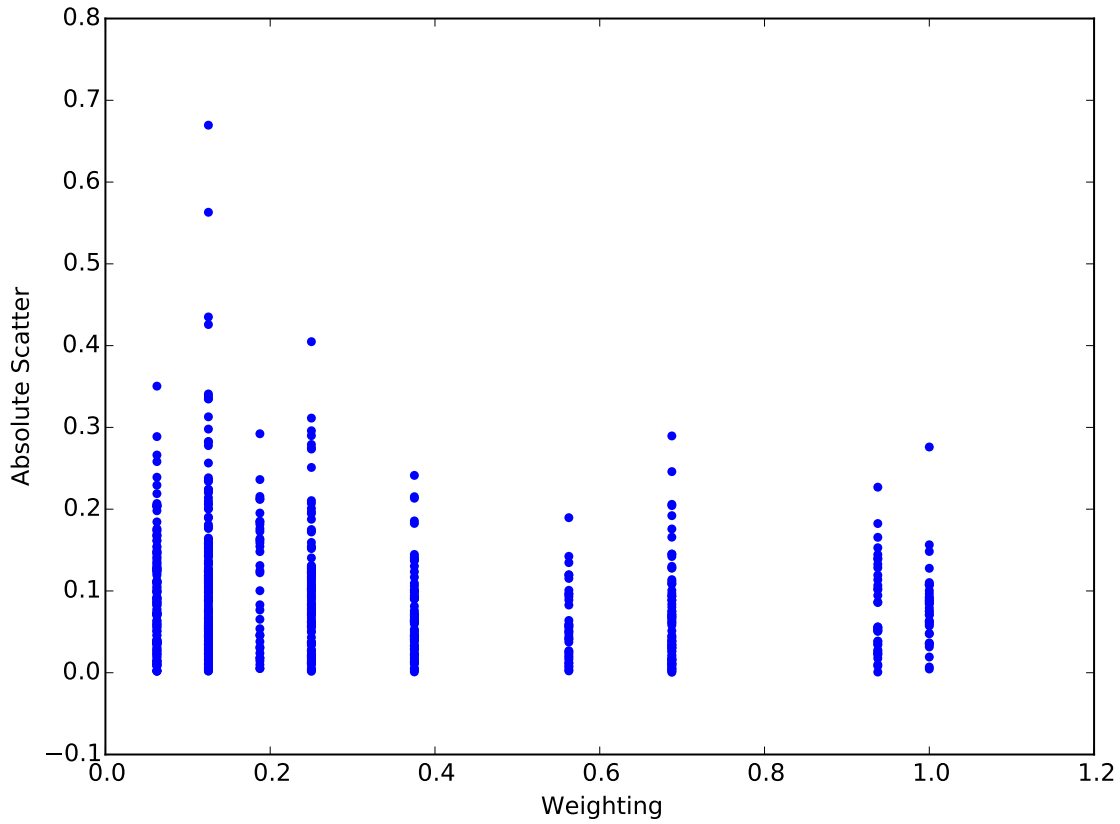

Figure 3.14. We plot the best fit models which were obtained when applying a weighting for each cloud with the number of parameters used varying from one to four.

To test for the effect of the varying N/O ratio with metallicity, we adopt the prescription from Pettini et al. (2008) and re-run MOCASSIN for three of the low metallicity clouds ($Z = 0.2Z_{\odot}$) with different sSFR and n_e (the age of the secondary burst is kept constant). We find that assuming a constant N/O could lead to an underestimation of the [CII] emission from the ionised of only 3.8- 7.7%. Since ionised regions contribute between 20-40% of the total [CII] emission (Sec. 3.1.5), this corresponds to an uncertainty on $f_{\rm [CII],mol}$ of less than 3%, less than the reported errors in Equations 3.8-3.12. This is therefore not a dominant source of uncertainty; the results for these runs are shown in Table 3.1.

3.4 Summary & Conclusions

To extend the analysis to the integrated [CII] emission from extragalactic objects, we employed a Hierarchical Bayesian Inference method to identify the simulated clouds that are representative of the physical conditions in local star-forming galaxies. This is possible

Table 3.1. To test for the effect of varying the N/O ratio as a function of metallicity we re-run three of our MOCASSIN runs. We find that, even in the most extreme cases, our calculations underestimate the [CII] emission from the ionised regions by 3.8-7.7%

Metallicity ($Z/Z_\odot$)	Log(sSFR) (yr^{-1})	n_e (cm^{-3})	[CII] with N/O constant ($L/L_\odot$)	[CII] with N/O varying ($L/L_\odot$)	Fractional difference (%)
0.2	-11.5	$10^{1.5}$	5.15×10^{-3}	5.19×10^{-3}	7.7
0.2	-10.5	$10^{2.0}$	11.32×10^{-3}	11.92×10^{-3}	5.3
0.2	-10.5	$10^{3.0}$	9.55×10^{-3}	9.91×10^{-3}	3.8

under the assumption that the physical conditions found in a simulated star-forming cloud can represent the average conditions found on galaxy-wide scales for objects with similar physical properties such as metallicity, sSFR, and density.

We find that $f_{\rm [CII],mol}$ is best predicted using four key parameters: n_e, sSFR, dust mass fraction and metallicity (Equation 3.8). We tested this prescription on the Milky Way and obtained an estimate that 75.9 ± 5.9% of its total [CII] emission arises from molecular regions, which is in very good agreement with observations (Pineda et al. 2013). Given that it is relatively rare for measurements of all four of these parameters to be available for large samples of galaxies, we provide alternative prescriptions which require fewer parameters. These other prescriptions (Equations 3.9-3.12) also produce estimates for the Milky Way consistent with direct observations, although the uncertainty on $f_{\rm [CII],mol}$ increases as the number of parameters involved in the prescription decreases. Of most practical use for many extragalactic studies is Equation 3.12 which relates $f_{\rm [CII],mol}$ to sSFR.

Applying the prescription to a sample of galaxies from the HRS, we find that typical galaxies in the local universe have 60-80% of their [CII] emission arising from molecular regions. Within this sample, $f_{\rm [CII],mol}$ increases with density, and decreases with sSFR. Combining the relations obtained through the bayesian analysis, we propose a decision tree in Figure 3.7 to help determine which equation to use depending on the type of galaxy and the data products available. Using this, it is possible to estimate the relative fraction of [CII] emerging from the molecular phase of the ISM when only galaxy-wide observations are available. Correcting integrated measurements for emission from other phases of the ISM is critical to correctly interpret [CII] emission as a star formation tracer.

Chapter 4

Deriving a multivariate α_{CO} conversion function using the [CII]/CO(1-0) ratio

We present the first results using xCOLD GASS, a legacy survey of molecular gas in nearby galaxies, now extending down to stellar masses of $10^9 M_\odot$ from its precursor survey COLD GASS. Using the IRAM 30m telescope we measure the CO(1−0) line and, with Herschel PACS observations, measure the [CII] 158μm emission line in a sub-sample of 24 intermediate mass ($9 < \log M_*/M_\odot < 10$) and low metallicity ($0.4 < Z/Z_\odot < 1.0$) galaxies. We provide the first scaling relations for the integrated and molecular region $L_{\rm [CII]}/L_{\rm CO(1\text{-}0)}$ ratio as a function of galaxy properties. After a Bayesian analysis we find that only two parameters, namely metallicity and position off the main sequence, Δ(MS), are needed to quantify variations in the luminosity ratio; metallicity describes the total dust content available to shield CO from UV radiation, while Δ(MS) describes the strength of this radiation field. We connect the $L_{\rm [CII]}/L_{\rm CO(1\text{-}0)}$ ratio to the CO-to-H_2 conversion factor and find a multivariate conversion function, which can be used up to $z \sim$2.5.

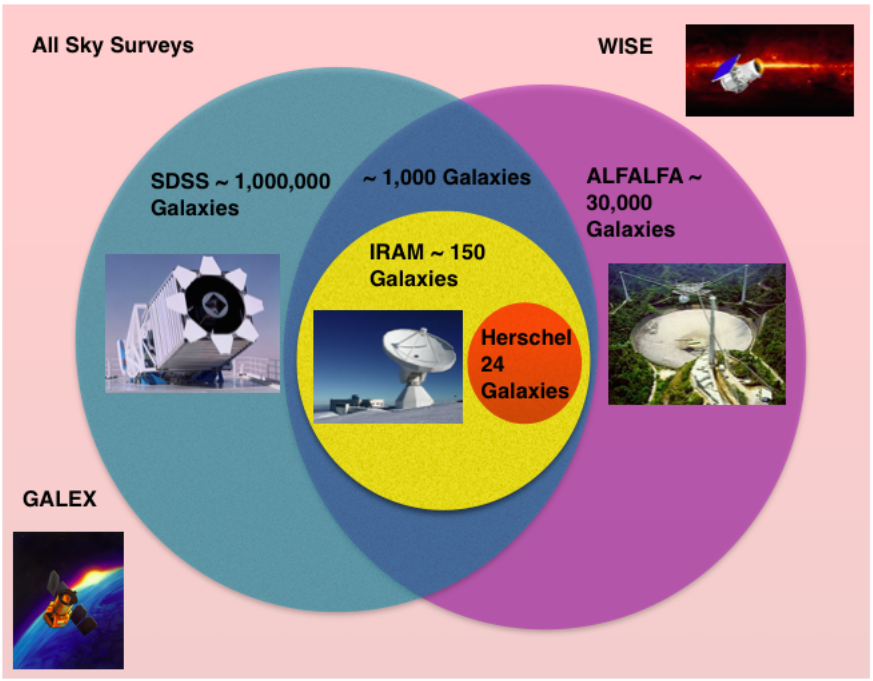

Figure 4.1. We provide a Venn diagram representing the sample selection of xCOLD GASS. The survey has a randomly selected sample of ∼150 galaxies from the regions of overlap between the SDSS, GALEX, WISE and ALFALFA HI surveys. Out of the total 150 galaxies we obtained Herschel PACS [CII] spectroscopic data for 24 of those.

4.1 Survey description and sample selection

The xCOLD GASS sample is a randomly selected sample of galaxies from the regions of overlap between the SDSS (Stoughton et al. 2002), GALEX (Martin et al. 2005), WISE (Wright et al. 2010*a*) and ALFALFA HI (Giovanelli et al. 2005) surveys. It is an unbiased sub-sample of all the galaxies in the redshift range $0.01< z <0.02$ and is stellar mass selected ($9< \log M_*/M_\odot < 10$). There is no other selection criteria based on colour, star formation rate, etc. The SDSS data provide us with optical imaging and spectroscopy over the central 3" of our galaxies and with the GALEX and WISE data we have FUV, NUV, 3.4μm, 4.5μm, 12μm and 22μm photometry. Moreover, we have HI fluxes from observations at the Arecibo observatory as part of the GASS survey (Catinella et al. 2010, 2013). The full xCOLD GASS sample contains 133 galaxies, which will be presented in full alongside all the CO(1-0) IRAM observations in Saintonge et al. 2016 (in prep). All of this is shown in Figure 4.1.

Our target selection for Herschel PACS observations involved removing from the to-

tal sample of 133 xCOLD GASS objects the passive elliptical galaxies, where Saintonge et al. (2011*a*) showed that molecular gas contributes insignificantly to the mass budget ($M_{H_2}/M_* < 0.2\%$), and one galaxy which already had adequate PACS observations. After this a mass-selected sample of 103 galaxies remain which allows for roughly 20 galaxies in 5 stellar mass bins between $9 < \log M_*/M_\odot < 10$. However the Herschel Space observatory (hereafter Herschel) exhausted its supply of liquid helium coolant midway through our observations and so, out of those 103 galaxies which were originally proposed, we here present the 24 galaxies for which the [CII] 158μm line was observed with PACS.

In order to provide a statistically robust prescription of the conversion function it is imperative to probe as large a parameter space as possible, hence we combine our data with literature data if possible. Unfortunately multi-wavelength data sets with accurate galaxy parameter measurements and observations of both CO and [CII] are rare. Cormier et al. (2014) do present data for a compilation of galaxies from the Dwarf Galaxy Survey (Madden et al. 2013) (DGS hereafter) which have good CO(1-0) and [CII] observations, which we therefore add to the xCOLD GASS objects. We are interested in objects with total galaxy-wide integrated detections in CO(1-0) and [CII]; we therefore have to eliminate all objects which have optical diameters greater than 47" (the PACS IFU map size), and objects which have resolved interferometric CO observations as aperture corrections are impossible due to the unresolved nature of the Herschel PACS data.

Overall we are able to add seven extremely low metallicity galaxies, $0.2Z_\odot < Z < 0.5Z_\odot$, from the DGS survey; these are Haro 11, Mrk 930, Haro 3, Mrk 1089, UM 448, Haro 2 and II Zw 40. Derived galaxy parameters are found within Madden et al. (2013) while observed [CII]/CO(1-0) ratios, with aperture corrections, and star formation rates are calculated here. We fold these galaxies into our sample and derive all necessary measurements consistently as detailed below.

4.1.1 SDSS observations

Optical and UV measurements from SDSS

For the xCOLD GASS galaxies parameters such as redshifts, sizes and magnitudes are retrieved from the SDSS DR7 database (Abazajian et al. 2009). We retrieve stellar masses and emission line fluxes from the MPA-JHU catalogue[1] where calculations were performed

[1]The data catalogues are available from http://www.mpa-garching.mpg.de/SDSS/

using the methods presented in Tremonti et al. (2004) and Kauffmann et al. (2003*b*). With these, we then calculate the gas-phase metallicity of the galaxies using the prescription from Pettini & Pagel (2004) (PP04 hereafter):

$$12 + \log(\mathrm{O/H}) = 8.73 - 0.32 \log \left(\frac{[\mathrm{OIII}]}{\mathrm{H}_\beta} / \frac{[\mathrm{NII}]}{\mathrm{H}_\alpha} \right) \tag{4.1}$$

which was calibrated down to the low metallicity range probed here. On this scale a value of $12 + \log(O/H) = 8.69$ corresponds to solar metallicity following the oxygen abundance of Asplund et al. (2009). We use this metallicity prescription as it was calibrated using star forming galaxies, similar to our sample of xCOLD GASS galaxies, and is valid for 12 + log(O/H) > 8.0. The stellar mass surface density is defined as:

$$\mu_* = \frac{M_*}{2\pi R_{50,z}^2} \tag{4.2}$$

where $R_{50,z}$ is the z-band 50% flux intensity Petrosian radius, in kiloparsecs, taken from the SDSS database.

For the DGS galaxies stellar masses and redshifts are taken from the catalogue presented in Madden et al. (2013), with an explanation on how these quantities were derived. Metallicities were calculated by collating line information from various literature sources, quoted in Madden et al. (2013), and converted to PP04 units using the methods from Kewley & Ellison (2008).

4.1.2 GALEX and WISE observations and data reduction

To account for unobscured star formation we use GALEX FUV (0.152μm) and NUV (0.227μm) images, downloaded from the public GALEX All-sky and Medium Imaging surveys (AIS and MIS respectively) detailed in Martin et al. (2005). To perform aperture photometry we employ a similar data reduction technique to Wang et al. (2010). We calculate total star formation rates and hence do not use the same aperture as the IRAM beam. We use a circular aperture of diameter equalling the D_{25} diameter from SDSS, defined as the isophotal diameter of the 25 mag arcsec^2 isophote in the g-band. We then calculate the background noise level within an annulus where the inner radius equals half the D_{25} diameter, and the outer radius equals 2.5 times the D_{25} diameter. To convert from count per second to magnitudes, in the AB system, we follow the prescription given in the GALEX documentation, detailed in Oke (1990). We finally convert the FUV and NUV band luminosities into unobscured UV star formation rates by using the prescriptions

detailed in Buat et al. (2011) and Schiminovich et al. (2007). The star formation rates derived from the NUV and FUV bands are in excellent agreement with each other so our choice of band is extraneous. We do this for both the xCOLD-GASS and DGS samples.

For the obscured star formation we use the all-sky infrared survey with the Wide-field Infrared Survey Explorer (WISE) satellite. This provides photometric data for a large sample of galaxies at 3.4, 4.6, 12 and 22 μm infrared bands with 5σ point-source sensitivities of at least 0.08, 0.11, 0.8, and 4 mJy, respectively (Wright et al. 2010*a*). We first download the 12 and 22 μm images of our galaxies using the WISE all-sky survey catalog and then perform aperture photometry as mentioned above. To convert 12μm and 22μm luminosities into IR star formation rates we use the observationally derived prescription in Jarrett et al. (2013). Of the two WISE bands for which we can calculate star formation rates, the 22μm is the optimal choice to compute SFR$_{IR}$ however the observations in this band are shallower relative to the 12μm band. Again, we do this for both the xCOLD-GASS and DGS samples with the caveats that **a)** stellar continuum from older stars is negligible at 22μm **b)** there are no AGN in our sample and so AGN contribution to the 22μm flux is negligible.

Out of the 24 xCOLD GASS objects here 22 have clear detections, with S/N $>$ 3, in the 22μm band, which we here use to calculate SFR$_{IR}$, while there's a 100% detection rate in the 12μm band. Therefore for the two objects which are undetected at 22μm, but detected at 12μm, we calculate SFR$_{IR}$ using the 12μm photometry after applying a small correction to account for a systematic trend between SFR$_{IR,12}$ and SFR$_{IR,22}$:

$$SFR_{IR} = 10^{0.0936+1.259 \log SFR_{IR,12}} . \tag{4.3}$$

Another benefit of using the 22μm SFR is that the 12μm emission is sensitive to PAH features which are enhanced in low metallicity galaxies, similar to the ones presented in (Haynes et al. 2010). Comparing the values of SFR$_{tot}$ = SFR$_{UV}$ + SFR$_{IR}$ with the measurements from optical-UV SED fitting reveals no systematic offset, in complete agreement with Huang & Kauffmann (2014). Such calibrated SFR ladders have been shown to be reliable when measuring SFRs across large galaxy samples including both passive and actively star-forming objects (Wuyts et al. 2011). For the seven DGS galaxies we have a 100% detection rate in the 22μm band. This technique to obtain total SFRs, from the combination of UV and IR photometry, is similar to that presented in Saintonge et al. (2016); we do this for both the xCOLD GASS and DGS samples.

From this it is possible to calculate, for both xCOLD GASS and DGS galaxies, the effective UV attenuation, A_{IRX}, where the log quantity is defined in Saintonge et al. (2013) as:

$$A_{\rm IRX} = \left(\frac{\rm SFR_{IR}}{\rm SFR_{UV}} + 1\right)^{2.5}. \tag{4.4}$$

This is another important quantity which may correlate with $\rm L_{[CII]}/L_{CO(1\text{-}0)}$ as it is a measure of dust emission in the FIR versus emission from young stars in the UV - we express it in this form, as opposed to the log quantity, for mathematical convenience when performing the statistical analysis described later in Section 4.3. We also want to allow for the possibility of a redshift dependence in our conversion function and so we measure the distance off the main sequence for each galaxy. Using the analytical definition of the main sequence by Whitaker et al. (2012), where:

$$\log(\rm sSFR_{\it ms}(\it z, M_*)) = -1.12 + 1.14\it z - 0.19\it z^2 - (0.3 + 0.13\it z) \times (\log \it M_* - 10.5)[\rm Gyr^{-1}] \tag{4.5}$$

with z and M_* denoting redshift and stellar mass, we can then define the distance off the main sequence as:

$$\Delta(\rm MS) = \frac{\rm sSFR_{measured}}{\rm sSFR_{\it ms}(\it z, M_*)} \tag{4.6}$$

which is applicable up to z$\sim$2.5, as stated in Whitaker et al. (2012). A similar definition was used in Genzel et al. (2015).

4.1.3 DSS observations and data reduction

To measure r-band magnitudes in a homogenous way between the xCOLD GASS and DGS samples we perform aperture photometry here; the DGS galaxies do not have SDSS photometric measurements unlike the former and so we utilise the ESO DSS (Digital Sky Survey). R-band images were downloaded from the ESO DSS Online Archive at http://archive.eso.org/dss/dss, where further information regarding the survey can be found. Aperture photometry was then carried out in the same way to the WISE and GALEX photometry, detailed above, to obtain r-band counts which were then converted to magnitudes in the AB system on the DSS website[2]. These were then combined with the NUV magnitudes, obtained in Section 4.1.2 for the xCOLD GASS and DGS galaxies, to provide the colour parameter of each galaxy calculated as NUV-r [magnitudes].

[2]See the conversion at http://gsss.stsci.edu/zzzOldWebSite/DSS/ PHOTOMETRY.

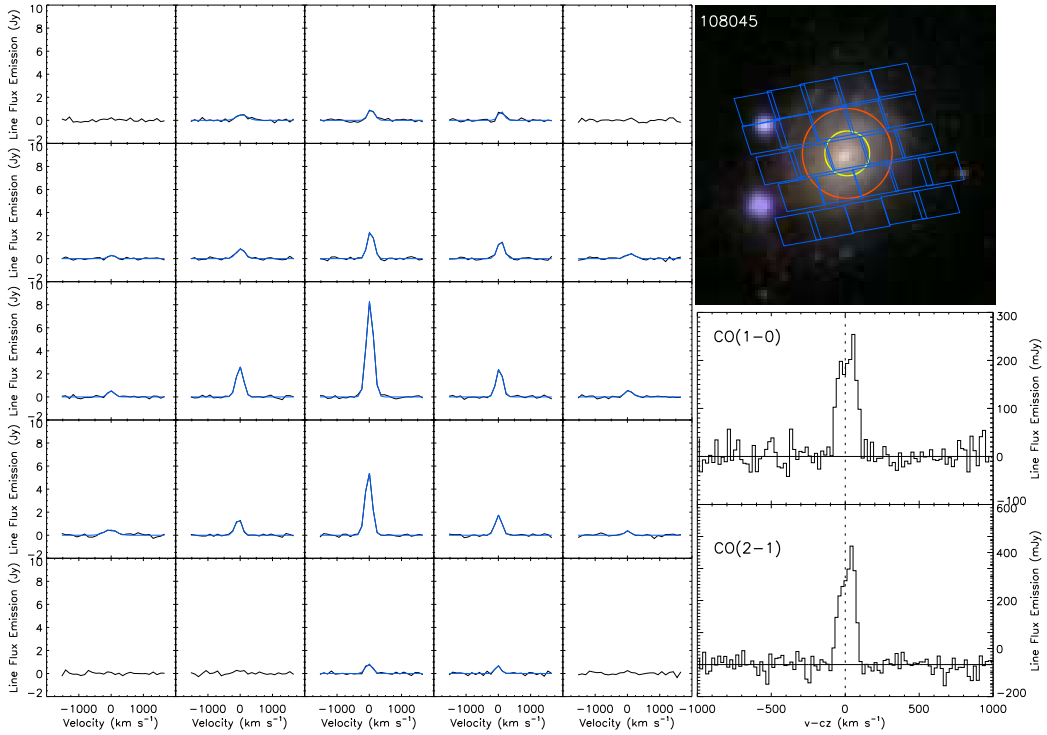

Figure 4.2. We provide a plot of the IRAM and Herschel spectroscopic data for an example galaxy. We observed the [CII] 158μm emission line using the PACS array, onboard Herschel, plotted as the blue grid overlaid onto the SDSS stamp, in the top right panel, for this galaxy. The gaussian fitted to the signal in each spaxel is provided by the five by five grid on the left. In the case where the S/N $>$ 3 we fit a gaussian, shown in blue, while in the case of spaxels with a S/N $<$ 3, no gaussian is fit. We overlay the CO(1-0) and CO(2-1) FWHM of their respective PSFs by the red and yellow circles respectively. In the bottom right, we plot the CO line spectroscopy obtained using the CLASS software where the spectroscopic data of the line is centred to a velocity of zero. The CO(2-1) beam conveniently fits in a very similar aperture to the central PACS spaxel, as can be seen, and provides a convenient way to combine the two datasets; however the analysis of this is beyond the scope of this Thesis as we shall focus solely on the CO(1-0) molecular data. Similar plots for all of our 24 galaxies can be found in Appendix B.

4.1.4 Herschel observations and data reduction

Twenty-four of the galaxies within the xCOLD GASS survey were observed with the PACS spectrometer (Poglitsch et al. 2010) onboard Herschel (Pilbratt et al. 2010) as part of the programme OT2_asainton_1, P.I. A. Saintonge. The seven DGS galaxies were observed as part of a guaranteed time key programme.

The PACS array is composed of 5x5 square spatial pixels each of side 9.4", covering a total field of view of 47". The observations were carried out in line-spectroscopy mode. The data were reduced using the Herschel Interactive Processing Environment (HIPE) (Ott 2010). We used standard scripts of the PACS spectrometer pipeline to reduce the data from the raw product to its level 2 processed form. From this, line fitting was done using IDL scripts, written by the author of this Thesis, employing routines within the IDL Astronomy User's Library found at (http://idlastro.gsfc.nasa.gov/). The lines are well fitted with a single gaussian using the IDL fitting routine GAUSSFIT[3]. The signal from each spaxel of the PACS array is fitted with a second order polynomial with the addition of a Gaussian for the baseline and emission line respectively. From this we calculate the S/N in each spaxel. To calculate the total flux for each individual galaxy, we add up the integrals of the fitted Gaussians from all the spaxels which have a S/N > 3. For total uncertainties we assume a 30% error of the total [CII] line flux, as justified in (Poglitsch et al. 2010). With Herschel all 24 xCOLD GASS galaxies show a clear detection in [CII] with a S/N > 3, while all seven DGS galaxies also show clear detections.

We want to directly compare the [CII] line luminosities with the CO(1-0) luminosity and to do this we convolve the PACS spaxel array with the IRAM CO(1-0) beam, detailed in Section 4.1.5. We approximate the 2-D IRAM beam point spread function as a Gaussian, with a FWHM of 21.4", where the peak is normalised to one[4]. We ensure the peak of this Gaussian is set to one to give maximum weighting to the central spaxel. We do this for all the xCOLD GASS objects. For the DGS objects we do different aperture corrections depending on the size of the beam PSF used for each individual CO(1-0) measurement Rémy-Ruyer et al. (2014).

[3] http://www.exelisvis.com/docs/GAUSSFIT.html

[4] The IRAM beam width and beam efficiencies used in these calculation can be found at http://www.iram.es/IRAMES/mainWiki/Iram30mEfficiencies.

4.1.5 IRAM observations and data reduction

Observations were carried out at the IRAM 30m Telescope, as part of the xCOLD GASS survey, using the Eight Mixer Receiver (EMIR) (Carter et al. 2012) to observe the CO(1−0) line, which has a rest frequency of 115.27 GHz. EMIR allows for observations on two sidebands with 8GHz bandwidth per sideband per polarisation. With a single tuning of the receiver at a frequency of 111.41 GHz, we are able to detect the redshifted CO(1−0) line for all galaxies in our sample with the 4GHz bandwidth covered by the spectrometers, resulting in greater time efficiency. The second band is tuned to a frequency of 222.81 GHz (E230 band) to cover the redshifted CO(2-1)[5]

Observations were carried out in fixed observing blocks and as poor-weather backups. We made real-time decisions on targets to accommodate to the variable weather conditions. We aimed to observe the bluer galaxies (prior knowledge taken from the SDSS spectra), whom are generally more CO-luminous, under poorer weather conditions. We have a clear detection of the CO(1-0) line in 23 out of our 24 galaxies. The CO observations were carried out in a very similar manner to COLD GASS, hence only brief details regarding the observing strategy have been given above. For more detailed information please see Saintonge et al. (2011*b*) and Saintonge et al. (2011*a*).

The xCOLD GASS data are reduced using the Continuum and Line Analysis Single-dish Software (CLASS)[6] which is part of the GILDAS software. All scans are visually inspected and those with anomalous features, such as distorted baselines or increased noise due to poor atmospheric conditions or high water vapour levels, are discarded. The individual scans for a single galaxy are baseline-subtracted, using a first order fit, and then combined. This average spectrum is then binned to achieve a resolution of $\sim$20kms^{-1} and the rms is obtained and recorded. The flux of the CO(1−0) line is measured by adding the signal within an appropriately defined frequency window; in the case of a detection this window is set by hand to match the observed line profile. For the null detection scenario the window is set to a width of 200kms^{-1} or to the full width of the HI line. If there is no detection then an upper limit for the flux is obtained.

Once the CO(1−0) line fluxes have been calculated we are able to calculate the total CO luminosity[7], using the prescription in Equation 1.18. We calculate the measurement

[5]The analysis of this Thesis will focus on the CO(1-0) data only.

[6]http://www.iram.fr/IRAMFR/GILDAS/doc/html/class-html/class.html.

[7]Calculated from the antenna temperature units using the conversion $I/T^{\star}_{a}$ = 6.36 Jy/K, the beam efficiency, specific for the IRAM 30m at our observing frequency of 115GHz.

error on the observed line flux, $S_{CO,cor}$, as:

$$\epsilon_{obs} = \frac{\sigma_{rms} W50_{CO}}{\sqrt{W50_{CO} \Delta w_{ch}^{-1}}} \tag{4.7}$$

where Δ w_{ch}, the width of each spectral channel, is equal to $\sim$21.57km s^{-1} with mild variations due to differing redshifts. The rms noise per spectral channel is denoted by σ_{rms} and $W50_{CO}$ is the FWHM of the CO(1$-$0) line.

As mentioned in Section 4.1.4 we convolve the PACS spaxel array with the IRAM CO(1-0) beam to measure the $L_{[CII]}/L_{CO(1\text{-}0)}$ ratio over the footprint of the IRAM beam (or for the different beam FWHMs for the CO(1-0) observations in the DGS sample). However all of the xCOLD GASS galaxies presented in this work lie within the tight redshift range $0.02 > z > 0.01$, and are all roughly 30" on the sky, meaning that not all of the galaxies can be observed with a single pointing of the IRAM 30m dish, which has a beam FWHM of $21.4''$ at a wavelength of 3mm. Therefore, when investigating the molecular gas scaling relations, in Section 5.1, we apply an aperture correction to the xCOLD GASS CO(1-0) measurements to account for flux missed by the IRAM beam; we follow the same technique presented in Saintonge et al. (2012) with aperture corrections, to the xCOLD GASS CO(1-0) measured fluxes, ranging from 5-120%.

We plot the IRAM and Herschel spectroscopic data for an example galaxy in Figure 4.2. Similar plots for all of our 24 galaxies can be found in Appendix B. For the DGS galaxies we use the CO(1-0) values compiled from the literature in Rémy-Ruyer et al. (2014).

4.2 Observational results - [CII]/CO scaling relations

In Figure 4.3, we present the $L_{[CII]}/L_{CO(1\text{-}0)}$ scaling relations for the 23 galaxies from the xCOLD GASS sample and the seven galaxies from the Dwarf Galaxy Survey, against a range of parameters describing the global physical properties of the galaxies. Although there is evident scatter, a clear dependence of $L_{[CII]}/L_{CO(1\text{-}0)}$ on many of the parameters is observed. We use the Pearson correlation coefficient, r, to quantify the strength of the dependence; a more refined statistical approach shall be employed later. Furthermore in Tables 4.1 and 4.2 we present a handful of physical properties of the galaxies in our sample with the measured $L_{[CII]}$ and $L_{CO(1\text{-}0)}$ luminosities.

The $L_{[CII]}/L_{CO(1\text{-}0)}$ depends most strongly on parameters which **a)** describe the

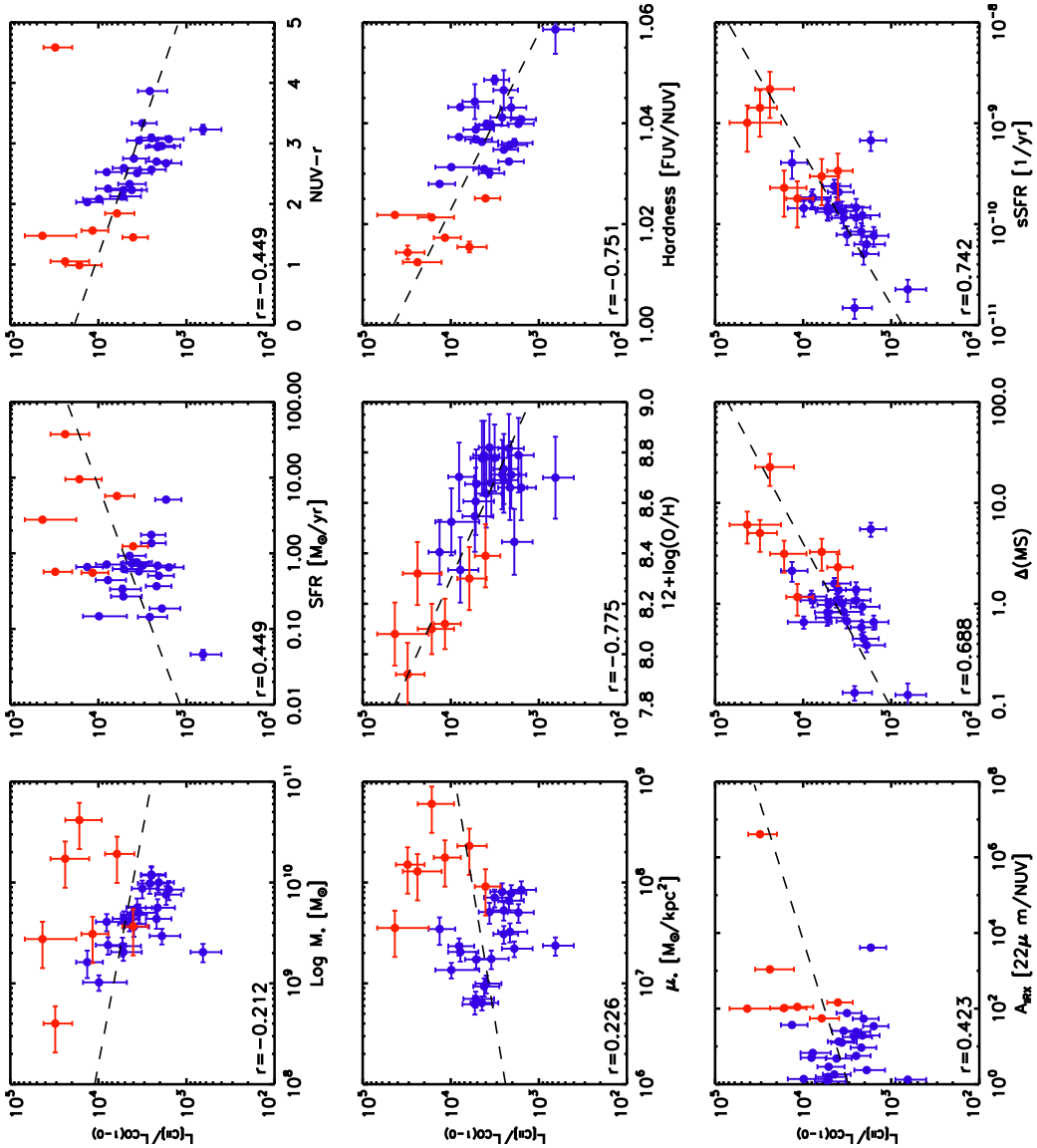

Figure 4.3. Observational Results - We provide the first scaling relations for the $L_{[\mathrm{CII}]}/L_{\mathrm{CO}(1\text{-}0)}$ ratio as a function of several galaxy parameters for a sample of 30 low mass, low metallicity, galaxies over a 2 dex $L_{[\mathrm{CII}]}/L_{\mathrm{CO}(1\text{-}0)}$ range. The blue points are the 23 xCOLD GASS objects, with CO detections, while the red are the seven DGS objects. The Pearson's Rank co-efficient can be found for each parameter in its own respective plot. In the bottom right panel we plot the position of each galaxy on the main sequence.

strength of the UV radiation field and **b)** describe the ability of the CO molecule to shield itself, via dust, from the UV radiation impinging on the surface of the the molecular regions deep inside the PDR. A clear dependence of $L_{[CII]}/L_{CO(1\text{-}0)}$ on the colour of the galaxies, parametrised by NUV-r photometry, is observed, as well as the specific star formation rate, distance from the main sequence, UV field hardness, and the gas-phase metallicity. The two former quantities are directly linked because NUV-r is a good proxy for sSFR since it relates a quantity tracing ongoing star formation activity (NUV) and a quantity sensitive to the older stellar population (r-band). Their differences arise as the sSFR takes into account internal dust attenuation while NUV-r is not dust corrected. Furthermore the gas-phase metallicity can be seen as a proxy for the total dust to gas mass fraction (via a metallicity dependent dust to gas ratio). The dust shields the CO molecule from the UV radiation, with decreasing metal content the systems become more dust poor allowing the UV radiation to penetrate deeper into the molecular clouds.

Overall the strongest dependencies in Figure 4.3 are on quantities that are sensitive to the amount of UV radiation penetrating into the molecular clouds, photodissociating CO into its ionised form. Of the four parameters mentioned above the dependence on metallicity is strongest, this will be further justified with the full multi-parameter Bayesian treatment in Section 4.3.

Conversely the $L_{[CII]}/L_{CO(1\text{-}0)}$ ratio does not depend strongly on parameters which describe the masses and structural properties of the galaxies. A low correlation is observed with the stellar mass of the systems, and with the morphology as measured by the stellar mass surface density, μ_*. This implies that CO photodissociation is happening on the small scales of molecular clouds as the large scale global properties of galaxies have a low correlation; global properties are likely less important than local ones.

Finally, rather interestingly, the $L_{[CII]}/L_{CO(1\text{-}0)}$ ratio does not depend strongly on the extinction, calculated from Equation 4.4 which is a measure of dust emission in the FIR versus emission from young stars in the UV. Importantly it is a tracer of gas density and metallicity; the clear dependance on metallicity, explained above, suggests that the gas density may not correlate strongly with $L_{[CII]}/L_{CO(1\text{-}0)}$. We speculate that the reason for this is that on small scales these low mass, low metallicity galaxies are flocculent with very clumpy structures, hence an averaged density across the galaxy washes out average variations of the $L_{[CII]}/L_{CO(1\text{-}0)}$ ratio on small scales. An alternative explanation for the low correlation with extinction is because, in particular at low stellar mass, NUV and

22μm emission do not originate from the same HII regions (Galametz et al. 2010), and so we are not tracing the extinction of the same star-forming clouds. It is difficult to disentangle these two effects, assuming both play a role, or to rule either one out.

Our results qualitatively imply that metallicity, colour, sSFR, Δ(MS) and/or hardness of the UV radiation field are responsible for variations in the $L_{[CII]}/L_{CO(1-0)}$ ratio as the latter three parameters are responsible for the total amount of UV radiation impinging onto the surface layer of molecular clouds. As these three parameters are correlated we may not need all three to statistically parametrise a prescription for $L_{[CII]}/L_{CO(1-0)}$ and hence the conversion function; a rigorous statistical approach, employing Bayesian methods, is shown below in Section 4.3.

4.2.1 Contamination of [CII] emission from non-PDR sources

The scaling relations in Figure 4.3 show integrated measurements across all phases of the ISM, however to accurately measure variations of the conversion function we must restrict our analysis to variations in the $L_{[CII]}/L_{CO(1-0)}$ ratio from molecular regions only. The CO(1-0) emission line only originates from molecular regions while [CII] emission originates from all phases of the ISM; therefore we must effectively clean for the contaminant [CII] emission arising from non-molecular regions.

The work in Chapters 2 and 3 (Accurso et al. 2016) provides a prescription to predict the fraction of [CII] emission originating from molecular regions as a function of galaxy properties. Through a Bayesian Inference method, several analytical functions were provided in those Chapters which can be used for the work here. Specifically, as we do not have HII region electron densities for the xCOLD GASS and DGS samples, we will use the prescription involving sSFR from Chapter 3 (Accurso et al. 2016) only, namely:

$$f_{[CII],\,mol} = -6.224 - 1.235\psi - 0.0543\psi^2\,. \tag{4.8}$$

where $f_{[CII],\,mol}$ is the fraction of [CII] emission originating from molecular regions out of the total integrated [CII] emission, $\psi = \log(\text{sSFR})$ and $\sigma_{f_{[CII],\,mol}} = 0.072$. We apply this to the 23 xCOLD GASS and seven DGS galaxies used in this work to estimate the relative fraction of [CII] emission arising from molecular regions only. These values are in the range of 48-79% as shown in Tables 4.1 and 4.2.

4.2.2 Caveat - DGS contamination of [CII] emission from non-PDR sources

Unfortunately some of the DGS objects used in this work have physical properties which lie outside the parameter space employed in Chapters 2 and 3 (Accurso et al. 2016), specifically the low metallicities, therefore the prescriptions provided there may be unreliable for these rarer objects outside of the parameter space. To estimate $f_{[\mathrm{CII}],\ \mathrm{mol}}$, and validate the method used above for the DGS, we utilise other FIR fine-structure lines, that have been measured for some of the DGS objects, alongside PDR modelling through an alternative empirically based method.

The [OI] $63\mu m$ and [OI] $145\mu m$ lines both originate solely in the PDR and molecular regions of the ISM owning to the fact that neutral oxygen has an ionisation potential similar to that of hydrogen. By measuring the [OI] $63\mu m$/[OI] $145\mu m$ line ratio it is possible to constrain the physical conditions within the PDRs through the use of a PDR code which solves the thermal balance and photochemistry ongoing within photodissociation regions. From the modelling we can then predict the expected [CII]/[OI] $63\mu m$ ratio from the PDR region, which allows an us to estimate the relative fraction of [CII] emission from the molecular regions through comparison with the observed [CII]/[OI] $63\mu m$ ratio integrated across the whole galaxy. We use the observed line fluxes for the DGS objects presented in Cormier et al. (2015). Furthermore we use 3D-PDR (Bisbas et al. 2012) and consider a three-dimensional, uniform density, spherically symmetric cloud illuminated from the center, while taking into account geometrical dilution effects of the UV field to obtain accurate 3D results. We assume a standard turbulent velocity of 1.5 kms^{-1} and fix the cosmic ray ionisation rate at the average Milky Way value. To estimate the strength of the FUV Draine field impinging upon the surface of the simulated PDRs we assume that all the energy from the Draine field is emitted in the FIR (predominantly dust in the PDR) and in the FUV range (unobscured star formation) of a galaxy. This assumption has been used in various studies including Okada et al. (2013), Cox et al. (2016) and Kaufman et al. (1999) so we use:

$$G_0 = \frac{4\pi}{1.6 \times 10^{-6}} \left(I_{FIR} + \frac{I_{FUV}}{0.46} \right) \tag{4.9}$$

where we have accounted for the attenuated FUV field using an empirical calibration of the A_{FUV}-TIR/FUV relations from Hao et al. (2011). We measure I_{FUV} from the GALEX FUV images, detailed in Section 4.1.2, and take I_{FIR} from Cormier et al. (2015) where both are total measurements across the galaxies. From this, and the observed [OI]

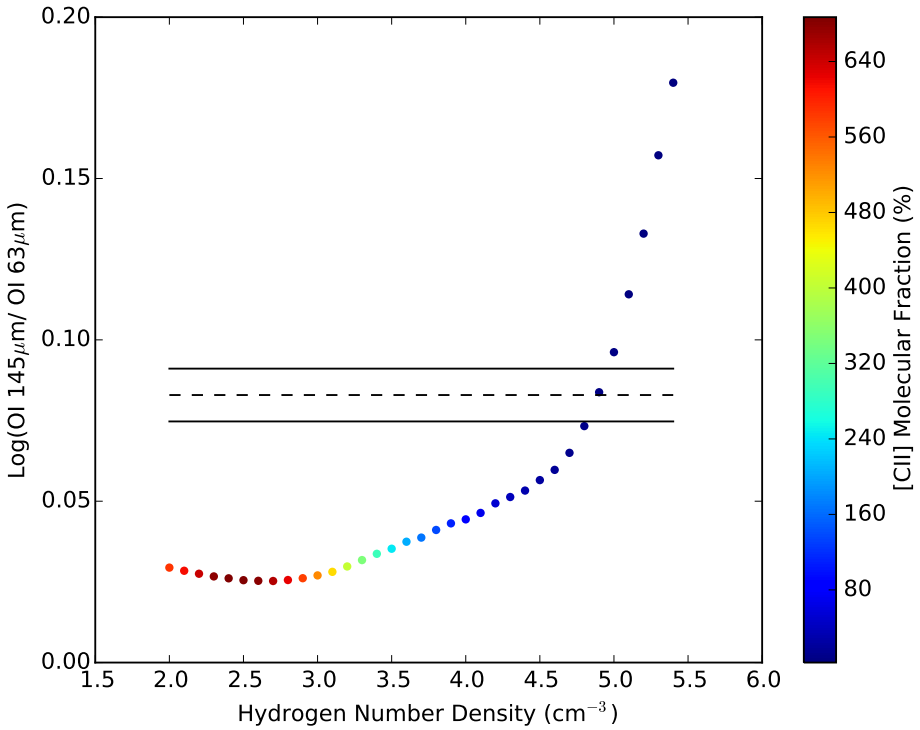

Figure 4.4. We plot the density parameter against the expected [OI] line ratio from the 3D-PDR simulation by running a model grid with varying densities, and with the calculated Draine field, for NGC 1140. It is possible to constrain which density leads to the observed [OI] line ratio, shown in the dashed line, while the one sigma error on the observed oxygen line flux ratio is given by the two solid lines, with the percentage fraction of [CII] emission emerging from the molecular regions is indicated in colour.

line ratio, it is possible to constrain the average hydrogen density within the PDR and hence predict the expected [CII] fraction from the molecular regions. Figure 4.4 shows an example set of results for NGC 1140.

By running a model grid with varying densities, and with the calculated Draine field, it is possible to constrain which density leads to the observed [OI] line ratio (dashed line in Figure 4.4). We also add a colourbar indicating the percentage fraction of [CII] emission emerging from the molecular regions of interest. Only fourteen galaxies within the whole DGS sample have observed [OI] 63μm and [OI] 145μm line fluxes and, of these, this method provides physically reasonable results (i.e fractions less than 100%) for eight of them. Cases where a solution is not reached, or when [CII] fractions exceed 100%, are due to optical depth issues with the [OI] 63μm line. Throughout our radiative transfer

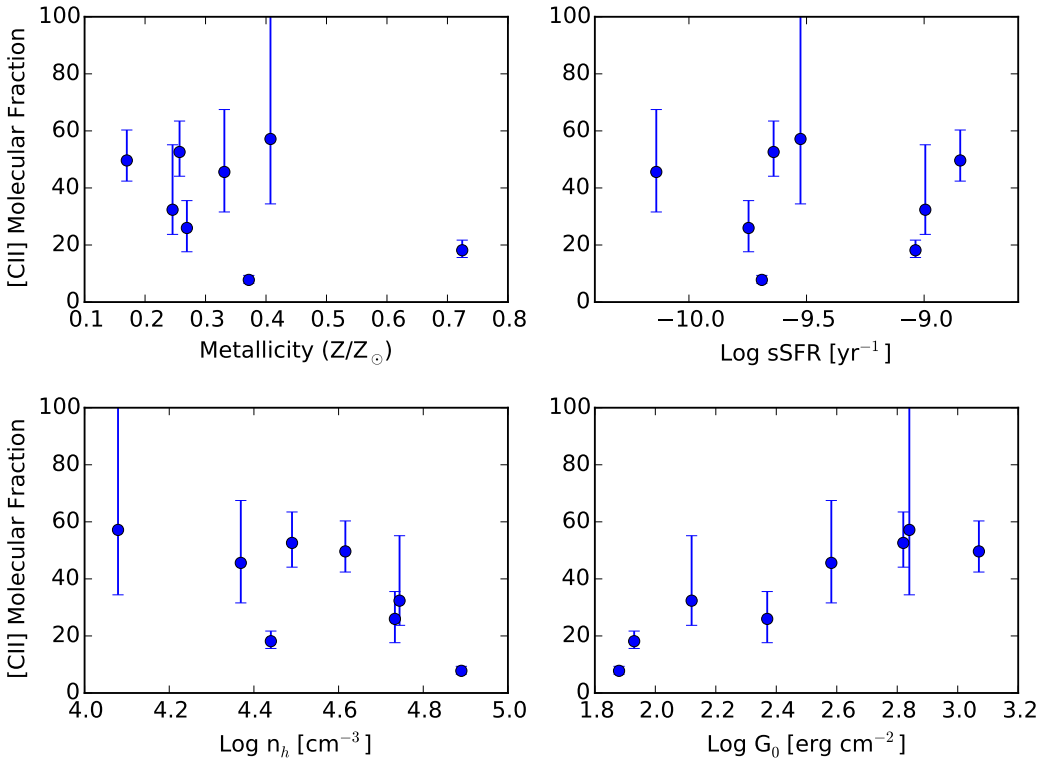

Figure 4.5. We present scaling relations for the percentage of [CII] emission arising from molecular regions for the eight DGS objects. Even though these objects are outside the parameter space probed in Chapters 2 and 3 (Accurso et al. 2016) we find a continuation of the trends presented there.

modelling we make the assumption that this line is optically thin, which is true in most cases, however when the [OI] $145\mu m$/[OI] $63\mu m$ ratio is greater than 0.1 it is known that the [OI] $63\mu m$ becomes optically thick (Liseau et al. 2006; Hughes et al. 2015). Treating the radiative line transfer in these environments is beyond the scope of this Thesis; fortunately the DGS objects presented in the scaling relations are optically thin so this will not affect the results of this Thesis. We present scaling relations for the percentage of [CII] emission arising from molecular regions for the eight DGS objects in Figure 4.5. Even though these objects are outside the parameter space probed in Chapters 2 and 3 we find a continuation of the trends presented there which validates the methodology used above. We show this in Figure 4.6 where, as can be seen, the two methods provide consistent results except from those with low predicted Draine fields, uncharacteristically low for bursty star forming galaxies above the main sequence. We attribute these low Draine fields to beam filling factors or [OI] optical depth issues which have not been taken into account leading to erroneous results. We are aware of beam filling factors and optical depth issues which can

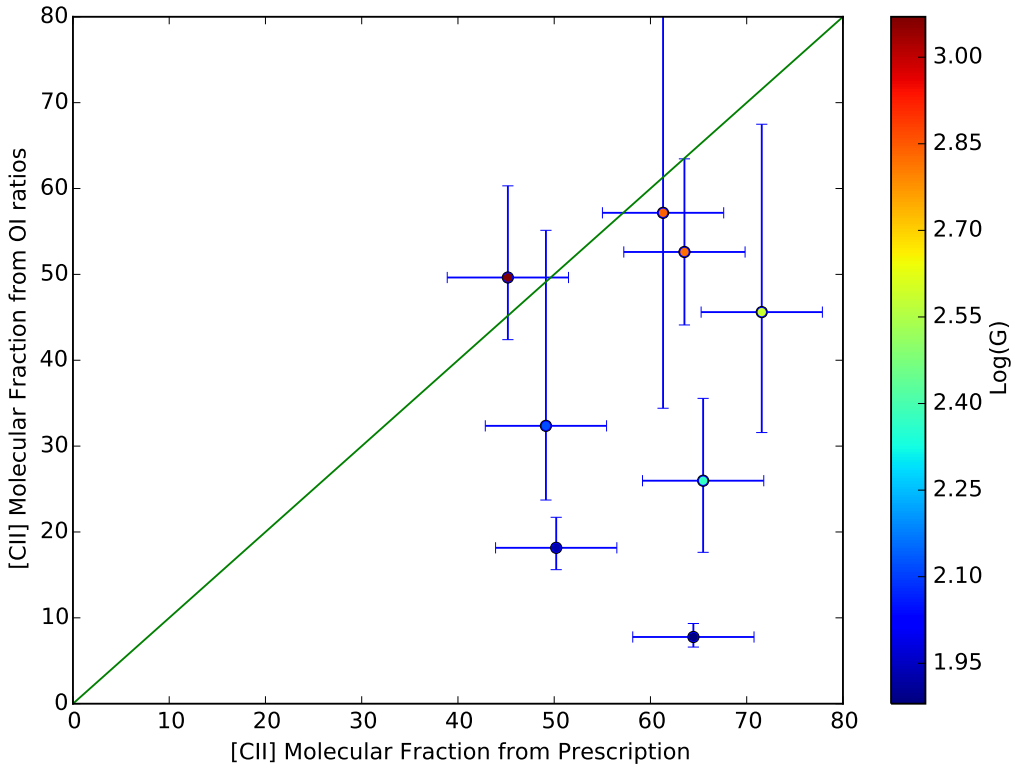

Figure 4.6. We plot the predicted $f_{[\mathrm{CII}],\mathrm{mol}}$ value obtained using the above OI ratio method against the predicted values using Equation 4.8, where colour of each point denotes the retrieved Draine field value predicted from the PDR modelling. As can be seen the two methods provide consistent results except from those with low predicted Draine fields.

arise from the [OI] modelling, hence the [OI] method is a somewhat poor and inaccurate method, hence why we use the values for $f_{[\mathrm{CII}],\mathrm{mol}}$ from the prescriptions in Chapter 3 as opposed to those from the [OI] modelling. It is reassuring that the [OI] method provides predictions which extend the scaling relations for $f_{[\mathrm{CII}],\mathrm{mol}}$ presented in Chapter 3, for galaxies with Draine fields greater than circa 100 Draines.

4.2.3 Corrected [CII]/CO scaling relations

In Figure 4.7 we present the $\mathrm{L}_{[\mathrm{CII}]}/\mathrm{L}_{\mathrm{CO(1\text{-}0)}}$ scaling relations for molecular regions by using the estimated fractions of ionised carbon emission arising from this phase of the ISM. As can be seen the correction for contaminant ionised carbon emission does not effect the qualitative trends shown in Section 4.2. There are mild changes in the statistical trends seen as, in most cases, the measure of correlation decreases as expected as the $\mathrm{L}_{[\mathrm{CII}]}/\mathrm{L}_{\mathrm{CO(1\text{-}0)}}$ numerical values have now decreased.

Our corrected scaling relation still imply that metallicity, colour, sSFR, Δ(MS) and/or hardness of the UV radiation field are responsible for variations in the conversion function.

4.3 Bayesian Inference

Following on from the observational scaling relations, shown in Figure 4.7, we now want **a)** to parametrise an analytic expression for the [CII]/CO luminosity ratio from molecular regions as a function of galaxy parameters and **b)** to determine the minimum number of parameters needed to provide a statistically robust fit to our data. With eight galaxy parameters[8] available we fit models with different number of free variables using all the possible combinations of parameters e.g we have ${}^8C_k$ number of models when we are fitting for k number of parameters, using the combinatoric notation where ${}^8C_k = \frac{8!}{k!(8-k)!}$. We perform a Bayesian inference method to find the best fit relations and to find the minimum number of variables needed to fit the data.

The first step is to assume that the measurement uncertainty associated with each [CII]/CO observation, for each galaxy, (y_i hereafter) is normally distributed. Therefore y_i is a random variable distributed like:

$$y_i = \mathcal{N}(y_{true,i}, \sigma^2_{y_i}) \,. \tag{4.10}$$

where σ_{y_i} is the measurement uncertainty associated with the observable y on the ith galaxy. As can be seen in Figure 4.7 all the observed scaling relations show evidence of either no correlation or a linear correlation between the log variables. We therefore use power law models in linear space as none of the above plots, in log space, show higher polynomial behaviour such that:

$$y_i = 10^{\alpha}(x_i^j)^{\beta_j} \,. \tag{4.11}$$

Where α and β_j are free variables to be found. We can say that the probability of observing our data, given the true value of the observables and the measurement uncertainties is:

$$P(y_i|y_{true,i}, \sigma_{y_i}) = \frac{1}{\sqrt{2\pi\sigma^2_{y_i}}} \exp\left(-\frac{(y_i - 10^{\alpha}(x_i^j)^{\beta_j})^2}{2\sigma^2_{y_i}}\right). \tag{4.12}$$

The next assumption to make is that all our [CII]/CO observables are independent, e.g each y_i and x_i^j are independent, which is perfectly reasonable as the result from one galaxy

[8] We do not include sSFR in our fitting procedure as this is very similar to Δ(MS) which itself can be used to include a redshift dependence applicable up to $z \sim 2.5$, the highest redshift probed in the Δ(MS) prescription of Whitaker et al. (2012).

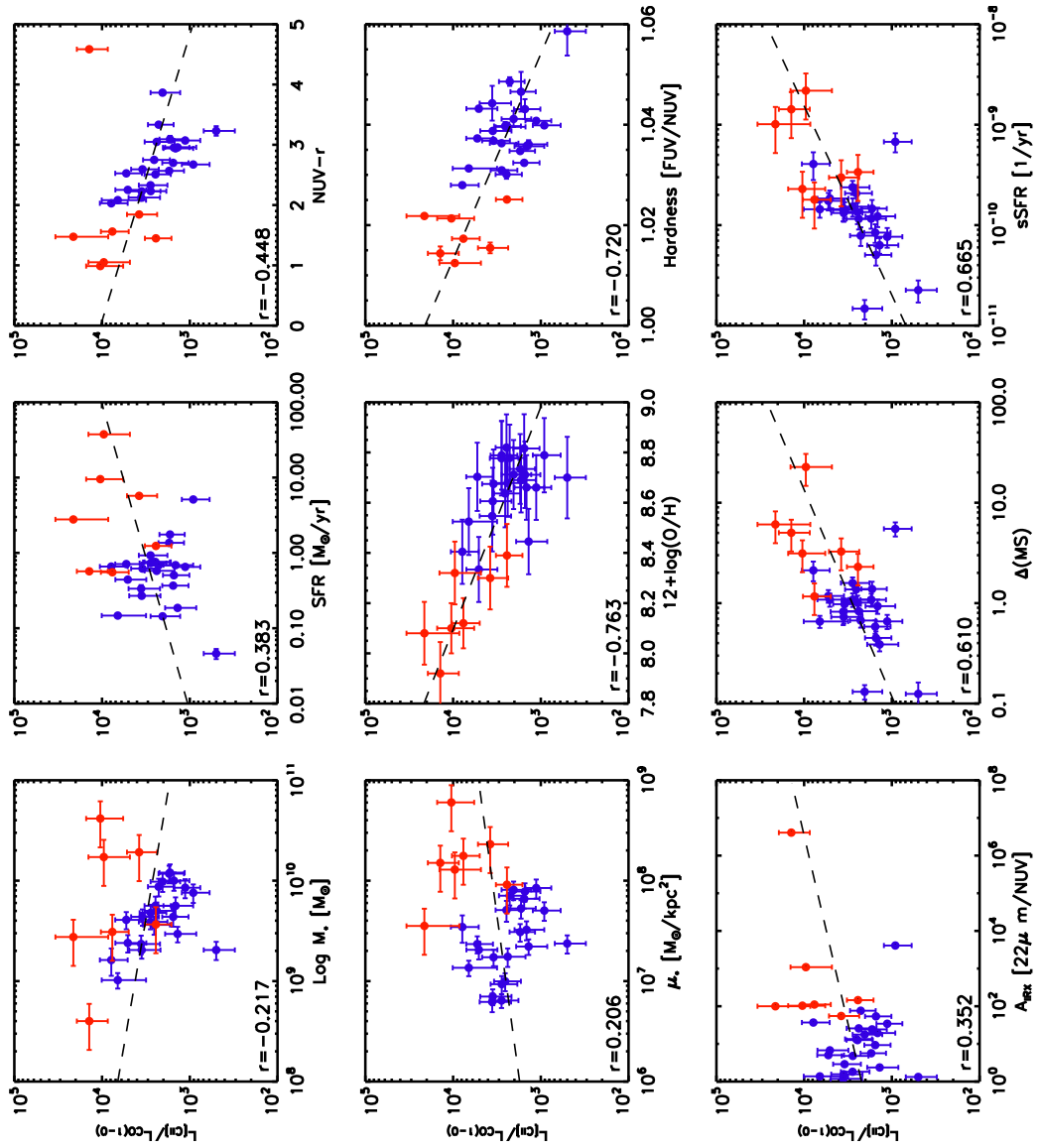

Figure 4.7. Corrected Observational Results - We provide the first scaling relations for the $L_{[\mathrm{CII}]}/L_{\mathrm{CO(1\text{-}0)}}$ ratio, from molecular ISM regions, as a function of several galaxy parameters for a sample of 30 low mass galaxies over a 2 dex $L_{[\mathrm{CII}]}/L_{\mathrm{CO(1\text{-}0)}}$ range. The blue points are the 23 xCOLD GASS objects, with CO detections, while the red are the seven DGS objects. The Pearson's Rank Co-efficient can be found for each parameter in its own respective plot.

xCOLD GASS ID	Log M_* [$M_\odot$]	Redshift	SFR [$M_\odot$ yr^{-1}]	Δ(MS)	Metallicity [O/H]	A_{IRX}	Log [CII] [$L_\odot$]	Log CO(1-0) [$L_\odot$]	Log sSFR [yr^{-1}]	$f_{[CII]\ mol}$ %
107026	9.37	0.0167	0.34	0.82	8.55	1.18	6.65	2.92	-9.84	67.21
108064	9.56	0.015	0.75	1.37	8.64	13.44	7.05	3.45	-9.68	64.4
108080	9.31	0.0153	0.05	0.12	8.7	1.32	5.81	2.99	-10.61	76.8
108093	9.94	0.0168	0.68	0.67	8.78	75.95	7.48	3.98	-10.11	71.3
108113	9.88	0.0199	5.12	5.49	8.79	4094.43	6.99	3.75	-9.17	53.62
108129	9.47	0.0175	0.19	0.39	8.45	2.37	6.39	3.11	-10.19	72.37
108142	9.61	0.019	0.71	1.18	8.7	5.03	7.27	3.36	-9.76	65.84
108147	9.64	0.0197	0.62	0.98	8.67	2.89	7.14	3.43	-9.85	67.37
101037	9.31	0.0164	0.27	0.73	8.61	1.56	6.93	3.22	-9.88	67.86
108050	9.75	0.0162	0.76	1.01	8.82	12.63	7.32	3.76	-9.87	67.7
108021	9.64	0.0173	0.37	0.58	8.82	9.3	7.2	3.86	-10.07	70.75
109066	9.99	0.0149	0.14	0.13	8.71	17.71	6.79	3.38	-10.84	78.42
109101	9.01	0.0104	0.15	0.66	8.52	1.38	6.31	2.31	-9.83	67.04
109038	9.21	0.0116	0.66	2.12	8.4	36.93	7.24	3.11	-9.39	58.62
109139	9.59	0.0188	0.93	1.59	8.78	1.82	7.25	3.6	-9.62	63.28
109092	9.7	0.018	0.58	0.83	8.68	25.83	7.12	3.58	-9.94	68.82
109072	9.68	0.0189	0.73	1.08	8.79	4.79	7.22	3.6	-9.82	66.87
109010	9.75	0.0102	0.69	0.93	8.66	19.47	6.87	3.54	-9.91	68.34
109102	9.38	0.0117	0.44	1.08	8.33	6.74	6.82	2.93	-9.74	65.49
110038	10.0	0.0166	0.51	0.45	8.71	53.84	7.03	3.72	-10.29	73.6
109109	9.08	0.0196	0.27	1.05	8.61	1.71	6.63	—	-9.65	63.85
108054	9.93	0.0125	0.65	0.66	8.66	34.31	6.85	3.65	-10.12	71.44
108045	10.08	0.015	1.76	1.38	8.69	24.28	7.62	4.22	-9.83	67.04
109028	10.07	0.0178	1.36	1.08	8.73	5.65	7.56	4.17	-9.94	68.82

Table 4.1. Derived observational quantities for the xCOLD-GASS galaxies.

DGS Name	Log M_* $[M_\odot]$	Redshift	SFR $[M_\odot\ yr^{-1}]$	Δ(MS)	Metallicity [O/H]	A_{IRX}	Log [CII] $[L_\odot]$	Log CO(1-0) $[L_\odot]$	Log sSFR $[yr^{-1}]$	$f_{[CII]\ mol}$ %
Haro 11	10.24	0.0206	37.53	22.67	8.32	1090.68	8.08	3.7	-8.67	40.3
Mrk 930	9.44	0.0183	2.78	6.07	8.08	99.8	7.44	2.81	-9.0	49.39
Haro 3	9.49	0.0031	0.55	1.17	8.12	110.96	6.49	2.42	-9.75	65.66
Mrk 1089	10.28	0.0134	5.72	3.26	8.3	55.09	7.59	3.8	-9.52	61.32
UM 448	10.62	0.0186	9.53	3.13	8.1	103.3	8.14	3.93	-9.64	63.66
Haro 2	9.56	0.0048	1.24	2.3	8.39	145.31	6.89	3.29	-9.47	60.3
II Zw 40	8.6	0.0026	0.57	5.02	7.92	4069710.0	6.41	1.92	-8.84	45.13

Table 4.2. Derived observational quantities for the seven DGS galaxies.

will not affect the result from another. With this, and using the definition of independent probabilities, we can simply multiply all the individual probabilities together. Therefore this product of probabilities is our Likelihood, denoted L. By taking the log-likelihood, $\mathcal{L}$, the product returns back to a sum so:

$$\mathcal{L} = -\frac{N}{2}\ln(2\pi) - \frac{1}{2}\sum_{i=1}^{N}\ln(\sigma_{y_i}^2) - \frac{1}{2}\sum_{i=1}^{N}\frac{(y_i - 10^{\alpha}(x_i^j)^{\beta_j})^2}{\sigma_{y_i}^2}, \tag{4.13}$$

where N is the sample size. Maximising this log-likelihood for all of our models, at fixed number of free parameters, will provide us with the best fitting models for a given number of free parameters.

4.3.1 Model comparison and sampling methods

We aim to maximise the likelihood for our fits where the number of degrees of freedom varies. To compare likelihoods from models with different numbers of free parameters we employ the Akaike Information Criterion (AIC) (Akaike 1981), and the Bayesian Information Criterion (BIC) (Schwarz 1978), similar to Chapter 3. We again use EMCEE to maximise our likelihood function.

4.3.2 Statistical results

In total we run $\sum_{i=1}^{8} {}^{8}C_i$ models with the results presented below. By maximising the likelihood for each number of free parameters (from one to eight), and then comparing models with different sample sizes, and using the BIC and AIC, we find that only two parameters are necessary to fully explain the trends seen in Figure 4.8.

For the two parameter case both the AIC and BIC retrieve metallicity and Δ(MS) as the two galaxy parameters needed to provide a good fit to the data (the two parameter model which has the highest likelihood value in both cases). The best fitting analytical prescription is:

$$\log\left(\frac{[\mathrm{CII}]}{\mathrm{CO}}\right)(\pm 0.223\ \mathrm{dex}) = 12.378 + 0.216\log\Delta(\mathrm{MS}) - 1.062[12 + \log(\mathrm{O/H})] \tag{4.14}$$

which has a regression correlation coefficient of 0.801 (these two parameters alone account for 80.1% of the correlation) with an error on the predicted $\log\left(\frac{[\mathrm{CII}]}{\mathrm{CO}}\right)$ value of 0.223. As the number of free parameters increases (from one to eight) the log posterior and log likelihoods also decrease; hence doing a likelihood ratio analysis would have been insufficient to recover our best fitting two parameter relation as this would have returned

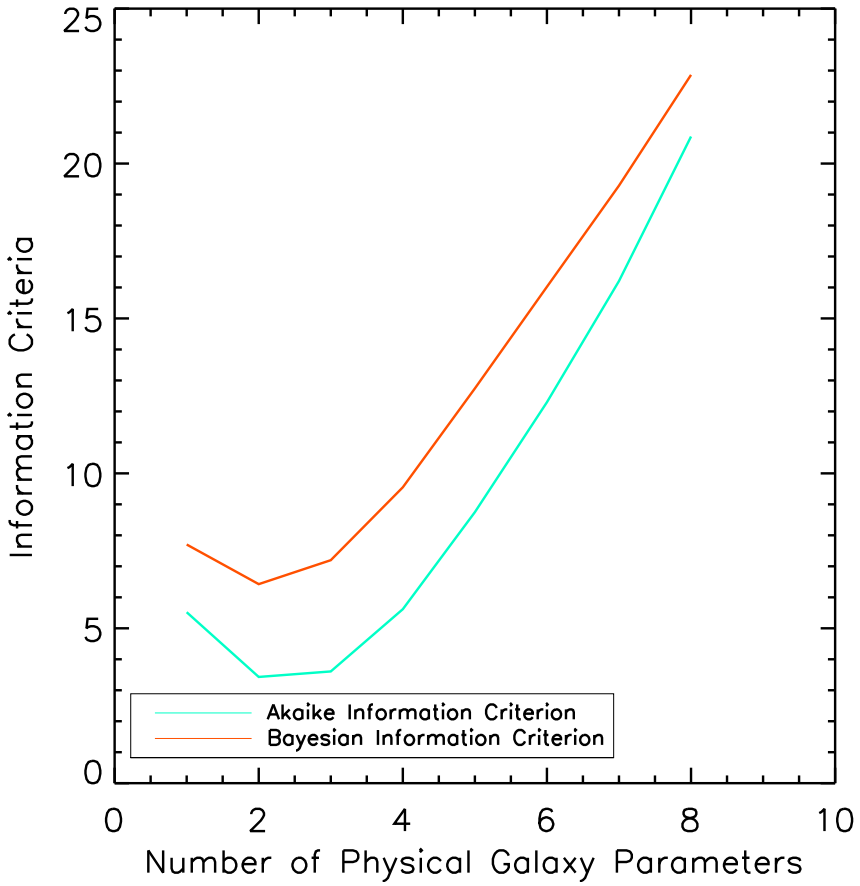

Figure 4.8. We provide a plot for the variation of the Akaike Information Criterion and the Bayesian Information Criteria, in turquoise and orange respectively, for the best fitting models when varying the number of galaxy parameters. It can be seen how, although they give different absolute numerical values (due to their different analytic expressions), they both reach a minimum at two galaxy parameters.

the eight parameter case as the best relation as these have the smallest posteriors. We stress that our aim was to find a relation which can explain the correlation with as few observables as possible. Only by employing the AIC and BIC, as above, were we able to find our best fitting relation with only two parameters.

4.4 Radiative transfer modelling - connecting [CII]/CO and α_{CO}

The objective in obtaining the above scaling relations is to be able to derive a parametrisation for the conversion function. There are two main parameters responsible for variations in the $L_{[CII]}/L_{CO(1\text{-}0)}$ fraction, namely metallicity and Δ(MS), and so it is necessary to

understand how to go from a $L_{[CII]}/L_{CO(1\text{-}0)}$ parametrisation to one for α_{CO}.

To better understand the astrochemical reactions involved in the photodissociation of CO we inspect the chemical reaction database employed in the PDR code 3D-PDR (Bisbas et al. 2012). The main reactions involved in photodissociation of CO arise from the interaction of molecular species with cosmic rays and UV photons. The dominant reactions[9] involving UV photons and CO are:

$$CO + \gamma \rightarrow O + C \tag{4.15}$$

$$C + \gamma \rightarrow C^{+} + e^{-} \tag{4.16}$$

indicating that, whenever CO interacts with UV photons, neutral carbon is formed first as an intermediate species, but then quickly gets ionised as the reaction rates are of the same order[10]; hence only ionised carbon forms when CO reacts with UV photons. Moreover the reaction of CO with cosmic rays (denoted CRP) happens either via the formation of a free radical, namely He^{+}, as follows,

$$He + CRP \rightarrow He^{+} + e^{-} \tag{4.17}$$

$$He^{+} + CO \rightarrow O + C^{+} + He \tag{4.18}$$

$$He^{+} + CO \rightarrow O^{+} + C + He \tag{4.19}$$

or directly as,

$$CO + CRP \rightarrow O + C. \tag{4.20}$$

These show how, via cosmic rays, the photodissociation of CO can lead to the formation of neutral and ionised carbon species. Recent work by Bisbas et al. (2015*b*) has shown that ionised carbon is the main product formed through the photodissociation of CO, but knowledge of how much neutral carbon forms is crucial to accurately constrain a prescription of α_{CO} as we only have observed CO and [CII], lacking CI observations.

To better understand the formation of neutral carbon we rely on the multi-phase ISM numerical simulations performed in Chapters 2 and 3. We take their simulated low-redshift cloud results, and here plot in Figure 4.9 the variations of the molecular region $L_{[CII]}/L_{CO(1\text{-}0)}$ against α_{CO} for the 2160 simulated clouds with colours indicating varying metallicities and Δ(MS) of the clouds. We find that these two parameters, along

[9] By this we mean the reactions with the highest reaction rates which provide the main routes for creation and destruction of molecular species

[10] The reaction rates for these two are 2.0x10^{-10} s^{-1} and 3.0x10^{-10} s^{-1} respectively.

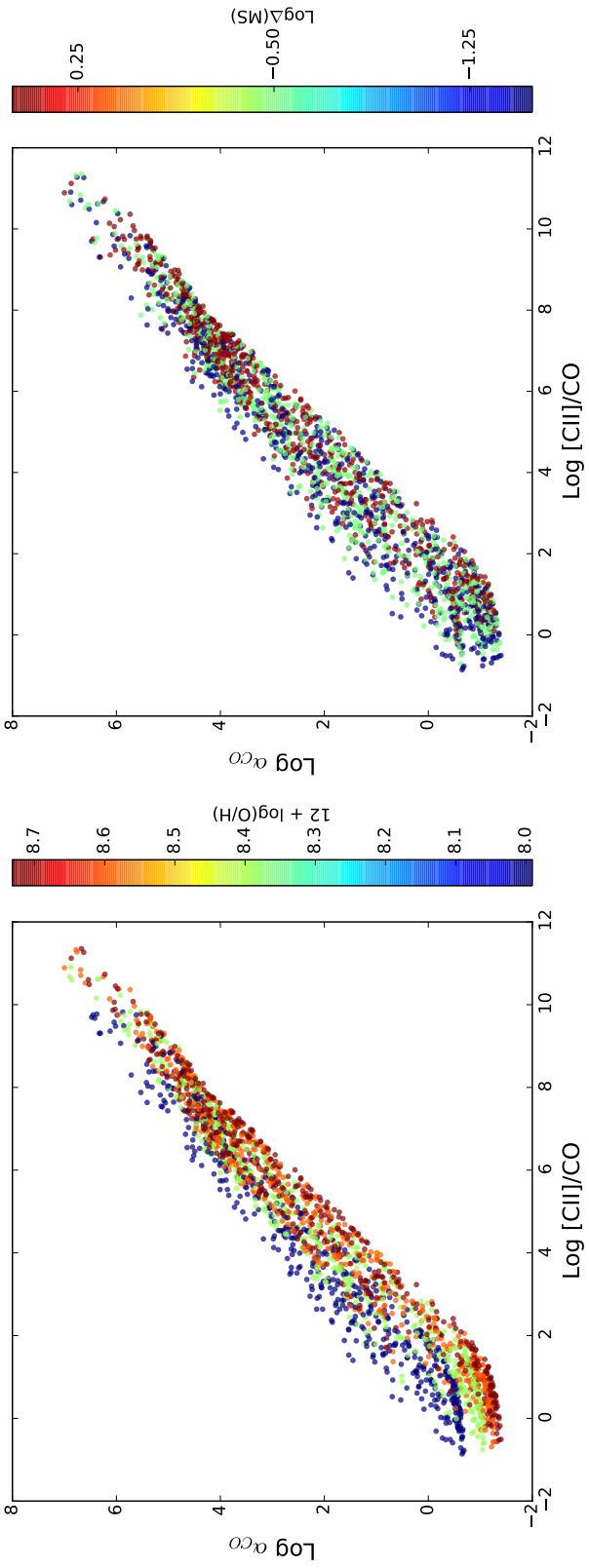

Figure 4.9. We here plot the variations of the molecular region $L_{[CII]}/L_{CO(1-0)}$ against α_{CO} for the 8640 simulated clouds in Chapters 2 and 3 Accurso et al. (2016). Colours indicate varying metallicities and Δ(MS) of the clouds, demonstrating that these two parameters can account for the scatter seen in the above plot. Please see Table A.1 in Appendix A for the full data.

with $L_{[CII]}/L_{CO(1\text{-}0)}$, account for 98.4% of the total correlation with α_{CO}. We therefore perform a three dimensional linear fit to the above data, using the Python SciPy routine CURVE-FIT, and find:

$$\log \alpha_{CO} = 0.742 \log \frac{L_{[CII]}}{L_{CO(1\text{-}0)}} - 0.944[12 + \log(O/H)] - 0.109 \log \Delta(MS) + 6.439 \,. \quad (4.21)$$

The errors on the estimated parameters are less than 0.01 dex and hence are negligible, owing to the high level of correlation retrieved from the fitting, and therefore can be ignored. This relationship has been normalised to the known Milky Way values for α_{CO}^{solar} = 4.36 $M_\odot$ (K km $s^{-1})^{-1}$ (helium corrected) and $(L_{[CII]}/L_{CO(1\text{-}0)})^{solar}$ = 1400 from Stacey et al. (1991). We then combine this with Equation 4.14 to arrive at a prescription for the CO conversion function:

$$\log \alpha_{CO}(\pm 0.165 \text{ dex}) = 15.623 - 1.732[12 + \log(O/H)] + 0.051 \log \Delta(MS), \quad (4.22)$$

where 12+log(O/H) is the metallicity in PP04 units, with an error on the predicted $\log \alpha_{CO}$ estimate of ±0.165. Metallicity predominantly drives variations in $\log \alpha_{CO}$ with Δ(MS) playing a minor, though statistically important, secondary role.

We hereby report with eclat a novel multivariate prescription of the CO-to-H_2 conversion function, on integrated galaxy wide scales, which involves metallicity and Δ(MS) for star forming galaxies, up to $z \sim 2.5$ (the highest redshift constrained by Equation 4.6 from Whitaker et al. (2012)). The dependence on metallicity is consistent with other conversion functions, explained further in Section 4.4.3, while the dependence on Δ(MS) is also consistent with recent numerical simulations performed by Clark & Glover (2015). The positive trend of $\log \alpha_{CO}$ with Δ(MS) emerges because as Δ(MS) increases, the number of ionising UV photons permeating through the ISM also increases which, at fixed metallicity, leads to further CO photodissociation.

4.4.1 Caveat - Suitability across the main sequence

We caution the reader when using Equation 4.22 as it is not valid for all galaxies. Our prescription should only be applied to galaxies within the parameter space constrained here, i.e for those with $7.9 < 12 + \log(O/H) < 8.8$ and $-0.8 < \log \Delta(MS) < 1.3$. For galaxies with $12 + \log(O/H) > 8.8$ we recommend using the value obtained when using $12 + \log(O/H) = 8.8$ as we expect the conversion factor to level out to a constant value at higher metallicities. Likewise for galaxies with $\log \Delta(MS) < -0.8$ we recommend using

the value obtained by setting $\log \Delta(\mathrm{MS}) = -0.8$ as we expect the conversion factor to level out to a constant value, roughly equal to the galactic conversion factor value (Davis et al. 2014; Saintonge et al. 2011*a*), once a galaxy moves below the main sequence. Furthermore for ULIRGS, LIRGS and possible starburst galaxies with $\log \Delta(\mathrm{MS}) > 1.3$, we advise the reader to use canonical values found in the literature. For ULIRG and LIRG galaxies a typical value for α_{CO} is 0.5 $\mathrm{M}_{\odot}$ $(\mathrm{K\ km\ s^{-1}})^{-1}$ (Feruglio et al. 2010).

A major implication of our prescription is the discontinuity of α_{CO} which emerges; when moving up off the main sequence α_{CO} increases and suddenly decreases as $\log \Delta(\mathrm{MS}) > 1.3$. This has also been recently suggested by Sargent et al. (2014) who find that α_{CO} increases with increasing sSFR and then suddenly decreases when entering the starburst regime. We speculate this is because ULIRGs and starburst galaxies have different physical environments to main sequence galaxies; while their sSFRs are much higher their densities are also significantly higher, hence CO is more easily shielded in these denser environments, leading to a rapid decline in α_{CO}.

4.4.2 Caveat - SDSS Metallicities

Metallicity gradients of different amplitudes have been observed in galaxies similar to those studied here (Magrini et al. 2016; Tissera et al. 2016; Wuyts et al. 2016; Ho et al. 2015) meaning that the SDSS fiber spectroscopy for our galaxies, which only probes the central 3", may not provide reliable metallicity measurements to use in the analysis of our [CII]/CO data. Star formation histories for these low mass objects are known to be bursty while ongoing star formation activity is known to be inhomogeneous with activity unevenly scattered across the galaxy (Guo et al. 2015; Domínguez et al. 2015). Hence, to accurately measure metallicity gradients we would need IFU data to get accurate spatial sampling out to the extended regions of our galaxies without *a priori* information of the location of the HII regions. IFU spectroscopy would be essential to determine the accurate light-weighted, integrated metallicity measurements over the area of the galaxies probed by the IRAM and Herschel observations. Obtaining IFU spectroscopy of our targets may reduce the scatter found in the metallicity dependent scaling relations and may further refine our conversion function.

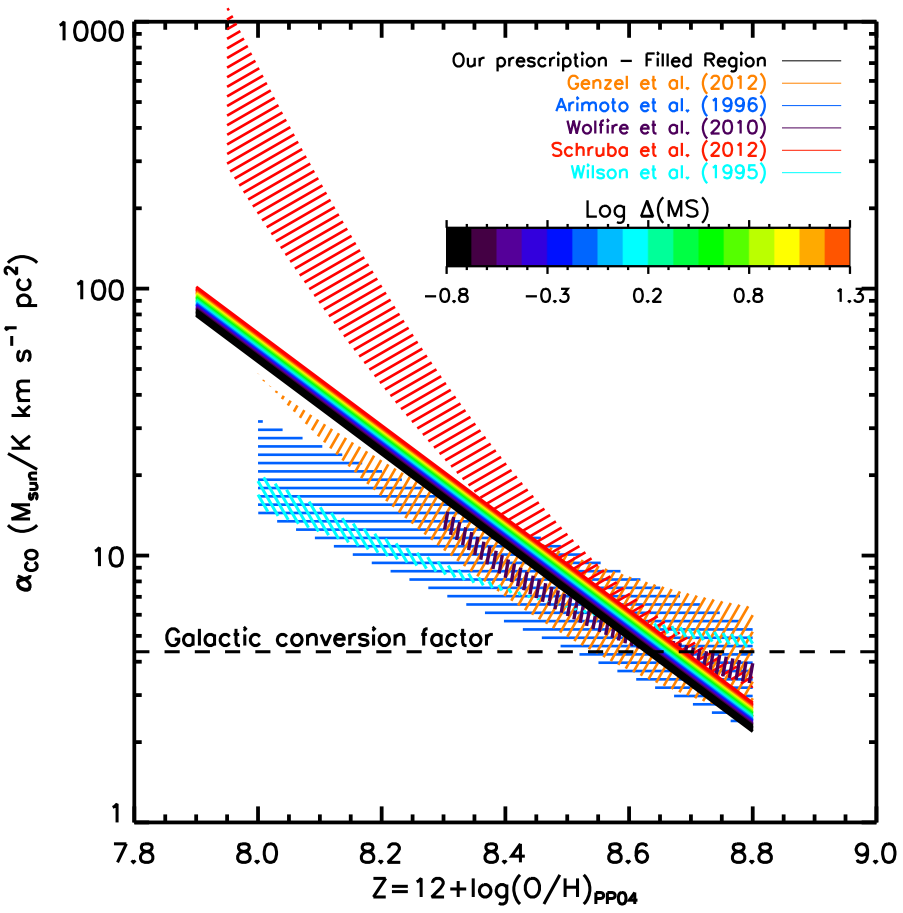

Figure 4.10. Our two parameter conversion function is presented here by the solid multicoloured filled surface, where colour represents Δ(MS), given by the colour-bar. The metallicity only prescription provided by other works, converted to PP04 units, are shown by the dashed coloured lines, described in the legend of the plot. We also plot the constant galactic conversion factor value by the dotted black horizontal line.

4.4.3 Comparison with previous studies

Studies concerning the CO-to-H2 conversion function have been ongoing for decades with a plethora of varying prescriptions; some of the earliest work was carried out by Solomon et al. (1987), Tielens & Hollenbach (1985) and van Dishoeck & Black (1988) and so, to interpret our prescription, we need to compare our results against the many found in the literature. We here discuss a handful of these and try to reconcile any discrepancies which may occur when comparing to ours. We plot our two parameter conversion function in Figure 4.10, where colour in the multi-coloured filled surface denotes varying Δ(MS), overlaid with various metallicity dependent prescriptions from the literature. As can be

seen metallicity predominantly drives variations in our conversion function with Δ(MS) playing a minor, though statistically important, role.

We first compare our prescription to the single variable metallicity dependent conversion functions of Schruba et al. (2012) and Genzel et al. (2012). These were derived by assuming a constant molecular gas depletion time and then using an inverse star formation law. Our prescription is approximately consistent with both around the high metallicity range, but then predicts different conversion factors for 12 + log(O/H)$\lesssim$8.25. The divergence between the two aforementioned prescriptions is because they both used different constant depletion timescales (1.8 and 1.0 Gyrs respectively); hence, as our predictions lie between these two, in the low metallicity regime, depletion times are not constant but do vary between these two values. However it is evident that the prescriptions in these aforementioned papers would both provide a reasonable one dimensional fit to the xCOLD GASS sample.

The novelty of our approach means that we are able to attribute the scatter found in these previous metallicity-only dependent relations to the position off the main sequence of those galaxies. Those systems with stronger radiation fields (due to higher Δ(MS) values), at fixed metallicity, will have higher conversion factors than their redder counterparts. Also galaxies which are metal poor, at a fixed position on the main sequence, will have higher conversion factors than their metal rich counterparts. The major implication, of the differences which arise here, is that depletion times do vary and lie somewhere between 1.0-1.8 Gyrs. This will be further explored in Chapter 5 when we discuss depletion timescale scaling relations.

We next compare our prescription to another metallicity dependent conversion function based on the PDR modelling of Wolfire et al. (2010). The lowest metallicity employed in their grid of models was 12 + log(O/H) = 8.38. It can be seen, in Figure 4.10, the trend in both conversion functions are in broad agreement for metallicities above 12 + log(O/H) = 8.38 to solar, however they are offset from one another with our prescription predicting higher conversion factors. Their grid of models allowed for a varying ionisation field (for which the sSFR/Δ(MS) contributes towards) and varying metallicities; while their parametrisation only involved metallicity ours can, again, attribute the scatter to the ionisation field caused by the varying sSFRs.

We now move onto a comparison with Wilson (1995) and Arimoto et al. (1996) who both measured virialised masses of molecular clouds for a sample of galaxies to infer the

dependence of their conversion function with metallicity. The resulting prescription is also in broad agreement with the trends seen in the Leroy et al. (2011) sample, who used a dust to gas ratio method. As can be seen in Figure 4.10 the trend in both conversion functions are in broad agreement for metallicities above 12 + log(O/H) = 8.25 to solar. However they are offset from one another with our prescription predicting conversion factors two to three times higher. We speculate that this is due to the integrated nature of our observations versus the highly resolved, cloud scale-resolution, of Wilson (1995) and Arimoto et al. (1996). On unresolved, galaxy wide, scales it is possible to see more diffuse H_2 molecular gas which is traced by [CII] and CI, as opposed to CO, hence the need for higher conversion factors to account for this. This is not seen on the resolved, cloud scale, observations in the aforementioned work, hence their predicted lower conversion factors. The spatial scale of the different approaches is the major/important difference leading to offset.

Overall our prescription agrees well with others in the literature that have used integrated, galaxy wide scale, observations and assume a constant depletion time, indicating that depletion times are not constant and vary between 1.0 to 1.8 Gyrs. Our prescription does not agree as well with those that have used a) a dust to gas ratio method, b) numerical modelling c) virialised gas mass estimates with observational resolution down to cloud scales. This is because our prescription accounts for the diffuse H_2 gas, not found in individual clouds and GMCs, which is better traced by ionised and neutral carbon versus its molecular counterpart.

4.5 Summary & Conclusions

We present here the first results using xCOLD GASS, a legacy survey of molecular gas in nearby galaxies. We provide the first scaling relations for the integrated $L_{[\mathrm{CII}]}/L_{\mathrm{CO(1\text{-}0)}}$ ratio as a function of several galaxy parameters for a sample of low metallicity galaxies over 2 dex in $L_{[\mathrm{CII}]}/L_{\mathrm{CO(1\text{-}0)}}$. From this, we corrected for contaminant [CII] emission from non-molecular phases of the ISM and provide the first scaling relations for the molecular region $L_{[\mathrm{CII}]}/L_{\mathrm{CO(1\text{-}0)}}$ ratio. We show that:

- The integrated and molecular $L_{[\mathrm{CII}]}/L_{\mathrm{CO(1\text{-}0)}}$ ratio depends most strongly on parameters which describe the strength of the UV radiation field and describe the ability of the CO molecule to shield itself, via dust, from the UV radiation im-

pinging on the surface of the the molecular regions deep inside the PDR. A clear dependence on the colour (NUV-r) of the galaxies, specific star formation rate, UV field hardness, gas-phase metallicity and Δ(MS) is observed.

- The $L_{[CII]}/L_{CO(1\text{-}0)}$ ratio does not depend strongly on large scale parameters which describe the masses and structural properties of the galaxies.

- After a Bayesian analysis only two parameters, metallicity and Δ(MS), are needed to robustly parametrise a prescription for variations in $L_{[CII]}/L_{CO(1\text{-}0)}$.

We use our parametrisation for $L_{[CII]}/L_{CO(1\text{-}0)}$, alongside radiative transfer modelling, to present a novel conversion function. Our prescription is consistent with previous metallicity only prescriptions, however we are now able to attribute the scatter found in previous studies to the Δ(MS) of the systems.

We are here arguing that, with our metallicity and ΔMS dependent conversion function, one can accurately make a prediction for α_{CO} across the whole main sequence up to z$\sim$2.5.

Chapter 5

Star formation efficiency and molecular gas fraction scaling laws

In this Chapter we apply our new prescription to the full xCOLD GASS and PHIBSS1 samples (Tacconi et al. 2013), while investigating molecular gas mass fraction and gas depletion time scaling relations, up to $z \sim 2.0$ and stellar masses $> 10^9$ $M_\odot$, hitherto unattempted. Star formation rates, stellar masses, CO luminosities and redshifts for the PHIBSS1 sample are taken from Tacconi et al. (2013). Metallicities are estimated using the Fundamental Mass-Metallicity Relation (FMR) from Mannucci et al. (2010) and then converted to PP04 units using Kewley & Ellison (2008), ensuring consistency with the metallicity units of the xCOLD GASS galaxies. The aim of this Chapter is to investigate the consequences of our conversion function on gas scaling relations and how these change when going from a standard constant conversion factor, oft-used in the literature, to our prescription presented in Equation 4.22. We do not include the DGS objects in this analysis as we are only interested in the statistical trends of the molecular gas scaling laws; we need a complete sample of galaxies at different redshifts and so use the xCOLD GASS and PHIBSS1 samples.

5.1 Bridging low and high redshift molecular gas studies

We first plot in Figure 5.1 a histogram showing the distribution of conversion factors for the high and low mass xCOLD GASS galaxies and the PHIBSS1 samples. For the original COLD GASS galaxies the distribution peaks at the galactic value ($\sim$ 4.36 $M_\odot$ (K km $s^{-1})^{-1}$) with other values clustered closely around this, hence we expect the low redshift molecular gas scaling relations to remain relatively unchanged for $M_* > 10^{10} M_\odot$. However for the lower mass galaxies the conversion factors are mostly larger than the galactic value and extend to high values, ergo we do expect gas laws to change. Furthermore, the predicted conversion factors for the high redshift galaxies are at most a factor of two larger or smaller than the galactic conversion factor value so we do not expect a major change in the gas scaling laws at high redshifts.

5.1.1 Molecular gas scaling relations up to z$\sim$2.0

We present scaling relations for the CO traced molecular gas mass fraction as a function of stellar mass, specific star formation rate and Δ(MS) (from left to right) for the full xCOLD GASS and PHIBSS1 samples in Figure 5.2. We aim to showcase our new prescription for α_{CO} and so, for now, only use the CO-detected galaxies in both samples.

The top row in Figure 5.2 presents the results obtained when using a constant galactic conversion factor; this had been previously explored for the COLD GASS sample in Saintonge et al. (2011*a*), only for galaxies with stellar masses $>10^{10}$ $M_\odot$ and so we are extending the sample to include galaxies with stellar masses $>10^9$ $M_\odot$, and for the PHIBSS1 sample in Tacconi et al. (2013) and Genzel et al. (2015). These aforementioned references all used a constant galactic conversion factor value and we want to explore how things change when our new conversion function is employed, shown in the bottom row. We fit quadratic polynomials to the xCOLD GASS data to qualitatively show the differences in the trends; we also present the product moment correlation co-efficient and scatter for each fit, calculated using the using the Python SciPy routine LINREGRESS.

As can been seen, the correlation with stellar mass remains unchanged for galaxies with $M_* > 10^{10} M_\odot$ at low redshift as the standard galactic conversion factor is a good approximation to the conversion function predicted from this work. However, due to the emergence of lower metallicities in galaxies with stellar masses less than 10^{10} $M_\odot$ the trend changes. We start to see a flattening of the molecular gas mass fraction for stellar masses

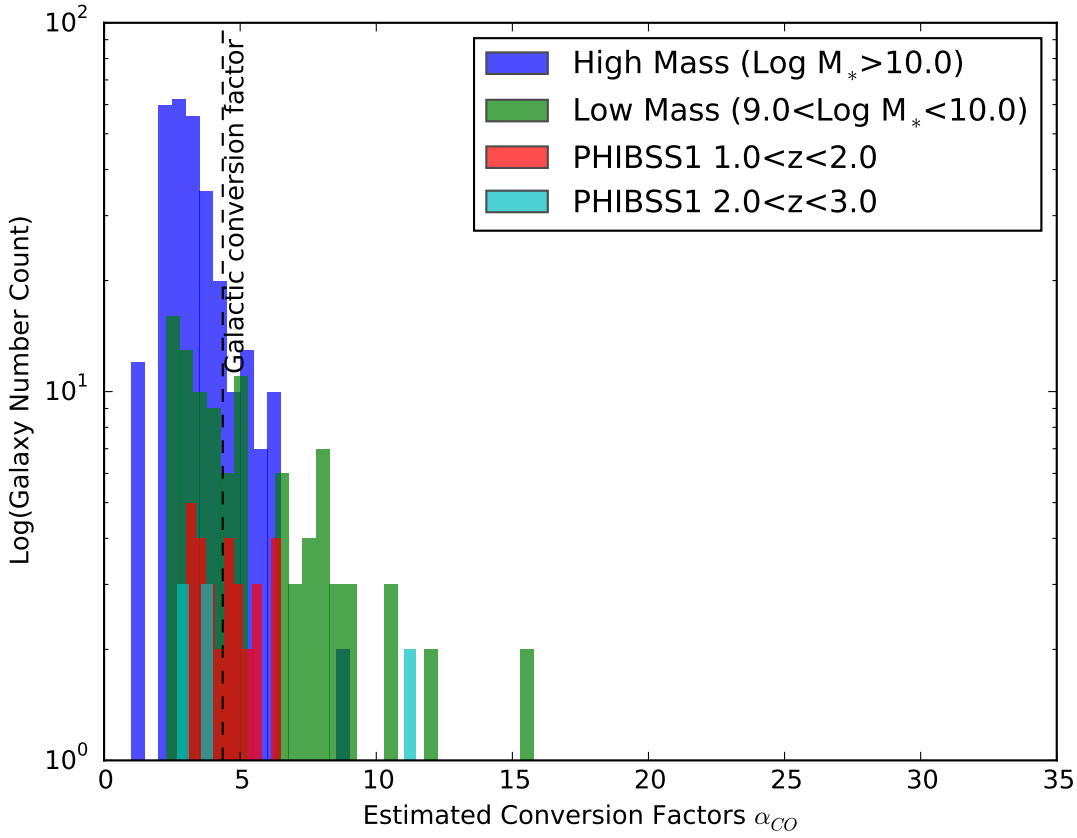

Figure 5.1. Distribution of conversion factors for the high and low mass xCOLD GASS and PHIBSS1 galaxies. For the xCOLD GASS high mass sample it can been seen that the galactic value is a good approximation to the predicted values using Equation 4.22. The xCOLD GASS low mass sample, due to their lower metallicities need higher conversion factors, similar to the PHIBSS1 galaxies that all have metallicities less than solar. We also overlay the position of the galactic conversion factor value.

between 10^9 -10^{10} $M_\odot$ for the low redshift galaxies, which is in excellent agreement with the trends found in Grossi et al. (2016) and the star formation models of Krumholz et al. (2009, 2008) demonstrated in Lu et al. (2015). In the star formation models, this flattening occurs as depletion timescales are independent of stellar mass, something which we shall explore in Section 5.1.2. This flattening also validates part of the ideal gas regulator model, where sSFR = constant (Lilly et al. 2013), for which no or very little dependence of gas fractions on stellar mass is expected, as we observe up to $M_*{\sim}10^{10}M_\odot$. This result is also of interest given the trend of increasing HI gas mass fraction with decreasing stellar mass, down to $M_*{\sim}10^9M_\odot$ (Brown et al. 2015), implying that low mass galaxies are less efficient at converting their HI gas reservoirs into molecular gas. For the high redshift objects the trend of increasing molecular gas fraction with decreasing stellar mass is still evident;

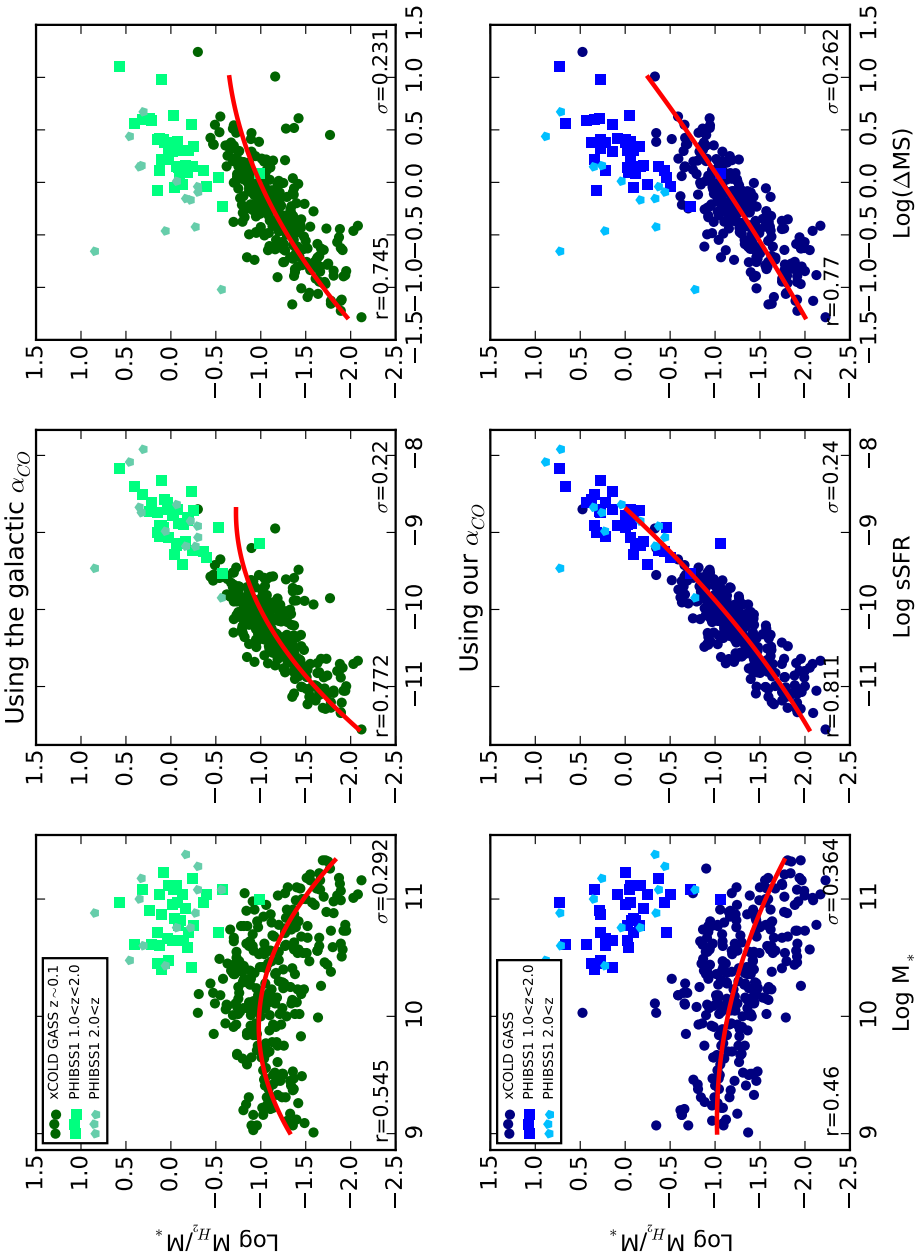

Figure 5.2. ***Top row:*** We present scaling relations for the CO traced molecular gas mass fraction as a function of stellar mass, specific star formation rate and Δ(MS) (from left to right), for the full xCOLD GASS and PHIBSS1 samples, in different shades of green, when using a constant galactic conversion factor. We fit quadratic polynomials, red lines, to the data to qualitatively show the trend which emerges for the xCOLD GASS data only. We also indicate the product moment correlation co-efficient and the one sigma scatter of the xCOLD GASS data only. ***Bottom row:*** The same as the top row but when using the prescription detailed in Equation 4.22, where each sample is given in different shades of blue. These are for all galaxies with CO detections across the whole main sequence in both samples.

this is true across all redshifts for $M_*>10^{10}M_\odot$ (Tacconi et al. 2013). The decreasing gas fractions as stellar mass increases, at all redshifts, is driven by the flattening of the SFR-M_* relation at high stellar masses.

The correlation with specific star formation rate strengthens when using the prescription presented here. A tight correlation between molecular gas and star formation is expected, confirming that the variable α_{CO} presented here outperforms a constant Galactic value. This is in agreement with the relations found in Saintonge et al. (2016) showing that star formation activity in a galaxy is controlled by the total available gas. Interestingly, the high redshift galaxies simply extend the trends found from the low redshift sample.

We also plot the correlation with Δ(MS) and find similar results to the trends with specific star formation rate for local universe galaxies. This is expected as $sSFR_{MS}$ is roughly constant in the local universe and therefore $\Delta(MS) \propto sSFR$ at low redshift. The high redshift galaxies are offset from the trend seen in the low redshift sample as a direct consequence of the evolution of sSFR on the main sequence with redshift (e.g Karim et al. (2011)) and the increase in the gas supply rate.

We now qualitatively investigate the scaling relations for the molecular gas depletion times for the full xCOLD GASS sample.

5.1.2 Star formation efficiency up to z∼2.0

We present scaling relations for the CO-traced molecular gas depletion times, where $t_{dep} = M_{H_2}/SFR$, as a function of stellar mass, specific star formation rate and Δ(MS) (from left to right) for the full xCOLD GASS and PHIBSS1 samples in Figure 5.3, again using corrected aperture CO fluxes, similar to those shown in Figure 5.2.

As can been seen the correlation with stellar mass, for local universe galaxies with $M_*>10^{10}$ $M_\odot$, remains marginally unchanged. However the depletion times do increase for the low redshift galaxies with stellar masses less than 10^{10} $M_\odot$ and and so we see a very shallow linear positive correlation across the whole sample; however this is statistically insignificant due to the low correlation coefficient ($r = 0.319$) and hence a flat distribution can not be ruled out statistically. Low redshift low mass galaxies have, on average, equal depletion times to higher mass galaxies, while higher redshift galaxies also have depletion times which do not vary with stellar mass, as seen by the PHIBSS1 galaxies. This is all in agreement with previous trends found in the low and high redshift universe by Genzel

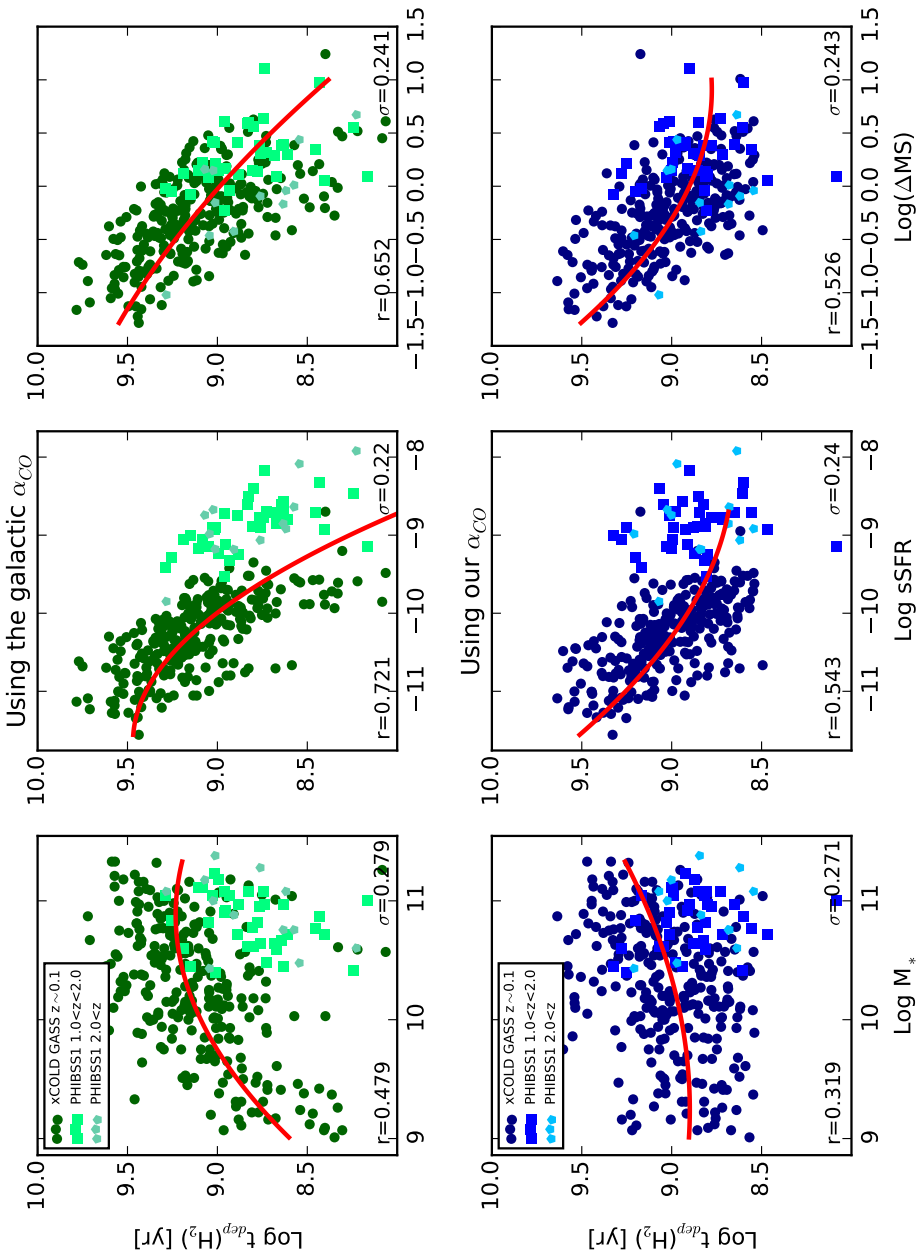

Figure 5.3. We present scaling relations for the CO traced molecular gas depletion time as a function of stellar mass, specific star formation rate and Δ(MS) where the format is identical to Figure 5.2

et al. (2015), Tacconi et al. (2013), Santini et al. (2014), Huang & Kauffmann (2014) and Sargent et al. (2014) who also claim depletion times have very little dependence on stellar mass. This important result validates part of the equilibrium model (Davé et al. 2012; Lilly et al. 2013) which states that gas depletion times are independent or have very little dependence on stellar mass.

Furthermore the correlation with specific star formation rate seen when using constant α_{CO} weakens when using the prescription presented here. The trends are identical for the lower specific star formation rate objects (these are the more massive galaxies) while the trend changes for the higher specific star formation rate objects as these are prescribed larger conversion factors than the galactic one. This trend, albeit weaker and shallower, re-affirms and is in agreement with the relations found in Saintonge et al. (2011*b*). Our shallower trend is expected because our prescription is dependent on Δ(MS). The trend observed here is in excellent agreement with that found in Hunt et al. (2015); the reason for this will be discussed below. Moreover the high redshift galaxies are offset from the trend seen in the low redshift sample. This is simply a direct consequence of the evolution of sSFR on the main sequence through redshift (Karim et al. 2011) and the increase in the gas supply rate, similar to the above. This suggests that the increase in star formation rates between the local universe and the peak of cosmic SFR is mainly driven by increased gas supply rate as opposed to changes in galaxy scale star formation efficiency. Galaxies at higher redshift, with the same gas depletion timescales to their low redshift counterparts, have higher molecular gas fractions, as noted above, and hence have higher sSFRs justifying the observed trend across redshift in the PHIBSS1 sample.

We also plot the correlation with Δ(MS) and find similar results to the trends with specific star formation rate for the COLD GASS objects as noted above. The high redshift galaxies follow the same trend found from the low redshift, suggesting that depletion timescales on the main sequence line change only slowly (if at all) with redshift, discussed further in Section 5.2.

Finally we plot in the left panel of Figure 5.4 the CO(1-0) luminosity versus star formation rate for the whole xCOLD GASS sample which, if a constant conversion factor is used, is identical to M_{H_2} versus star formation rate. The left plot demonstrates that low redshift galaxies with stellar mass $< 10^{10}$ $M_{\odot}$ have much lower CO luminosities, ergo total molecular gas mass, per unit star formation than their higher mass counterparts. Is this due to a higher star formation efficiency in lower mass galaxies or due to the

photodissociation of CO leading to higher conversion factors? To this end we plot M_{H_2} versus star formation rate, using our conversion function, for the entire xCOLD GASS sample and find that low mass galaxies lie on the same trend of increasing M_{H_2} with SFR i.e they are indeed equally efficient at forming stars. The divergence away from the trend, in the left plot, is therefore fully accounted for by the photodissociation of CO. A single mode of star formation, rather than a bimodal one, emerges when using a continuous conversion function which is in excellent agreement and consistent with the theoretical modelling results of Narayanan et al. (2012), who find the same star formation law as we find here.

It now becomes apparent why our trend for the depletion time versus sSFR, presented in Figure 5.3, is in agreement with that presented in Hunt et al. (2015); their conversion function was derived under the assumption that the L_{CO} versus SFR trend for the high mass sample continues down to the low star formation rates of the low mass sample in xCOLD GASS. e.g Hunt et al. (2015) assumed that the divergence away from the trend in the left panel of Figure 5.4 was purely caused by CO photodissociation. We have here validated that assumption to be correct.

5.2 Redshift evolution of gas fractions and depletion times

We qualitatively explore variations in molecular gas fractions and gas depletion times with redshift in Figure 5.5. In the left panel we plot redshift versus depletion time for the full xCOLD GASS and PHIBSS1 surveys in blue and red respectively. We also overlay the predictions from **a)** Tacconi et al. (2013) where $t_{dep} \propto (1+z)^{-1.0}$ using CO PHIBBS1 measurements **b)** Davé et al. (2012) where the equilibrium model states $t_{dep} \propto (1+z)^{-1.5}$ from their analytical formalism and **c)** Genzel et al. (2015) who find $t_{dep} \propto (1+z)^{-0.16}$ using a compilation of dust and CO measurements from the literature. We find the depletion time changes slowly with redshift which is in broad agreement with the trends found in **a** and **c** while our trend is shallower than that from the equilibrium model **b**. This suggests that the process of star formation on the main sequence is driven by similar physical mechanisms across cosmic time, as found previously by Saintonge et al. (2013). As a result the evolution of the molecular gas fraction, in the right panel, simply tracks the evolution of sSFR which, in turn, is driven by the gas cycling in and out of galaxies (Magdis et al. 2012; Tacconi et al. 2013; Santini et al. 2014).

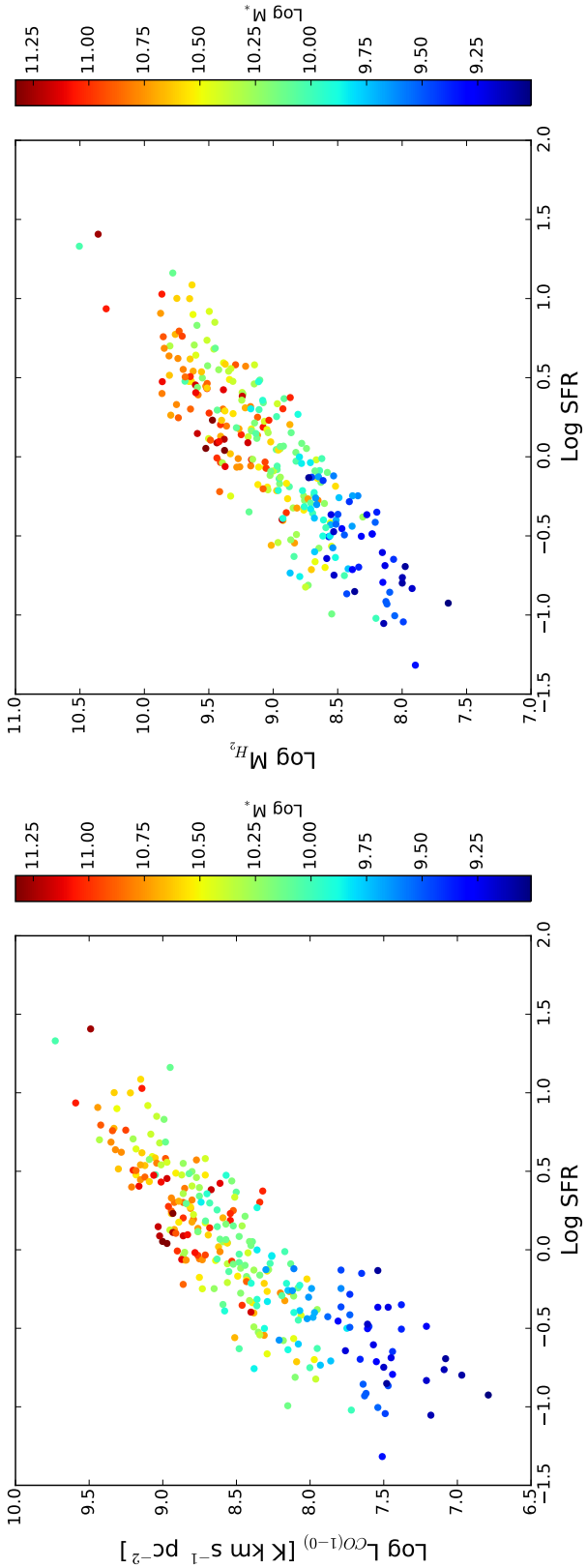

Figure 5.4. Left: Galaxies with stellar mass $< 10^{10}$ $M_\odot$ have much lower CO luminosities, ergo total molecular gas mass, per unit star formation than their higher mass counterparts. Is this due to a higher star formation efficiency in lower mass galaxies or due to the photodissociation of CO leading to higher conversion factors? **Right:** To this end we plot M_{H_2} versus star formation rate, using our conversion factor prescription, for the whole COLD GASS sample and find that low mass galaxies are indeed equally efficient at forming stars than higher mass galaxies. The divergence away from the trend, in the left plot, is fully accounted for by the photodissociation of CO.

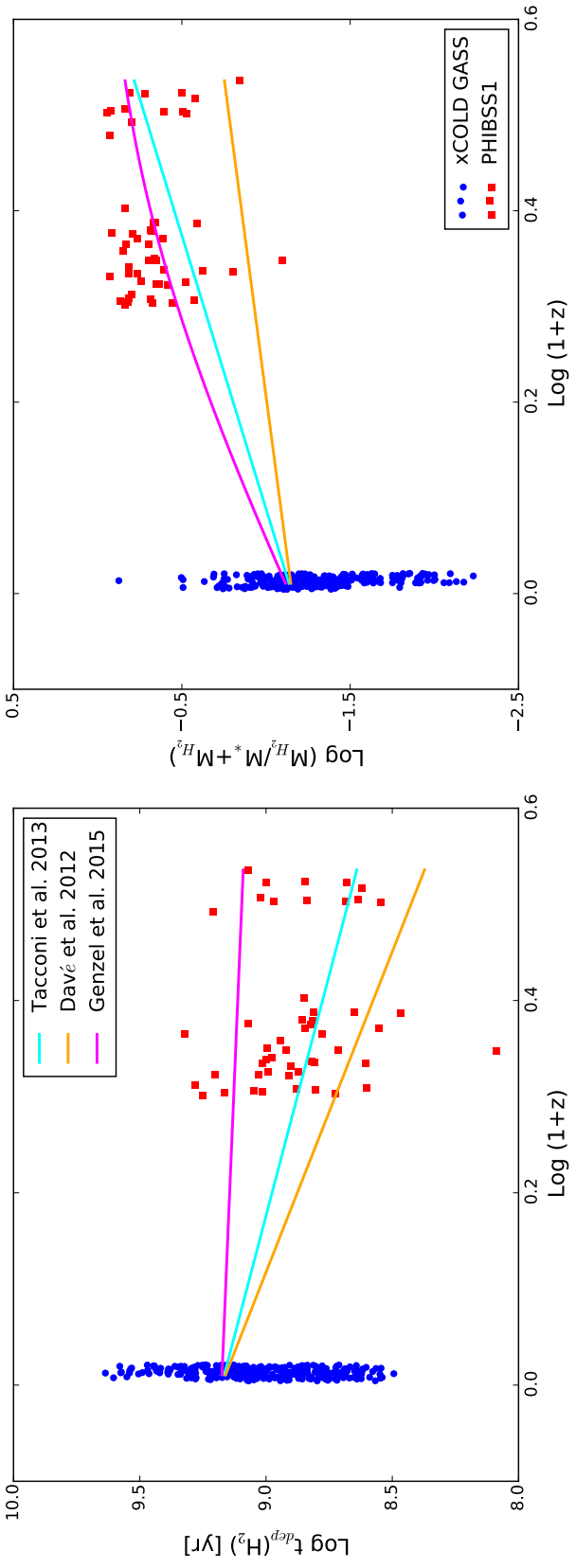

Figure 5.5. Left: We plot variations in redshift versus depletion time for the full xCOLD GASS and PHIBSS1 surveys in blue and red respectively with the predictions from Tacconi et al. (2013), Davé et al. (2012) and Genzel et al. (2015) overlaid. **Right:** We likewise plot the molecular gas fraction versus redshift with an identical format to the left panel.

We similarly overlay the predictions from **a)** Tacconi et al. (2013) where $\frac{M_{H_2}}{M_*+M_{H_2}} \propto (1+z)^{1.75}$ **b)** Davé et al. (2012) where the equilibrium model states $\frac{M_{H_2}}{M_*+M_{H_2}} \propto (1+z)^{0.75}$ and **c)** Genzel et al. (2015) who find $\frac{M_{H_2}}{M_*} \propto (1+z)^{2.71}$; our results are in broad agreement with all three scaling laws. The resulting steep redshift dependence of the molecular gas fraction reflects the evolution of the main sequence across cosmic time and the increased gas supply rate up to z∼2, rather than changes in star formation efficiency across cosmic time, consistent with the equilibrium model, as noted by Genzel et al. (2015) and Saintonge et al. (2013). This becomes even clearer if we express the gas fraction in Figure 5.5 as:

$$f_{gas} = \frac{1}{1 + (t_{dep}\ \mathrm{sSFR})^{-1}}\,. \tag{5.1}$$

emphasising that, due to the very slow evolution of the depletion time with redshift, the steep evolution of sSFR and the main sequence is a direct consequence of the evolution of f_{gas}. As redshift increases a combination of an increasing gas fraction and slowly decreasing depletion timescales causes a larger sSFR at constant M_*. We stress that the above is only a qualitative treatment of the redshift evolution of depletion times and molecular gas fractions. A robust statistical analysis would require weightings assigned to each galaxy to account for the different properties in each redshift bin. For example a direct statistical comparison of the sources at z=0 with those at z=1-2 is non-trivial due to the different number of galaxies, and hence dispersion, in each bin. However, as stressed, we here only aim to qualitatively explore the redshift evolution of the data and so a qualitative analysis is unnecessary.

5.3 Summary & Conclusions

We applied our new conversion function from Chapter 4 to the full xCOLD-GASS sample, including the low mass galaxy sample and the higher mass objects presented in Saintonge et al. (2011*a*) - and the PHIBSS1 sample (Tacconi et al. 2013). We investigate, qualitatively, molecular gas mass fraction and gas depletion time scaling relations, up to $z \sim 2.0$, for stellar masses $> 10^9$ $M_\odot$. We find:

- A flattening of the molecular gas mass fraction against stellar mass, for $z \sim 0$, as stellar mass decreases.

- Non-universal gas depletion timescales and a shallower trend with sSFR as previously reported. The depletion times do not vary significantly with stellar mass.

- The lower L_{CO} to SFR ratios in low mass local galaxies are entirely due to photodissociation of CO. On average lower mass galaxies are equally efficient at forming stars than their high mass counterparts.

- Depletion times change slowly with redshift suggesting that the process of star formation on the main sequence is driven by similar physical mechanisms across cosmic time.

- The steep redshift dependence of the molecular gas fraction reflects the evolution of SFRs across cosmic time and the increased gas supply rate up to $z \sim 2$, rather than changes in star formation efficiency.

The major implication of our work regards the non-universality of depletion times as galaxies higher up the main sequence deplete their gas reservoirs quicker than those with a lower Δ(MS). Depletion times are also, on average, independent of stellar mass which validates part of the framework which makes up the equilibrium model. These results extend those presented in Saintonge et al. (2016) into the low mass and low metallicity regime, in the local universe, while utilising our novel conversion function, something hitherto unused.

Chapter 6

JINGLE: A new galaxy survey to use dust as a tracer of gas

The work throughout this Thesis has highlighted how much cold gas properties can vary from galaxy to galaxy. As cold gas is such a central ingredient in current galaxy evolution theories, it is essential that we not only continue to investigate how the cold ISM mass scales with other galaxy properties, but also that we refine our measurement tools; as was done for the conversion function in Chapter 4. How then can we refine another technique, the dust-to-gas ratio method, introduced in Chapter 1? If we want to refine our methods when using dust as an alternative cold ISM tracer, then a new systematic survey of gas and dust properties of galaxies is indispensable. This will help to quantify if and how quantities such as the dust temperature, emissivity and dust- to-gas ratio vary systematically across the galaxy population. This Chapter discusses the planning of such a survey, the science goals which can be achieved, and the latest software being developed to extract dust properties from the FIR data.

6.1 The JINGLE survey

The JINGLE (JCMT dust and gas In Nearby Galaxies Legacy Exploration) survey, P.Is Dr A. Saintonge, Prof C. Wilson and Dr T. Xiao, was successfully proposed to the EAO JCMT (East Asian Observatory James Clerk Maxwell Telescope). We are now able to

measure CO(2-1) line fluxes, enabling the derivation of molecular gas masses using the conversion function in Chapter 4, and to measure 850μm continuum fluxes (complementing H-ATLAS[1] FIR photometry) to quantify dust properties (such as dust masses, temperatures and emissivities). By using the JCMT, in combination with an extensive multi-wavelength dataset, we can quantify the dust and molecular gas properties of a sample of $\sim$200 nearby galaxies via independent methods.

While xCOLD GASS measured CO(1-0) fluxes and molecular gas masses for a sample of $\sim$ 500 galaxies (Chapter 5), it lacks information on their dust content. Conversely, large blind FIR surveys, such as H-ATLAS (Eales et al. 2010), are not accompanied by any significant CO effort. Unfortunately the HRS is the only survey to-date which has combined measurements of the dust and gas contents of galaxies, using FIR and sub-mm CO data; however it is not statistically complete[2] and extra FIR photometric data is necessary to reduce the degeneracy in fitted dust parameters. JINGLE will therefore bridge this gap to provide a statistically complete picture with robust dust and gas measurements.

In this Chapter, the first results from JINGLE are presented, demonstrating the potential of the survey and highlighting the work carried out by this author.

6.1.1 Science goals

Several interesting goals can be achieved due to the unique availability of both CO(2-1) and 850μm data, with wide topics ranging from using CO data to study gas within merger and close pairs of galaxies, through to studying non-thermal contamination from AGN in the FIR. However, I shall focus solely on the goals of this survey which I have contributed towards and worked on; goals which are an extension of the science questions explored in previous Chapters of this Thesis. Our objectives for JINGLE include:

- investigating variations in the dust-to-gas mass ratio. The combination of the CO(2-1) and dust FIR data sets (along with HI data) will allow us to determine reliable dust-to-gas mass ratios for all the galaxies in our sample. Much of the existing work has focused on relatively small samples of nearby luminous galaxies e.g Sandstrom et al. (2013), Rémy-Ruyer et al. (2014). Here, we will establish for the first time if and how this ratio varies as a function of stellar mass, metallicity and SFR across a homogenous representative sample, thus improving our understanding of the dust

[1] See Section 6.1.4 for further details.

[2] Approximately half of the galaxies are in the Virgo cluster and it is stellar mass (K-band) selected.

physics within galaxies.

- understanding how dust measurements from FIR continuum SED fitting (dust masses, temperatures, emissivities) vary when different dust models are used. Currently within the literature simple modified black body fitting is usually employed (Dunne et al. 2000; Vlahakis et al. 2005) where the intensity, S_ν, is expressed as

$$S_\nu \propto B_\nu(T)\nu^\beta, \tag{6.1}$$

where $B_\nu(T)$ is the Planck function and β is the dust emissivity index, which in the case of idealised spherical dielectric grains a value of $\beta = 2$ is adopted. Gordon et al. (2014) recently proposed three different dust models which, when applied to the LMC and SMC, give different measurements for the dust properties. With the uniqueness and size of our sample we can establish which models perform best as a function of stellar mass, metallicity, SFR, etc thus improving our understanding of the dust physics within galaxies.

- understanding whether dust is as reliable a gas mass tracer as currently thought. Continuum measurements can be used to infer gas masses in low-redshift galaxies (Eales et al. 2012). Understanding the quality and scatter in these correlations further provides a vital underpinning for observations of high redshift galaxies, where fast continuum observations in the FIR are increasingly used as a proxy for CO (long integration times) gas measurements (Scoville et al. 2014).

Throughout this Chapter I will focus on dust measurements and the science aimed at using dust as an alternative gas tracer to sub-mm CO.

6.1.2 Survey strategy and sample selection

To achieve the above science goals, we need to observe a statistically-large galaxy sample and obtain homogeneous data products with the JCMT. We make use of both the RxA heterodyne receiver for the CO(2-1) observations, and the SCUBA-2 continuum camera (Holland et al. 2013) for the 850μm continuum observations. We also require the following ancillary multi-wavelength data products:

- Herschel PACS and SPIRE photometry to combine with the JCMT 850μm photometric fluxes to derive accurate dust masses, temperatures and emissivities.

- HI observations to quantify atomic gas masses within the same physical region of the galaxies as the CO and FIR measurements.

- Optical IFS to derive spatially-resolved stellar and ionised-gas properties, including metallicities.

We identify as the ideal fields the North Galactic Pole (NGP) region and three of the equatorial GAMA fields (GAMA09, GAMA12 and GAMA15). These four fields are part of H-ATLAS and therefore have Herschel-SPIRE and PACS coverage, and are also all within the footprint of either the MaNGA or SAMI IFU surveys. The GAMA survey provides multi-wavelength coverage and redshifts for galaxies in these fields[3]. Finally, all four fields are within the footprint of the ALFALFA survey, so integrated HI masses are already available.

We define as our parent sample all galaxies within our four fields that are found within the SDSS spectroscopic survey to have $M_{\odot} > 10^9 M_{\odot}$ and $0.01<z<0.05$. There are 2853 galaxies matching these selection criteria, out of which about half have been selected by MaNGA as possible targets. Out of this parent sample, we select for JCMT observations those galaxies with detections at the 3σ level at both 250 and 350μm in the H-ATLAS survey. As shown in Fig 6.1, under standard assumptions for T_{dust} and β, the depth of the H-ATLAS SPIRE maps, and the sensitivity of SCUBA-2, we find that we can expect the SCUBA-2 850μm observations to be sensitive to lower dust masses than Herschel at 500μm. On the other hand, a galaxy with a dust mass detectable with SCUBA-2 would almost certainly be detected at both 250 and 350μm (and for most objects but those with the coldest dust and lowest β, we will also have strong PACS detections at 100 and 160μm).

There are 284 galaxies in the parent sample that pass our Herschel selection criterion at 250 and 350μm. In order to have as uniform coverage as possible of the SFR-M_* plane, we extract $\sim$200 galaxies from this sample with a flat stellar mass distribution, shown in Figure 6.2. Since the mass distribution of the parent sample is well known, we

[3]Further details can be found at http://www.gama-survey.org/

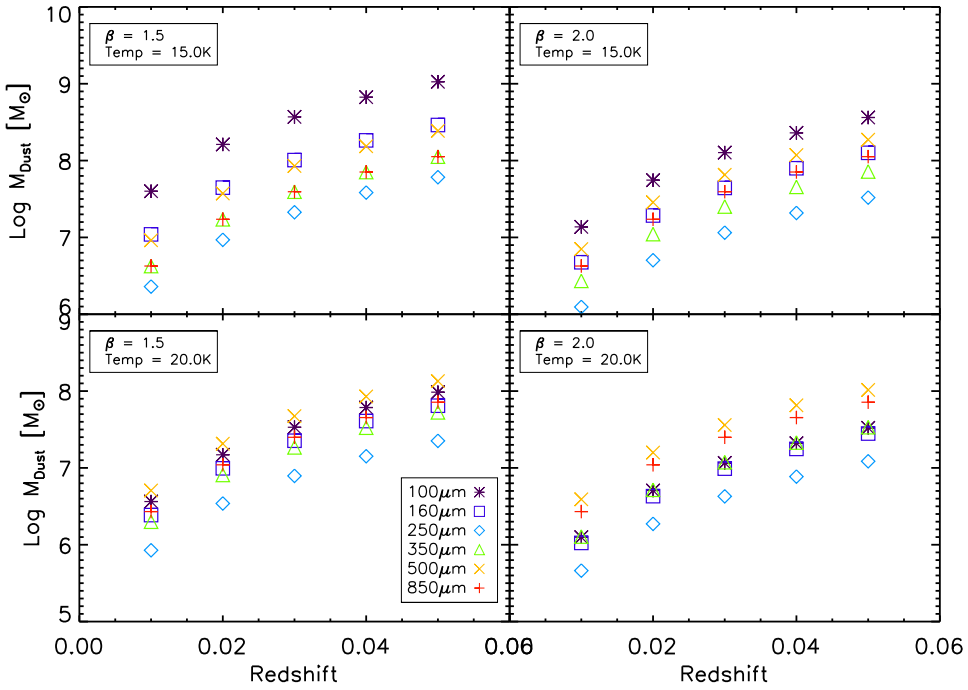

Figure 6.1. Minimum dust mass, in solar units, detectable at the 4σ limit, for an on source integration time of 2 hours in Grade 1 weather using SCUBA-2, as compared to the dust mass levels detectable with SPIRE and PACS in the H-ATLAS survey. The noise levels are 25.0, 30.0, 7.4, 9.4 and 10.2 mJy/Beam at 100μm, 160μm, 250μm, 350μm and 500μm respectively. SCUBA-2 is less sensitive than SPIRE at 250 and 350μm but more so than at 500μm.

can statistically correct for the flat stellar mass distribution in any science analysis we perform (as was done in the xCOLD GASS survey and will be done in MaNGA). Roughly 70 of these galaxies will also be observed with RxA and hence we will have CO(2-1) measurements for a subsample of the ∼200 SCUBA-2 targets.

6.1.3 Dust time estimation

Sensitivity calculations for the 850μm flux were predicted from the modified black-body fitting done to the Herschel FIR data, while using the optical diameters of our galaxies to estimate how many pixels will cover each object. Time calculations were conducted by this author, using the time estimator on the JCMT website, with matched beam filtering, to calculate the total integration time required to achieve the desired sensitivity under different weather conditions.

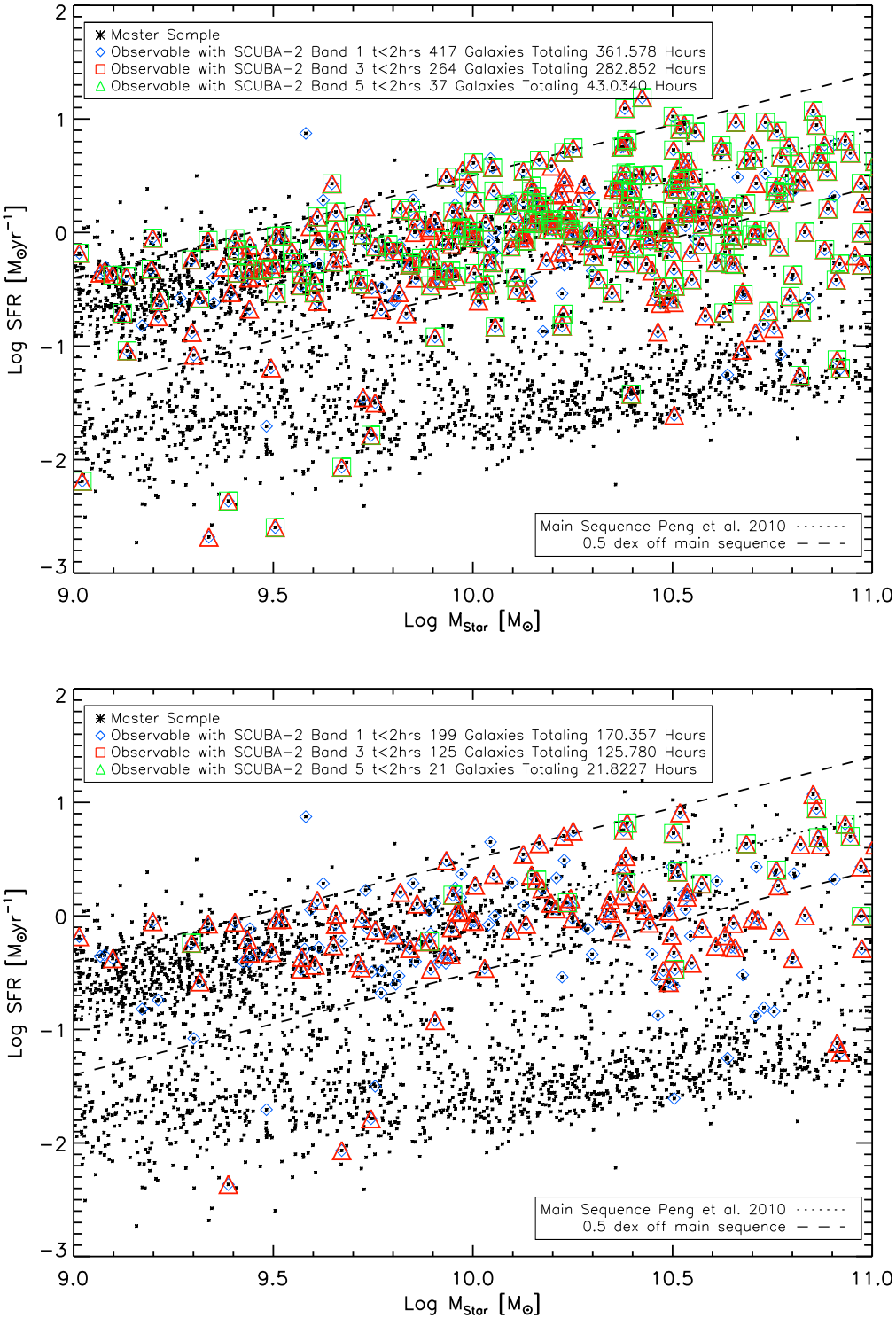

Figure 6.2. Distribution of the targeted and parent samples in the SFR-M_* plane. **Top:** Coloured symbols show the galaxies from the parent sample where 850μm fluxes are predicted to be detectable at the 4σ level within 2 hours of integration in the different weather bands. **Bottom:** A summary of our final sample selection, where galaxies with predicted 850μm fluxes are detectable at the 4σ level within 2 hours of integration and who also are scheduled to be observed with MaNGA.

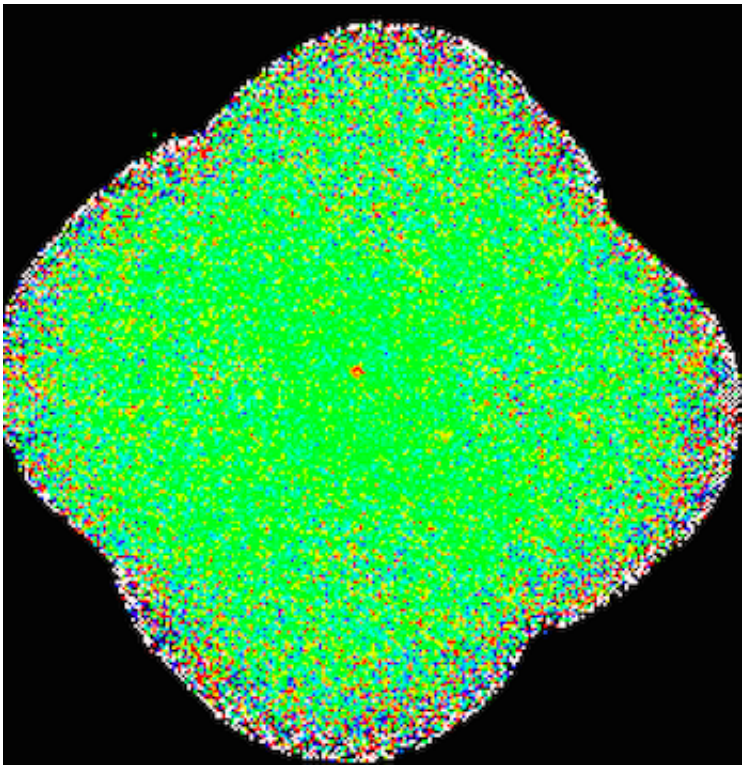

Figure 6.3. An example reduced SCUBA-2 map of 'J131101.71+293442.0', see Table 6.1, where the detected galaxy can be seen in the centre of the image with S/N=4.3.

6.1.4 Ancillary data - H-ATLAS

The success of JINGLE relies not only on the quality of the JCMT data products, but also on the availability of several ancillary data sets and on coordination with two surveys: H-ATLAS and MaNGA.

The Herschel-ATLAS (H-ATLAS; Eales et al. (2010)) was the largest open-time key project undertaken by the Herschel Space Observatory. It is a blind extragalactic wide-area survey observing an area of 550deg^2 with both the PACS (Poglitsch et al. 2010) and SPIRE (Griffin et al. 2010) instruments. In the first 160 deg^2, over 10^5 sources were detected at $\geqslant 4\sigma$ significance. The point source sensitivities are 7.4, 9.4 and 10.2mJy (1σ total noise) with a FWHM of 18, 24 and 35" at 250, 350 and 500μm, respectively (Valiante et al. 2016). H-ATLAS has created the first extensive and unbiased census of dust in galaxies, and, being a wide-area survey, also picks up many rare objects e.g. ultra-luminous IR galaxies and dust-obscured AGN (Dunne et al. 2011; Bourne et al. 2012; Rowlands et al. 2014; Clark et al. 2015).

6.2 Scuba-2 850μm flux extraction

To date, continuum observations have been taken with SCUBA-2 at 850μm for ∼100 galaxies. Our sources are only partially extended with angular sizes of ∼ 20-50", hence we use a Daisy mapping scheme to increase the S/N in the centre of the images where each of our galaxies are expected. The raw images were reduced by Dr Matthew Smith (a co-author on the proposal), using standard scripts within STARLINK and SMURF, with a filter size of 100"; an example of a reduced image can be seen in Figure 6.3 with our galaxy detected in the centre of the image. Each map is ∼ 400"x400" and each pixel has an angular size of 4". Software has been developed to perform aperture photometry on these reduced images using IDL scripts written by this author. The 850μm flux for each galaxy is measured within a central circular aperture with radius equal to the optical radius from SDSS for each of our objects. Background noise is calculated within an annulus, around and outside the aforementioned circular aperture, with a width equaling the optical radius of the galaxy. We run our flux extraction pipeline on a test sample of nine JINGLE sources (these were selected as galaxies with a range of sizes and expected fluxes) with results shown in table 6.1.

6.2.1 Contaminant CO(3-2) flux predictions using Machine Learning

The 850μm emission we measure from the reduced maps can, however, also arise from various sources other than the dust (e.g gas, old stars) and hence, the dust emission, could be contaminated. The ^{12}CO(3-2) line is one of the brightest molecular lines in the sub-millimetre. As RxA CO(2-1) observations haven't been conducted yet for all SCUBA-2 targets (some SCUBA-2 targets will not be observed with RxA) it is important to be able to predict the CO(3-2) line emission from each source in a different manner, so that we can quantify dust contamination.

To do this we employ a Random Forest supervised learning technique (as discussed and explained in Chapter 3) to make predictions for the CO(1-0) emission for the aforementioned sample of nine JINGLE sources. We use the full xCOLD-GASS sample as a training set, with the stellar mass and SFRs as training features. By using the stellar masses and SFRs from the MPA-JHU SDSS catalogue for our JINGLE targets we can then predict the expected CO(1-0) flux for each galaxy. We then use a standard conservative line ratio of 0.7 for the CO(3-2)/CO(1-0) lines (Harris et al. 2010). To convert from

sub-mm emission line units of K km s^{-1} to SCUBA-2 continuum fluxes in mJy $beam^{-1}$ we use the conversion factors given in Drabek et al. (2012). The results from this are presented in Table 6.1.

For galaxies with a signal-to-noise, S/N $\geqslant$ 4 (six galaxies) the average CO(3-2) contamination is 10.2%, with values ranging from 1%-33.3%. These numbers are in agreement with contamination values found in the NGLS sample (Wilson et al. 2012) through a direct measurement of the CO(3-2) emission line. Values of 10% and 37% were found for NGC 4631 and M82 respectively. An average value of 25% is found through their sample, consistent with the range of values found here (private communication with Prof. Christine Wilson). This agreement demonstrates that this machine learning technique provides a reliable alternative method to predict CO(3-2) contamination for galaxies where we will not have RxA data. Galaxy 'J125453.68+282501.1' has an extreme contamination at 82% due to the low S/N of the 850μm continuum; this is probably due to poor calibration or a sub-optimum data reduction method.

6.3 Software Development: Dust properties from Herschel & SCUBA-2

To measure dust properties, e.g masses, temperatures and emissivities, there are two ideal methods which seem ubiquitous within the literature: **a)** Spectral energy distribution (SED) fitting of data across the whole ultraviolet to far-infrared/sub-mm regime using up-to-date dust models and energy balance/radiative transfer techniques (Zubko et al. 2004; Draine & Li 2007; Bianchi 2008; da Cunha et al. 2008) **b)** Assuming simple single/double modified black-body emission (Dunne et al. 2000; Vlahakis et al. 2005) and fitting for the FIR SED only. Throughout the remainder of this Chapter I will focus on the second option to measure dust properties via modified black body SED fitting.

The identification of a variable emissivity index, β, in galaxies spanning a wide range of metallicity and star formation properties (Smith et al. 2012; Rémy-Ruyer et al. 2013; Draine et al. 2014; Kirkpatrick et al. 2014) clearly demonstrates that dust properties vary from galaxy to galaxy. Constraining the variation of the dust emissivity with wavelength is thus an absolute prerequisite to deriving accurate dust masses for our sample galaxies, particularly for the coldest, most massive dust component, hence why we will allow this to vary in the following sections.

JINGLE ID	850μm flux	S/N	Predicted CO(3-2) flux	850μm contamination from the CO(3-2) flux	Log M_*	Metallicity	SFR	Optical Radius
	[mJy]		[mJy]	%	[$M_\odot$]	[O/H]	[$M_\odot$ yr^{-1}]	"
J091750.80-001642.5	18.86	5.51	0.74	3.91	10.40	8.70	1.05	22.08
J125453.68+282501.1	0.79	0.41	0.65	82.28	10.39	8.67	0.38	11.23
J125837.28+271035.8	4.58	4.21	0.78	17.00	9.63	8.71	1.37	8.48
J131101.71+293442.0	13.70	4.29	0.44	3.21	10.96	8.84	7.59	29.17
J131615.95+301552.2	2.37	1.24	1.28	54.21	10.74	8.66	8.81	8.91
J131620.53+304042.0	5.75	4.31	1.92	33.33	10.16	8.65	0.69	15.60
J132515.15+324016.1	7.00	3.42	0.48	6.86	10.83	8.77	1.61	12.70
J133457.27+340238.7	41.36	4.94	0.40	0.96	10.56	8.86	4.32	24.69
J144307.78+010600.0	13.81	4.00	0.40	2.87	10.29	8.71	1.16	10.06

Table 6.1. Derived observational quantities for a test sample of JINGLE galaxies. Stellar masses, SFRs, metallicities and optical radii are taken from SDSS.

6.3.1 Different Physical Dust models

Our sample selection criteria in Section 6.1.2 ensured that we have at least two Herschel data points per galaxy as we targeted galaxies with SPIRE 250 and 350μm detections. We also have 100, 160 and 500μm when detections are available, and we additionally obtain here the integrated flux at 450 and 850μm from SCUBA-2. This allows us to perform modified blackbody (MBB) SED fitting, constraining the dust temperatures, $\mathrm{T_{dust}}$, and emissivity indices, β, and to simultaneously estimate the total dust masses, $\mathrm{M_{dust}}$, depending on the functional form of the blackbody model to be used.

Similar to Gordon et al. (2014), we use three different models to fit the FIR/sub-millimetre flux measurements:

- **SMBB:** The first model is a single temperature blackbody modified by a single power-law emissivity (SMBB) (Hildebrand 1983) where the flux density emitted at a frequency ν, $\mathrm{F_{\nu}^{SMBB}}$, is modelled as,

$$F_{\nu}^{\mathrm{SMBB}} = \frac{M_{\mathrm{dust}} \kappa_{\nu}^{\mathrm{SMBB}} B_{\nu}(T_{\mathrm{dust}})}{D^2} \tag{6.2}$$

  where $B_{\nu}(T_{\mathrm{dust}})$ represents the Planck function given by,

$$B_{\nu}(T_{\mathrm{dust}}) = \frac{2h\nu^3}{c^2} \frac{1}{\exp\left(\frac{h\nu}{k_b T_{\mathrm{dust}}}\right) - 1} \tag{6.3}$$

  for a dust temperature T_{dust}, h is the Planck constant while $\mathrm{k_b}$ is the Boltzmann constant. D is the distance to the galaxy while $\kappa_{\nu}^{\mathrm{SMBB}}$, the dust mass absorption co-efficient, at frequency ν given by:

$$\kappa_{\nu}^{\mathrm{SMBB}} = \kappa_{\nu_0} \left(\frac{\nu}{\nu_0}\right)^{\beta} \tag{6.4}$$

  where β is the dust emissivity, a free parameter. We will assume a reference dust mass absorption coefficient $\kappa(100\mu\mathrm{m}) = 4.5\ \mathrm{m^2 kg^{-1}}$ from James et al. (2002). In this model we have three free parameters namely $\mathrm{M_{dust}}$, $\mathrm{T_{dust}}$ and β.

- **BEMBB:** Many studies using SMBB have shown that it is not possible to reproduce the FIR SEDs of low-metallicity galaxies owing to an excess of observed emission at sub-millimeter (sub-mm) wavelengths (Lisenfeld et al. 2002; Galliano et al. 2003;

Bendo et al. 2006; Gordon et al. 2014). This is known as the 'submm excess' problem and its origin is unclear. The existence of a large amount of cold dust could, in principle, produce the observed shape, but the required dust mass is unreasonably high. This 'submm excess' problem disappears if more than one temperature component is used (Clark et al. 2015). The second model is inspired by this, and assumes that the sub-millimetre excess emission is due to variations in the wavelength dependence of the dust emissivity law that is parameterised by a broken power law (BEMBB) (Gordon et al. 2014). Hence the flux density emitted at a frequency ν, $\mathrm{F}_{\nu}^{\mathrm{BEMBB}}$, is modelled as,

$$F_{\nu}^{\mathrm{BEMBB}} = \frac{M_{\mathrm{dust}} \kappa_{\nu}^{\mathrm{BEMBB}} B_{\nu}(T_{\mathrm{dust}})}{D^2} \tag{6.5}$$

where the Planck function is defined as above but now the emissivity law is broken such that,

$$\kappa_{\nu}^{\mathrm{BEMBB}} = \begin{cases} \kappa_{\nu_0} \left(\frac{\nu}{\nu_0}\right)^{\beta} & \text{if } \nu > \nu_b \\ \kappa_{\nu_0} \left(\frac{\nu_b}{\nu_0}\right)^{\beta_1} \left(\frac{\nu}{\nu_b}\right)^{\beta_2} & \text{if } \nu < \nu_b \end{cases}$$

where ν_b is the break frequency, a free parameter, and κ_{ν_0} is defined as above. Physically this means that dust has a different emissivity law at longer wavelengths, hence the broken nature of Equation 6.5. In this model we have five free parameters namely $\mathrm{M}_{\mathrm{dust}}$, $\mathrm{T}_{\mathrm{dust}}$, β_1, β_2 and ν_b.

- **TTMBB:** The third model assumes that the sub-millimetre excess emission is due to a second, lower temperature population of dust grains (TTMBB). Therefore the whole SED comprises of two distinct dust populations with different dust temperatures (a cold and warm component), masses and emissivities modified by two single (SMBB) emissivity laws. Therefore the flux density emitted at a frequency ν, $\mathrm{F}_{\nu}^{\mathrm{TTMBB}}$, is modelled as,

$$F_{\nu}^{\mathrm{TTMBB}} = F_{\nu}^{\mathrm{SMBB,1}} + F_{\nu}^{\mathrm{SMBB,2}} \tag{6.6}$$

  where in this model we have five free parameters namely $\mathrm{M}_{\mathrm{dust,\,1}}$, $\mathrm{T}_{\mathrm{dust,\,1}}$, $\mathrm{M}_{\mathrm{dust,\,2}}$, $\mathrm{T}_{\mathrm{dust,\,2}}$ and β. In the TTMBB model the two different dust components are assumed to have the same emissivity index β as they both contain the same dust species.

All of our models assume equilibrium heating only and thus we restrict our fits to using only data $\geqslant$100μm.

6.3.2 A multi-dust model Bayesian SED fitting code

A software package has been developed by this author in preparation for the JINGLE survey. It is now possible to fit all of the three above dust models to the FIR Herschel (PACS+SPIRE) + SCUBA-2 850μm fluxes via a Bayesian Inference methodology. As discussed in Chapters 3 and 4, Bayesian interference fitting methods have been successfully employed in several, wide-ranging, astrophysical scenarios, not to mention throughout this Thesis.

The first step is to acknowledge that, unlike in Chapters 3 and 4, each flux density measurement, at a frequency ν, (f_{ν_i} hereafter) are not independent from each other. In fact, due to known correlated measurement errors between the SPIRE bands from Parkin et al. (2012), we now have correlations between the different fluxes. The correlated errors arise because, during observations, all the different SPIRE band measurements were calibrated simultaneously using the same source, while the model assumed for the calibrator source is the same for each SPIRE band. We therefore assume correlated gaussian errors so that $L_{\nu_{1,2,\ldots,n}}$, our likelihood function for each galaxy, is a random variable distributed like:

$$L_{\nu_{1,2,\ldots,n}} = \frac{1}{(2\pi)^{n/2}\sqrt{\det \Sigma}} \exp\left\{-\frac{1}{2}(f_\nu^j - \mathcal{M}_\nu^j(\theta))(\Sigma_j^i)^{-1}(f_{\nu_i} - \mathcal{M}_{\nu_i}(\theta))\right\} \quad (6.7)$$

where Σ_j^i is the covariance matrix denoting the measurement uncertainty associated with the flux density on the ith and jth frequency and n is the number of different flux measurements we have i.e the number of data points per galaxy. We fit for the three different dust models above, where any model prediction for the flux density emitted at a frequency ν_i is denoted by $\mathcal{M}_{\nu_i}(\theta)$, where θ is an array of the free parameters depending on the choice of model, and f_ν^j and $\mathcal{M}_\nu^j(\theta)$ are the transpose vectors of f_{ν_i} and $\mathcal{M}_{\nu_i}(\theta)$. The log likelihood, $\mathcal{L}_{\nu_{1,2,\ldots,n}}$, is therefore:

$$\mathcal{L}_{\nu_{1,2,\ldots,n}} = -\frac{n}{2}\ln(2\pi) - \frac{1}{2}\ln(\det \Sigma) - \frac{1}{2}(f_\nu^j - \mathcal{M}_\nu^j(\theta))(\Sigma_j^i)^{-1}(f_{\nu_i} - \mathcal{M}_{\nu_i}(\theta)). \quad (6.8)$$

The above assumes that all the FIR fluxes are clear detections with gaussian distributed errors. However for the case of a non-detection in any of the Herschel or SCUBA-2 bands we can modify our likelihood to include the upper limits of non-detections. We do this by using the formalism detailed in Sawicki (2012) where the upper limits of each observation provide a limit on the evaluation of a definite integral. For an observation, y_i, which is clearly detected, and assumed to be a random gaussian variable, we can say

that the probability of observing our data, given the true value of the observables and the measurement uncertainties is:

$$P(y_i|y_{true,i},\sigma_{y_i}) = \frac{1}{\sqrt{2\pi\sigma_{y_i}^2}} \exp\left(-\frac{(y_i - y_{true,i})^2}{2\sigma_{y_i}^2}\right), \tag{6.9}$$

where everything is defined as in Chapter 4. But now, in the case of a single non-detection, we have the upper limit $y_{lim,i}$ such that:

$$P(y_i|y_{true,i},\sigma_{y_i}) = \int_{-\infty}^{y_{lim}} \frac{1}{\sqrt{2\pi\sigma_{y_i}^2}} \exp\left(-\frac{(y_i - y_{true,i})^2}{2\sigma_{y_i}^2}\right) dy_i. \tag{6.10}$$

We can now fold this into the above and find that, in the case of a non-detection on the kth flux measurement, our likelihood is:

$$L_{\nu_{1,2,\ldots,n}} = \int_{-\infty}^{f_{\nu_{lim,k}}} \frac{1}{(2\pi)^{n/2}\sqrt{\det\Sigma}} \exp\left\{-\frac{1}{2}(f_\nu^j - \mathcal{M}_\nu^j(\theta))(\Sigma_j^i)^{-1}(f_{\nu_i} - \mathcal{M}_{\nu_i}(\theta))\right\} df_{\nu_k}, \tag{6.11}$$

where $f_{\nu_{lim,k}}$ is the flux density upper limit at the kth frequency. Finally the log likelihood, $\mathcal{L}_{\nu_{1,2,\ldots,n}}$ is:

$$\begin{aligned}\mathcal{L}_{\nu_{1,2,\ldots,n}} = &-\frac{n}{2}\ln(2\pi) - \frac{1}{2}\ln(\det\Sigma) \\ &- \ln\int_{-\infty}^{f_{\nu_{lim,k}}} \exp\left\{-\frac{1}{2}(f_\nu^j - \mathcal{M}_\nu^j(\theta))(\Sigma_j^i)^{-1}(f_{\nu_i} - \mathcal{M}_{\nu_i}(\theta))\right\} df_{\nu_k}\end{aligned} \tag{6.12}$$

Maximising this log-likelihood for all of our models will provide us with the best fitting parameters in our models. We again use the well tested Python implementation of the affine-invariant ensemble sampler for Markov Chain Monte Carlo (MCMC) EMCEE [4] (Goodman & Weare 2010). A simplified version of this newly created software product is available on the JINGLE GitHub page, https://github.com/SURVEY-JINGLE.

6.4 Early statistical results

We apply the aforementioned Bayesian software package to fit for the three different dust models to four interesting example galaxies which have flux measurements from 100-850μm. We provide example SED fits for all three different dust models and the triangular posterior distribution of the three fitted parameters for the SMBB fit in Figures

[4] An example of the code can be found at http://dan.iel.fm/emcee/current/.

6.4, 6.5, 6.6 and 6.7. This is done to demonstrate the capability of the code and to qualitatively investigate how dust properties change depending on what physical dust model is used, one of the science goals from above. As we do not have CO(2-1) measurements yet for these galaxies (still to be observed with RxA heterodyne receiver) we apply a 10.2% correction to the 850μm flux to account for the possible CO(3-2) contamination. For this early science work we calculate errors by simply measuring the noise in the continuum maps at each frequency. Additional errors, such as calibration errors, are irrelevant at this stage as we simply want to showcase the new SED fitting code. We use uniform priors for the free parameters in each dust model and, most importantly, we allow dust temperatures to only vary between 40-12K. The lower limit is motivated as 12K represents some of the coldest dust temperatures observed in the Planck mission (Planck Collaboration et al. 2011), while there is evidence that gas outside galaxies can be heated to temperatures as high as 20K by the interstellar radiation field (Gomez et al. 2010)[5]. Preliminary results are presented below which demonstrate the code's capabilities and the early science which can be achieved with such software.

6.4.1 Showcasing example dust SEDs

We first present two example galaxies, "J12561097+280947" and "J12581823+290743" that are both interesting as the 100 and 160μm fluxes are approximately equal and hence a two temperature dust model should be more physically reasonable. A SMBB fit only provides a useful approximation if the large grains have a narrow range of temperatures (Mattsson et al. 2015), which appears not to be the case for this galaxy because of the flatter SED. A similar argument was provided in Clark et al. (2015).

The best fitting parameters are provided in the upper left hand corners in Figures 6.4 and 6.5 in each of the SED plots. It can be seen, for both galaxies, how neither the SMBB, BEMBB or TTMBB best fitting parameters are in good agreement. The SED exhibits a broken power law behaviour as the high wavelength end of both SEDs are steeply falling, revealing a secondary beta component. The TTMBB reveals a substantially massive cold dust component in both cases with a very low temperature.

Furthermore the top right plot in Figures 6.4 and 6.5 demonstrates the correlation between the best fitting parameters for the SMBB fit, indicated by the ellipticity of the

[5] A user can easily change these priors and are not 'hard-coded'. We only aim to showcase the ability of the code, hence our choice of prior at this stage isn't important.

contours. Only via the robust MCMC fitting procedure presented here is it possible to retrieve such information indicating the errors on the best fitting parameters.

A further interesting case is galaxy "J130713.20+280249.0" where the SMBB and TTMBB produce dust properties in agreement with each other, while the BEMBB is retrieving a cold dust component, shown in Figure 6.6. This occurs because either **a)** there seems to be a minor 850μm excess caused by a cold dust component **b)** synchrotron radiation is dominating at longer wavelengths. In cases such as this, where the SMBB and TTMBB agree, a single component may seem to be more reasonable, though further investigation will be needed. Moreover photometry can be an issue, as is observed in this galaxy, as **a)** Herschel 500μm fluxes can be blended/confused and lead to overestimated fluxes **b)** SCUBA-2's aggressive map filtering can lead to underestimated 450 and 850μm fluxes. These could further explain the discrepancies between the three different dust model fits.

A final interesting case is "J130801.65+264555.3" where the dust properties from all three dust models do not seem to agree, but now the SED is still rising at the shorter wavelength end (at 100 and 160μm), shown in Figure 6.7. The continued rise would imply that a two body dust SED would not be accurate, on physical grounds, as the SED should be flattening at the shorter wavelengths, such as in "J12561097+280947" and "J12581823+290743". However the SMBB and BEMBB do not agree either, indicating a group of galaxies where a new multi-temperature dust model may be needed. For cases like this it will be crucial to obtain fluxes at even shorter wavelengths to constrain the falling part of the spectrum and possibly constrain new multi-temperature dust SED models; again further work will be needed e.g a hot dust component can contribute to PACS fluxes (shorter wavelengths) (Bendo et al. 2010).

The above plots aim to demonstrate the capability of the code presented here and the varying dust properties retrieved depending on the choice of dust model. Similar results were obtained for the LMC and SMC by Gordon et al. (2014) where the TTMBB gave higher dust masses (by an order of magnitude) and the BEMBB and SMBB did not always agree. The work here implies the necessity to use different dust models for different galaxies, depending on their properties; further exploration will be needed. However, now that we can retrieve dust parameters robustly across a representative sample, with all these different dust models, it will be possible to investigate dust scaling relations and constrain variations in the gas to dust ratio for each model once all the data has been

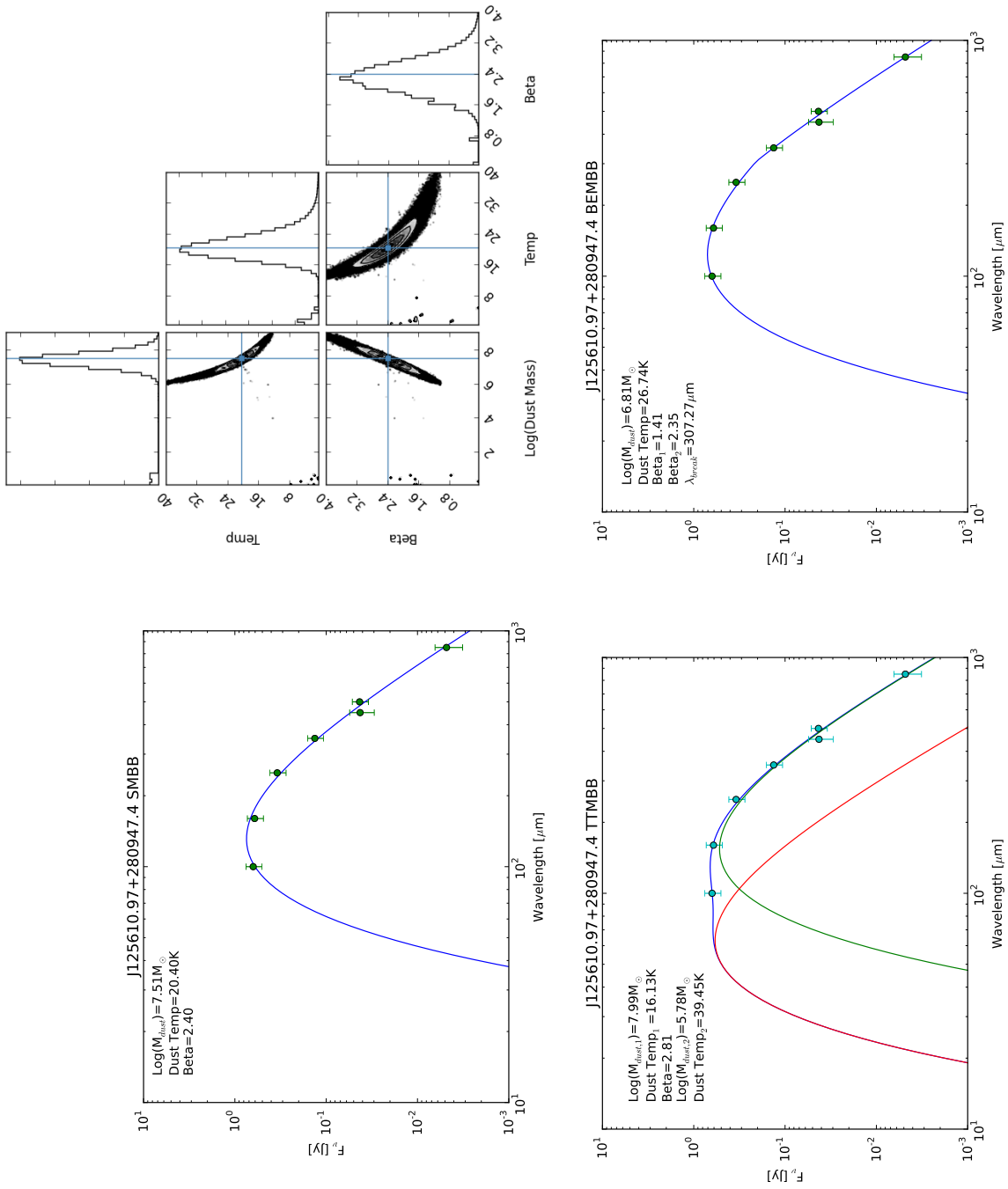

Figure 6.4. We plot above the combined Herschel and SCUBA-2 photometric data for galaxy "J125610.97+280947" with the best fit using the three different dust models. The difference between the SMBB and BEMBB indicate that a single component fit does not suffice, hence a TTMBB is necessary. In the top right plot we also show the triangular posterior distribution for the SMBB best fitting parameters.

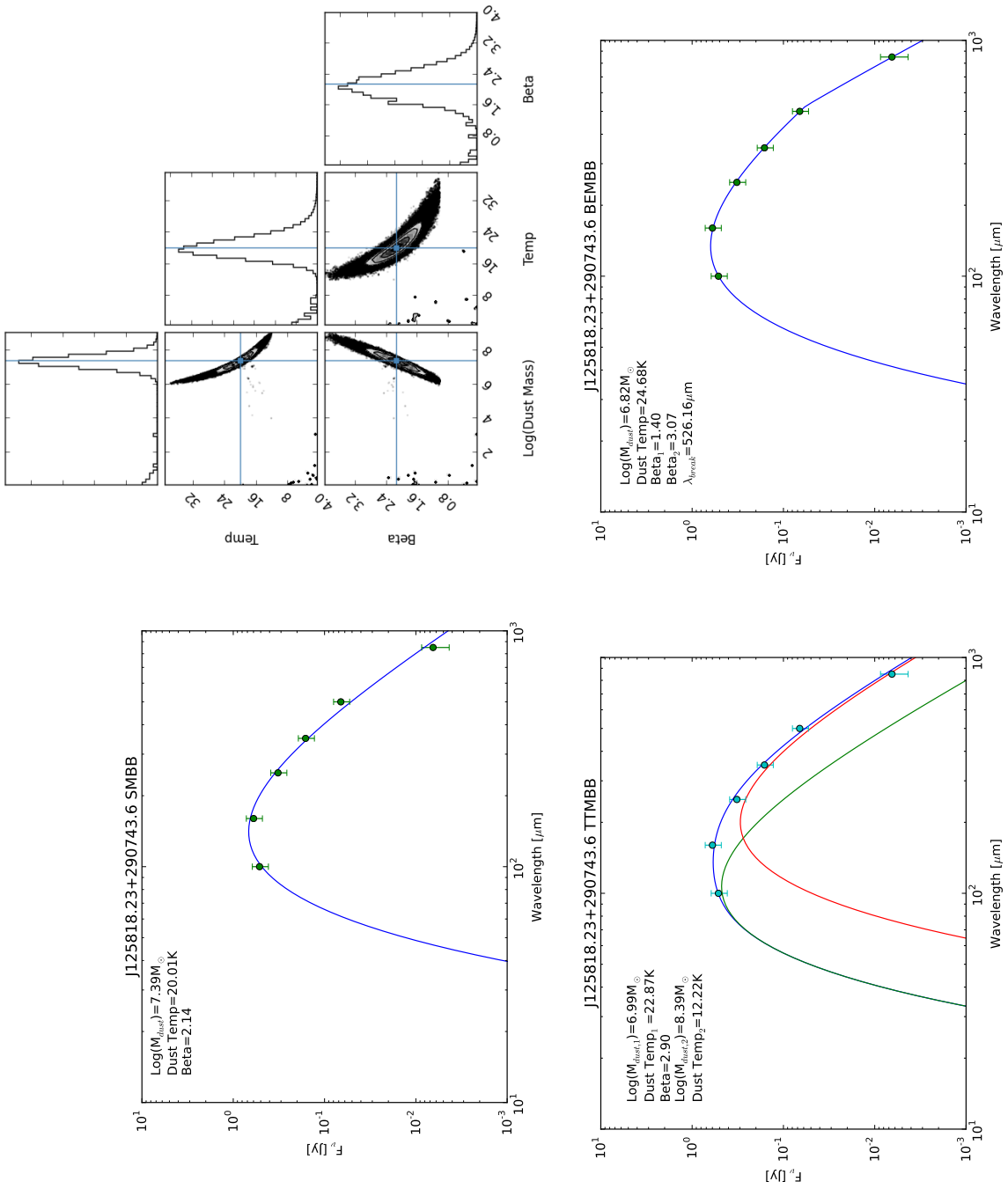

Figure 6.5. The same as Figure 6.4, for "J12581823+290743", where the dust parameters from the different dust models vary in a similar way to "J12561097+280947".

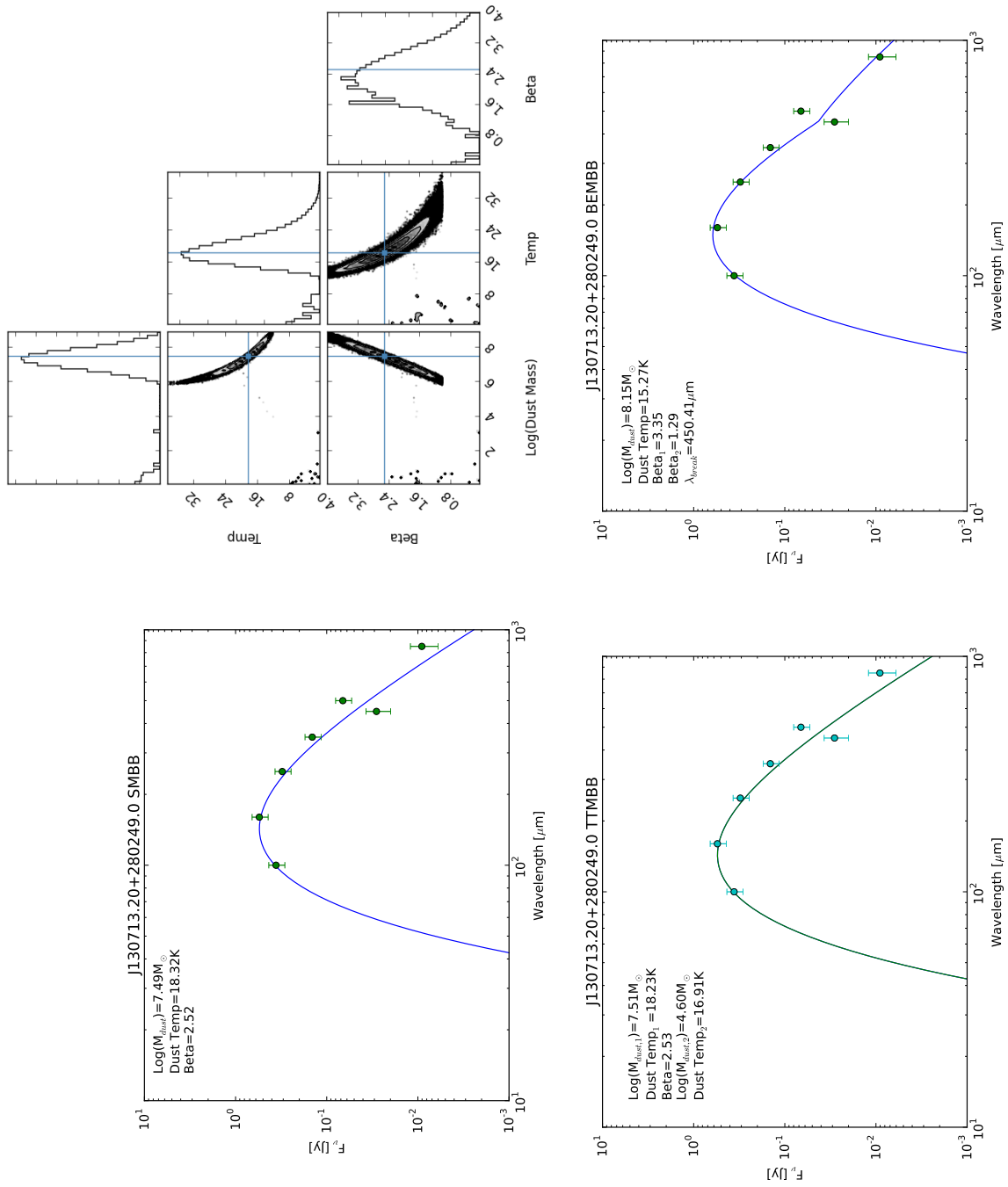

Figure 6.6. The same as Figure 6.4, for "J130713.20+280249.0", but now the dust properties using the SMBB and TTMBB models agree. Photometry can be an issue, as is observed, as **a)** Herschel 500μm fluxes can be blended/confused and lead to overestimated fluxes **b)** SCUBA-2's aggressive map filtering can lead to underestimated 450 and 850μm fluxes.

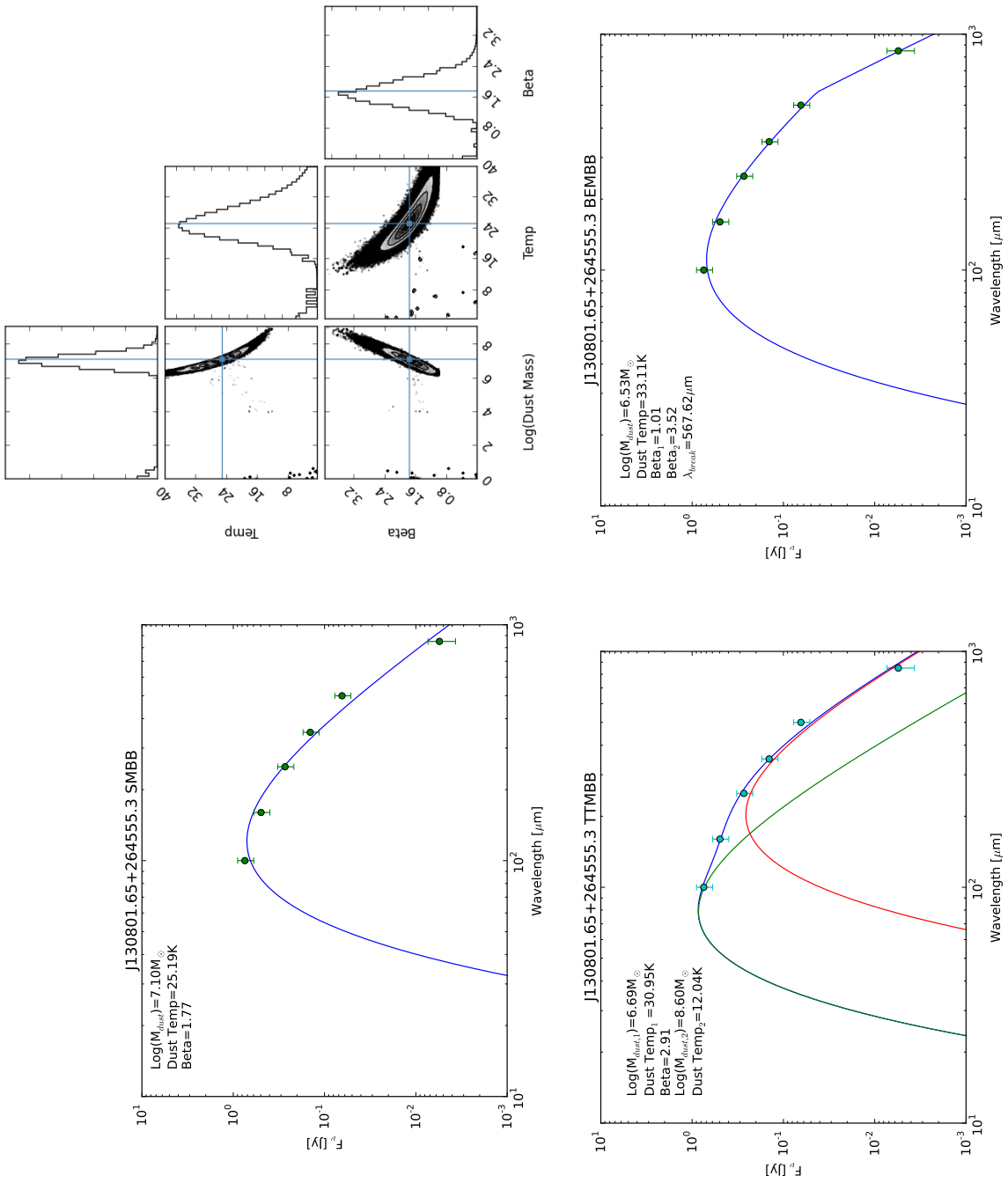

Figure 6.7. The same as Figure 6.4, for "J130801.65+264555.3", where the dust properties using the SMBB, BEMBB and TTMBB models don't agree, indicating the possible need for a new multi-temperature dust model.

acquired and fully reduced.

6.5 Summary & Conclusions

We present here the survey planning and the latest software development for the ongoing JINGLE survey, which aims to simultaneously quantify gas and dust content for a large sample of galaxies. The first results from JINGLE are presented, demonstrating the potential of the survey and highlighting the work carried out by this author. This author has:

- Carried out a machine learning task to predict the CO(1-0) fluxes for the JINGLE targets, using the xCOLD GASS sample as a training set, to estimate the possible 850μm flux contamination from the CO(3-2) line for a sample of nine galaxies. We find the average CO(3-2) contamination is 10.2%, with values ranging from 1%-33.3% in agreement with a handful of NGLS galaxies.

- Built a multi-dust model Bayesian SED fitting code to extract dust properties from the combination of Herschel and SCUBA-2 photometric data. We find the TTMBB model in most cases predicts higher dust masses due to the retrieval of a cold dust component, while the BEMBB and SMBB are not always in agreement.

The future acquisition of the full JINGLE 850μm flux measurements, HI and H_2 gas masses will allow us to investigate how quantities such as the dust temperature, emissivity and dust-to-gas ratio vary systematically across the galaxy population; refining an alternative method to quantify gas masses of galaxies. We shall also accurately constrain dust scaling relations, using different dust models, and investigate how effective dust is as an alternative gas tracer.

Chapter 7

Conclusions and Future Work

The equilibrium model was first postulated more than two decades ago (White & Frenk 1991), with its revival and subsequent re-formulation in the current decade (Davé et al. 2012; Lilly et al. 2013; Bouché et al. 2010). Throughout this time, astrophysicists have mounted substantial evidence supporting and strengthening its theoretical foundations. Advancements in instrumentation and technology allowed for CO observations to be pushed into the regime of normal star forming galaxies at high redshift (Tacconi et al. 2010) providing a huge breakthrough for the theory. However CO observations in the low mass and low metallicity regime, which allowed the theory to be further tested in extreme ISM conditions, alluded to a more efficient possible mode of star formation. Extremely low $\frac{L_{\rm CO}}{\rm SFR}$ ratios, an indirect measure of star formation efficiency, were observed, in contradiction with the proposed single mode of star formation, throwing the paradigm into question. These low metallicity and low mass galaxies therefore provide the perfect opportunity to test the equilibrium model and investigate divergences of the theoretical predictions from the observations. Furthermore, radiative transfer simulations suggested that CO photodissociation is enhanced in these low metallicity ISM environments and could explain the low $\frac{L_{\rm CO}}{\rm SFR}$ ratios. The degeneracy between enhanced star formation efficiency and CO photodissociation was however impossible to break. Several questions were being asked by the scientific community: How can we accurately trace the total molecular gas in sub-solar metallicity environments where photodissociation of CO occurs? Is there a fundamentally different star formation efficiency in these systems compared to their

high mass counterparts? This work has now answered these questions by formulating an accurate method to measure the molecular gas content in galaxies. This was followed by its application to CO observations to investigate molecular gas scaling laws and test the current paradigm, and then moving beyond using CO as a gas tracer.

7.1 Summary

The hypothesis here is that the equilibrium model does indeed hold in the low mass and low metallicity regime. While this extrapolation is warranted by observations of gas in massive galaxies, it has yet to be tested in this different regime. In this Thesis evidence was presented in strong support of this paradigm through a novel observational and modelling approach.

7.1.1 Where does a galaxy's [CII] come from?

To accurately measure molecular gas masses from low metallicity galaxies, using CO, one needs a tracer of the "dark CO" molecular gas. Theoretical radiative transfer predictions suggest that ionised carbon is one of the best tracers of this gas, as CO photodissociates easily into ionised carbon; we therefore aimed to use [CII] as a tracer of the dark molecular gas. However, [CII] can arise from all phases of the ISM, while we are only interested in the contribution to the total emission from molecular regions. To quantify how much of the total [CII] emission from a galaxy originates from the cold molecular ISM ($f_{\rm [CII],mol}$), under varying conditions, we built a new 3D multi-phase radiative transfer interface through the combination of STARBURST99, MOCASSIN and 3D-PDR. This interface was used to simulate a broad family of spherically-symmetric star-forming regions, across all phases of the interstellar medium, from ionised to molecular, where photoionisation and photochemistry dominates.

An analysis of the relations obtained between $f_{\rm [CII],mol}$ and the key input parameters of the multi-phase code for these star-forming regions showed that an increase in the strength of the UV radiation field (whether by increasing the current SFR or having a recent burst of star formation) leads to a decrease of $f_{\rm [CII],mol}$. Metallicity variations can lead to both an increase and a reduction of $f_{\rm [CII],mol}$ depending on other global parameters, as it can both affect the cooling rate and the level of photodissociation of the CO molecule.

To extend the analysis to the integrated [CII] emission from extragalactic objects, we

employed a Hierarchical Bayesian Inference method to identify the simulated clouds that are representative of the physical conditions in local star-forming galaxies, as found in the Herschel Reference Survey. This is possible under the assumption that the physical conditions found in a simulated star-forming cloud can represent the average conditions found on galaxy-wide scales for objects with similar physical properties such as metallicity, SSFR, and density.

We found that $f_{\rm [CII],mol}$ is best predicted using four key parameters: n_e, SSFR, dust mass fraction and metallicity (equation 3.8). We tested this prescription on the Milky Way and obtained an estimate that 75.9 ± 5.9% of its total [CII] emission arises from molecular regions, which is in very good agreement with observations of Pineda et al. (2013). Given that it is relatively rare for measurements of all four of these parameters to be available for large samples of galaxies, alternative prescriptions were provided which invoke fewer parameters. These other prescriptions (equations 3.9-3.12) also produce estimates for the Milky Way consistent with direct observations, although the uncertainty on $f_{\rm [CII],mol}$ increases as the number of parameters used to derive $f_{\rm [CII],mol}$ decreases. Of most practical use for many extragalactic studies is Equation 3.12 which relates $f_{\rm [CII],mol}$ to SSFR. Using this, it has now become possible to estimate the relative fraction of [CII] emerging from the molecular phase of the ISM when only galaxy-wide observations are available.

7.1.2 Deriving a multivariate α_{CO} conversion function.

Armed with the above prescriptions it became possible to proceed with observations of the [CII] and CO(1-0) emission lines, across a sample of low metallicity galaxies, aiming to use the luminosity ratio of these two lines to constrain variations on the conversion function, α_{CO}. Using a multi-wavelength suite of observations we here provided the first scaling relations for the integrated $L_{\rm [CII]}/L_{\rm CO(1\text{-}0)}$ ratio as a function of several galaxy parameters for a sample of low mass galaxies over 2 dex in $L_{\rm [CII]}/L_{\rm CO(1\text{-}0)}$.

We first found that the $L_{\rm [CII]}/L_{\rm CO(1\text{-}0)}$ ratio depends most strongly on parameters which describe the strength of the UV radiation field and the ability of the CO molecule to shield itself, via dust, from the UV radiation impinging on the surface of the molecular regions deep inside the PDR. A clear dependence on the colour (NUV-r) of the galaxies, specific star formation rate, UV field hardness, gas-phase metallicity and position off the main sequence, Δ(MS), was observed. The $\rm L_{[CII]}/L_{CO(1\text{-}0)}$ ratio does not depend strongly on large scale parameters which describe the masses and structural properties of

the galaxies.

From this we corrected for contaminant [CII] emission from non-molecular phases of the ISM, and then employed a Bayesian analysis to provide a parametrisation for the molecular region $L_{[\mathrm{CII}]}/L_{\mathrm{CO(1\text{-}0)}}$ ratio, using as few observables as possible. We found that the best fitting model involves two parameters: metallicity and Δ(MS). We used our parametrisation for $\mathrm{L_{[CII]}/L_{CO(1\text{-}0)}}$, alongside the aforementioned radiative transfer modelling, to present a novel conversion function which can be used to trace molecular gas masses in low metallicity ISM conditions.

7.1.3 Star formation efficiency and molecular gas fraction scaling laws

With the new conversion function it finally became possible to test the equilibrium model down to the low mass and low metallicity regime, uncharted territory until now. We applied our new prescription to the full xCOLD GASS sample and investigated gas scaling relations.

It was here observed, for the first time across a large sample, that molecular gas depletion times do not vary significantly with stellar mass. The lower $\mathrm{L_{CO}}$ to SFR ratios in low mass local galaxies are entirely due to photodissociation of CO, meaning that on average lower mass galaxies are equally efficient at forming stars than their high mass counterparts. We found a flattening of the molecular gas mass fraction against stellar mass, for $z \sim 0$, as stellar mass decreases in accordance with the equilibrium model, a consequence of the observed constant star formation efficiency.

7.1.4 Bridging low and high redshift molecular gas studies

We then proceeded to apply our new prescription to the high redshift PHIBSS1 sample to make a comparison across redshift. It was seen how depletion times change slowly with redshift, another prediction from the current paradigm, suggesting that the process of star formation on the main sequence is driven by similar physical mechanisms across cosmic time. The steep redshift dependence of the molecular gas fraction reflects the evolution of SFRs across cosmic time and the increased gas supply rate up to $z \sim 2$, rather than strong changes in star formation efficiency.

7.2 Future work

The equilibrium model has now been thoroughly tested in the local universe although at high redshift more work needs to be done. It is important to continue to test its predictions in lower metallicity galaxies at higher redshifts where ISM conditions become even more extreme. Low mass galaxies further out to z$\sim$1-2 provide excellent candidates to further test the theory. Also any galaxies at z$>$3 will be interesting to observe so that we can constrain where galaxies are out of equilibrium, and at what redshift the equilibrium model starts to break down.

Furthermore, unless for an extremely timely and fortuitous technological advancement in sub-mm CO observations, dust FIR continuum observations could become the most convenient way to probe the ISM at high redshift. This has become extremely popular of late, even though current measurements rely on single variable prescriptions for the dust-to-gas ratio. It is therefore crucial to turn our attention to simultaneously studying gas and dust in a sample of nearby galaxies to probe how accurate dust is as an ISM tracer, and how the gas-to-dust ratio varies as a function of multiple parameters. Furthermore, investigating how dust scaling relations change when different dust models are used is another important element when conducting dust studies. To answer such questions the JINGLE survey has commenced with the survey planning and software development presented here. We look forward to the acquisition of the JINGLE data to answer these questions, aiming to improve our tools with which we measure molecular gas masses. The results from this will have huge ramifications for high redshift ISM studies, with ALMA and NOEMA, aiming to further refine and test the equilibrium model.

Appendix A

Appendix A

A.1 Numerical modelling results

Below we present a table with the numerical results from the simulated star forming regions using the full multi-phase interface. The first column provides the fraction of [CII] emission arising from the molecular regions of each simulated cloud, $f_{[CII]\ mol}$, with the next six columns listing the free parameters used in the simulations; we only show the simulated results for clouds with a cosmic ray ionisation rate parameter equalling the Milky Way value. In columns 8 and 9 we present the results from the simulations used to obtain Figure 4.9.

$f_{[CII]\ mol}$ %	Metallicity [O/H]	Log M_* [$M_\odot$]	Log(Age) yrs	log SFR [$M_\odot\ yr^{-1}$]	Log(n_e) cm^{-3}	$\log M_{dust}/M_\odot$	α_{CO}	$([CII]/CO)_{mol}$
0.000	0.200	3.988	8.000	-7.500	1.500	-3.747	3.060e+08	0.000e+00
0.000	0.200	3.988	8.000	-7.500	1.500	-3.241	2.178e+07	0.000e+00
0.445	0.200	3.988	8.000	-7.500	1.500	-2.779	2.565e+05	4.318e+07
0.582	0.200	3.988	8.000	-7.500	1.500	-2.402	5.345e+03	1.273e+05
0.605	0.200	3.988	8.000	-7.500	1.500	-2.001	4.595e+02	3.052e+03
0.000	0.200	3.988	8.000	-7.500	2.000	-3.780	1.176e+07	0.000e+00
0.402	0.200	3.988	8.000	-7.500	2.000	-3.280	1.143e+05	4.239e+07
0.486	0.200	3.988	8.000	-7.500	2.000	-2.928	5.868e+02	2.993e+04
0.487	0.200	3.988	8.000	-7.500	2.000	-2.500	1.125e+02	1.425e+03
0.487	0.200	3.988	8.000	-7.500	2.000	-2.056	3.387e+01	1.370e+02
0.374	0.200	3.988	8.000	-7.500	2.500	-3.771	1.066e+05	1.937e+08
0.479	0.200	3.988	8.000	-7.500	2.500	-3.419	1.981e+02	3.184e+04
0.479	0.200	3.988	8.000	-7.500	2.500	-3.009	2.366e+01	9.198e+02
0.479	0.200	3.988	8.000	-7.500	2.500	-2.541	2.532e+00	2.881e+01
0.479	0.200	3.988	8.000	-7.500	2.500	-2.082	1.525e+00	5.771e+00
0.512	0.200	3.988	8.000	-7.500	3.000	-3.887	3.930e+02	2.044e+05
0.513	0.200	3.988	8.000	-7.500	3.000	-3.480	2.958e+00	3.088e+02
0.513	0.200	3.988	8.000	-7.500	3.000	-3.017	4.576e-01	1.357e+01
0.513	0.200	3.988	8.000	-7.500	3.000	-2.520	3.312e-01	2.948e+00

0.513	0.200	3.988	8.000	-7.500	3.000	-2.049	3.069e-01	9.059e-01
0.000	0.200	3.989	8.000	-6.500	1.500	-3.791	2.229e+08	0.000e+00
0.000	0.200	3.989	8.000	-6.500	1.500	-3.263	2.606e+07	0.000e+00
0.377	0.200	3.989	8.000	-6.500	1.500	-2.756	3.391e+05	7.560e+07
0.514	0.200	3.989	8.000	-6.500	1.500	-2.429	1.014e+04	3.394e+05
0.544	0.200	3.989	8.000	-6.500	1.500	-2.005	4.375e+02	3.421e+03
0.000	0.200	3.989	8.000	-6.500	2.000	-3.781	1.265e+07	0.000e+00
0.399	0.200	3.989	8.000	-6.500	2.000	-3.279	1.220e+05	4.821e+07
0.484	0.200	3.989	8.000	-6.500	2.000	-2.928	6.137e+02	3.236e+04
0.486	0.200	3.989	8.000	-6.500	2.000	-2.501	1.139e+02	1.486e+03
0.486	0.200	3.989	8.000	-6.500	2.000	-2.057	3.424e+01	1.423e+02
0.379	0.200	3.989	8.000	-6.500	2.500	-3.771	1.122e+05	2.192e+08
0.484	0.200	3.989	8.000	-6.500	2.500	-3.420	2.080e+02	3.443e+04
0.485	0.200	3.989	8.000	-6.500	2.500	-3.010	2.399e+01	9.573e+02
0.485	0.200	3.989	8.000	-6.500	2.500	-2.542	2.554e+00	2.979e+01
0.485	0.200	3.989	8.000	-6.500	2.500	-2.084	1.528e+00	5.927e+00
0.511	0.200	3.989	8.000	-6.500	3.000	-3.887	4.204e+02	2.248e+05
0.513	0.200	3.989	8.000	-6.500	3.000	-3.481	3.016e+00	3.216e+02
0.513	0.200	3.989	8.000	-6.500	3.000	-3.018	4.595e-01	1.390e+01
0.513	0.200	3.989	8.000	-6.500	3.000	-2.522	3.315e-01	3.009e+00
0.513	0.200	3.989	8.000	-6.500	3.000	-2.050	3.069e-01	9.238e-01
0.000	0.200	4.000	8.000	-5.500	1.500	-3.955	-NaN	-NaN
0.000	0.200	4.000	8.000	-5.500	1.500	-3.306	3.848e+07	0.000e+00
0.177	0.200	4.000	8.000	-5.500	1.500	-2.775	2.035e+06	2.037e+09
0.392	0.200	4.000	8.000	-5.500	1.500	-2.368	3.250e+04	2.231e+06
0.434	0.200	4.000	8.000	-5.500	1.500	-1.990	5.148e+02	7.291e+03
0.000	0.200	4.000	8.000	-5.500	2.000	-3.875	2.037e+07	0.000e+00
0.219	0.200	4.000	8.000	-5.500	2.000	-3.265	1.038e+06	3.017e+09
0.452	0.200	4.000	8.000	-5.500	2.000	-2.881	1.048e+04	1.721e+06
0.468	0.200	4.000	8.000	-5.500	2.000	-2.492	1.435e+02	4.372e+03
0.468	0.200	4.000	8.000	-5.500	2.000	-1.995	2.911e+01	2.206e+02
0.163	0.200	4.000	8.000	-5.500	2.500	-3.794	7.552e+05	6.632e+09
0.475	0.200	4.000	8.000	-5.500	2.500	-3.379	2.789e+03	9.539e+05
0.482	0.200	4.000	8.000	-5.500	2.500	-2.960	2.844e+01	1.660e+03
0.482	0.200	4.000	8.000	-5.500	2.500	-2.555	3.132e+00	5.906e+01
0.482	0.200	4.000	8.000	-5.500	2.500	-2.055	1.373e+00	7.583e+00
0.485	0.200	4.000	8.000	-5.500	3.000	-3.852	2.325e+04	4.190e+07
0.533	0.200	4.000	8.000	-5.500	3.000	-3.469	5.691e+00	1.126e+03
0.533	0.200	4.000	8.000	-5.500	3.000	-2.984	5.100e-01	2.347e+01
0.533	0.200	4.000	8.000	-5.500	3.000	-2.549	3.329e-01	5.165e+00
0.533	0.200	4.000	8.000	-5.500	3.000	-2.031	2.960e-01	1.347e+00
0.234	0.200	3.987	8.500	-7.500	1.500	-3.745	2.998e+06	5.000e+09
0.589	0.200	3.987	8.500	-7.500	1.500	-3.304	1.029e+05	2.711e+07
0.720	0.200	3.987	8.500	-7.500	1.500	-2.895	6.889e+03	2.456e+05
0.742	0.200	3.987	8.500	-7.500	1.500	-2.489	3.375e+02	3.238e+03
0.744	0.200	3.987	8.500	-7.500	1.500	-2.062	1.405e+02	4.351e+02
0.607	0.200	3.987	8.500	-7.500	2.000	-3.794	1.245e+05	1.297e+08
0.736	0.200	3.987	8.500	-7.500	2.000	-3.402	3.321e+03	3.928e+05
0.744	0.200	3.987	8.500	-7.500	2.000	-2.963	8.164e+01	2.045e+03
0.744	0.200	3.987	8.500	-7.500	2.000	-2.513	2.529e+01	1.917e+02
0.744	0.200	3.987	8.500	-7.500	2.000	-2.069	1.164e+01	3.017e+01
0.770	0.200	3.987	8.500	-7.500	2.500	-3.897	6.260e+03	3.102e+06
0.786	0.200	3.987	8.500	-7.500	2.500	-3.494	1.895e+01	1.800e+03
0.786	0.200	3.987	8.500	-7.500	2.500	-3.010	2.367e+00	5.808e+01
0.786	0.200	3.987	8.500	-7.500	2.500	-2.543	8.697e-01	6.823e+00
0.786	0.200	3.987	8.500	-7.500	2.500	-2.094	7.165e-01	1.955e+00
0.786	0.200	3.987	8.500	-7.500	3.000	-3.947	1.040e+01	2.701e+03

0.786	0.200	3.987	8.500	-7.500	3.000	-3.524	6.127e-01	4.381e+01
0.786	0.200	3.987	8.500	-7.500	3.000	-3.004	2.948e-01	5.700e+00
0.786	0.200	3.987	8.500	-7.500	3.000	-2.519	2.586e-01	1.589e+00
0.786	0.200	3.987	8.500	-7.500	3.000	-2.058	2.492e-01	5.259e-01
0.062	0.200	3.989	8.500	-6.500	1.500	-3.812	2.612e+06	4.691e+09
0.464	0.200	3.989	8.500	-6.500	1.500	-3.300	2.647e+05	1.306e+08
0.634	0.200	3.989	8.500	-6.500	1.500	-2.875	1.011e+04	5.520e+05
0.661	0.200	3.989	8.500	-6.500	1.500	-2.482	3.121e+02	4.311e+03
0.662	0.200	3.989	8.500	-6.500	1.500	-2.029	1.081e+02	4.352e+02
0.501	0.200	3.989	8.500	-6.500	2.000	-3.791	1.732e+05	2.501e+08
0.658	0.200	3.989	8.500	-6.500	2.000	-3.398	4.711e+03	6.614e+05
0.670	0.200	3.989	8.500	-6.500	2.000	-2.969	8.368e+01	2.413e+03
0.670	0.200	3.989	8.500	-6.500	2.000	-2.525	2.679e+01	2.329e+02
0.670	0.200	3.989	8.500	-6.500	2.000	-2.083	1.144e+01	3.408e+01
0.745	0.200	3.989	8.500	-6.500	2.500	-3.862	5.486e+03	2.771e+06
0.758	0.200	3.989	8.500	-6.500	2.500	-3.450	1.530e+01	1.447e+03
0.758	0.200	3.989	8.500	-6.500	2.500	-3.027	2.458e+00	7.098e+01
0.758	0.200	3.989	8.500	-6.500	2.500	-2.567	8.267e-01	7.706e+00
0.758	0.200	3.989	8.500	-6.500	2.500	-2.028	6.585e-01	1.727e+00
0.744	0.200	3.989	8.500	-6.500	3.000	-3.943	1.368e+01	4.018e+03
0.744	0.200	3.989	8.500	-6.500	3.000	-3.524	6.448e-01	5.127e+01
0.744	0.200	3.989	8.500	-6.500	3.000	-3.006	2.972e-01	6.359e+00
0.744	0.200	3.989	8.500	-6.500	3.000	-2.521	2.591e-01	1.760e+00
0.744	0.200	3.989	8.500	-6.500	3.000	-2.061	2.494e-01	5.815e-01
0.000	0.200	4.021	8.500	-5.500	1.500	-3.977	-NaN	-NaN
0.060	0.200	4.021	8.500	-5.500	1.500	-3.307	2.810e+06	5.666e+09
0.368	0.200	4.021	8.500	-5.500	1.500	-2.781	1.303e+05	3.372e+07
0.468	0.200	4.021	8.500	-5.500	1.500	-2.424	2.208e+03	8.714e+04
0.474	0.200	4.021	8.500	-5.500	1.500	-2.029	2.172e+02	2.276e+03
0.000	0.200	4.021	8.500	-5.500	2.000	-3.876	2.161e+06	0.000e+00
0.435	0.200	4.021	8.500	-5.500	2.000	-3.286	1.024e+05	9.481e+07
0.546	0.200	4.021	8.500	-5.500	2.000	-2.936	1.131e+03	1.214e+05
0.549	0.200	4.021	8.500	-5.500	2.000	-2.468	6.245e+01	1.321e+03
0.549	0.200	4.021	8.500	-5.500	2.000	-2.036	1.455e+01	9.985e+01
0.449	0.200	4.021	8.500	-5.500	2.500	-3.805	7.744e+04	2.424e+08
0.589	0.200	4.021	8.500	-5.500	2.500	-3.427	2.899e+02	6.915e+04
0.590	0.200	4.021	8.500	-5.500	2.500	-2.993	1.080e+01	5.590e+02
0.590	0.200	4.021	8.500	-5.500	2.500	-2.515	1.215e+00	1.799e+01
0.590	0.200	4.021	8.500	-5.500	2.500	-2.012	8.302e-01	3.680e+00
0.579	0.200	4.021	8.500	-5.500	3.000	-3.913	7.714e+01	3.144e+04
0.580	0.200	4.021	8.500	-5.500	3.000	-3.491	1.339e+00	1.227e+02
0.580	0.200	4.021	8.500	-5.500	3.000	-3.022	3.759e-01	1.006e+01
0.580	0.200	4.021	8.500	-5.500	3.000	-2.526	2.993e-01	2.434e+00
0.580	0.200	4.021	8.500	-5.500	3.000	-2.055	2.825e-01	7.664e-01
0.623	0.200	3.984	9.000	-7.500	1.500	-3.834	3.445e+04	3.623e+06
0.751	0.200	3.984	9.000	-7.500	1.500	-3.451	4.808e+03	1.635e+05
0.779	0.200	3.984	9.000	-7.500	1.500	-2.977	1.760e+02	1.562e+03
0.780	0.200	3.984	9.000	-7.500	1.500	-2.555	7.009e+01	2.109e+02
0.780	0.200	3.984	9.000	-7.500	1.500	-2.048	2.813e+01	2.525e+01
0.824	0.200	3.984	9.000	-7.500	2.000	-3.914	1.071e+03	8.430e+04
0.828	0.200	3.984	9.000	-7.500	2.000	-3.519	4.333e+01	1.008e+03
0.828	0.200	3.984	9.000	-7.500	2.000	-2.996	1.361e+01	8.308e+01
0.828	0.200	3.984	9.000	-7.500	2.000	-2.552	6.197e+00	1.316e+01
0.828	0.200	3.984	9.000	-7.500	2.000	-2.062	4.938e+00	3.345e+00
0.880	0.200	3.984	9.000	-7.500	2.500	-3.979	1.226e+01	8.288e+02
0.880	0.200	3.984	9.000	-7.500	2.500	-3.550	1.807e+00	3.941e+01
0.880	0.200	3.984	9.000	-7.500	2.500	-3.009	5.870e-01	3.488e+00

0.880	0.200	3.984	9.000	-7.500	2.500	-2.559	4.893e-01	1.017e+00
0.880	0.200	3.984	9.000	-7.500	2.500	-2.065	4.613e-01	3.059e-01
0.883	0.200	3.984	9.000	-7.500	3.000	-3.991	4.681e-01	2.449e+01
0.883	0.200	3.984	9.000	-7.500	3.000	-3.533	2.711e-01	4.619e+00
0.883	0.200	3.984	9.000	-7.500	3.000	-3.056	2.360e-01	1.311e+00
0.883	0.200	3.984	9.000	-7.500	3.000	-2.507	2.258e-01	3.513e-01
0.883	0.200	3.984	9.000	-7.500	3.000	-2.107	2.236e-01	1.382e-01
0.250	0.200	3.993	9.000	-6.500	1.500	-3.809	1.436e+05	6.546e+07
0.494	0.200	3.993	9.000	-6.500	1.500	-3.367	3.109e+04	2.852e+06
0.593	0.200	3.993	9.000	-6.500	1.500	-2.950	9.569e+02	2.181e+04
0.600	0.200	3.993	9.000	-6.500	1.500	-2.539	1.252e+02	8.757e+02
0.600	0.200	3.993	9.000	-6.500	1.500	-2.007	4.116e+01	7.630e+01
0.629	0.200	3.993	9.000	-6.500	2.000	-3.856	1.961e+04	5.520e+06
0.696	0.200	3.993	9.000	-6.500	2.000	-3.475	3.612e+02	2.353e+04
0.697	0.200	3.993	9.000	-6.500	2.000	-3.035	3.256e+01	5.702e+02
0.697	0.200	3.993	9.000	-6.500	2.000	-2.523	7.444e+00	3.628e+01
0.697	0.200	3.993	9.000	-6.500	2.000	-2.089	4.838e+00	8.457e+00
0.781	0.200	3.993	9.000	-6.500	2.500	-3.952	6.430e+02	1.422e+05
0.784	0.200	3.993	9.000	-6.500	2.500	-3.478	6.310e+00	3.062e+02
0.784	0.200	3.993	9.000	-6.500	2.500	-3.057	8.783e-01	1.446e+01
0.784	0.200	3.993	9.000	-6.500	2.500	-2.530	5.048e-01	2.362e+00
0.784	0.200	3.993	9.000	-6.500	2.500	-2.089	4.553e-01	7.643e-01
0.774	0.200	3.993	9.000	-6.500	3.000	-4.010	8.054e-01	7.795e+01
0.774	0.200	3.993	9.000	-6.500	3.000	-3.553	3.221e-01	9.705e+00
0.774	0.200	3.993	9.000	-6.500	3.000	-3.071	2.576e-01	2.465e+00
0.774	0.200	3.993	9.000	-6.500	3.000	-2.516	2.413e-01	6.343e-01
0.774	0.200	3.993	9.000	-6.500	3.000	-2.008	2.374e-01	1.931e-01
0.000	0.200	4.079	9.000	-5.500	1.500	-3.992	5.401e+06	0.000e+00
0.134	0.200	4.079	9.000	-5.500	1.500	-3.298	1.320e+06	2.288e+09
0.383	0.200	4.079	9.000	-5.500	1.500	-2.813	4.678e+04	7.371e+06
0.459	0.200	4.079	9.000	-5.500	1.500	-2.438	9.129e+02	2.560e+04
0.462	0.200	4.079	9.000	-5.500	1.500	-2.016	1.716e+02	1.299e+03
0.075	0.200	4.079	9.000	-5.500	2.000	-3.862	9.680e+05	5.588e+09
0.492	0.200	4.079	9.000	-5.500	2.000	-3.328	5.199e+04	2.880e+07
0.568	0.200	4.079	9.000	-5.500	2.000	-2.928	2.352e+02	1.631e+04
0.569	0.200	4.079	9.000	-5.500	2.000	-2.484	4.189e+01	7.256e+02
0.569	0.200	4.079	9.000	-5.500	2.000	-2.043	1.102e+01	6.227e+01
0.558	0.200	4.079	9.000	-5.500	2.500	-3.816	3.610e+04	5.405e+07
0.632	0.200	4.079	9.000	-5.500	2.500	-3.461	9.931e+01	1.881e+04
0.632	0.200	4.079	9.000	-5.500	2.500	-3.005	6.104e+00	2.634e+02
0.632	0.200	4.079	9.000	-5.500	2.500	-2.514	9.947e-01	1.227e+01
0.632	0.200	4.079	9.000	-5.500	2.500	-2.002	7.508e-01	2.744e+00
0.625	0.200	4.079	9.000	-5.500	3.000	-3.947	2.106e+01	6.939e+03
0.625	0.200	4.079	9.000	-5.500	3.000	-3.504	8.485e-01	6.574e+01
0.625	0.200	4.079	9.000	-5.500	3.000	-3.023	3.401e-01	7.684e+00
0.625	0.200	4.079	9.000	-5.500	3.000	-2.518	2.860e-01	1.944e+00
0.625	0.200	4.079	9.000	-5.500	3.000	-2.042	2.735e-01	6.147e-01
0.000	0.500	3.988	8.000	-7.500	1.500	-3.813	1.285e+07	0.000e+00
0.200	0.500	3.988	8.000	-7.500	1.500	-3.266	7.213e+06	3.975e+10
0.593	0.500	3.988	8.000	-7.500	1.500	-2.803	1.537e+05	1.402e+08
0.747	0.500	3.988	8.000	-7.500	1.500	-2.388	1.894e+04	2.848e+06
0.779	0.500	3.988	8.000	-7.500	1.500	-2.012	1.022e+03	4.937e+04
0.042	0.500	3.988	8.000	-7.500	2.000	-3.795	7.567e+06	8.071e+10
0.510	0.500	3.988	8.000	-7.500	2.000	-3.281	1.260e+05	3.676e+08
0.665	0.500	3.988	8.000	-7.500	2.000	-2.911	8.674e+03	4.141e+06
0.684	0.500	3.988	8.000	-7.500	2.000	-2.531	1.288e+02	1.737e+04
0.684	0.500	3.988	8.000	-7.500	2.000	-2.035	3.363e+01	1.211e+03

0.381	0.500	3.988	8.000	-7.500	2.500	-3.820	1.947e+05	2.990e+09
0.642	0.500	3.988	8.000	-7.500	2.500	-3.407	6.751e+03	1.021e+07
0.665	0.500	3.988	8.000	-7.500	2.500	-3.008	1.804e+01	6.497e+03
0.665	0.500	3.988	8.000	-7.500	2.500	-2.510	8.286e-01	7.765e+01
0.665	0.500	3.988	8.000	-7.500	2.500	-2.076	3.084e-01	1.011e+01
0.564	0.500	3.988	8.000	-7.500	3.000	-3.902	3.278e+03	7.855e+06
0.584	0.500	3.988	8.000	-7.500	3.000	-3.463	8.560e-01	4.230e+02
0.584	0.500	3.988	8.000	-7.500	3.000	-3.043	1.902e-01	3.046e+01
0.584	0.500	3.988	8.000	-7.500	3.000	-2.531	1.288e-01	5.961e+00
0.584	0.500	3.988	8.000	-7.500	3.000	-2.047	1.176e-01	1.757e+00
0.000	0.500	3.989	8.000	-6.500	1.500	-3.779	1.812e+08	0.000e+00
0.185	0.500	3.989	8.000	-6.500	1.500	-3.275	7.967e+06	4.736e+10
0.570	0.500	3.989	8.000	-6.500	1.500	-2.816	1.519e+05	1.518e+08
0.729	0.500	3.989	8.000	-6.500	1.500	-2.406	2.004e+04	3.257e+06
0.763	0.500	3.989	8.000	-6.500	1.500	-2.035	1.071e+03	5.598e+04
0.000	0.500	3.989	8.000	-6.500	2.000	-3.794	8.846e+06	0.000e+00
0.466	0.500	3.989	8.000	-6.500	2.000	-3.276	1.403e+05	4.121e+08
0.631	0.500	3.989	8.000	-6.500	2.000	-2.903	9.123e+03	4.285e+06
0.652	0.500	3.989	8.000	-6.500	2.000	-2.521	1.355e+02	1.784e+04
0.652	0.500	3.989	8.000	-6.500	2.000	-2.023	3.550e+01	1.238e+03
0.354	0.500	3.989	8.000	-6.500	2.500	-3.821	2.097e+05	3.313e+09
0.624	0.500	3.989	8.000	-6.500	2.500	-3.407	7.055e+03	1.080e+07
0.648	0.500	3.989	8.000	-6.500	2.500	-3.009	1.852e+01	6.726e+03
0.648	0.500	3.989	8.000	-6.500	2.500	-2.511	8.426e-01	7.945e+01
0.648	0.500	3.989	8.000	-6.500	2.500	-2.077	3.097e-01	1.021e+01
0.463	0.500	3.989	8.000	-6.500	3.000	-3.876	1.929e+04	7.363e+07
0.542	0.500	3.989	8.000	-6.500	3.000	-3.489	7.523e+00	6.157e+03
0.542	0.500	3.989	8.000	-6.500	3.000	-3.038	1.949e-01	4.338e+01
0.542	0.500	3.989	8.000	-6.500	3.000	-2.511	1.225e-01	7.438e+00
0.542	0.500	3.989	8.000	-6.500	3.000	-2.066	1.117e-01	2.381e+00
0.000	0.500	3.999	8.000	-5.500	1.500	-3.952	-NaN	-NaN
0.000	0.500	3.999	8.000	-5.500	1.500	-3.298	9.910e+06	0.000e+00
0.327	0.500	3.999	8.000	-5.500	1.500	-2.797	4.340e+05	1.043e+09
0.549	0.500	3.999	8.000	-5.500	1.500	-2.374	3.100e+04	9.089e+06
0.613	0.500	3.999	8.000	-5.500	1.500	-1.956	1.115e+03	7.877e+04
0.000	0.500	3.999	8.000	-5.500	2.000	-3.872	1.997e+07	0.000e+00
0.378	0.500	3.999	8.000	-5.500	2.000	-3.290	3.907e+05	3.033e+09
0.618	0.500	3.999	8.000	-5.500	2.000	-2.885	2.181e+04	1.752e+07
0.660	0.500	3.999	8.000	-5.500	2.000	-2.453	1.445e+02	2.403e+04
0.660	0.500	3.999	8.000	-5.500	2.000	-1.998	3.529e+01	1.686e+03
0.295	0.500	3.999	8.000	-5.500	2.500	-3.786	3.422e+05	6.629e+09
0.575	0.500	3.999	8.000	-5.500	2.500	-3.393	1.160e+04	2.038e+07
0.608	0.500	3.999	8.000	-5.500	2.500	-2.999	2.549e+01	9.992e+03
0.608	0.500	3.999	8.000	-5.500	2.500	-2.500	1.108e+00	1.096e+02
0.608	0.500	3.999	8.000	-5.500	2.500	-2.064	3.355e-01	1.147e+01
0.395	0.500	3.999	8.000	-5.500	3.000	-3.866	3.034e+04	1.418e+08
0.489	0.500	3.999	8.000	-5.500	3.000	-3.487	1.040e+01	9.534e+03
0.489	0.500	3.999	8.000	-5.500	3.000	-3.038	2.036e-01	4.936e+01
0.489	0.500	3.999	8.000	-5.500	3.000	-2.509	1.245e-01	8.132e+00
0.489	0.500	3.999	8.000	-5.500	3.000	-2.063	1.129e-01	2.574e+00
0.453	0.500	3.986	8.500	-7.500	1.500	-3.766	5.774e+05	1.892e+09
0.719	0.500	3.986	8.500	-7.500	1.500	-3.324	5.753e+04	3.282e+07
0.822	0.500	3.986	8.500	-7.500	1.500	-2.936	1.577e+04	2.410e+06
0.853	0.500	3.986	8.500	-7.500	1.500	-2.501	8.450e+02	3.967e+04
0.855	0.500	3.986	8.500	-7.500	1.500	-2.056	1.677e+02	2.506e+03
0.683	0.500	3.986	8.500	-7.500	2.000	-3.840	5.428e+04	1.224e+08
0.815	0.500	3.986	8.500	-7.500	2.000	-3.414	7.094e+03	3.406e+06

0.834	0.500	3.986	8.500	-7.500	2.000	-2.991	1.241e+02	1.705e+04
0.835	0.500	3.986	8.500	-7.500	2.000	-2.517	2.132e+01	8.544e+02
0.835	0.500	3.986	8.500	-7.500	2.000	-2.056	2.524e+00	3.346e+01
0.625	0.500	3.986	8.500	-7.500	2.500	-3.921	1.003e+04	1.779e+07
0.728	0.500	3.986	8.500	-7.500	2.500	-3.508	1.441e+02	7.896e+04
0.729	0.500	3.986	8.500	-7.500	2.500	-3.037	8.361e-01	1.241e+02
0.729	0.500	3.986	8.500	-7.500	2.500	-2.549	2.233e-01	1.006e+01
0.729	0.500	3.986	8.500	-7.500	2.500	-2.045	1.685e-01	2.324e+00
0.774	0.500	3.986	8.500	-7.500	3.000	-4.001	6.635e+00	4.058e+03
0.774	0.500	3.986	8.500	-7.500	3.000	-3.501	2.022e-01	3.278e+01
0.774	0.500	3.986	8.500	-7.500	3.000	-3.068	1.330e-01	7.593e+00
0.774	0.500	3.986	8.500	-7.500	3.000	-2.584	1.160e-01	2.137e+00
0.774	0.500	3.986	8.500	-7.500	3.000	-2.063	1.114e-01	6.142e-01
0.206	0.500	3.989	8.500	-6.500	1.500	-3.806	8.161e+05	3.858e+09
0.516	0.500	3.989	8.500	-6.500	1.500	-3.332	6.585e+04	5.772e+07
0.688	0.500	3.989	8.500	-6.500	1.500	-2.917	1.753e+04	3.609e+06
0.741	0.500	3.989	8.500	-6.500	1.500	-2.479	8.222e+02	4.963e+04
0.743	0.500	3.989	8.500	-6.500	1.500	-1.989	1.392e+02	2.348e+03
0.541	0.500	3.989	8.500	-6.500	2.000	-3.824	5.103e+04	1.469e+08
0.747	0.500	3.989	8.500	-6.500	2.000	-3.416	1.196e+04	8.447e+06
0.791	0.500	3.989	8.500	-6.500	2.000	-2.981	1.832e+02	3.512e+04
0.791	0.500	3.989	8.500	-6.500	2.000	-2.504	2.036e+01	1.097e+03
0.791	0.500	3.989	8.500	-6.500	2.000	-2.000	1.365e+00	2.178e+01
0.690	0.500	3.989	8.500	-6.500	2.500	-3.904	8.986e+03	1.531e+07
0.736	0.500	3.989	8.500	-6.500	2.500	-3.500	5.500e+01	2.570e+04
0.736	0.500	3.989	8.500	-6.500	2.500	-3.050	9.411e-01	1.292e+02
0.736	0.500	3.989	8.500	-6.500	2.500	-2.566	2.708e-01	1.147e+01
0.736	0.500	3.989	8.500	-6.500	2.500	-2.006	1.937e-01	2.211e+00
0.717	0.500	3.989	8.500	-6.500	3.000	-4.013	7.368e+00	5.092e+03
0.717	0.500	3.989	8.500	-6.500	3.000	-3.523	1.994e-01	3.671e+01
0.717	0.500	3.989	8.500	-6.500	3.000	-3.002	1.257e-01	6.599e+00
0.717	0.500	3.989	8.500	-6.500	3.000	-2.514	1.127e-01	1.890e+00
0.717	0.500	3.989	8.500	-6.500	3.000	-2.097	1.094e-01	6.991e-01
0.000	0.500	4.017	8.500	-5.500	1.500	-3.970	-NaN	-NaN
0.169	0.500	4.017	8.500	-5.500	1.500	-3.301	5.946e+05	2.508e+09
0.423	0.500	4.017	8.500	-5.500	1.500	-2.814	4.425e+04	2.669e+07
0.544	0.500	4.017	8.500	-5.500	1.500	-2.457	9.886e+03	1.671e+06
0.570	0.500	4.017	8.500	-5.500	1.500	-2.022	2.751e+02	1.294e+04
0.111	0.500	4.017	8.500	-5.500	2.000	-3.873	8.389e+05	1.693e+10
0.505	0.500	4.017	8.500	-5.500	2.000	-3.338	4.821e+04	1.030e+08
0.644	0.500	4.017	8.500	-5.500	2.000	-2.959	3.802e+03	1.809e+06
0.657	0.500	4.017	8.500	-5.500	2.000	-2.509	4.408e+01	5.225e+03
0.657	0.500	4.017	8.500	-5.500	2.000	-2.058	7.894e+00	2.942e+02
0.435	0.500	4.017	8.500	-5.500	2.500	-3.852	5.484e+04	3.333e+08
0.623	0.500	4.017	8.500	-5.500	2.500	-3.452	1.398e+03	1.499e+06
0.631	0.500	4.017	8.500	-5.500	2.500	-2.976	3.544e+00	8.446e+02
0.631	0.500	4.017	8.500	-5.500	2.500	-2.541	4.145e-01	3.252e+01
0.631	0.500	4.017	8.500	-5.500	2.500	-2.021	2.222e-01	5.042e+00
0.470	0.500	4.017	8.500	-5.500	3.000	-3.919	4.642e+03	1.142e+07
0.512	0.500	4.017	8.500	-5.500	3.000	-3.512	1.047e+00	6.184e+02
0.512	0.500	4.017	8.500	-5.500	3.000	-3.058	1.464e-01	2.515e+01
0.512	0.500	4.017	8.500	-5.500	3.000	-2.538	1.095e-01	5.329e+00
0.512	0.500	4.017	8.500	-5.500	3.000	-2.007	1.023e-01	1.436e+00
0.588	0.500	3.984	9.000	-7.500	1.500	-3.921	1.507e+04	3.806e+06
0.737	0.500	3.984	9.000	-7.500	1.500	-3.498	4.776e+03	5.395e+05
0.782	0.500	3.984	9.000	-7.500	1.500	-3.034	2.712e+02	1.070e+04
0.783	0.500	3.984	9.000	-7.500	1.500	-2.508	5.348e+01	5.804e+02

0.783	0.500	3.984	9.000	-7.500	1.500	-2.065	1.685e+01	6.439e+01
0.862	0.500	3.984	9.000	-7.500	2.000	-3.961	1.589e+03	5.068e+05
0.874	0.500	3.984	9.000	-7.500	2.000	-3.528	4.957e+01	5.222e+03
0.874	0.500	3.984	9.000	-7.500	2.000	-3.062	6.786e+00	2.254e+02
0.874	0.500	3.984	9.000	-7.500	2.000	-2.515	7.332e-01	6.723e+00
0.874	0.500	3.984	9.000	-7.500	2.000	-2.012	4.508e-01	1.288e+00
0.827	0.500	3.984	9.000	-7.500	2.500	-3.990	2.084e+01	5.945e+03
0.827	0.500	3.984	9.000	-7.500	2.500	-3.526	4.894e-01	4.344e+01
0.827	0.500	3.984	9.000	-7.500	2.500	-3.040	1.935e-01	5.425e+00
0.827	0.500	3.984	9.000	-7.500	2.500	-2.579	1.566e-01	1.501e+00
0.827	0.500	3.984	9.000	-7.500	2.500	-2.076	1.470e-01	4.410e-01
0.778	0.500	3.984	9.000	-7.500	3.000	-4.002	1.928e-01	3.620e+01
0.778	0.500	3.984	9.000	-7.500	3.000	-3.520	1.062e-01	6.239e+00
0.778	0.500	3.984	9.000	-7.500	3.000	-3.022	9.394e-02	1.727e+00
0.778	0.500	3.984	9.000	-7.500	3.000	-2.554	9.101e-02	5.660e-01
0.778	0.500	3.984	9.000	-7.500	3.000	-2.046	9.002e-02	1.735e-01
0.265	0.500	3.992	9.000	-6.500	1.500	-3.858	2.693e+04	1.533e+07
0.503	0.500	3.992	9.000	-6.500	1.500	-3.415	1.321e+04	2.859e+06
0.612	0.500	3.992	9.000	-6.500	1.500	-2.989	1.424e+03	1.189e+05
0.626	0.500	3.992	9.000	-6.500	1.500	-2.542	8.873e+01	2.379e+03
0.626	0.500	3.992	9.000	-6.500	1.500	-2.065	3.287e+01	2.780e+02
0.624	0.500	3.992	9.000	-6.500	2.000	-3.905	1.028e+04	7.092e+06
0.715	0.500	3.992	9.000	-6.500	2.000	-3.463	3.946e+02	9.074e+04
0.718	0.500	3.992	9.000	-6.500	2.000	-3.035	1.444e+01	1.069e+03
0.718	0.500	3.992	9.000	-6.500	2.000	-2.576	1.760e+00	4.267e+01
0.718	0.500	3.992	9.000	-6.500	2.000	-2.039	5.139e-01	3.537e+00
0.714	0.500	3.992	9.000	-6.500	2.500	-3.977	6.161e+02	4.418e+05
0.727	0.500	3.992	9.000	-6.500	2.500	-3.507	2.056e+00	4.114e+02
0.727	0.500	3.992	9.000	-6.500	2.500	-3.063	2.477e-01	1.655e+01
0.727	0.500	3.992	9.000	-6.500	2.500	-2.514	1.534e-01	2.812e+00
0.727	0.500	3.992	9.000	-6.500	2.500	-2.061	1.397e-01	8.952e-01
0.572	0.500	3.992	9.000	-6.500	3.000	-4.009	3.917e+00	1.801e+03
0.572	0.500	3.992	9.000	-6.500	3.000	-3.512	1.304e-01	1.624e+01
0.572	0.500	3.992	9.000	-6.500	3.000	-3.052	9.746e-02	4.023e+00
0.572	0.500	3.992	9.000	-6.500	3.000	-2.576	9.049e-02	1.228e+00
0.572	0.500	3.992	9.000	-6.500	3.000	-2.027	8.829e-02	3.370e-01
0.000	0.500	4.064	9.000	-5.500	1.500	-3.999	4.540e+06	0.000e+00
0.189	0.500	4.064	9.000	-5.500	1.500	-3.329	1.857e+05	4.120e+08
0.421	0.500	4.064	9.000	-5.500	1.500	-2.861	2.746e+04	1.096e+07
0.519	0.500	4.064	9.000	-5.500	1.500	-2.493	3.917e+03	4.966e+05
0.533	0.500	4.064	9.000	-5.500	1.500	-2.043	1.652e+02	5.930e+03
0.198	0.500	4.064	9.000	-5.500	2.000	-3.855	2.263e+05	2.090e+09
0.531	0.500	4.064	9.000	-5.500	2.000	-3.382	2.779e+04	3.789e+07
0.645	0.500	4.064	9.000	-5.500	2.000	-2.940	6.705e+02	2.027e+05
0.648	0.500	4.064	9.000	-5.500	2.000	-2.523	3.085e+01	2.797e+03
0.648	0.500	4.064	9.000	-5.500	2.000	-2.065	2.956e+00	8.538e+01
0.539	0.500	4.064	9.000	-5.500	2.500	-3.866	2.745e+04	9.181e+07
0.664	0.500	4.064	9.000	-5.500	2.500	-3.480	4.076e+02	3.277e+05
0.666	0.500	4.064	9.000	-5.500	2.500	-2.983	1.667e+00	3.073e+02
0.666	0.500	4.064	9.000	-5.500	2.500	-2.539	3.088e-01	1.884e+01
0.666	0.500	4.064	9.000	-5.500	2.500	-2.013	2.006e-01	3.531e+00
0.468	0.500	4.064	9.000	-5.500	3.000	-3.961	1.565e+03	2.918e+06
0.491	0.500	4.064	9.000	-5.500	3.000	-3.484	3.228e-01	1.286e+02
0.491	0.500	4.064	9.000	-5.500	3.000	-3.005	1.230e-01	1.422e+01
0.491	0.500	4.064	9.000	-5.500	3.000	-2.551	1.037e-01	4.048e+00
0.491	0.500	4.064	9.000	-5.500	3.000	-2.019	9.822e-02	1.111e+00
0.000	0.800	3.988	8.000	-7.500	1.500	-3.883	1.415e+08	0.000e+00

0.231	0.800	3.988	8.000	-7.500	1.500	-3.292	4.856e+06	5.114e+10
0.606	0.800	3.988	8.000	-7.500	1.500	-2.798	1.596e+05	2.530e+08
0.765	0.800	3.988	8.000	-7.500	1.500	-2.416	2.935e+04	1.151e+07
0.821	0.800	3.988	8.000	-7.500	1.500	-1.995	3.248e+03	4.080e+05
0.125	0.800	3.988	8.000	-7.500	2.000	-3.798	5.722e+06	1.888e+11
0.516	0.800	3.988	8.000	-7.500	2.000	-3.318	1.926e+05	9.870e+08
0.704	0.800	3.988	8.000	-7.500	2.000	-2.929	1.972e+04	2.054e+07
0.748	0.800	3.988	8.000	-7.500	2.000	-2.534	5.194e+02	1.690e+05
0.749	0.800	3.988	8.000	-7.500	2.000	-2.024	4.848e+01	4.094e+03
0.293	0.800	3.988	8.000	-7.500	2.500	-3.835	2.242e+05	3.740e+09
0.579	0.800	3.988	8.000	-7.500	2.500	-3.409	1.087e+04	2.840e+07
0.627	0.800	3.988	8.000	-7.500	2.500	-2.981	4.372e+01	3.006e+04
0.628	0.800	3.988	8.000	-7.500	2.500	-2.537	7.078e-01	1.495e+02
0.628	0.800	3.988	8.000	-7.500	2.500	-2.002	2.089e-01	1.217e+01
0.519	0.800	3.988	8.000	-7.500	3.000	-3.899	6.529e+03	2.512e+07
0.569	0.800	3.988	8.000	-7.500	3.000	-3.493	9.728e+00	1.012e+04
0.569	0.800	3.988	8.000	-7.500	3.000	-3.065	1.581e-01	5.186e+01
0.569	0.800	3.988	8.000	-7.500	3.000	-2.543	9.201e-02	8.523e+00
0.569	0.800	3.988	8.000	-7.500	3.000	-2.053	8.206e-02	2.416e+00
0.000	0.800	3.989	8.000	-6.500	1.500	-3.777	2.203e+08	0.000e+00
0.268	0.800	3.989	8.000	-6.500	1.500	-3.246	3.971e+06	3.322e+10
0.591	0.800	3.989	8.000	-6.500	1.500	-2.829	2.012e+05	3.177e+08
0.771	0.800	3.989	8.000	-6.500	1.500	-2.393	2.916e+04	9.370e+06
0.821	0.800	3.989	8.000	-6.500	1.500	-2.005	4.053e+03	4.678e+05
0.111	0.800	3.989	8.000	-6.500	2.000	-3.801	5.983e+06	2.110e+11
0.512	0.800	3.989	8.000	-6.500	2.000	-3.277	1.531e+05	6.609e+08
0.675	0.800	3.989	8.000	-6.500	2.000	-2.936	2.025e+04	2.216e+07
0.724	0.800	3.989	8.000	-6.500	2.000	-2.469	2.603e+02	7.175e+04
0.724	0.800	3.989	8.000	-6.500	2.000	-2.040	4.707e+01	4.210e+03
0.308	0.800	3.989	8.000	-6.500	2.500	-3.802	1.991e+05	2.956e+09
0.569	0.800	3.989	8.000	-6.500	2.500	-3.409	1.168e+04	3.131e+07
0.618	0.800	3.989	8.000	-6.500	2.500	-2.981	4.477e+01	3.144e+04
0.618	0.800	3.989	8.000	-6.500	2.500	-2.538	7.203e-01	1.552e+02
0.618	0.800	3.989	8.000	-6.500	2.500	-2.003	2.098e-01	1.246e+01
0.508	0.800	3.989	8.000	-6.500	3.000	-3.905	6.794e+03	2.668e+07
0.560	0.800	3.989	8.000	-6.500	3.000	-3.507	8.342e+00	8.982e+03
0.560	0.800	3.989	8.000	-6.500	3.000	-3.005	1.301e-01	3.650e+01
0.560	0.800	3.989	8.000	-6.500	3.000	-2.569	8.996e-02	8.802e+00
0.560	0.800	3.989	8.000	-6.500	3.000	-2.083	8.032e-02	2.517e+00
0.000	0.800	3.999	8.000	-5.500	1.500	-3.756	-NaN	-NaN
0.011	0.800	3.999	8.000	-5.500	1.500	-3.348	1.000e+07	7.775e+10
0.324	0.800	3.999	8.000	-5.500	1.500	-2.793	3.160e+05	9.805e+08
0.547	0.800	3.999	8.000	-5.500	1.500	-2.401	4.308e+04	2.784e+07
0.650	0.800	3.999	8.000	-5.500	1.500	-2.009	6.453e+03	1.319e+06
0.000	0.800	3.999	8.000	-5.500	2.000	-3.880	2.057e+07	0.000e+00
0.386	0.800	3.999	8.000	-5.500	2.000	-3.296	3.858e+05	3.694e+09
0.640	0.800	3.999	8.000	-5.500	2.000	-2.873	2.907e+04	4.105e+07
0.703	0.800	3.999	8.000	-5.500	2.000	-2.472	6.210e+02	2.504e+05
0.704	0.800	3.999	8.000	-5.500	2.000	-2.006	4.695e+01	5.311e+03
0.102	0.800	3.999	8.000	-5.500	2.500	-3.871	5.454e+05	2.306e+10
0.451	0.800	3.999	8.000	-5.500	2.500	-3.369	2.915e+04	1.112e+08
0.549	0.800	3.999	8.000	-5.500	2.500	-2.989	2.090e+02	2.291e+05
0.550	0.800	3.999	8.000	-5.500	2.500	-2.551	1.286e+00	4.040e+02
0.550	0.800	3.999	8.000	-5.500	2.500	-2.071	2.268e-01	2.180e+01
0.122	0.800	3.999	8.000	-5.500	3.000	-3.911	7.485e+04	6.957e+08
0.362	0.800	3.999	8.000	-5.500	3.000	-3.466	2.145e+02	4.401e+05
0.365	0.800	3.999	8.000	-5.500	3.000	-3.042	2.022e-01	1.131e+02

0.365	0.800	3.999	8.000	-5.500	3.000	-2.506	8.187e-02	1.185e+01
0.365	0.800	3.999	8.000	-5.500	3.000	-2.005	7.235e-02	3.206e+00
0.362	0.800	3.986	8.500	-7.500	1.500	-3.823	2.383e+05	8.880e+08
0.676	0.800	3.986	8.500	-7.500	1.500	-3.363	4.458e+04	4.104e+07
0.808	0.800	3.986	8.500	-7.500	1.500	-2.973	1.755e+04	6.036e+06
0.859	0.800	3.986	8.500	-7.500	1.500	-2.511	1.785e+03	2.117e+05
0.864	0.800	3.986	8.500	-7.500	1.500	-2.005	1.371e+02	4.667e+03
0.519	0.800	3.986	8.500	-7.500	2.000	-3.862	3.796e+04	1.105e+08
0.741	0.800	3.986	8.500	-7.500	2.000	-3.437	1.069e+04	1.117e+07
0.798	0.800	3.986	8.500	-7.500	2.000	-3.020	4.681e+02	1.792e+05
0.800	0.800	3.986	8.500	-7.500	2.000	-2.526	1.762e+01	1.903e+03
0.800	0.800	3.986	8.500	-7.500	2.000	-2.009	9.864e-01	3.097e+01
0.795	0.800	3.986	8.500	-7.500	2.500	-3.926	5.204e+03	9.526e+06
0.824	0.800	3.986	8.500	-7.500	2.500	-3.522	8.850e+01	5.444e+04
0.824	0.800	3.986	8.500	-7.500	2.500	-3.011	1.339e+00	2.229e+02
0.824	0.800	3.986	8.500	-7.500	2.500	-2.524	2.662e-01	1.389e+01
0.824	0.800	3.986	8.500	-7.500	2.500	-2.105	1.831e-01	3.606e+00
0.726	0.800	3.986	8.500	-7.500	3.000	-3.983	1.981e+01	2.184e+04
0.726	0.800	3.986	8.500	-7.500	3.000	-3.543	1.904e-01	6.606e+01
0.726	0.800	3.986	8.500	-7.500	3.000	-3.012	8.952e-02	8.688e+00
0.726	0.800	3.986	8.500	-7.500	3.000	-2.517	7.805e-02	2.388e+00
0.726	0.800	3.986	8.500	-7.500	3.000	-2.095	7.552e-02	8.719e-01
0.218	0.800	3.989	8.500	-6.500	1.500	-3.820	4.198e+05	2.138e+09
0.522	0.800	3.989	8.500	-6.500	1.500	-3.351	5.714e+04	6.524e+07
0.709	0.800	3.989	8.500	-6.500	1.500	-2.908	1.738e+04	6.059e+06
0.771	0.800	3.989	8.500	-6.500	1.500	-2.509	2.345e+03	3.201e+05
0.780	0.800	3.989	8.500	-6.500	1.500	-2.007	1.511e+02	5.932e+03
0.599	0.800	3.989	8.500	-6.500	2.000	-3.850	7.158e+04	2.667e+08
0.769	0.800	3.989	8.500	-6.500	2.000	-3.452	1.457e+04	1.632e+07
0.818	0.800	3.989	8.500	-6.500	2.000	-3.021	5.374e+02	1.977e+05
0.820	0.800	3.989	8.500	-6.500	2.000	-2.538	2.568e+01	2.722e+03
0.820	0.800	3.989	8.500	-6.500	2.000	-2.070	2.509e+00	8.650e+01
0.639	0.800	3.989	8.500	-6.500	2.500	-3.919	1.127e+04	3.019e+07
0.720	0.800	3.989	8.500	-6.500	2.500	-3.484	1.240e+02	1.075e+05
0.721	0.800	3.989	8.500	-6.500	2.500	-3.005	7.827e-01	1.927e+02
0.721	0.800	3.989	8.500	-6.500	2.500	-2.587	2.027e-01	1.827e+01
0.721	0.800	3.989	8.500	-6.500	2.500	-2.019	1.360e-01	3.246e+00
0.709	0.800	3.989	8.500	-6.500	3.000	-3.983	2.636e+01	3.192e+04
0.709	0.800	3.989	8.500	-6.500	3.000	-3.544	2.000e-01	7.572e+01
0.709	0.800	3.989	8.500	-6.500	3.000	-3.014	9.011e-02	9.518e+00
0.709	0.800	3.989	8.500	-6.500	3.000	-2.520	7.819e-02	2.602e+00
0.709	0.800	3.989	8.500	-6.500	3.000	-2.098	7.557e-02	9.487e-01
0.000	0.800	4.017	8.500	-5.500	1.500	-3.970	-NaN	-NaN
0.151	0.800	4.017	8.500	-5.500	1.500	-3.317	3.602e+05	1.659e+09
0.381	0.800	4.017	8.500	-5.500	1.500	-2.875	5.291e+04	5.287e+07
0.547	0.800	4.017	8.500	-5.500	1.500	-2.448	1.241e+04	3.783e+06
0.591	0.800	4.017	8.500	-5.500	1.500	-1.979	3.819e+02	3.449e+04
0.111	0.800	4.017	8.500	-5.500	2.000	-3.885	4.509e+05	9.214e+09
0.479	0.800	4.017	8.500	-5.500	2.000	-3.362	5.707e+04	1.701e+08
0.650	0.800	4.017	8.500	-5.500	2.000	-2.956	6.115e+03	5.375e+06
0.677	0.800	4.017	8.500	-5.500	2.000	-2.542	9.959e+01	2.755e+04
0.677	0.800	4.017	8.500	-5.500	2.000	-1.995	4.975e+00	3.450e+02
0.382	0.800	4.017	8.500	-5.500	2.500	-3.845	6.697e+04	4.316e+08
0.594	0.800	4.017	8.500	-5.500	2.500	-3.451	2.717e+03	5.108e+06
0.617	0.800	4.017	8.500	-5.500	2.500	-3.006	1.254e+01	6.459e+03
0.617	0.800	4.017	8.500	-5.500	2.500	-2.561	3.365e-01	5.572e+01
0.617	0.800	4.017	8.500	-5.500	2.500	-2.029	1.618e-01	7.574e+00

0.352	0.800	4.017	8.500	-5.500	3.000	-3.939	6.548e+03	2.272e+07
0.428	0.800	4.017	8.500	-5.500	3.000	-3.511	5.430e+00	5.373e+03
0.428	0.800	4.017	8.500	-5.500	3.000	-3.034	9.981e-02	2.776e+01
0.428	0.800	4.017	8.500	-5.500	3.000	-2.575	7.481e-02	6.887e+00
0.428	0.800	4.017	8.500	-5.500	3.000	-2.038	6.907e-02	1.812e+00
0.607	0.800	3.984	9.000	-7.500	1.500	-3.926	1.174e+04	4.873e+06
0.759	0.800	3.984	9.000	-7.500	1.500	-3.470	3.585e+03	7.312e+05
0.802	0.800	3.984	9.000	-7.500	1.500	-3.041	3.150e+02	2.676e+04
0.805	0.800	3.984	9.000	-7.500	1.500	-2.501	3.494e+01	8.163e+02
0.805	0.800	3.984	9.000	-7.500	1.500	-2.051	6.348e+00	5.167e+01
0.825	0.800	3.984	9.000	-7.500	2.000	-4.001	2.790e+03	1.818e+06
0.854	0.800	3.984	9.000	-7.500	2.000	-3.549	1.214e+02	2.885e+04
0.855	0.800	3.984	9.000	-7.500	2.000	-3.067	7.025e+00	5.156e+02
0.855	0.800	3.984	9.000	-7.500	2.000	-2.507	5.657e-01	1.117e+01
0.855	0.800	3.984	9.000	-7.500	2.000	-2.101	3.263e-01	2.512e+00
0.836	0.800	3.984	9.000	-7.500	2.500	-3.984	3.612e+01	2.017e+04
0.836	0.800	3.984	9.000	-7.500	2.500	-3.499	3.796e-01	6.417e+01
0.836	0.800	3.984	9.000	-7.500	2.500	-3.085	1.396e-01	8.884e+00
0.836	0.800	3.984	9.000	-7.500	2.500	-2.522	1.043e-01	1.799e+00
0.836	0.800	3.984	9.000	-7.500	2.500	-2.010	9.865e-02	5.219e-01
0.754	0.800	3.984	9.000	-7.500	3.000	-4.031	2.636e-01	9.654e+01
0.754	0.800	3.984	9.000	-7.500	3.000	-3.533	7.359e-02	8.140e+00
0.754	0.800	3.984	9.000	-7.500	3.000	-3.022	6.321e-02	2.119e+00
0.754	0.800	3.984	9.000	-7.500	3.000	-2.543	6.139e-02	6.804e-01
0.754	0.800	3.984	9.000	-7.500	3.000	-2.027	6.082e-02	2.051e-01
0.234	0.800	3.992	9.000	-6.500	1.500	-3.897	1.972e+04	1.638e+07
0.473	0.800	3.992	9.000	-6.500	1.500	-3.443	1.182e+04	4.573e+06
0.601	0.800	3.992	9.000	-6.500	1.500	-2.989	1.841e+03	3.055e+05
0.625	0.800	3.992	9.000	-6.500	1.500	-2.516	1.002e+02	5.460e+03
0.625	0.800	3.992	9.000	-6.500	1.500	-2.020	2.574e+01	4.292e+02
0.619	0.800	3.992	9.000	-6.500	2.000	-3.936	9.057e+03	1.084e+07
0.727	0.800	3.992	9.000	-6.500	2.000	-3.522	9.394e+02	4.965e+05
0.741	0.800	3.992	9.000	-6.500	2.000	-3.015	2.139e+01	3.245e+03
0.741	0.800	3.992	9.000	-6.500	2.000	-2.537	1.012e+00	4.887e+01
0.741	0.800	3.992	9.000	-6.500	2.000	-2.081	3.380e-01	5.630e+00
0.595	0.800	3.992	9.000	-6.500	2.500	-3.997	7.822e+02	1.028e+06
0.628	0.800	3.992	9.000	-6.500	2.500	-3.507	5.078e+00	1.990e+03
0.628	0.800	3.992	9.000	-6.500	2.500	-3.048	1.735e-01	2.216e+01
0.628	0.800	3.992	9.000	-6.500	2.500	-2.570	1.048e-01	4.352e+00
0.628	0.800	3.992	9.000	-6.500	2.500	-2.019	9.282e-02	1.077e+00
0.438	0.800	3.992	9.000	-6.500	3.000	-4.021	9.858e+00	7.881e+03
0.438	0.800	3.992	9.000	-6.500	3.000	-3.510	9.334e-02	1.980e+01
0.438	0.800	3.992	9.000	-6.500	3.000	-3.037	6.340e-02	4.338e+00
0.438	0.800	3.992	9.000	-6.500	3.000	-2.548	5.880e-02	1.287e+00
0.438	0.800	3.992	9.000	-6.500	3.000	-2.086	5.756e-02	4.332e-01
0.000	0.800	4.064	9.000	-5.500	1.500	-3.996	4.945e+06	0.000e+00
0.187	0.800	4.064	9.000	-5.500	1.500	-3.322	1.062e+05	2.453e+08
0.406	0.800	4.064	9.000	-5.500	1.500	-2.886	2.830e+04	1.821e+07
0.527	0.800	4.064	9.000	-5.500	1.500	-2.488	5.835e+03	1.412e+06
0.553	0.800	4.064	9.000	-5.500	1.500	-2.009	1.861e+02	1.321e+04
0.199	0.800	4.064	9.000	-5.500	2.000	-3.874	1.395e+05	1.348e+09
0.543	0.800	4.064	9.000	-5.500	2.000	-3.376	2.771e+04	5.267e+07
0.664	0.800	4.064	9.000	-5.500	2.000	-2.990	2.288e+03	1.567e+06
0.677	0.800	4.064	9.000	-5.500	2.000	-2.491	3.061e+01	5.472e+03
0.677	0.800	4.064	9.000	-5.500	2.000	-2.009	1.710e+00	9.401e+01
0.444	0.800	4.064	9.000	-5.500	2.500	-3.893	3.675e+04	1.631e+08
0.622	0.800	4.064	9.000	-5.500	2.500	-3.484	8.834e+02	1.293e+06

0.631	0.800	4.064	9.000	-5.500	2.500	-3.025	3.860e+00	1.558e+03
0.631	0.800	4.064	9.000	-5.500	2.500	-2.574	2.349e-01	3.096e+01
0.631	0.800	4.064	9.000	-5.500	2.500	-2.041	1.404e-01	5.263e+00
0.343	0.800	4.064	9.000	-5.500	3.000	-3.978	2.343e+03	6.603e+06
0.391	0.800	4.064	9.000	-5.500	3.000	-3.532	8.555e-01	6.622e+02
0.391	0.800	4.064	9.000	-5.500	3.000	-3.049	8.757e-02	1.944e+01
0.391	0.800	4.064	9.000	-5.500	3.000	-2.504	6.912e-02	4.196e+00
0.391	0.800	4.064	9.000	-5.500	3.000	-2.052	6.596e-02	1.397e+00
0.000	1.100	3.988	8.000	-7.500	1.500	-3.797	2.470e+08	0.000e+00
0.289	1.100	3.988	8.000	-7.500	1.500	-3.257	3.331e+06	3.081e+10
0.607	1.100	3.988	8.000	-7.500	1.500	-2.835	2.402e+05	4.473e+08
0.777	1.100	3.988	8.000	-7.500	1.500	-2.451	4.860e+04	2.678e+07
0.853	1.100	3.988	8.000	-7.500	1.500	-1.977	8.010e+03	1.460e+06
0.025	1.100	3.988	8.000	-7.500	2.000	-3.889	4.248e+06	1.841e+11
0.375	1.100	3.988	8.000	-7.500	2.000	-3.304	1.982e+05	1.262e+09
0.594	1.100	3.988	8.000	-7.500	2.000	-2.925	2.895e+04	5.284e+07
0.677	1.100	3.988	8.000	-7.500	2.000	-2.508	1.107e+03	6.861e+05
0.681	1.100	3.988	8.000	-7.500	2.000	-2.034	5.391e+01	9.701e+03
0.106	1.100	3.988	8.000	-7.500	2.500	-3.890	2.204e+05	4.748e+09
0.433	1.100	3.988	8.000	-7.500	2.500	-3.420	2.483e+04	1.011e+08
0.561	1.100	3.988	8.000	-7.500	2.500	-2.973	1.752e+02	2.274e+05
0.562	1.100	3.988	8.000	-7.500	2.500	-2.509	6.775e-01	2.549e+02
0.562	1.100	3.988	8.000	-7.500	2.500	-2.013	1.574e-01	1.786e+01
0.686	1.100	3.988	8.000	-7.500	3.000	-3.943	5.726e+03	2.486e+07
0.733	1.100	3.988	8.000	-7.500	3.000	-3.530	2.754e+01	3.592e+04
0.733	1.100	3.988	8.000	-7.500	3.000	-2.998	1.442e-01	4.700e+01
0.733	1.100	3.988	8.000	-7.500	3.000	-2.598	8.797e-02	1.100e+01
0.733	1.100	3.988	8.000	-7.500	3.000	-2.064	7.430e-02	2.675e+00
0.000	1.100	3.989	8.000	-6.500	1.500	-3.880	1.725e+08	0.000e+00
0.195	1.100	3.989	8.000	-6.500	1.500	-3.271	3.456e+06	4.003e+10
0.498	1.100	3.989	8.000	-6.500	1.500	-2.819	2.257e+05	4.731e+08
0.694	1.100	3.989	8.000	-6.500	1.500	-2.423	4.405e+04	2.624e+07
0.780	1.100	3.989	8.000	-6.500	1.500	-1.987	7.261e+03	1.537e+06
0.024	1.100	3.989	8.000	-6.500	2.000	-3.891	4.687e+06	2.258e+11
0.363	1.100	3.989	8.000	-6.500	2.000	-3.304	2.101e+05	1.394e+09
0.582	1.100	3.989	8.000	-6.500	2.000	-2.924	3.017e+04	5.624e+07
0.667	1.100	3.989	8.000	-6.500	2.000	-2.509	1.165e+03	7.358e+05
0.671	1.100	3.989	8.000	-6.500	2.000	-2.036	5.512e+01	1.010e+04
0.102	1.100	3.989	8.000	-6.500	2.500	-3.890	2.417e+05	5.612e+09
0.424	1.100	3.989	8.000	-6.500	2.500	-3.418	2.631e+04	1.091e+08
0.554	1.100	3.989	8.000	-6.500	2.500	-2.970	1.855e+02	2.435e+05
0.555	1.100	3.989	8.000	-6.500	2.500	-2.505	7.062e-01	2.671e+02
0.555	1.100	3.989	8.000	-6.500	2.500	-2.008	1.596e-01	1.814e+01
0.682	1.100	3.989	8.000	-6.500	3.000	-3.949	6.218e+03	2.714e+07
0.731	1.100	3.989	8.000	-6.500	3.000	-3.536	2.884e+01	3.837e+04
0.731	1.100	3.989	8.000	-6.500	3.000	-3.004	1.443e-01	4.811e+01
0.731	1.100	3.989	8.000	-6.500	3.000	-2.500	8.322e-02	8.342e+00
0.731	1.100	3.989	8.000	-6.500	3.000	-2.071	7.401e-02	2.732e+00
0.000	1.100	3.999	8.000	-5.500	1.500	-3.950	-NaN	-NaN
0.082	1.100	3.999	8.000	-5.500	1.500	-3.292	7.393e+06	1.323e+11
0.345	1.100	3.999	8.000	-5.500	1.500	-2.817	3.942e+05	1.327e+09
0.572	1.100	3.999	8.000	-5.500	1.500	-2.414	6.206e+04	4.998e+07
0.696	1.100	3.999	8.000	-5.500	1.500	-1.956	8.847e+03	2.262e+06
0.000	1.100	3.999	8.000	-5.500	2.000	-3.876	1.266e+07	0.000e+00
0.346	1.100	3.999	8.000	-5.500	2.000	-3.285	3.740e+05	3.446e+09
0.587	1.100	3.999	8.000	-5.500	2.000	-2.894	4.427e+04	9.164e+07
0.683	1.100	3.999	8.000	-5.500	2.000	-2.478	1.846e+03	1.241e+06

0.689	1.100	3.999	8.000	-5.500	2.000	-2.000	7.092e+01	1.345e+04
0.249	1.100	3.999	8.000	-5.500	2.500	-3.823	4.778e+05	1.191e+10
0.545	1.100	3.999	8.000	-5.500	2.500	-3.408	3.086e+04	1.282e+08
0.650	1.100	3.999	8.000	-5.500	2.500	-2.970	2.247e+02	2.739e+05
0.650	1.100	3.999	8.000	-5.500	2.500	-2.511	1.636e+00	5.816e+02
0.650	1.100	3.999	8.000	-5.500	2.500	-2.058	2.327e-01	2.753e+01
0.446	1.100	3.999	8.000	-5.500	3.000	-3.914	2.157e+04	1.250e+08
0.564	1.100	3.999	8.000	-5.500	3.000	-3.511	5.167e+01	9.606e+04
0.564	1.100	3.999	8.000	-5.500	3.000	-2.998	1.451e-01	6.685e+01
0.564	1.100	3.999	8.000	-5.500	3.000	-2.551	7.634e-02	1.194e+01
0.564	1.100	3.999	8.000	-5.500	3.000	-2.056	6.580e-02	3.227e+00
0.355	1.100	3.987	8.500	-7.500	1.500	-3.822	2.032e+05	7.928e+08
0.667	1.100	3.987	8.500	-7.500	1.500	-3.355	5.174e+04	5.673e+07
0.809	1.100	3.987	8.500	-7.500	1.500	-2.936	1.886e+04	8.599e+06
0.860	1.100	3.987	8.500	-7.500	1.500	-2.515	3.206e+03	6.220e+05
0.871	1.100	3.987	8.500	-7.500	1.500	-1.998	1.841e+02	1.060e+04
0.602	1.100	3.987	8.500	-7.500	2.000	-3.859	6.329e+04	2.171e+08
0.777	1.100	3.987	8.500	-7.500	2.000	-3.430	1.266e+04	1.648e+07
0.827	1.100	3.987	8.500	-7.500	2.000	-3.033	9.174e+02	4.975e+05
0.832	1.100	3.987	8.500	-7.500	2.000	-2.537	5.002e+01	7.956e+03
0.832	1.100	3.987	8.500	-7.500	2.000	-2.061	2.378e+00	1.218e+02
0.752	1.100	3.987	8.500	-7.500	2.500	-3.945	8.503e+03	2.312e+07
0.806	1.100	3.987	8.500	-7.500	2.500	-3.530	2.501e+02	2.588e+05
0.808	1.100	3.987	8.500	-7.500	2.500	-3.011	2.989e+00	8.332e+02
0.808	1.100	3.987	8.500	-7.500	2.500	-2.517	2.410e-01	2.082e+01
0.808	1.100	3.987	8.500	-7.500	2.500	-2.095	1.541e-01	4.989e+00
0.726	1.100	3.987	8.500	-7.500	3.000	-3.985	6.435e+01	1.103e+05
0.726	1.100	3.987	8.500	-7.500	3.000	-3.534	2.352e-01	1.231e+02
0.726	1.100	3.987	8.500	-7.500	3.000	-3.087	7.621e-02	1.360e+01
0.726	1.100	3.987	8.500	-7.500	3.000	-2.593	6.302e-02	3.538e+00
0.726	1.100	3.987	8.500	-7.500	3.000	-2.063	6.037e-02	9.956e-01
0.217	1.100	3.989	8.500	-6.500	1.500	-3.820	2.984e+05	1.494e+09
0.512	1.100	3.989	8.500	-6.500	1.500	-3.349	6.361e+04	8.272e+07
0.694	1.100	3.989	8.500	-6.500	1.500	-2.937	2.131e+04	1.115e+07
0.771	1.100	3.989	8.500	-6.500	1.500	-2.524	4.103e+03	9.192e+05
0.789	1.100	3.989	8.500	-6.500	1.500	-2.011	2.076e+02	1.399e+04
0.367	1.100	3.989	8.500	-6.500	2.000	-3.866	5.527e+04	2.231e+08
0.627	1.100	3.989	8.500	-6.500	2.000	-3.424	1.382e+04	2.247e+07
0.718	1.100	3.989	8.500	-6.500	2.000	-2.985	7.570e+02	4.805e+05
0.724	1.100	3.989	8.500	-6.500	2.000	-2.549	4.334e+01	9.274e+03
0.724	1.100	3.989	8.500	-6.500	2.000	-2.027	9.884e-01	6.076e+01
0.549	1.100	3.989	8.500	-6.500	2.500	-3.955	1.505e+04	5.333e+07
0.680	1.100	3.989	8.500	-6.500	2.500	-3.511	3.129e+02	4.355e+05
0.684	1.100	3.989	8.500	-6.500	2.500	-3.024	2.574e+00	1.026e+03
0.684	1.100	3.989	8.500	-6.500	2.500	-2.510	1.548e-01	1.806e+01
0.684	1.100	3.989	8.500	-6.500	2.500	-2.027	1.099e-01	4.164e+00
0.681	1.100	3.989	8.500	-6.500	3.000	-4.005	8.691e+01	1.665e+05
0.682	1.100	3.989	8.500	-6.500	3.000	-3.561	3.214e-01	1.911e+02
0.682	1.100	3.989	8.500	-6.500	3.000	-3.026	7.396e-02	1.212e+01
0.682	1.100	3.989	8.500	-6.500	3.000	-2.527	6.148e-02	3.150e+00
0.682	1.100	3.989	8.500	-6.500	3.000	-2.104	5.913e-02	1.137e+00
0.000	1.100	4.017	8.500	-5.500	1.500	-3.968	-NaN	-NaN
0.166	1.100	4.017	8.500	-5.500	1.500	-3.321	2.415e+05	9.975e+08
0.402	1.100	4.017	8.500	-5.500	1.500	-2.876	5.728e+04	6.392e+07
0.565	1.100	4.017	8.500	-5.500	1.500	-2.473	1.572e+04	7.067e+06
0.628	1.100	4.017	8.500	-5.500	1.500	-1.986	7.098e+02	1.032e+05
0.110	1.100	4.017	8.500	-5.500	2.000	-3.888	3.352e+05	5.862e+09

0.447	1.100	4.017	8.500	-5.500	2.000	-3.376	5.864e+04	1.910e+08
0.635	1.100	4.017	8.500	-5.500	2.000	-2.942	6.052e+03	7.110e+06
0.669	1.100	4.017	8.500	-5.500	2.000	-2.498	1.196e+02	4.565e+04
0.669	1.100	4.017	8.500	-5.500	2.000	-2.014	7.252e+00	8.334e+02
0.299	1.100	4.017	8.500	-5.500	2.500	-3.891	7.100e+04	4.808e+08
0.553	1.100	4.017	8.500	-5.500	2.500	-3.446	2.699e+03	6.480e+06
0.585	1.100	4.017	8.500	-5.500	2.500	-3.043	3.313e+01	2.728e+04
0.585	1.100	4.017	8.500	-5.500	2.500	-2.511	2.484e-01	5.390e+01
0.585	1.100	4.017	8.500	-5.500	2.500	-2.061	1.295e-01	9.700e+00
0.466	1.100	4.017	8.500	-5.500	3.000	-3.973	2.452e+03	9.507e+06
0.513	1.100	4.017	8.500	-5.500	3.000	-3.489	1.694e+00	1.709e+03
0.513	1.100	4.017	8.500	-5.500	3.000	-3.044	8.185e-02	2.670e+01
0.513	1.100	4.017	8.500	-5.500	3.000	-2.513	6.023e-02	5.564e+00
0.513	1.100	4.017	8.500	-5.500	3.000	-2.019	5.682e-02	1.663e+00
0.628	1.100	3.984	9.000	-7.500	1.500	-3.968	1.203e+04	7.365e+06
0.784	1.100	3.984	9.000	-7.500	1.500	-3.502	4.435e+03	1.439e+06
0.837	1.100	3.984	9.000	-7.500	1.500	-2.991	3.301e+02	4.080e+04
0.840	1.100	3.984	9.000	-7.500	1.500	-2.513	4.282e+01	1.718e+03
0.840	1.100	3.984	9.000	-7.500	1.500	-2.057	6.312e+00	8.722e+01
0.841	1.100	3.984	9.000	-7.500	2.000	-3.967	2.750e+03	2.499e+06
0.872	1.100	3.984	9.000	-7.500	2.000	-3.560	2.238e+02	8.926e+04
0.874	1.100	3.984	9.000	-7.500	2.000	-3.066	2.034e+01	2.494e+03
0.874	1.100	3.984	9.000	-7.500	2.000	-2.597	7.086e-01	2.891e+01
0.874	1.100	3.984	9.000	-7.500	2.000	-2.086	2.707e-01	3.388e+00
0.812	1.100	3.984	9.000	-7.500	2.500	-4.011	7.383e+01	6.762e+04
0.813	1.100	3.984	9.000	-7.500	2.500	-3.518	9.818e-01	2.707e+02
0.813	1.100	3.984	9.000	-7.500	2.500	-3.008	1.110e-01	9.243e+00
0.813	1.100	3.984	9.000	-7.500	2.500	-2.531	8.332e-02	2.293e+00
0.813	1.100	3.984	9.000	-7.500	2.500	-2.015	7.825e-02	6.551e-01
0.698	1.100	3.984	9.000	-7.500	3.000	-4.039	6.949e-01	3.777e+02
0.698	1.100	3.984	9.000	-7.500	3.000	-3.528	6.215e-02	9.852e+00
0.698	1.100	3.984	9.000	-7.500	3.000	-3.004	4.943e-02	2.307e+00
0.698	1.100	3.984	9.000	-7.500	3.000	-2.517	4.795e-02	7.253e-01
0.698	1.100	3.984	9.000	-7.500	3.000	-2.101	4.761e-02	2.761e-01
0.242	1.100	3.993	9.000	-6.500	1.500	-3.922	1.773e+04	1.787e+07
0.489	1.100	3.993	9.000	-6.500	1.500	-3.452	1.059e+04	5.682e+06
0.613	1.100	3.993	9.000	-6.500	1.500	-3.036	2.335e+03	6.337e+05
0.648	1.100	3.993	9.000	-6.500	1.500	-2.561	1.423e+02	1.358e+04
0.648	1.100	3.993	9.000	-6.500	1.500	-2.065	3.020e+01	8.879e+02
0.601	1.100	3.993	9.000	-6.500	2.000	-3.943	8.341e+03	1.324e+07
0.721	1.100	3.993	9.000	-6.500	2.000	-3.503	8.983e+02	6.687e+05
0.739	1.100	3.993	9.000	-6.500	2.000	-3.045	3.626e+01	9.215e+03
0.739	1.100	3.993	9.000	-6.500	2.000	-2.562	1.052e+00	8.459e+01
0.739	1.100	3.993	9.000	-6.500	2.000	-2.005	2.420e-01	5.324e+00
0.613	1.100	3.993	9.000	-6.500	2.500	-3.992	7.082e+02	1.222e+06
0.654	1.100	3.993	9.000	-6.500	2.500	-3.539	1.391e+01	8.453e+03
0.654	1.100	3.993	9.000	-6.500	2.500	-2.999	1.303e-01	2.142e+01
0.654	1.100	3.993	9.000	-6.500	2.500	-2.503	7.911e-02	4.083e+00
0.654	1.100	3.993	9.000	-6.500	2.500	-2.036	7.254e-02	1.270e+00
0.563	1.100	3.993	9.000	-6.500	3.000	-4.036	3.936e+00	3.398e+03
0.563	1.100	3.993	9.000	-6.500	3.000	-3.526	7.056e-02	1.748e+01
0.563	1.100	3.993	9.000	-6.500	3.000	-3.001	5.090e-02	3.682e+00
0.563	1.100	3.993	9.000	-6.500	3.000	-2.512	4.862e-02	1.135e+00
0.563	1.100	3.993	9.000	-6.500	3.000	-2.096	4.808e-02	4.290e-01
0.000	1.100	4.076	9.000	-5.500	1.500	-3.987	4.468e+06	0.000e+00
0.195	1.100	4.076	9.000	-5.500	1.500	-3.347	8.692e+04	1.878e+08
0.401	1.100	4.076	9.000	-5.500	1.500	-2.942	3.337e+04	2.804e+07

0.553	1.100	4.076	9.000	-5.500	1.500	-2.464	5.614e+03	1.764e+06
0.582	1.100	4.076	9.000	-5.500	1.500	-2.032	2.817e+02	3.163e+04
0.170	1.100	4.076	9.000	-5.500	2.000	-3.875	9.169e+04	6.627e+08
0.478	1.100	4.076	9.000	-5.500	2.000	-3.405	2.603e+04	5.854e+07
0.616	1.100	4.076	9.000	-5.500	2.000	-2.992	2.178e+03	2.031e+06
0.634	1.100	4.076	9.000	-5.500	2.000	-2.541	5.426e+01	1.618e+04
0.634	1.100	4.076	9.000	-5.500	2.000	-2.057	1.486e+00	1.368e+02
0.367	1.100	4.076	9.000	-5.500	2.500	-3.922	3.181e+04	1.451e+08
0.570	1.100	4.076	9.000	-5.500	2.500	-3.485	8.663e+02	1.622e+06
0.584	1.100	4.076	9.000	-5.500	2.500	-2.998	4.917e+00	2.560e+03
0.584	1.100	4.076	9.000	-5.500	2.500	-2.529	1.600e-01	2.654e+01
0.584	1.100	4.076	9.000	-5.500	2.500	-2.076	1.099e-01	6.306e+00
0.455	1.100	4.076	9.000	-5.500	3.000	-3.973	3.668e+02	1.016e+06
0.467	1.100	4.076	9.000	-5.500	3.000	-3.520	3.325e-01	2.583e+02
0.467	1.100	4.076	9.000	-5.500	3.000	-3.071	6.983e-02	1.781e+01
0.467	1.100	4.076	9.000	-5.500	3.000	-2.540	5.617e-02	4.085e+00
0.467	1.100	4.076	9.000	-5.500	3.000	-2.046	5.378e-02	1.243e+00
0.000	0.200	2.988	8.000	-8.500	1.500	-3.755	7.221e+07	0.000e+00
0.000	0.200	2.988	8.000	-8.500	1.500	-3.269	1.091e+07	0.000e+00
0.505	0.200	2.988	8.000	-8.500	1.500	-2.735	5.180e+05	1.990e+08
0.690	0.200	2.988	8.000	-8.500	1.500	-2.334	3.464e+04	1.766e+06
0.754	0.200	2.988	8.000	-8.500	1.500	-1.962	1.486e+03	2.174e+04
0.000	0.200	2.988	8.000	-8.500	2.000	-3.736	3.922e+06	0.000e+00
0.456	0.200	2.988	8.000	-8.500	2.000	-3.267	2.596e+05	3.618e+08
0.647	0.200	2.988	8.000	-8.500	2.000	-2.896	1.744e+04	2.792e+06
0.686	0.200	2.988	8.000	-8.500	2.000	-2.444	1.666e+02	4.809e+03
0.686	0.200	2.988	8.000	-8.500	2.000	-2.019	6.056e+01	5.360e+02
0.427	0.200	2.988	8.000	-8.500	2.500	-3.754	1.738e+05	9.971e+08
0.660	0.200	2.988	8.000	-8.500	2.500	-3.368	1.080e+04	5.257e+06
0.688	0.200	2.988	8.000	-8.500	2.500	-2.941	3.949e+01	3.300e+03
0.688	0.200	2.988	8.000	-8.500	2.500	-2.488	9.008e+00	2.107e+02
0.688	0.200	2.988	8.000	-8.500	2.500	-2.036	1.739e+00	1.339e+01
0.664	0.200	2.988	8.000	-8.500	3.000	-3.822	1.636e+04	2.558e+07
0.709	0.200	2.988	8.000	-8.500	3.000	-3.453	2.439e+01	6.452e+03
0.709	0.200	2.988	8.000	-8.500	3.000	-3.019	1.338e+00	9.514e+01
0.709	0.200	2.988	8.000	-8.500	3.000	-2.539	3.985e-01	8.486e+00
0.709	0.200	2.988	8.000	-8.500	3.000	-2.076	3.087e-01	2.196e+00
0.000	0.200	2.989	8.000	-7.500	1.500	-3.804	1.014e+07	0.000e+00
0.181	0.200	2.989	8.000	-7.500	1.500	-3.236	2.380e+06	5.936e+09
0.566	0.200	2.989	8.000	-7.500	1.500	-2.784	2.057e+05	1.018e+08
0.711	0.200	2.989	8.000	-7.500	1.500	-2.373	9.086e+03	5.518e+05
0.736	0.200	2.989	8.000	-7.500	1.500	-1.978	2.932e+02	4.649e+03
0.000	0.200	2.989	8.000	-7.500	2.000	-3.747	3.449e+06	0.000e+00
0.510	0.200	2.989	8.000	-7.500	2.000	-3.236	1.950e+05	2.443e+08
0.662	0.200	2.989	8.000	-7.500	2.000	-2.875	9.911e+03	1.478e+06
0.687	0.200	2.989	8.000	-7.500	2.000	-2.491	1.651e+02	5.784e+03
0.687	0.200	2.989	8.000	-7.500	2.000	-1.985	5.060e+01	4.365e+02
0.415	0.200	2.989	8.000	-7.500	2.500	-3.755	1.919e+05	1.217e+09
0.651	0.200	2.989	8.000	-7.500	2.500	-3.367	1.154e+04	5.883e+06
0.680	0.200	2.989	8.000	-7.500	2.500	-2.941	4.074e+01	3.515e+03
0.680	0.200	2.989	8.000	-7.500	2.500	-2.489	9.197e+00	2.215e+02
0.680	0.200	2.989	8.000	-7.500	2.500	-2.038	1.756e+00	1.392e+01
0.646	0.200	2.989	8.000	-7.500	3.000	-3.819	1.726e+04	2.723e+07
0.694	0.200	2.989	8.000	-7.500	3.000	-3.449	2.586e+01	6.781e+03
0.694	0.200	2.989	8.000	-7.500	3.000	-3.014	1.399e+00	9.781e+01
0.694	0.200	2.989	8.000	-7.500	3.000	-2.532	4.045e-01	8.426e+00
0.694	0.200	2.989	8.000	-7.500	3.000	-2.068	3.120e-01	2.164e+00

0.000	0.200	3.000	8.000	-6.500	1.500	-3.955	-NaN	-NaN
0.000	0.200	3.000	8.000	-6.500	1.500	-3.316	1.295e+06	0.000e+00
0.390	0.200	3.000	8.000	-6.500	1.500	-2.758	2.355e+05	2.375e+08
0.584	0.200	3.000	8.000	-6.500	1.500	-2.354	2.504e+04	3.353e+06
0.632	0.200	3.000	8.000	-6.500	1.500	-1.969	3.831e+02	1.138e+04
0.000	0.200	3.000	8.000	-6.500	2.000	-3.868	3.613e+06	0.000e+00
0.256	0.200	3.000	8.000	-6.500	2.000	-3.262	7.206e+05	3.072e+09
0.575	0.200	3.000	8.000	-6.500	2.000	-2.797	4.488e+04	1.662e+07
0.642	0.200	3.000	8.000	-6.500	2.000	-2.424	4.812e+02	3.097e+04
0.643	0.200	3.000	8.000	-6.500	2.000	-2.028	7.704e+01	1.432e+03
0.219	0.200	3.000	8.000	-6.500	2.500	-3.791	4.154e+05	5.657e+09
0.622	0.200	3.000	8.000	-6.500	2.500	-3.335	3.301e+04	3.867e+07
0.684	0.200	3.000	8.000	-6.500	2.500	-2.962	1.371e+02	2.354e+04
0.684	0.200	3.000	8.000	-6.500	2.500	-2.531	1.260e+01	5.550e+02
0.684	0.200	3.000	8.000	-6.500	2.500	-2.050	1.485e+00	1.925e+01
0.576	0.200	3.000	8.000	-6.500	3.000	-3.806	2.711e+04	5.535e+07
0.644	0.200	3.000	8.000	-6.500	3.000	-3.440	4.043e+01	1.175e+04
0.644	0.200	3.000	8.000	-6.500	3.000	-3.007	1.735e+00	1.292e+02
0.644	0.200	3.000	8.000	-6.500	3.000	-2.523	4.303e-01	9.398e+00
0.644	0.200	3.000	8.000	-6.500	3.000	-2.057	3.218e-01	2.321e+00
0.357	0.200	2.987	8.500	-8.500	1.500	-3.748	8.317e+05	1.165e+09
0.694	0.200	2.987	8.500	-8.500	1.500	-3.264	1.381e+05	3.505e+07
0.809	0.200	2.987	8.500	-8.500	1.500	-2.897	2.291e+04	1.295e+06
0.859	0.200	2.987	8.500	-8.500	1.500	-2.445	9.416e+02	1.345e+04
0.866	0.200	2.987	8.500	-8.500	1.500	-2.030	1.883e+02	8.961e+02
0.657	0.200	2.987	8.500	-8.500	2.000	-3.772	8.950e+04	6.557e+07
0.778	0.200	2.987	8.500	-8.500	2.000	-3.395	1.028e+04	1.307e+06
0.807	0.200	2.987	8.500	-8.500	2.000	-2.996	2.985e+02	9.824e+03
0.809	0.200	2.987	8.500	-8.500	2.000	-2.573	6.015e+01	6.138e+02
0.809	0.200	2.987	8.500	-8.500	2.000	-2.086	2.433e+01	7.504e+01
0.824	0.200	2.987	8.500	-8.500	2.500	-3.884	7.264e+03	3.077e+06
0.844	0.200	2.987	8.500	-8.500	2.500	-3.501	8.998e+01	9.287e+03
0.844	0.200	2.987	8.500	-8.500	2.500	-3.057	1.013e+01	2.973e+02
0.844	0.200	2.987	8.500	-8.500	2.500	-2.515	1.640e+00	1.275e+01
0.844	0.200	2.987	8.500	-8.500	2.500	-2.011	8.886e-01	2.117e+00
0.866	0.200	2.987	8.500	-8.500	3.000	-3.952	5.135e+01	1.339e+04
0.866	0.200	2.987	8.500	-8.500	3.000	-3.504	1.387e+00	9.822e+01
0.866	0.200	2.987	8.500	-8.500	3.000	-3.015	3.965e-01	8.354e+00
0.866	0.200	2.987	8.500	-8.500	3.000	-2.547	2.927e-01	2.045e+00
0.866	0.200	2.987	8.500	-8.500	3.000	-2.037	2.686e-01	5.749e-01
0.250	0.200	2.989	8.500	-7.500	1.500	-3.795	9.589e+04	1.055e+08
0.573	0.200	2.989	8.500	-7.500	1.500	-3.304	4.090e+04	1.072e+07
0.720	0.200	2.989	8.500	-7.500	1.500	-2.918	7.770e+03	5.757e+05
0.758	0.200	2.989	8.500	-7.500	1.500	-2.460	1.825e+02	3.415e+03
0.758	0.200	2.989	8.500	-7.500	1.500	-2.048	5.740e+01	3.600e+02
0.556	0.200	2.989	8.500	-7.500	2.000	-3.789	6.373e+04	9.537e+07
0.743	0.200	2.989	8.500	-7.500	2.000	-3.372	1.890e+04	4.407e+06
0.791	0.200	2.989	8.500	-7.500	2.000	-2.969	4.371e+02	2.315e+04
0.793	0.200	2.989	8.500	-7.500	2.000	-2.552	4.530e+01	7.145e+02
0.793	0.200	2.989	8.500	-7.500	2.000	-2.036	1.546e+01	6.731e+01
0.818	0.200	2.989	8.500	-7.500	2.500	-3.830	1.449e+04	1.055e+07
0.862	0.200	2.989	8.500	-7.500	2.500	-3.430	2.168e+02	3.394e+04
0.862	0.200	2.989	8.500	-7.500	2.500	-3.027	7.756e+00	3.622e+02
0.862	0.200	2.989	8.500	-7.500	2.500	-2.500	1.229e+00	1.521e+01
0.862	0.200	2.989	8.500	-7.500	2.500	-2.053	6.645e-01	2.860e+00
0.824	0.200	2.989	8.500	-7.500	3.000	-3.947	7.018e+01	2.071e+04
0.824	0.200	2.989	8.500	-7.500	3.000	-3.504	1.503e+00	1.182e+02

0.824	0.200	2.989	8.500	-7.500	3.000	-3.017	4.089e-01	9.519e+00
0.824	0.200	2.989	8.500	-7.500	3.000	-2.549	2.950e-01	2.275e+00
0.824	0.200	2.989	8.500	-7.500	3.000	-2.040	2.691e-01	6.355e-01
0.000	0.200	3.021	8.500	-6.500	1.500	-3.976	-NaN	-NaN
0.184	0.200	3.021	8.500	-6.500	1.500	-3.327	8.096e+04	9.260e+07
0.453	0.200	3.021	8.500	-6.500	1.500	-2.833	3.148e+04	7.511e+06
0.581	0.200	3.021	8.500	-6.500	1.500	-2.427	1.854e+03	1.109e+05
0.592	0.200	3.021	8.500	-6.500	1.500	-1.970	7.082e+01	1.064e+03
0.018	0.200	3.021	8.500	-6.500	2.000	-3.870	3.758e+05	1.388e+09
0.472	0.200	3.021	8.500	-6.500	2.000	-3.282	8.038e+04	9.555e+07
0.647	0.200	3.021	8.500	-6.500	2.000	-2.874	7.683e+03	1.330e+06
0.673	0.200	3.021	8.500	-6.500	2.000	-2.488	1.056e+02	4.490e+03
0.673	0.200	3.021	8.500	-6.500	2.000	-2.014	2.535e+01	2.906e+02
0.522	0.200	3.021	8.500	-6.500	2.500	-3.795	5.241e+04	2.418e+08
0.724	0.200	3.021	8.500	-6.500	2.500	-3.385	6.500e+03	3.336e+06
0.746	0.200	3.021	8.500	-6.500	2.500	-2.985	2.929e+01	3.127e+03
0.746	0.200	3.021	8.500	-6.500	2.500	-2.535	4.404e+00	1.327e+02
0.746	0.200	3.021	8.500	-6.500	2.500	-2.050	9.089e-01	8.315e+00
0.706	0.200	3.021	8.500	-6.500	3.000	-3.867	5.440e+03	5.509e+06
0.727	0.200	3.021	8.500	-6.500	3.000	-3.483	5.733e+00	1.213e+03
0.727	0.200	3.021	8.500	-6.500	3.000	-3.045	7.050e-01	4.299e+01
0.727	0.200	3.021	8.500	-6.500	3.000	-2.568	3.255e-01	6.131e+00
0.727	0.200	3.021	8.500	-6.500	3.000	-2.013	2.698e-01	1.378e+00
0.551	0.200	2.984	9.000	-8.500	1.500	-3.865	1.330e+04	8.078e+05
0.729	0.200	2.984	9.000	-8.500	1.500	-3.435	3.706e+03	9.731e+04
0.785	0.200	2.984	9.000	-8.500	1.500	-3.023	4.314e+02	4.469e+03
0.793	0.200	2.984	9.000	-8.500	1.500	-2.554	7.281e+01	2.352e+02
0.793	0.200	2.984	9.000	-8.500	1.500	-2.063	3.390e+01	3.383e+01
0.824	0.200	2.984	9.000	-8.500	2.000	-3.931	3.028e+03	2.618e+05
0.850	0.200	2.984	9.000	-8.500	2.000	-3.494	1.307e+02	3.454e+03
0.850	0.200	2.984	9.000	-8.500	2.000	-3.066	1.894e+01	1.648e+02
0.850	0.200	2.984	9.000	-8.500	2.000	-2.552	6.437e+00	1.629e+01
0.850	0.200	2.984	9.000	-8.500	2.000	-2.069	3.389e+00	2.781e+00
0.909	0.200	2.984	9.000	-8.500	2.500	-3.996	1.073e+02	9.365e+03
0.910	0.200	2.984	9.000	-8.500	2.500	-3.526	2.714e+00	6.804e+01
0.910	0.200	2.984	9.000	-8.500	2.500	-3.080	7.567e-01	6.449e+00
0.910	0.200	2.984	9.000	-8.500	2.500	-2.557	4.281e-01	1.072e+00
0.910	0.200	2.984	9.000	-8.500	2.500	-2.070	3.788e-01	3.075e-01
0.921	0.200	2.984	9.000	-8.500	3.000	-3.997	1.123e+00	7.818e+01
0.921	0.200	2.984	9.000	-8.500	3.000	-3.553	3.368e-01	7.822e+00
0.921	0.200	2.984	9.000	-8.500	3.000	-3.004	2.377e-01	1.517e+00
0.921	0.200	2.984	9.000	-8.500	3.000	-2.551	2.215e-01	4.943e-01
0.921	0.200	2.984	9.000	-8.500	3.000	-2.056	2.161e-01	1.536e-01
0.213	0.200	2.993	9.000	-7.500	1.500	-3.882	7.561e+03	9.448e+05
0.454	0.200	2.993	9.000	-7.500	1.500	-3.412	4.181e+03	2.332e+05
0.568	0.200	2.993	9.000	-7.500	1.500	-2.973	4.138e+02	9.131e+03
0.576	0.200	2.993	9.000	-7.500	1.500	-2.505	3.035e+01	2.013e+02
0.576	0.200	2.993	9.000	-7.500	1.500	-2.041	1.066e+01	2.306e+01
0.588	0.200	2.993	9.000	-7.500	2.000	-3.885	1.018e+04	2.254e+06
0.714	0.200	2.993	9.000	-7.500	2.000	-3.465	1.034e+03	7.544e+04
0.727	0.200	2.993	9.000	-7.500	2.000	-2.987	2.527e+01	4.880e+02
0.727	0.200	2.993	9.000	-7.500	2.000	-2.494	6.646e+00	3.756e+01
0.727	0.200	2.993	9.000	-7.500	2.000	-2.075	2.589e+00	5.424e+00
0.789	0.200	2.993	9.000	-7.500	2.500	-3.951	2.295e+03	5.410e+05
0.818	0.200	2.993	9.000	-7.500	2.500	-3.492	2.168e+01	1.387e+03
0.818	0.200	2.993	9.000	-7.500	2.500	-3.029	1.423e+00	2.740e+01
0.818	0.200	2.993	9.000	-7.500	2.500	-2.514	4.831e-01	2.711e+00

0.818	0.200	2.993	9.000	-7.500	2.500	-2.082	3.888e-01	7.975e-01
0.851	0.200	2.993	9.000	-7.500	3.000	-4.010	5.517e+00	8.387e+02
0.851	0.200	2.993	9.000	-7.500	3.000	-3.500	4.365e-01	1.751e+01
0.851	0.200	2.993	9.000	-7.500	3.000	-3.019	2.691e-01	3.422e+00
0.851	0.200	2.993	9.000	-7.500	3.000	-2.561	2.379e-01	1.040e+00
0.851	0.200	2.993	9.000	-7.500	3.000	-2.061	2.285e-01	3.141e-01
0.000	0.200	3.079	9.000	-6.500	1.500	-4.009	4.404e+04	0.000e+00
0.213	0.200	3.079	9.000	-6.500	1.500	-3.343	2.907e+04	1.510e+07
0.461	0.200	3.079	9.000	-6.500	1.500	-2.868	1.272e+04	1.737e+06
0.552	0.200	3.079	9.000	-6.500	1.500	-2.448	4.024e+02	1.581e+04
0.555	0.200	3.079	9.000	-6.500	1.500	-2.037	4.412e+01	5.442e+02
0.113	0.200	3.079	9.000	-6.500	2.000	-3.857	1.919e+05	8.831e+08
0.491	0.200	3.079	9.000	-6.500	2.000	-3.319	4.126e+04	2.796e+07
0.640	0.200	3.079	9.000	-6.500	2.000	-2.912	3.146e+03	3.775e+05
0.655	0.200	3.079	9.000	-6.500	2.000	-2.503	5.580e+01	1.713e+03
0.655	0.200	3.079	9.000	-6.500	2.000	-2.011	1.752e+01	1.465e+02
0.603	0.200	3.079	9.000	-6.500	2.500	-3.799	3.114e+04	6.865e+07
0.745	0.200	3.079	9.000	-6.500	2.500	-3.391	1.630e+03	5.056e+05
0.753	0.200	3.079	9.000	-6.500	2.500	-3.008	1.291e+01	1.051e+03
0.753	0.200	3.079	9.000	-6.500	2.500	-2.544	2.354e+00	5.508e+01
0.753	0.200	3.079	9.000	-6.500	2.500	-2.050	7.417e-01	5.259e+00
0.736	0.200	3.079	9.000	-6.500	3.000	-3.911	1.987e+03	1.478e+06
0.746	0.200	3.079	9.000	-6.500	3.000	-3.505	2.538e+00	4.217e+02
0.746	0.200	3.079	9.000	-6.500	3.000	-3.052	5.020e-01	2.440e+01
0.746	0.200	3.079	9.000	-6.500	3.000	-2.566	2.957e-01	4.423e+00
0.746	0.200	3.079	9.000	-6.500	3.000	-2.004	2.587e-01	1.041e+00
0.000	0.500	2.988	8.000	-8.500	1.500	-3.809	2.886e+07	0.000e+00
0.357	0.500	2.988	8.000	-8.500	1.500	-3.277	2.431e+06	1.434e+10
0.739	0.500	2.988	8.000	-8.500	1.500	-2.764	9.777e+04	9.584e+07
0.851	0.500	2.988	8.000	-8.500	1.500	-2.398	2.701e+04	6.741e+06
0.899	0.500	2.988	8.000	-8.500	1.500	-1.963	4.854e+03	3.627e+05
0.299	0.500	2.988	8.000	-8.500	2.000	-3.739	2.301e+06	4.144e+10
0.683	0.500	2.988	8.000	-8.500	2.000	-3.307	1.396e+05	5.388e+08
0.831	0.500	2.988	8.000	-8.500	2.000	-2.909	2.245e+04	1.601e+07
0.876	0.500	2.988	8.000	-8.500	2.000	-2.496	1.456e+03	2.961e+05
0.880	0.500	2.988	8.000	-8.500	2.000	-2.061	6.655e+01	4.175e+03
0.601	0.500	2.988	8.000	-8.500	2.500	-3.770	1.107e+05	1.246e+09
0.805	0.500	2.988	8.000	-8.500	2.500	-3.358	1.515e+04	2.709e+07
0.847	0.500	2.988	8.000	-8.500	2.500	-3.010	5.130e+02	2.980e+05
0.850	0.500	2.988	8.000	-8.500	2.500	-2.547	8.456e+00	1.338e+03
0.850	0.500	2.988	8.000	-8.500	2.500	-2.086	8.856e-01	4.482e+01
0.680	0.500	2.988	8.000	-8.500	3.000	-3.846	2.654e+04	1.130e+08
0.781	0.500	2.988	8.000	-8.500	3.000	-3.487	3.496e+02	4.502e+05
0.785	0.500	2.988	8.000	-8.500	3.000	-3.027	7.651e-01	2.568e+02
0.785	0.500	2.988	8.000	-8.500	3.000	-2.523	1.629e-01	1.558e+01
0.785	0.500	2.988	8.000	-8.500	3.000	-2.042	1.239e-01	3.818e+00
0.000	0.500	2.989	8.000	-7.500	1.500	-3.799	8.291e+06	0.000e+00
0.490	0.500	2.989	8.000	-7.500	1.500	-3.265	5.652e+05	3.298e+09
0.751	0.500	2.989	8.000	-7.500	1.500	-2.820	5.531e+04	5.811e+07
0.849	0.500	2.989	8.000	-7.500	1.500	-2.439	1.566e+04	4.394e+06
0.880	0.500	2.989	8.000	-7.500	1.500	-2.019	9.124e+02	8.069e+04
0.272	0.500	2.989	8.000	-7.500	2.000	-3.751	2.197e+06	4.182e+10
0.683	0.500	2.989	8.000	-7.500	2.000	-3.272	1.004e+05	3.318e+08
0.823	0.500	2.989	8.000	-7.500	2.000	-2.877	1.828e+04	1.185e+07
0.863	0.500	2.989	8.000	-7.500	2.000	-2.455	7.737e+02	1.429e+05
0.865	0.500	2.989	8.000	-7.500	2.000	-2.013	4.113e+01	2.321e+03
0.566	0.500	2.989	8.000	-7.500	2.500	-3.773	1.292e+05	1.529e+09

0.782	0.500	2.989	8.000	-7.500	2.500	-3.363	1.582e+04	2.950e+07
0.831	0.500	2.989	8.000	-7.500	2.500	-2.949	2.461e+02	1.215e+05
0.832	0.500	2.989	8.000	-7.500	2.500	-2.558	8.352e+00	1.386e+03
0.832	0.500	2.989	8.000	-7.500	2.500	-2.001	6.346e-01	2.670e+01
0.675	0.500	2.989	8.000	-7.500	3.000	-3.844	2.782e+04	1.222e+08
0.778	0.500	2.989	8.000	-7.500	3.000	-3.487	3.730e+02	4.911e+05
0.782	0.500	2.989	8.000	-7.500	3.000	-3.027	7.829e-01	2.679e+02
0.782	0.500	2.989	8.000	-7.500	3.000	-2.524	1.634e-01	1.592e+01
0.782	0.500	2.989	8.000	-7.500	3.000	-2.044	1.241e-01	3.892e+00
0.000	0.500	2.999	8.000	-6.500	1.500	-3.953	-NaN	-NaN
0.131	0.500	2.999	8.000	-6.500	1.500	-3.316	7.024e+05	5.553e+09
0.457	0.500	2.999	8.000	-6.500	1.500	-2.800	6.616e+04	1.108e+08
0.662	0.500	2.999	8.000	-6.500	1.500	-2.375	1.839e+04	7.314e+06
0.731	0.500	2.999	8.000	-6.500	1.500	-1.988	1.599e+03	2.136e+05
0.000	0.500	2.999	8.000	-6.500	2.000	-3.866	3.697e+06	0.000e+00
0.450	0.500	2.999	8.000	-6.500	2.000	-3.293	2.228e+05	1.750e+09
0.700	0.500	2.999	8.000	-6.500	2.000	-2.872	3.220e+04	4.319e+07
0.791	0.500	2.999	8.000	-6.500	2.000	-2.464	2.606e+03	8.905e+05
0.802	0.500	2.999	8.000	-6.500	2.000	-2.042	6.515e+01	6.694e+03
0.345	0.500	2.999	8.000	-6.500	2.500	-3.816	2.549e+05	6.677e+09
0.689	0.500	2.999	8.000	-6.500	2.500	-3.355	3.027e+04	9.886e+07
0.784	0.500	2.999	8.000	-6.500	2.500	-2.983	1.234e+03	1.060e+06
0.792	0.500	2.999	8.000	-6.500	2.500	-2.515	8.192e+00	1.777e+03
0.792	0.500	2.999	8.000	-6.500	2.500	-2.003	6.007e-01	3.611e+01
0.429	0.500	2.999	8.000	-6.500	3.000	-3.826	5.291e+04	3.951e+08
0.656	0.500	2.999	8.000	-6.500	3.000	-3.446	1.477e+03	2.739e+06
0.674	0.500	2.999	8.000	-6.500	3.000	-3.016	1.381e+00	6.746e+02
0.674	0.500	2.999	8.000	-6.500	3.000	-2.497	1.647e-01	2.124e+01
0.674	0.500	2.999	8.000	-6.500	3.000	-2.054	1.213e-01	5.442e+00
0.575	0.500	2.986	8.500	-8.500	1.500	-3.796	1.463e+05	2.714e+08
0.807	0.500	2.986	8.500	-8.500	1.500	-3.336	2.889e+04	1.356e+07
0.887	0.500	2.986	8.500	-8.500	1.500	-2.952	1.377e+04	2.341e+06
0.920	0.500	2.986	8.500	-8.500	1.500	-2.531	2.089e+03	1.357e+05
0.928	0.500	2.986	8.500	-8.500	1.500	-2.010	1.482e+02	2.760e+03
0.825	0.500	2.986	8.500	-8.500	2.000	-3.807	2.502e+04	3.760e+07
0.900	0.500	2.986	8.500	-8.500	2.000	-3.401	8.846e+03	3.891e+06
0.922	0.500	2.986	8.500	-8.500	2.000	-3.035	8.798e+02	1.534e+05
0.926	0.500	2.986	8.500	-8.500	2.000	-2.498	4.131e+01	1.851e+03
0.926	0.500	2.986	8.500	-8.500	2.000	-2.096	1.616e+01	2.744e+02
0.897	0.500	2.986	8.500	-8.500	2.500	-3.892	7.539e+03	9.908e+06
0.922	0.500	2.986	8.500	-8.500	2.500	-3.522	4.016e+02	1.984e+05
0.924	0.500	2.986	8.500	-8.500	2.500	-3.045	7.394e+00	1.047e+03
0.924	0.500	2.986	8.500	-8.500	2.500	-2.579	6.895e-01	3.146e+01
0.924	0.500	2.986	8.500	-8.500	2.500	-2.068	2.744e-01	3.778e+00
0.851	0.500	2.986	8.500	-8.500	3.000	-3.968	9.792e+02	1.289e+06
0.869	0.500	2.986	8.500	-8.500	3.000	-3.525	4.052e+00	1.684e+03
0.869	0.500	2.986	8.500	-8.500	3.000	-3.057	1.635e-01	2.108e+01
0.869	0.500	2.986	8.500	-8.500	3.000	-2.567	1.073e-01	4.342e+00
0.869	0.500	2.986	8.500	-8.500	3.000	-2.005	9.762e-02	1.070e+00
0.301	0.500	2.989	8.500	-7.500	1.500	-3.813	2.984e+04	4.561e+07
0.597	0.500	2.989	8.500	-7.500	1.500	-3.364	2.014e+04	1.103e+07
0.760	0.500	2.989	8.500	-7.500	1.500	-2.928	7.669e+03	1.649e+06
0.812	0.500	2.989	8.500	-7.500	1.500	-2.519	6.730e+02	5.781e+04
0.817	0.500	2.989	8.500	-7.500	1.500	-1.991	3.949e+01	9.144e+02
0.665	0.500	2.989	8.500	-7.500	2.000	-3.812	2.933e+04	5.845e+07
0.812	0.500	2.989	8.500	-7.500	2.000	-3.426	1.120e+04	7.535e+06
0.868	0.500	2.989	8.500	-7.500	2.000	-2.965	7.325e+02	1.553e+05

0.873	0.500	2.989	8.500	-7.500	2.000	-2.507	3.554e+01	2.317e+03
0.873	0.500	2.989	8.500	-7.500	2.000	-2.056	6.827e+00	1.488e+02
0.803	0.500	2.989	8.500	-7.500	2.500	-3.904	9.911e+03	1.803e+07
0.877	0.500	2.989	8.500	-7.500	2.500	-3.456	4.607e+02	2.862e+05
0.882	0.500	2.989	8.500	-7.500	2.500	-3.012	5.497e+00	1.060e+03
0.882	0.500	2.989	8.500	-7.500	2.500	-2.535	3.996e-01	2.399e+01
0.882	0.500	2.989	8.500	-7.500	2.500	-2.077	2.047e-01	4.192e+00
0.769	0.500	2.989	8.500	-7.500	3.000	-3.963	1.386e+03	2.065e+06
0.799	0.500	2.989	8.500	-7.500	3.000	-3.525	5.043e+00	2.382e+03
0.799	0.500	2.989	8.500	-7.500	3.000	-3.059	1.662e-01	2.422e+01
0.799	0.500	2.989	8.500	-7.500	3.000	-2.570	1.078e-01	4.920e+00
0.799	0.500	2.989	8.500	-7.500	3.000	-2.008	9.771e-02	1.208e+00
0.000	0.500	3.017	8.500	-6.500	1.500	-3.971	-NaN	-NaN
0.177	0.500	3.017	8.500	-6.500	1.500	-3.337	3.383e+04	5.553e+07
0.431	0.500	3.017	8.500	-6.500	1.500	-2.872	1.989e+04	1.039e+07
0.593	0.500	3.017	8.500	-6.500	1.500	-2.445	5.089e+03	9.933e+05
0.635	0.500	3.017	8.500	-6.500	1.500	-2.040	2.532e+02	1.803e+04
0.128	0.500	3.017	8.500	-6.500	2.000	-3.871	1.416e+05	1.358e+09
0.514	0.500	3.017	8.500	-6.500	2.000	-3.347	2.848e+04	5.353e+07
0.706	0.500	3.017	8.500	-6.500	2.000	-2.915	6.635e+03	3.681e+06
0.754	0.500	3.017	8.500	-6.500	2.000	-2.472	1.878e+02	3.167e+04
0.755	0.500	3.017	8.500	-6.500	2.000	-2.032	1.607e+01	8.632e+02
0.505	0.500	3.017	8.500	-6.500	2.500	-3.850	3.096e+04	1.750e+08
0.739	0.500	3.017	8.500	-6.500	2.500	-3.434	7.448e+03	1.149e+07
0.790	0.500	3.017	8.500	-6.500	2.500	-2.981	7.115e+01	3.041e+04
0.790	0.500	3.017	8.500	-6.500	2.500	-2.565	1.394e+00	1.978e+02
0.790	0.500	3.017	8.500	-6.500	2.500	-2.060	2.956e-01	1.235e+01
0.680	0.500	3.017	8.500	-6.500	3.000	-3.900	8.801e+03	2.413e+07
0.748	0.500	3.017	8.500	-6.500	3.000	-3.465	2.793e+01	2.140e+04
0.748	0.500	3.017	8.500	-6.500	3.000	-3.057	3.065e-01	7.783e+01
0.748	0.500	3.017	8.500	-6.500	3.000	-2.556	1.321e-01	9.913e+00
0.748	0.500	3.017	8.500	-6.500	3.000	-2.081	1.108e-01	2.731e+00
0.590	0.500	2.984	9.000	-8.500	1.500	-3.951	4.061e+03	6.159e+05
0.760	0.500	2.984	9.000	-8.500	1.500	-3.495	1.339e+03	1.149e+05
0.816	0.500	2.984	9.000	-8.500	1.500	-3.000	1.392e+02	4.655e+03
0.819	0.500	2.984	9.000	-8.500	1.500	-2.509	1.308e+01	1.363e+02
0.819	0.500	2.984	9.000	-8.500	1.500	-2.005	3.256e+00	1.044e+01
0.872	0.500	2.984	9.000	-8.500	2.000	-4.000	1.911e+03	5.840e+05
0.902	0.500	2.984	9.000	-8.500	2.000	-3.523	1.211e+02	1.382e+04
0.904	0.500	2.984	9.000	-8.500	2.000	-3.071	9.303e+00	3.555e+02
0.904	0.500	2.984	9.000	-8.500	2.000	-2.540	9.431e-01	1.030e+01
0.904	0.500	2.984	9.000	-8.500	2.000	-2.047	3.867e-01	1.346e+00
0.903	0.500	2.984	9.000	-8.500	2.500	-4.013	1.312e+02	4.613e+04
0.907	0.500	2.984	9.000	-8.500	2.500	-3.498	1.782e+00	1.790e+02
0.907	0.500	2.984	9.000	-8.500	2.500	-3.020	2.359e-01	7.629e+00
0.907	0.500	2.984	9.000	-8.500	2.500	-2.565	1.493e-01	1.675e+00
0.907	0.500	2.984	9.000	-8.500	2.500	-2.067	1.326e-01	4.709e-01
0.884	0.500	2.984	9.000	-8.500	3.000	-4.005	1.962e+00	5.072e+02
0.884	0.500	2.984	9.000	-8.500	3.000	-3.532	1.450e-01	1.196e+01
0.884	0.500	2.984	9.000	-8.500	3.000	-3.043	9.587e-02	2.519e+00
0.884	0.500	2.984	9.000	-8.500	3.000	-2.581	8.963e-02	8.080e-01
0.884	0.500	2.984	9.000	-8.500	3.000	-2.078	8.813e-02	2.489e-01
0.195	0.500	2.992	9.000	-7.500	1.500	-3.892	1.318e+04	3.846e+06
0.415	0.500	2.992	9.000	-7.500	1.500	-3.454	7.942e+03	1.255e+06
0.573	0.500	2.992	9.000	-7.500	1.500	-2.988	1.373e+03	1.024e+05
0.616	0.500	2.992	9.000	-7.500	1.500	-2.558	1.374e+02	4.022e+03
0.618	0.500	2.992	9.000	-7.500	1.500	-2.021	2.324e+01	1.877e+02

0.606	0.500	2.992	9.000	-7.500	2.000	-3.921	6.610e+03	3.464e+06
0.741	0.500	2.992	9.000	-7.500	2.000	-3.482	1.025e+03	2.471e+05
0.771	0.500	2.992	9.000	-7.500	2.000	-3.003	4.278e+01	3.404e+03
0.771	0.500	2.992	9.000	-7.500	2.000	-2.551	3.261e+00	8.659e+01
0.771	0.500	2.992	9.000	-7.500	2.000	-2.021	5.779e-01	4.427e+00
0.768	0.500	2.992	9.000	-7.500	2.500	-3.980	1.121e+03	7.832e+05
0.817	0.500	2.992	9.000	-7.500	2.500	-3.520	3.192e+01	8.256e+03
0.817	0.500	2.992	9.000	-7.500	2.500	-3.025	4.291e-01	3.271e+01
0.817	0.500	2.992	9.000	-7.500	2.500	-2.566	1.666e-01	4.300e+00
0.817	0.500	2.992	9.000	-7.500	2.500	-2.033	1.308e-01	9.785e-01
0.818	0.500	2.992	9.000	-7.500	3.000	-4.019	1.622e+01	8.435e+03
0.818	0.500	2.992	9.000	-7.500	3.000	-3.544	2.089e-01	3.308e+01
0.818	0.500	2.992	9.000	-7.500	3.000	-3.048	1.089e-01	5.331e+00
0.818	0.500	2.992	9.000	-7.500	3.000	-2.579	9.577e-02	1.578e+00
0.818	0.500	2.992	9.000	-7.500	3.000	-2.070	9.271e-02	4.716e-01
0.000	0.500	3.064	9.000	-6.500	1.500	-3.993	3.792e+05	0.000e+00
0.160	0.500	3.064	9.000	-6.500	1.500	-3.355	3.815e+04	4.034e+07
0.394	0.500	3.064	9.000	-6.500	1.500	-2.872	1.766e+04	5.954e+06
0.534	0.500	3.064	9.000	-6.500	1.500	-2.458	4.057e+03	5.434e+05
0.574	0.500	3.064	9.000	-6.500	1.500	-2.022	2.075e+02	9.542e+03
0.194	0.500	3.064	9.000	-6.500	2.000	-3.861	4.367e+04	1.894e+08
0.541	0.500	3.064	9.000	-6.500	2.000	-3.364	1.687e+04	1.875e+07
0.691	0.500	3.064	9.000	-6.500	2.000	-2.960	3.325e+03	1.383e+06
0.724	0.500	3.064	9.000	-6.500	2.000	-2.506	7.148e+01	9.131e+03
0.724	0.500	3.064	9.000	-6.500	2.000	-2.063	8.533e+00	3.573e+02
0.557	0.500	3.064	9.000	-6.500	2.500	-3.866	1.793e+04	5.681e+07
0.749	0.500	3.064	9.000	-6.500	2.500	-3.432	2.262e+03	2.331e+06
0.775	0.500	3.064	9.000	-6.500	2.500	-3.005	2.364e+01	7.596e+03
0.775	0.500	3.064	9.000	-6.500	2.500	-2.504	4.950e-01	4.462e+01
0.775	0.500	3.064	9.000	-6.500	2.500	-2.076	2.236e-01	7.278e+00
0.647	0.500	3.064	9.000	-6.500	3.000	-3.943	3.449e+03	7.180e+06
0.695	0.500	3.064	9.000	-6.500	3.000	-3.491	7.068e+00	4.110e+03
0.695	0.500	3.064	9.000	-6.500	3.000	-2.998	1.797e-01	2.936e+01
0.695	0.500	3.064	9.000	-6.500	3.000	-2.573	1.182e-01	7.001e+00
0.695	0.500	3.064	9.000	-6.500	3.000	-2.098	1.043e-01	2.039e+00
0.000	0.800	2.988	8.000	-8.500	1.500	-3.780	3.143e+07	0.000e+00
0.510	0.800	2.988	8.000	-8.500	1.500	-3.272	9.182e+05	5.774e+09
0.785	0.800	2.988	8.000	-8.500	1.500	-2.816	7.156e+04	8.964e+07
0.889	0.800	2.988	8.000	-8.500	1.500	-2.399	2.303e+04	8.601e+06
0.926	0.800	2.988	8.000	-8.500	1.500	-1.986	6.772e+03	9.980e+05
0.354	0.800	2.988	8.000	-8.500	2.000	-3.782	1.780e+06	4.727e+10
0.728	0.800	2.988	8.000	-8.500	2.000	-3.292	1.073e+05	4.762e+08
0.864	0.800	2.988	8.000	-8.500	2.000	-2.874	2.251e+04	2.514e+07
0.905	0.800	2.988	8.000	-8.500	2.000	-2.507	3.833e+03	1.734e+06
0.916	0.800	2.988	8.000	-8.500	2.000	-2.061	1.640e+02	2.484e+04
0.442	0.800	2.988	8.000	-8.500	2.500	-3.829	1.225e+05	1.878e+09
0.752	0.800	2.988	8.000	-8.500	2.500	-3.379	2.471e+04	8.621e+07
0.845	0.800	2.988	8.000	-8.500	2.500	-2.964	1.182e+03	1.481e+06
0.855	0.800	2.988	8.000	-8.500	2.500	-2.534	2.102e+01	8.562e+03
0.855	0.800	2.988	8.000	-8.500	2.500	-2.009	4.250e-01	4.755e+01
0.411	0.800	2.988	8.000	-8.500	3.000	-3.862	4.320e+04	2.694e+08
0.666	0.800	2.988	8.000	-8.500	3.000	-3.457	1.339e+03	3.443e+06
0.697	0.800	2.988	8.000	-8.500	3.000	-3.000	4.484e+00	3.345e+03
0.697	0.800	2.988	8.000	-8.500	3.000	-2.544	1.187e-01	2.820e+01
0.697	0.800	2.988	8.000	-8.500	3.000	-2.005	7.776e-02	5.151e+00
0.035	0.800	2.989	8.000	-7.500	1.500	-3.808	4.895e+06	6.941e+10
0.529	0.800	2.989	8.000	-7.500	1.500	-3.265	3.164e+05	2.001e+09

0.776	0.800	2.989	8.000	-7.500	1.500	-2.813	4.893e+04	6.660e+07
0.864	0.800	2.989	8.000	-7.500	1.500	-2.465	1.889e+04	9.988e+06
0.904	0.800	2.989	8.000	-7.500	1.500	-2.024	2.446e+03	4.675e+05
0.260	0.800	2.989	8.000	-7.500	2.000	-3.800	9.001e+05	2.411e+10
0.678	0.800	2.989	8.000	-7.500	2.000	-3.284	1.003e+05	4.954e+08
0.835	0.800	2.989	8.000	-7.500	2.000	-2.880	2.450e+04	3.273e+07
0.887	0.800	2.989	8.000	-7.500	2.000	-2.490	3.179e+03	1.618e+06
0.898	0.800	2.989	8.000	-7.500	2.000	-1.991	8.591e+01	1.257e+04
0.397	0.800	2.989	8.000	-7.500	2.500	-3.830	1.222e+05	2.030e+09
0.716	0.800	2.989	8.000	-7.500	2.500	-3.383	2.569e+04	9.288e+07
0.820	0.800	2.989	8.000	-7.500	2.500	-2.972	1.259e+03	1.643e+06
0.832	0.800	2.989	8.000	-7.500	2.500	-2.546	2.185e+01	9.332e+03
0.832	0.800	2.989	8.000	-7.500	2.500	-2.024	5.084e-01	5.996e+01
0.409	0.800	2.989	8.000	-7.500	3.000	-3.860	4.726e+04	3.003e+08
0.665	0.800	2.989	8.000	-7.500	3.000	-3.453	1.448e+03	3.758e+06
0.697	0.800	2.989	8.000	-7.500	3.000	-2.991	4.792e+00	3.585e+03
0.697	0.800	2.989	8.000	-7.500	3.000	-2.532	1.210e-01	2.859e+01
0.697	0.800	2.989	8.000	-7.500	3.000	-2.085	8.134e-02	6.651e+00
0.000	0.800	2.999	8.000	-6.500	1.500	-3.951	-NaN	-NaN
0.079	0.800	2.999	8.000	-6.500	1.500	-3.308	1.355e+06	1.381e+10
0.356	0.800	2.999	8.000	-6.500	1.500	-2.784	1.126e+05	2.450e+08
0.567	0.800	2.999	8.000	-6.500	1.500	-2.396	3.063e+04	2.013e+07
0.700	0.800	2.999	8.000	-6.500	1.500	-1.967	9.515e+03	2.232e+06
0.000	0.800	2.999	8.000	-6.500	2.000	-3.875	3.062e+06	0.000e+00
0.445	0.800	2.999	8.000	-6.500	2.000	-3.305	1.742e+05	1.504e+09
0.704	0.800	2.999	8.000	-6.500	2.000	-2.875	3.517e+04	6.897e+07
0.805	0.800	2.999	8.000	-6.500	2.000	-2.493	5.979e+03	4.294e+06
0.831	0.800	2.999	8.000	-6.500	2.000	-2.055	1.870e+02	4.449e+04
0.368	0.800	2.999	8.000	-6.500	2.500	-3.788	2.219e+05	5.241e+09
0.689	0.800	2.999	8.000	-6.500	2.500	-3.354	4.001e+04	1.778e+08
0.812	0.800	2.999	8.000	-6.500	2.500	-2.946	2.127e+03	3.138e+06
0.828	0.800	2.999	8.000	-6.500	2.500	-2.519	3.263e+01	1.542e+04
0.828	0.800	2.999	8.000	-6.500	2.500	-2.085	9.694e-01	1.544e+02
0.348	0.800	2.999	8.000	-6.500	3.000	-3.841	6.490e+04	5.884e+08
0.624	0.800	2.999	8.000	-6.500	3.000	-3.442	2.510e+03	7.563e+06
0.667	0.800	2.999	8.000	-6.500	3.000	-2.987	6.397e+00	5.500e+03
0.667	0.800	2.999	8.000	-6.500	3.000	-2.528	1.317e-01	3.516e+01
0.667	0.800	2.999	8.000	-6.500	3.000	-2.079	8.369e-02	7.672e+00
0.606	0.800	2.986	8.500	-8.500	1.500	-3.787	5.938e+04	1.130e+08
0.803	0.800	2.986	8.500	-8.500	1.500	-3.375	2.305e+04	1.599e+07
0.888	0.800	2.986	8.500	-8.500	1.500	-2.970	1.191e+04	3.612e+06
0.924	0.800	2.986	8.500	-8.500	1.500	-2.525	2.235e+03	2.846e+05
0.934	0.800	2.986	8.500	-8.500	1.500	-2.081	2.319e+02	1.112e+04
0.771	0.800	2.986	8.500	-8.500	2.000	-3.850	2.251e+04	4.800e+07
0.884	0.800	2.986	8.500	-8.500	2.000	-3.437	9.034e+03	8.406e+06
0.923	0.800	2.986	8.500	-8.500	2.000	-2.998	1.060e+03	4.112e+05
0.930	0.800	2.986	8.500	-8.500	2.000	-2.520	5.623e+01	7.141e+03
0.930	0.800	2.986	8.500	-8.500	2.000	-2.057	6.732e+00	2.825e+02
0.802	0.800	2.986	8.500	-8.500	2.500	-3.935	8.566e+03	2.026e+07
0.885	0.800	2.986	8.500	-8.500	2.500	-3.501	7.380e+02	8.183e+05
0.897	0.800	2.986	8.500	-8.500	2.500	-3.039	1.756e+01	6.529e+03
0.897	0.800	2.986	8.500	-8.500	2.500	-2.548	3.873e-01	4.407e+01
0.897	0.800	2.986	8.500	-8.500	2.500	-2.081	1.457e-01	5.563e+00
0.750	0.800	2.986	8.500	-8.500	3.000	-3.981	1.228e+03	2.547e+06
0.800	0.800	2.986	8.500	-8.500	3.000	-3.514	9.505e+00	7.050e+03
0.800	0.800	2.986	8.500	-8.500	3.000	-3.025	1.303e-01	2.898e+01
0.800	0.800	2.986	8.500	-8.500	3.000	-2.517	7.103e-02	4.786e+00

0.800	0.800	2.986	8.500	-8.500	3.000	-2.041	6.492e-02	1.449e+00
0.213	0.800	2.989	8.500	-7.500	1.500	-3.839	7.886e+04	1.912e+08
0.513	0.800	2.989	8.500	-7.500	1.500	-3.355	2.469e+04	1.950e+07
0.688	0.800	2.989	8.500	-7.500	1.500	-2.966	1.427e+04	5.194e+06
0.786	0.800	2.989	8.500	-7.500	1.500	-2.515	3.355e+03	5.181e+05
0.817	0.800	2.989	8.500	-7.500	1.500	-2.026	2.536e+02	1.355e+04
0.648	0.800	2.989	8.500	-7.500	2.000	-3.841	2.805e+04	7.335e+07
0.811	0.800	2.989	8.500	-7.500	2.000	-3.433	1.124e+04	1.230e+07
0.874	0.800	2.989	8.500	-7.500	2.000	-3.002	1.495e+03	6.820e+05
0.887	0.800	2.989	8.500	-7.500	2.000	-2.529	6.711e+01	1.019e+04
0.887	0.800	2.989	8.500	-7.500	2.000	-2.069	8.387e+00	4.211e+02
0.749	0.800	2.989	8.500	-7.500	2.500	-3.923	1.129e+04	3.016e+07
0.854	0.800	2.989	8.500	-7.500	2.500	-3.494	1.026e+03	1.276e+06
0.872	0.800	2.989	8.500	-7.500	2.500	-3.033	2.280e+01	9.546e+03
0.872	0.800	2.989	8.500	-7.500	2.500	-2.541	4.277e-01	5.434e+01
0.872	0.800	2.989	8.500	-7.500	2.500	-2.073	1.500e-01	6.366e+00
0.662	0.800	2.989	8.500	-7.500	3.000	-3.975	1.748e+03	3.987e+06
0.731	0.800	2.989	8.500	-7.500	3.000	-3.510	1.272e+01	1.055e+04
0.731	0.800	2.989	8.500	-7.500	3.000	-3.020	1.356e-01	3.336e+01
0.731	0.800	2.989	8.500	-7.500	3.000	-2.510	7.167e-02	5.308e+00
0.731	0.800	2.989	8.500	-7.500	3.000	-2.032	6.538e-02	1.597e+00
0.000	0.800	3.017	8.500	-6.500	1.500	-3.969	-NaN	-NaN
0.133	0.800	3.017	8.500	-6.500	1.500	-3.342	5.995e+04	1.364e+08
0.354	0.800	3.017	8.500	-6.500	1.500	-2.888	2.432e+04	1.957e+07
0.534	0.800	3.017	8.500	-6.500	1.500	-2.466	1.101e+04	3.823e+06
0.622	0.800	3.017	8.500	-6.500	1.500	-2.020	1.136e+03	1.556e+05
0.122	0.800	3.017	8.500	-6.500	2.000	-3.887	8.989e+04	9.022e+08
0.483	0.800	3.017	8.500	-6.500	2.000	-3.380	2.869e+04	7.361e+07
0.701	0.800	3.017	8.500	-6.500	2.000	-2.924	7.976e+03	7.720e+06
0.765	0.800	3.017	8.500	-6.500	2.000	-2.513	5.271e+02	2.050e+05
0.770	0.800	3.017	8.500	-6.500	2.000	-2.061	2.696e+01	3.400e+03
0.458	0.800	3.017	8.500	-6.500	2.500	-3.847	3.900e+04	2.276e+08
0.709	0.800	3.017	8.500	-6.500	2.500	-3.446	8.650e+03	2.106e+07
0.788	0.800	3.017	8.500	-6.500	2.500	-3.019	2.603e+02	2.436e+05
0.792	0.800	3.017	8.500	-6.500	2.500	-2.512	2.683e+00	6.890e+02
0.792	0.800	3.017	8.500	-6.500	2.500	-2.076	2.238e-01	2.024e+01
0.605	0.800	3.017	8.500	-6.500	3.000	-3.913	1.128e+04	4.358e+07
0.725	0.800	3.017	8.500	-6.500	3.000	-3.514	1.444e+02	2.334e+05
0.729	0.800	3.017	8.500	-6.500	3.000	-3.024	3.838e-01	1.711e+02
0.729	0.800	3.017	8.500	-6.500	3.000	-2.505	8.877e-02	1.135e+01
0.729	0.800	3.017	8.500	-6.500	3.000	-2.018	7.361e-02	3.019e+00
0.551	0.800	2.984	9.000	-8.500	1.500	-3.974	4.603e+03	1.269e+06
0.739	0.800	2.984	9.000	-8.500	1.500	-3.492	1.381e+03	2.232e+05
0.808	0.800	2.984	9.000	-8.500	1.500	-3.028	1.976e+02	1.464e+04
0.816	0.800	2.984	9.000	-8.500	1.500	-2.517	2.031e+01	4.680e+02
0.816	0.800	2.984	9.000	-8.500	1.500	-2.089	4.837e+00	4.101e+01
0.757	0.800	2.984	9.000	-8.500	2.000	-4.001	1.098e+03	5.146e+05
0.854	0.800	2.984	9.000	-8.500	2.000	-3.498	1.455e+02	3.288e+04
0.864	0.800	2.984	9.000	-8.500	2.000	-3.010	9.954e+00	7.416e+02
0.864	0.800	2.984	9.000	-8.500	2.000	-2.559	6.092e-01	1.571e+01
0.864	0.800	2.984	9.000	-8.500	2.000	-2.035	1.936e-01	1.479e+00
0.916	0.800	2.984	9.000	-8.500	2.500	-4.023	1.445e+02	1.007e+05
0.922	0.800	2.984	9.000	-8.500	2.500	-3.565	6.075e+00	1.484e+03
0.922	0.800	2.984	9.000	-8.500	2.500	-3.000	1.788e-01	1.156e+01
0.922	0.800	2.984	9.000	-8.500	2.500	-2.537	9.721e-02	2.145e+00
0.922	0.800	2.984	9.000	-8.500	2.500	-2.033	8.587e-02	5.916e-01
0.873	0.800	2.984	9.000	-8.500	3.000	-4.003	3.761e+00	1.756e+03

0.873	0.800	2.984	9.000	-8.500	3.000	-3.515	1.070e-01	1.553e+01
0.873	0.800	2.984	9.000	-8.500	3.000	-3.013	6.239e-02	2.810e+00
0.873	0.800	2.984	9.000	-8.500	3.000	-2.542	5.768e-02	8.737e-01
0.873	0.800	2.984	9.000	-8.500	3.000	-2.032	5.711e-02	2.667e-01
0.176	0.800	2.992	9.000	-7.500	1.500	-3.927	1.019e+04	4.845e+06
0.391	0.800	2.992	9.000	-7.500	1.500	-3.476	6.598e+03	1.875e+06
0.564	0.800	2.992	9.000	-7.500	1.500	-2.980	1.396e+03	1.974e+05
0.621	0.800	2.992	9.000	-7.500	1.500	-2.521	1.514e+02	8.576e+03
0.624	0.800	2.992	9.000	-7.500	1.500	-2.042	1.994e+01	3.660e+02
0.581	0.800	2.992	9.000	-7.500	2.000	-3.957	4.964e+03	4.636e+06
0.735	0.800	2.992	9.000	-7.500	2.000	-3.496	9.840e+02	4.730e+05
0.778	0.800	2.992	9.000	-7.500	2.000	-2.996	5.199e+01	8.797e+03
0.778	0.800	2.992	9.000	-7.500	2.000	-2.529	3.237e+00	1.798e+02
0.778	0.800	2.992	9.000	-7.500	2.000	-2.082	3.895e-01	7.616e+00
0.711	0.800	2.992	9.000	-7.500	2.500	-4.002	9.724e+02	1.211e+06
0.790	0.800	2.992	9.000	-7.500	2.500	-3.526	4.235e+01	2.221e+04
0.792	0.800	2.992	9.000	-7.500	2.500	-3.014	5.615e-01	8.541e+01
0.792	0.800	2.992	9.000	-7.500	2.500	-2.542	1.135e-01	5.703e+00
0.792	0.800	2.992	9.000	-7.500	2.500	-2.093	8.717e-02	1.545e+00
0.756	0.800	2.992	9.000	-7.500	3.000	-4.009	2.887e+01	2.696e+04
0.757	0.800	2.992	9.000	-7.500	3.000	-3.512	2.309e-01	6.383e+01
0.757	0.800	2.992	9.000	-7.500	3.000	-2.998	7.423e-02	6.135e+00
0.757	0.800	2.992	9.000	-7.500	3.000	-2.518	6.272e-02	1.701e+00
0.757	0.800	2.992	9.000	-7.500	3.000	-2.106	6.118e-02	6.413e-01
0.000	0.800	3.064	9.000	-6.500	1.500	-3.990	6.002e+05	0.000e+00
0.150	0.800	3.064	9.000	-6.500	1.500	-3.350	3.154e+04	4.151e+07
0.346	0.800	3.064	9.000	-6.500	1.500	-2.924	1.733e+04	9.967e+06
0.510	0.800	3.064	9.000	-6.500	1.500	-2.483	6.393e+03	1.644e+06
0.579	0.800	3.064	9.000	-6.500	1.500	-2.019	4.399e+02	4.230e+04
0.172	0.800	3.064	9.000	-6.500	2.000	-3.884	3.292e+04	1.653e+08
0.509	0.800	3.064	9.000	-6.500	2.000	-3.394	1.626e+04	2.776e+07
0.686	0.800	3.064	9.000	-6.500	2.000	-2.960	3.865e+03	2.917e+06
0.735	0.800	3.064	9.000	-6.500	2.000	-2.538	1.830e+02	5.379e+04
0.737	0.800	3.064	9.000	-6.500	2.000	-1.998	6.881e+00	5.359e+02
0.480	0.800	3.064	9.000	-6.500	2.500	-3.897	2.346e+04	9.471e+07
0.710	0.800	3.064	9.000	-6.500	2.500	-3.486	3.885e+03	7.503e+06
0.770	0.800	3.064	9.000	-6.500	2.500	-2.980	4.487e+01	2.707e+04
0.771	0.800	3.064	9.000	-6.500	2.500	-2.533	6.680e-01	1.324e+02
0.771	0.800	3.064	9.000	-6.500	2.500	-2.003	1.514e-01	8.589e+00
0.626	0.800	3.064	9.000	-6.500	3.000	-3.948	4.691e+03	1.446e+07
0.712	0.800	3.064	9.000	-6.500	3.000	-3.525	4.043e+01	4.853e+04
0.713	0.800	3.064	9.000	-6.500	3.000	-3.019	1.915e-01	6.323e+01
0.713	0.800	3.064	9.000	-6.500	3.000	-2.585	8.578e-02	1.007e+01
0.713	0.800	3.064	9.000	-6.500	3.000	-2.001	7.072e-02	2.131e+00
0.000	1.100	2.988	8.000	-8.500	1.500	-3.753	4.973e+07	0.000e+00
0.496	1.100	2.988	8.000	-8.500	1.500	-3.261	1.173e+06	7.325e+09
0.771	1.100	2.988	8.000	-8.500	1.500	-2.841	1.318e+05	2.144e+08
0.895	1.100	2.988	8.000	-8.500	1.500	-2.402	3.535e+04	1.769e+07
0.939	1.100	2.988	8.000	-8.500	1.500	-1.976	1.621e+04	3.501e+06
0.313	1.100	2.988	8.000	-8.500	2.000	-3.788	9.491e+05	2.393e+10
0.690	1.100	2.988	8.000	-8.500	2.000	-3.314	1.209e+05	6.738e+08
0.852	1.100	2.988	8.000	-8.500	2.000	-2.897	2.880e+04	5.233e+07
0.907	1.100	2.988	8.000	-8.500	2.000	-2.489	4.960e+03	3.843e+06
0.922	1.100	2.988	8.000	-8.500	2.000	-2.067	3.005e+02	9.030e+04
0.373	1.100	2.988	8.000	-8.500	2.500	-3.828	1.346e+05	1.910e+09
0.683	1.100	2.988	8.000	-8.500	2.500	-3.412	3.267e+04	1.451e+08
0.822	1.100	2.988	8.000	-8.500	2.500	-2.984	2.217e+03	4.293e+06

0.845	1.100	2.988	8.000	-8.500	2.500	-2.545	5.325e+01	3.630e+04
0.845	1.100	2.988	8.000	-8.500	2.500	-2.011	5.553e-01	1.027e+02
0.300	1.100	2.988	8.000	-8.500	3.000	-3.870	3.895e+04	3.574e+08
0.585	1.100	2.988	8.000	-8.500	3.000	-3.473	2.396e+03	8.698e+06
0.654	1.100	2.988	8.000	-8.500	3.000	-3.013	1.483e+01	1.742e+04
0.654	1.100	2.988	8.000	-8.500	3.000	-2.552	1.224e-01	4.480e+01
0.654	1.100	2.988	8.000	-8.500	3.000	-2.006	6.197e-02	6.220e+00
0.000	1.100	2.989	8.000	-7.500	1.500	-3.798	5.245e+07	0.000e+00
0.367	1.100	2.989	8.000	-7.500	1.500	-3.279	1.057e+06	7.744e+09
0.690	1.100	2.989	8.000	-7.500	1.500	-2.809	1.061e+05	1.733e+08
0.834	1.100	2.989	8.000	-7.500	1.500	-2.418	3.959e+04	2.309e+07
0.897	1.100	2.989	8.000	-7.500	1.500	-2.027	1.577e+04	4.211e+06
0.267	1.100	2.989	8.000	-7.500	2.000	-3.789	1.042e+06	2.819e+10
0.641	1.100	2.989	8.000	-7.500	2.000	-3.312	1.273e+05	7.430e+08
0.823	1.100	2.989	8.000	-7.500	2.000	-2.896	2.997e+04	5.584e+07
0.888	1.100	2.989	8.000	-7.500	2.000	-2.489	5.115e+03	4.050e+06
0.906	1.100	2.989	8.000	-7.500	2.000	-2.068	3.165e+02	9.738e+04
0.339	1.100	2.989	8.000	-7.500	2.500	-3.828	1.428e+05	2.133e+09
0.650	1.100	2.989	8.000	-7.500	2.500	-3.409	3.382e+04	1.556e+08
0.800	1.100	2.989	8.000	-7.500	2.500	-2.984	2.333e+03	4.616e+06
0.826	1.100	2.989	8.000	-7.500	2.500	-2.546	5.515e+01	3.846e+04
0.827	1.100	2.989	8.000	-7.500	2.500	-2.013	5.671e-01	1.071e+02
0.296	1.100	2.989	8.000	-7.500	3.000	-3.897	5.542e+04	3.859e+08
0.582	1.100	2.989	8.000	-7.500	3.000	-3.483	2.666e+03	9.478e+06
0.653	1.100	2.989	8.000	-7.500	3.000	-3.018	1.568e+01	1.863e+04
0.653	1.100	2.989	8.000	-7.500	3.000	-2.555	1.236e-01	4.602e+01
0.653	1.100	2.989	8.000	-7.500	3.000	-2.008	6.204e-02	6.346e+00
0.000	1.100	2.999	8.000	-6.500	1.500	-3.950	-NaN	-NaN
0.101	1.100	2.999	8.000	-6.500	1.500	-3.297	1.102e+06	1.145e+10
0.368	1.100	2.999	8.000	-6.500	1.500	-2.802	1.313e+05	3.176e+08
0.593	1.100	2.999	8.000	-6.500	1.500	-2.398	3.884e+04	3.168e+07
0.723	1.100	2.999	8.000	-6.500	1.500	-2.012	1.577e+04	5.831e+06
0.025	1.100	2.999	8.000	-6.500	2.000	-3.872	1.664e+06	5.427e+10
0.436	1.100	2.999	8.000	-6.500	2.000	-3.297	1.710e+05	1.385e+09
0.684	1.100	2.999	8.000	-6.500	2.000	-2.903	4.488e+04	1.146e+08
0.805	1.100	2.999	8.000	-6.500	2.000	-2.501	8.573e+03	9.154e+06
0.844	1.100	2.999	8.000	-6.500	2.000	-2.047	4.063e+02	1.567e+05
0.311	1.100	2.999	8.000	-6.500	2.500	-3.820	2.611e+05	6.039e+09
0.640	1.100	2.999	8.000	-6.500	2.500	-3.387	5.093e+04	2.762e+08
0.803	1.100	2.999	8.000	-6.500	2.500	-2.964	3.675e+03	8.102e+06
0.834	1.100	2.999	8.000	-6.500	2.500	-2.526	7.932e+01	6.159e+04
0.834	1.100	2.999	8.000	-6.500	2.500	-2.084	1.745e+00	4.520e+02
0.297	1.100	2.999	8.000	-6.500	3.000	-3.881	8.299e+04	7.432e+08
0.594	1.100	2.999	8.000	-6.500	3.000	-3.465	4.392e+03	1.745e+07
0.677	1.100	2.999	8.000	-6.500	3.000	-2.996	2.213e+01	2.917e+04
0.677	1.100	2.999	8.000	-6.500	3.000	-2.527	1.372e-01	5.509e+01
0.677	1.100	2.999	8.000	-6.500	3.000	-2.070	6.756e-02	9.163e+00
0.652	1.100	2.987	8.500	-8.500	1.500	-3.798	7.256e+04	1.602e+08
0.841	1.100	2.987	8.500	-8.500	1.500	-3.361	2.713e+04	2.236e+07
0.909	1.100	2.987	8.500	-8.500	1.500	-2.990	1.547e+04	6.507e+06
0.944	1.100	2.987	8.500	-8.500	1.500	-2.525	4.418e+03	8.284e+05
0.956	1.100	2.987	8.500	-8.500	1.500	-2.066	5.515e+02	4.213e+04
0.801	1.100	2.987	8.500	-8.500	2.000	-3.895	2.760e+04	7.716e+07
0.907	1.100	2.987	8.500	-8.500	2.000	-3.470	1.038e+04	1.431e+07
0.943	1.100	2.987	8.500	-8.500	2.000	-3.017	1.636e+03	1.028e+06
0.952	1.100	2.987	8.500	-8.500	2.000	-2.528	9.537e+01	2.095e+04
0.952	1.100	2.987	8.500	-8.500	2.000	-2.059	1.270e+01	9.171e+02

0.792	1.100	2.987	8.500	-8.500	2.500	-3.929	8.634e+03	2.539e+07
0.884	1.100	2.987	8.500	-8.500	2.500	-3.528	1.102e+03	1.860e+06
0.905	1.100	2.987	8.500	-8.500	2.500	-3.055	3.606e+01	2.229e+04
0.905	1.100	2.987	8.500	-8.500	2.500	-2.555	5.948e-01	1.111e+02
0.905	1.100	2.987	8.500	-8.500	2.500	-2.083	1.271e-01	7.874e+00
0.696	1.100	2.987	8.500	-8.500	3.000	-3.959	1.184e+03	3.175e+06
0.770	1.100	2.987	8.500	-8.500	3.000	-3.538	2.300e+01	2.704e+04
0.771	1.100	2.987	8.500	-8.500	3.000	-3.045	1.662e-01	5.759e+01
0.771	1.100	2.987	8.500	-8.500	3.000	-2.533	5.698e-02	5.906e+00
0.771	1.100	2.987	8.500	-8.500	3.000	-2.053	4.986e-02	1.697e+00
0.256	1.100	2.989	8.500	-7.500	1.500	-3.843	6.370e+04	1.631e+08
0.549	1.100	2.989	8.500	-7.500	1.500	-3.395	2.653e+04	2.710e+07
0.745	1.100	2.989	8.500	-7.500	1.500	-2.931	1.388e+04	6.475e+06
0.825	1.100	2.989	8.500	-7.500	1.500	-2.519	4.329e+03	1.005e+06
0.861	1.100	2.989	8.500	-7.500	1.500	-2.014	3.763e+02	3.201e+04
0.655	1.100	2.989	8.500	-7.500	2.000	-3.884	3.403e+04	1.114e+08
0.825	1.100	2.989	8.500	-7.500	2.000	-3.464	1.263e+04	1.964e+07
0.891	1.100	2.989	8.500	-7.500	2.000	-3.016	2.131e+03	1.515e+06
0.910	1.100	2.989	8.500	-7.500	2.000	-2.529	1.227e+02	3.097e+04
0.910	1.100	2.989	8.500	-7.500	2.000	-2.061	1.446e+01	1.197e+03
0.713	1.100	2.989	8.500	-7.500	2.500	-3.918	1.126e+04	3.627e+07
0.836	1.100	2.989	8.500	-7.500	2.500	-3.520	1.468e+03	2.713e+06
0.868	1.100	2.989	8.500	-7.500	2.500	-3.047	4.550e+01	3.113e+04
0.868	1.100	2.989	8.500	-7.500	2.500	-2.547	7.260e-01	1.489e+02
0.868	1.100	2.989	8.500	-7.500	2.500	-2.073	1.313e-01	8.889e+00
0.627	1.100	2.989	8.500	-7.500	3.000	-3.959	1.699e+03	4.868e+06
0.719	1.100	2.989	8.500	-7.500	3.000	-3.535	3.068e+01	3.989e+04
0.720	1.100	2.989	8.500	-7.500	3.000	-3.039	1.827e-01	6.969e+01
0.720	1.100	2.989	8.500	-7.500	3.000	-2.524	5.757e-02	6.532e+00
0.720	1.100	2.989	8.500	-7.500	3.000	-2.042	5.028e-02	1.865e+00
0.000	1.100	3.017	8.500	-6.500	1.500	-3.968	-NaN	-NaN
0.149	1.100	3.017	8.500	-6.500	1.500	-3.348	5.671e+04	1.312e+08
0.364	1.100	3.017	8.500	-6.500	1.500	-2.921	2.775e+04	2.744e+07
0.560	1.100	3.017	8.500	-6.500	1.500	-2.473	1.247e+04	5.773e+06
0.663	1.100	3.017	8.500	-6.500	1.500	-1.998	1.710e+03	3.278e+05
0.126	1.100	3.017	8.500	-6.500	2.000	-3.896	6.637e+04	5.750e+08
0.477	1.100	3.017	8.500	-6.500	2.000	-3.398	2.902e+04	8.332e+07
0.690	1.100	3.017	8.500	-6.500	2.000	-2.968	8.535e+03	1.196e+07
0.775	1.100	3.017	8.500	-6.500	2.000	-2.476	5.113e+02	2.744e+05
0.782	1.100	3.017	8.500	-6.500	2.000	-2.002	3.202e+01	5.511e+03
0.368	1.100	3.017	8.500	-6.500	2.500	-3.893	4.169e+04	2.516e+08
0.670	1.100	3.017	8.500	-6.500	2.500	-3.441	7.528e+03	2.189e+07
0.771	1.100	3.017	8.500	-6.500	2.500	-2.983	2.602e+02	3.195e+05
0.776	1.100	3.017	8.500	-6.500	2.500	-2.533	8.942e+00	3.629e+03
0.776	1.100	3.017	8.500	-6.500	2.500	-1.998	1.753e-01	1.996e+01
0.296	1.100	3.017	8.500	-6.500	3.000	-3.930	1.379e+04	5.643e+07
0.527	1.100	3.017	8.500	-6.500	3.000	-3.491	2.841e+02	6.481e+05
0.547	1.100	3.017	8.500	-6.500	3.000	-3.009	8.324e-01	5.717e+02
0.547	1.100	3.017	8.500	-6.500	3.000	-2.547	7.177e-02	1.616e+01
0.547	1.100	3.017	8.500	-6.500	3.000	-2.006	5.197e-02	3.308e+00
0.614	1.100	2.984	9.000	-8.500	1.500	-3.956	5.477e+03	2.122e+06
0.779	1.100	2.984	9.000	-8.500	1.500	-3.490	1.889e+03	4.412e+05
0.849	1.100	2.984	9.000	-8.500	1.500	-2.992	2.901e+02	3.099e+04
0.860	1.100	2.984	9.000	-8.500	1.500	-2.529	4.731e+01	1.836e+03
0.860	1.100	2.984	9.000	-8.500	1.500	-2.087	1.093e+01	1.509e+02
0.776	1.100	2.984	9.000	-8.500	2.000	-3.997	9.563e+02	6.792e+05
0.866	1.100	2.984	9.000	-8.500	2.000	-3.529	1.825e+02	6.992e+04

0.882	1.100	2.984	9.000	-8.500	2.000	-3.033	1.629e+01	2.150e+03
0.882	1.100	2.984	9.000	-8.500	2.000	-2.576	9.083e-01	4.096e+01
0.882	1.100	2.984	9.000	-8.500	2.000	-2.046	1.600e-01	2.108e+00
0.910	1.100	2.984	9.000	-8.500	2.500	-3.989	1.384e+02	1.364e+05
0.918	1.100	2.984	9.000	-8.500	2.500	-3.508	7.531e+00	2.555e+03
0.918	1.100	2.984	9.000	-8.500	2.500	-3.010	2.159e-01	2.279e+01
0.918	1.100	2.984	9.000	-8.500	2.500	-2.542	8.348e-02	2.973e+00
0.918	1.100	2.984	9.000	-8.500	2.500	-2.033	6.780e-02	7.467e-01
0.850	1.100	2.984	9.000	-8.500	3.000	-4.029	8.202e+00	5.965e+03
0.850	1.100	2.984	9.000	-8.500	3.000	-3.535	1.319e-01	2.942e+01
0.850	1.100	2.984	9.000	-8.500	3.000	-3.027	5.023e-02	3.432e+00
0.850	1.100	2.984	9.000	-8.500	3.000	-2.552	4.372e-02	9.953e-01
0.850	1.100	2.984	9.000	-8.500	3.000	-2.038	4.329e-02	3.015e-01
0.212	1.100	2.993	9.000	-7.500	1.500	-3.948	8.759e+03	5.444e+06
0.450	1.100	2.993	9.000	-7.500	1.500	-3.483	5.388e+03	2.147e+06
0.613	1.100	2.993	9.000	-7.500	1.500	-3.027	1.402e+03	3.127e+05
0.682	1.100	2.993	9.000	-7.500	1.500	-2.492	1.305e+02	1.060e+04
0.685	1.100	2.993	9.000	-7.500	1.500	-2.001	2.083e+01	5.380e+02
0.601	1.100	2.993	9.000	-7.500	2.000	-3.968	3.798e+03	4.857e+06
0.757	1.100	2.993	9.000	-7.500	2.000	-3.489	7.726e+02	5.351e+05
0.800	1.100	2.993	9.000	-7.500	2.000	-3.043	6.932e+01	2.023e+04
0.801	1.100	2.993	9.000	-7.500	2.000	-2.577	8.291e+00	8.067e+02
0.801	1.100	2.993	9.000	-7.500	2.000	-2.036	2.904e-01	8.017e+00
0.691	1.100	2.993	9.000	-7.500	2.500	-4.001	7.483e+02	1.224e+06
0.785	1.100	2.993	9.000	-7.500	2.500	-3.506	3.981e+01	2.879e+04
0.787	1.100	2.993	9.000	-7.500	2.500	-3.049	1.456e+00	3.531e+02
0.787	1.100	2.993	9.000	-7.500	2.500	-2.575	1.085e-01	8.664e+00
0.787	1.100	2.993	9.000	-7.500	2.500	-2.028	6.629e-02	1.493e+00
0.712	1.100	2.993	9.000	-7.500	3.000	-4.046	5.266e+01	7.396e+04
0.717	1.100	2.993	9.000	-7.500	3.000	-3.549	5.065e-01	2.149e+02
0.717	1.100	2.993	9.000	-7.500	3.000	-3.035	6.044e-02	7.654e+00
0.717	1.100	2.993	9.000	-7.500	3.000	-2.554	4.680e-02	1.943e+00
0.717	1.100	2.993	9.000	-7.500	3.000	-2.036	4.569e-02	5.736e-01
0.000	1.100	3.076	9.000	-6.500	1.500	-3.981	5.837e+05	0.000e+00
0.168	1.100	3.076	9.000	-6.500	1.500	-3.382	2.690e+04	3.729e+07
0.379	1.100	3.076	9.000	-6.500	1.500	-2.942	1.637e+04	1.149e+07
0.553	1.100	3.076	9.000	-6.500	1.500	-2.466	5.439e+03	1.808e+06
0.621	1.100	3.076	9.000	-6.500	1.500	-2.047	6.351e+02	9.407e+04
0.172	1.100	3.076	9.000	-6.500	2.000	-3.914	2.692e+04	1.245e+08
0.508	1.100	3.076	9.000	-6.500	2.000	-3.426	1.479e+04	3.051e+07
0.693	1.100	3.076	9.000	-6.500	2.000	-2.966	3.068e+03	3.131e+06
0.747	1.100	3.076	9.000	-6.500	2.000	-2.521	1.714e+02	7.039e+04
0.749	1.100	3.076	9.000	-6.500	2.000	-2.048	1.144e+01	1.502e+03
0.425	1.100	3.076	9.000	-6.500	2.500	-3.926	2.083e+04	8.707e+07
0.682	1.100	3.076	9.000	-6.500	2.500	-3.492	3.059e+03	7.275e+06
0.756	1.100	3.076	9.000	-6.500	2.500	-3.026	8.190e+01	7.684e+04
0.757	1.100	3.076	9.000	-6.500	2.500	-2.575	1.947e+00	6.038e+02
0.757	1.100	3.076	9.000	-6.500	2.500	-2.043	1.259e-01	1.114e+01
0.547	1.100	3.076	9.000	-6.500	3.000	-3.950	3.608e+03	1.310e+07
0.663	1.100	3.076	9.000	-6.500	3.000	-3.510	4.385e+01	6.746e+04
0.663	1.100	3.076	9.000	-6.500	3.000	-3.071	2.964e-01	1.498e+02
0.663	1.100	3.076	9.000	-6.500	3.000	-2.545	6.414e-02	9.282e+00
0.663	1.100	3.076	9.000	-6.500	3.000	-2.054	5.347e-02	2.472e+00
0.000	0.200	1.988	8.000	-9.500	1.500	-3.771	9.675e+06	0.000e+00
0.093	0.200	1.988	8.000	-9.500	1.500	-3.259	2.129e+06	2.026e+09
0.595	0.200	1.988	8.000	-9.500	1.500	-2.754	2.476e+05	1.074e+08
0.766	0.200	1.988	8.000	-9.500	1.500	-2.352	4.361e+04	3.511e+06

0.845	0.200	1.988	8.000	-9.500	1.500	-1.915	3.260e+03	6.567e+04
0.100	0.200	1.988	8.000	-9.500	2.000	-3.754	1.105e+06	3.766e+09
0.608	0.200	1.988	8.000	-9.500	2.000	-3.240	1.027e+05	1.085e+08
0.755	0.200	1.988	8.000	-9.500	2.000	-2.850	1.482e+04	2.535e+06
0.799	0.200	1.988	8.000	-9.500	2.000	-2.483	6.997e+02	3.409e+04
0.804	0.200	1.988	8.000	-9.500	2.000	-2.032	5.473e+01	7.460e+02
0.456	0.200	1.988	8.000	-9.500	2.500	-3.767	1.253e+05	6.106e+08
0.701	0.200	1.988	8.000	-9.500	2.500	-3.353	2.095e+04	1.267e+07
0.766	0.200	1.988	8.000	-9.500	2.500	-2.967	5.966e+02	7.912e+04
0.771	0.200	1.988	8.000	-9.500	2.500	-2.555	2.681e+01	1.030e+03
0.771	0.200	1.988	8.000	-9.500	2.500	-2.071	7.263e+00	8.117e+01
0.731	0.200	1.988	8.000	-9.500	3.000	-3.822	1.722e+04	2.768e+07
0.796	0.200	1.988	8.000	-9.500	3.000	-3.440	2.750e+02	8.907e+04
0.798	0.200	1.988	8.000	-9.500	3.000	-2.989	2.580e+00	2.126e+02
0.798	0.200	1.988	8.000	-9.500	3.000	-2.531	7.070e-01	1.833e+01
0.798	0.200	1.988	8.000	-9.500	3.000	-2.023	3.561e-01	2.766e+00
0.295	0.200	1.989	8.000	-8.500	1.500	-3.793	2.254e+04	5.939e+07
0.694	0.200	1.989	8.000	-8.500	1.500	-3.282	1.710e+04	1.505e+07
0.851	0.200	1.989	8.000	-8.500	1.500	-2.851	8.966e+03	2.542e+06
0.895	0.200	1.989	8.000	-8.500	1.500	-2.435	4.725e+02	4.124e+04
0.897	0.200	1.989	8.000	-8.500	1.500	-1.989	1.367e+01	3.422e+02
0.548	0.200	1.989	8.000	-8.500	2.000	-3.776	6.523e+04	4.262e+08
0.812	0.200	1.989	8.000	-8.500	2.000	-3.292	2.328e+04	2.696e+07
0.880	0.200	1.989	8.000	-8.500	2.000	-2.906	2.602e+03	6.591e+05
0.889	0.200	1.989	8.000	-8.500	2.000	-2.508	4.296e+01	3.014e+03
0.889	0.200	1.989	8.000	-8.500	2.000	-2.059	6.528e+00	1.384e+02
0.554	0.200	1.989	8.000	-8.500	2.500	-3.756	9.465e+04	6.964e+08
0.792	0.200	1.989	8.000	-8.500	2.500	-3.297	2.060e+04	1.723e+07
0.843	0.200	1.989	8.000	-8.500	2.500	-2.938	8.260e+02	1.577e+05
0.847	0.200	1.989	8.000	-8.500	2.500	-2.520	2.072e+01	1.082e+03
0.847	0.200	1.989	8.000	-8.500	2.500	-1.997	4.327e+00	5.901e+01
0.727	0.200	1.989	8.000	-8.500	3.000	-3.807	1.796e+04	2.947e+07
0.794	0.200	1.989	8.000	-8.500	3.000	-3.420	2.853e+02	9.074e+04
0.796	0.200	1.989	8.000	-8.500	3.000	-3.048	4.999e+00	5.013e+02
0.796	0.200	1.989	8.000	-8.500	3.000	-2.502	7.575e-01	1.880e+01
0.796	0.200	1.989	8.000	-8.500	3.000	-2.096	4.017e-01	3.795e+00
0.000	0.200	2.000	8.000	-7.500	1.500	-3.955	-NaN	-NaN
0.256	0.200	2.000	8.000	-7.500	1.500	-3.368	3.430e+03	1.775e+06
0.531	0.200	2.000	8.000	-7.500	1.500	-2.922	3.753e+03	9.952e+05
0.700	0.200	2.000	8.000	-7.500	1.500	-2.469	8.074e+02	9.978e+04
0.726	0.200	2.000	8.000	-7.500	1.500	-2.016	1.279e+01	5.152e+02
0.018	0.200	2.000	8.000	-7.500	2.000	-3.867	5.066e+04	2.375e+08
0.515	0.200	2.000	8.000	-7.500	2.000	-3.281	2.769e+04	5.249e+07
0.736	0.200	2.000	8.000	-7.500	2.000	-2.854	1.328e+04	5.910e+06
0.800	0.200	2.000	8.000	-7.500	2.000	-2.434	3.484e+02	3.829e+04
0.802	0.200	2.000	8.000	-7.500	2.000	-2.027	1.258e+01	4.237e+02
0.315	0.200	2.000	8.000	-7.500	2.500	-3.784	1.393e+05	1.731e+09
0.690	0.200	2.000	8.000	-7.500	2.500	-3.312	3.193e+04	6.206e+07
0.799	0.200	2.000	8.000	-7.500	2.500	-2.927	3.139e+03	1.033e+06
0.813	0.200	2.000	8.000	-7.500	2.500	-2.525	3.738e+01	3.118e+03
0.813	0.200	2.000	8.000	-7.500	2.500	-2.065	5.802e+00	1.399e+02
0.657	0.200	2.000	8.000	-7.500	3.000	-3.780	2.633e+04	1.194e+08
0.794	0.200	2.000	8.000	-7.500	3.000	-3.409	2.503e+03	1.721e+06
0.806	0.200	2.000	8.000	-7.500	3.000	-3.015	1.029e+01	1.755e+03
0.806	0.200	2.000	8.000	-7.500	3.000	-2.558	9.877e-01	4.882e+01
0.806	0.200	2.000	8.000	-7.500	3.000	-2.010	3.553e-01	4.658e+00
0.500	0.200	1.987	8.500	-9.500	1.500	-3.790	7.924e+04	4.421e+07

0.765	0.200	1.987	8.500	-9.500	1.500	-3.330	3.394e+04	5.360e+06
0.872	0.200	1.987	8.500	-9.500	1.500	-2.896	7.319e+03	3.390e+05
0.907	0.200	1.987	8.500	-9.500	1.500	-2.457	7.658e+02	1.190e+04
0.914	0.200	1.987	8.500	-9.500	1.500	-2.063	1.373e+02	7.991e+02
0.779	0.200	1.987	8.500	-9.500	2.000	-3.791	2.856e+04	1.776e+07
0.874	0.200	1.987	8.500	-9.500	2.000	-3.372	8.001e+03	1.112e+06
0.902	0.200	1.987	8.500	-9.500	2.000	-2.981	5.975e+02	2.648e+04
0.906	0.200	1.987	8.500	-9.500	2.000	-2.483	3.825e+01	4.485e+02
0.906	0.200	1.987	8.500	-9.500	2.000	-2.001	1.528e+01	5.499e+01
0.884	0.200	1.987	8.500	-9.500	2.500	-3.882	1.098e+04	5.769e+06
0.919	0.200	1.987	8.500	-9.500	2.500	-3.449	5.336e+02	7.072e+04
0.922	0.200	1.987	8.500	-9.500	2.500	-3.011	1.948e+01	7.552e+02
0.922	0.200	1.987	8.500	-9.500	2.500	-2.571	4.606e+00	5.919e+01
0.922	0.200	1.987	8.500	-9.500	2.500	-2.078	1.135e+00	4.537e+00
0.938	0.200	1.987	8.500	-9.500	3.000	-3.954	9.497e+02	3.887e+05
0.942	0.200	1.987	8.500	-9.500	3.000	-3.533	1.002e+01	1.202e+03
0.942	0.200	1.987	8.500	-9.500	3.000	-3.068	7.010e-01	2.553e+01
0.942	0.200	1.987	8.500	-9.500	3.000	-2.518	3.106e-01	3.058e+00
0.942	0.200	1.987	8.500	-9.500	3.000	-2.012	2.567e-01	7.789e-01
0.259	0.200	1.990	8.500	-8.500	1.500	-3.892	2.377e+03	4.209e+05
0.534	0.200	1.990	8.500	-8.500	1.500	-3.429	2.129e+03	2.176e+05
0.702	0.200	1.990	8.500	-8.500	1.500	-2.985	6.358e+02	3.476e+04
0.740	0.200	1.990	8.500	-8.500	1.500	-2.493	2.981e+01	5.373e+02
0.740	0.200	1.990	8.500	-8.500	1.500	-2.049	3.322e+00	2.027e+01
0.657	0.200	1.990	8.500	-8.500	2.000	-3.832	7.963e+03	3.642e+06
0.804	0.200	1.990	8.500	-8.500	2.000	-3.433	3.568e+03	6.812e+05
0.850	0.200	1.990	8.500	-8.500	2.000	-2.968	1.321e+02	7.894e+03
0.851	0.200	1.990	8.500	-8.500	2.000	-2.534	5.767e+00	1.109e+02
0.851	0.200	1.990	8.500	-8.500	2.000	-2.075	1.621e+00	1.028e+01
0.826	0.200	1.990	8.500	-8.500	2.500	-3.853	8.617e+03	5.133e+06
0.892	0.200	1.990	8.500	-8.500	2.500	-3.455	1.312e+03	2.642e+05
0.902	0.200	1.990	8.500	-8.500	2.500	-3.019	2.572e+01	1.529e+03
0.902	0.200	1.990	8.500	-8.500	2.500	-2.513	1.825e+00	3.001e+01
0.902	0.200	1.990	8.500	-8.500	2.500	-2.082	6.524e-01	3.847e+00
0.906	0.200	1.990	8.500	-8.500	3.000	-3.946	1.365e+03	6.617e+05
0.913	0.200	1.990	8.500	-8.500	3.000	-3.531	1.447e+01	2.024e+03
0.913	0.200	1.990	8.500	-8.500	3.000	-3.069	7.750e-01	3.260e+01
0.913	0.200	1.990	8.500	-8.500	3.000	-2.521	3.185e-01	3.612e+00
0.913	0.200	1.990	8.500	-8.500	3.000	-2.015	2.585e-01	9.026e-01
0.000	0.200	2.021	8.500	-7.500	1.500	-3.976	-NaN	-NaN
0.165	0.200	2.021	8.500	-7.500	1.500	-3.445	1.701e+03	3.083e+05
0.390	0.200	2.021	8.500	-7.500	1.500	-2.963	1.131e+03	1.201e+05
0.533	0.200	2.021	8.500	-7.500	1.500	-2.484	1.496e+02	7.397e+03
0.544	0.200	2.021	8.500	-7.500	1.500	-2.015	2.864e+00	4.525e+01
0.140	0.200	2.021	8.500	-7.500	2.000	-3.859	8.883e+03	1.437e+07
0.480	0.200	2.021	8.500	-7.500	2.000	-3.370	8.971e+03	4.490e+06
0.682	0.200	2.021	8.500	-7.500	2.000	-2.927	2.917e+03	5.157e+05
0.726	0.200	2.021	8.500	-7.500	2.000	-2.484	6.196e+01	3.312e+03
0.726	0.200	2.021	8.500	-7.500	2.000	-2.007	4.241e+00	6.576e+01
0.528	0.200	2.021	8.500	-7.500	2.500	-3.803	1.749e+04	4.763e+07
0.761	0.200	2.021	8.500	-7.500	2.500	-3.352	9.074e+03	5.026e+06
0.813	0.200	2.021	8.500	-7.500	2.500	-2.957	2.450e+02	3.711e+04
0.815	0.200	2.021	8.500	-7.500	2.500	-2.527	5.907e+00	2.618e+02
0.815	0.200	2.021	8.500	-7.500	2.500	-2.061	1.261e+00	1.745e+01
0.780	0.200	2.021	8.500	-7.500	3.000	-3.843	1.122e+04	1.680e+07
0.841	0.200	2.021	8.500	-7.500	3.000	-3.474	3.261e+02	1.268e+05
0.843	0.200	2.021	8.500	-7.500	3.000	-2.995	1.416e+00	1.320e+02

0.843	0.200	2.021	8.500	-7.500	3.000	-2.525	4.122e-01	1.182e+01
0.843	0.200	2.021	8.500	-7.500	3.000	-2.070	2.795e-01	2.730e+00
0.599	0.200	1.984	9.000	-9.500	1.500	-3.967	5.586e+02	2.369e+04
0.702	0.200	1.984	9.000	-9.500	1.500	-3.492	1.049e+02	2.043e+03
0.711	0.200	1.984	9.000	-9.500	1.500	-3.019	8.010e+00	5.122e+01
0.711	0.200	1.984	9.000	-9.500	1.500	-2.568	1.343e+00	2.959e+00
0.711	0.200	1.984	9.000	-9.500	1.500	-2.022	5.365e-01	3.331e-01
0.800	0.200	1.984	9.000	-9.500	2.000	-3.961	9.086e+02	5.713e+04
0.840	0.200	1.984	9.000	-9.500	2.000	-3.499	8.712e+01	2.049e+03
0.842	0.200	1.984	9.000	-9.500	2.000	-3.041	5.628e+00	4.292e+01
0.842	0.200	1.984	9.000	-9.500	2.000	-2.566	1.651e+00	4.088e+00
0.842	0.200	1.984	9.000	-9.500	2.000	-2.018	7.074e-01	4.903e-01
0.890	0.200	1.984	9.000	-9.500	2.500	-4.008	3.114e+02	2.528e+04
0.898	0.200	1.984	9.000	-9.500	2.500	-3.552	1.416e+01	3.758e+02
0.898	0.200	1.984	9.000	-9.500	2.500	-3.045	1.092e+00	8.467e+00
0.898	0.200	1.984	9.000	-9.500	2.500	-2.527	4.298e-01	9.902e-01
0.898	0.200	1.984	9.000	-9.500	2.500	-2.043	3.406e-01	2.564e-01
0.922	0.200	1.984	9.000	-9.500	3.000	-4.027	1.547e+01	1.232e+03
0.922	0.200	1.984	9.000	-9.500	3.000	-3.544	4.737e-01	1.143e+01
0.922	0.200	1.984	9.000	-9.500	3.000	-3.014	2.477e-01	1.718e+00
0.922	0.200	1.984	9.000	-9.500	3.000	-2.574	2.155e-01	5.388e-01
0.922	0.200	1.984	9.000	-9.500	3.000	-2.089	2.064e-01	1.685e-01
0.119	0.200	1.993	9.000	-8.500	1.500	-3.962	7.650e+02	3.479e+04
0.280	0.200	1.993	9.000	-8.500	1.500	-3.486	4.333e+02	1.237e+04
0.405	0.200	1.993	9.000	-8.500	1.500	-3.020	1.163e+02	1.690e+03
0.422	0.200	1.993	9.000	-8.500	1.500	-2.517	7.407e+00	3.357e+01
0.422	0.200	1.993	9.000	-8.500	1.500	-2.012	1.210e+00	1.663e+00
0.472	0.200	1.993	9.000	-8.500	2.000	-3.937	1.889e+03	2.161e+05
0.638	0.200	1.993	9.000	-8.500	2.000	-3.479	4.005e+02	2.252e+04
0.668	0.200	1.993	9.000	-8.500	2.000	-2.992	1.783e+01	3.198e+02
0.668	0.200	1.993	9.000	-8.500	2.000	-2.561	1.956e+00	1.233e+01
0.668	0.200	1.993	9.000	-8.500	2.000	-2.035	5.766e-01	1.057e+00
0.831	0.200	1.993	9.000	-8.500	2.500	-3.970	5.219e+02	1.005e+05
0.844	0.200	1.993	9.000	-8.500	2.500	-3.492	6.973e+00	4.030e+02
0.844	0.200	1.993	9.000	-8.500	2.500	-3.013	5.984e-01	1.069e+01
0.844	0.200	1.993	9.000	-8.500	2.500	-2.518	3.023e-01	1.690e+00
0.844	0.200	1.993	9.000	-8.500	2.500	-2.051	2.555e-01	4.846e-01
0.895	0.200	1.993	9.000	-8.500	3.000	-3.970	6.737e+01	1.156e+04
0.895	0.200	1.993	9.000	-8.500	3.000	-3.536	1.095e+00	6.068e+01
0.895	0.200	1.993	9.000	-8.500	3.000	-3.076	3.297e-01	6.016e+00
0.895	0.200	1.993	9.000	-8.500	3.000	-2.538	2.366e-01	1.229e+00
0.895	0.200	1.993	9.000	-8.500	3.000	-2.042	2.194e-01	3.617e-01
0.009	0.200	2.079	9.000	-7.500	1.500	-3.969	6.309e+02	2.576e+05
0.170	0.200	2.079	9.000	-7.500	1.500	-3.444	1.153e+03	1.404e+05
0.365	0.200	2.079	9.000	-7.500	1.500	-2.966	5.408e+02	4.017e+04
0.467	0.200	2.079	9.000	-7.500	1.500	-2.513	6.703e+01	2.262e+03
0.471	0.200	2.079	9.000	-7.500	1.500	-2.041	1.551e+00	1.660e+01
0.160	0.200	2.079	9.000	-7.500	2.000	-3.848	9.786e+03	1.025e+07
0.472	0.200	2.079	9.000	-7.500	2.000	-3.362	7.632e+03	2.557e+06
0.648	0.200	2.079	9.000	-7.500	2.000	-2.933	1.941e+03	2.355e+05
0.682	0.200	2.079	9.000	-7.500	2.000	-2.508	5.499e+01	2.112e+03
0.682	0.200	2.079	9.000	-7.500	2.000	-2.002	5.456e+00	5.746e+01
0.570	0.200	2.079	9.000	-7.500	2.500	-3.811	1.269e+04	1.852e+07
0.758	0.200	2.079	9.000	-7.500	2.500	-3.394	5.297e+03	2.021e+06
0.798	0.200	2.079	9.000	-7.500	2.500	-2.977	9.827e+01	1.050e+04
0.798	0.200	2.079	9.000	-7.500	2.500	-2.529	3.856e+00	1.214e+02
0.798	0.200	2.079	9.000	-7.500	2.500	-2.050	8.846e-01	8.648e+00

0.794	0.200	2.079	9.000	-7.500	3.000	-3.893	7.634e+03	7.905e+06
0.839	0.200	2.079	9.000	-7.500	3.000	-3.453	5.531e+01	1.344e+04
0.840	0.200	2.079	9.000	-7.500	3.000	-3.010	9.308e-01	6.581e+01
0.840	0.200	2.079	9.000	-7.500	3.000	-2.532	3.448e-01	7.537e+00
0.840	0.200	2.079	9.000	-7.500	3.000	-2.072	2.599e-01	1.931e+00
0.000	0.500	1.988	8.000	-9.500	1.500	-3.769	1.256e+07	0.000e+00
0.453	0.500	1.988	8.000	-9.500	1.500	-3.277	6.950e+05	2.412e+09
0.752	0.500	1.988	8.000	-9.500	1.500	-2.821	7.223e+04	5.961e+07
0.871	0.500	1.988	8.000	-9.500	1.500	-2.407	2.268e+04	5.044e+06
0.918	0.500	1.988	8.000	-9.500	1.500	-2.016	1.003e+04	8.648e+05
0.427	0.500	1.988	8.000	-9.500	2.000	-3.753	5.458e+05	6.832e+09
0.758	0.500	1.988	8.000	-9.500	2.000	-3.287	5.400e+04	1.542e+08
0.876	0.500	1.988	8.000	-9.500	2.000	-2.886	1.708e+04	1.282e+07
0.920	0.500	1.988	8.000	-9.500	2.000	-2.471	3.404e+03	8.825e+05
0.933	0.500	1.988	8.000	-9.500	2.000	-2.045	2.354e+02	2.187e+04
0.679	0.500	1.988	8.000	-9.500	2.500	-3.792	4.392e+04	3.950e+08
0.856	0.500	1.988	8.000	-9.500	2.500	-3.382	1.603e+04	3.730e+07
0.912	0.500	1.988	8.000	-9.500	2.500	-2.986	2.120e+03	1.734e+06
0.925	0.500	1.988	8.000	-9.500	2.500	-2.538	5.750e+01	1.502e+04
0.925	0.500	1.988	8.000	-9.500	2.500	-2.088	1.913e+00	1.619e+02
0.708	0.500	1.988	8.000	-9.500	3.000	-3.857	2.593e+04	1.178e+08
0.855	0.500	1.988	8.000	-9.500	3.000	-3.458	2.262e+03	4.053e+06
0.881	0.500	1.988	8.000	-9.500	3.000	-3.018	2.327e+01	1.356e+04
0.881	0.500	1.988	8.000	-9.500	3.000	-2.532	2.901e-01	4.929e+01
0.881	0.500	1.988	8.000	-9.500	3.000	-2.064	1.299e-01	7.251e+00
0.209	0.500	1.989	8.000	-8.500	1.500	-3.779	1.640e+05	1.149e+09
0.610	0.500	1.989	8.000	-8.500	1.500	-3.300	4.987e+04	1.226e+08
0.809	0.500	1.989	8.000	-8.500	1.500	-2.878	1.787e+04	1.502e+07
0.890	0.500	1.989	8.000	-8.500	1.500	-2.473	7.124e+03	2.295e+06
0.919	0.500	1.989	8.000	-8.500	1.500	-2.003	4.477e+02	4.924e+04
0.522	0.500	1.989	8.000	-8.500	2.000	-3.760	1.551e+05	1.788e+09
0.799	0.500	1.989	8.000	-8.500	2.000	-3.292	3.161e+04	8.234e+07
0.889	0.500	1.989	8.000	-8.500	2.000	-2.923	1.258e+04	1.074e+07
0.926	0.500	1.989	8.000	-8.500	2.000	-2.450	8.367e+02	2.205e+05
0.931	0.500	1.989	8.000	-8.500	2.000	-2.025	4.988e+01	4.518e+03
0.711	0.500	1.989	8.000	-8.500	2.500	-3.796	4.527e+04	4.260e+08
0.874	0.500	1.989	8.000	-8.500	2.500	-3.390	1.650e+04	4.021e+07
0.928	0.500	1.989	8.000	-8.500	2.500	-2.932	1.342e+03	9.825e+05
0.935	0.500	1.989	8.000	-8.500	2.500	-2.555	6.072e+01	1.695e+04
0.936	0.500	1.989	8.000	-8.500	2.500	-2.012	1.197e+00	8.625e+01
0.711	0.500	1.989	8.000	-8.500	3.000	-3.843	2.700e+04	1.296e+08
0.858	0.500	1.989	8.000	-8.500	3.000	-3.438	2.413e+03	4.280e+06
0.883	0.500	1.989	8.000	-8.500	3.000	-2.988	2.417e+01	1.355e+04
0.883	0.500	1.989	8.000	-8.500	3.000	-2.492	3.067e-01	4.909e+01
0.883	0.500	1.989	8.000	-8.500	3.000	-2.017	1.352e-01	7.005e+00
0.000	0.500	1.999	8.000	-7.500	1.500	-3.953	-NaN	-NaN
0.208	0.500	1.999	8.000	-7.500	1.500	-3.343	1.286e+04	2.164e+07
0.503	0.500	1.999	8.000	-7.500	1.500	-2.874	1.002e+04	8.002e+06
0.695	0.500	1.999	8.000	-7.500	1.500	-2.448	4.336e+03	1.775e+06
0.770	0.500	1.999	8.000	-7.500	1.500	-1.999	2.900e+02	4.812e+04
0.043	0.500	1.999	8.000	-7.500	2.000	-3.865	1.999e+05	3.275e+09
0.484	0.500	1.999	8.000	-7.500	2.000	-3.294	3.651e+04	1.336e+08
0.729	0.500	1.999	8.000	-7.500	2.000	-2.855	1.517e+04	1.661e+07
0.825	0.500	1.999	8.000	-7.500	2.000	-2.447	2.954e+03	1.198e+06
0.849	0.500	1.999	8.000	-7.500	2.000	-2.041	1.501e+02	2.239e+04
0.443	0.500	1.999	8.000	-7.500	2.500	-3.820	6.477e+04	9.549e+08
0.778	0.500	1.999	8.000	-7.500	2.500	-3.322	1.906e+04	5.734e+07

0.872	0.500	1.999	8.000	-7.500	2.500	-2.937	3.719e+03	3.963e+06
0.896	0.500	1.999	8.000	-7.500	2.500	-2.475	7.484e+01	2.429e+04
0.896	0.500	1.999	8.000	-7.500	2.500	-2.061	3.009e+00	3.392e+02
0.468	0.500	1.999	8.000	-7.500	3.000	-3.831	3.032e+04	1.906e+08
0.734	0.500	1.999	8.000	-7.500	3.000	-3.445	7.399e+03	1.782e+07
0.812	0.500	1.999	8.000	-7.500	3.000	-2.979	5.986e+01	4.653e+04
0.813	0.500	1.999	8.000	-7.500	3.000	-2.553	4.975e-01	1.265e+02
0.813	0.500	1.999	8.000	-7.500	3.000	-2.037	1.307e-01	9.592e+00
0.631	0.500	1.987	8.500	-9.500	1.500	-3.833	2.058e+04	1.495e+07
0.831	0.500	1.987	8.500	-9.500	1.500	-3.381	1.340e+04	4.075e+06
0.905	0.500	1.987	8.500	-9.500	1.500	-2.956	5.013e+03	7.015e+05
0.933	0.500	1.987	8.500	-9.500	1.500	-2.546	8.493e+02	5.468e+04
0.941	0.500	1.987	8.500	-9.500	1.500	-2.048	9.489e+01	2.005e+03
0.879	0.500	1.987	8.500	-9.500	2.000	-3.839	1.296e+04	1.402e+07
0.931	0.500	1.987	8.500	-9.500	2.000	-3.447	4.744e+03	2.177e+06
0.951	0.500	1.987	8.500	-9.500	2.000	-3.016	5.315e+02	9.910e+04
0.956	0.500	1.987	8.500	-9.500	2.000	-2.492	3.247e+01	1.766e+03
0.956	0.500	1.987	8.500	-9.500	2.000	-2.099	4.067e+00	8.649e+01
0.940	0.500	1.987	8.500	-9.500	2.500	-3.918	5.260e+03	6.692e+06
0.962	0.500	1.987	8.500	-9.500	2.500	-3.491	5.461e+02	2.920e+05
0.966	0.500	1.987	8.500	-9.500	2.500	-3.023	2.404e+01	4.296e+03
0.966	0.500	1.987	8.500	-9.500	2.500	-2.567	9.478e-01	5.627e+01
0.966	0.500	1.987	8.500	-9.500	2.500	-2.065	2.420e-01	4.429e+00
0.945	0.500	1.987	8.500	-9.500	3.000	-3.973	1.040e+03	1.301e+06
0.956	0.500	1.987	8.500	-9.500	3.000	-3.503	2.152e+01	9.413e+03
0.956	0.500	1.987	8.500	-9.500	3.000	-3.001	3.714e-01	4.763e+01
0.956	0.500	1.987	8.500	-9.500	3.000	-2.525	1.258e-01	5.264e+00
0.956	0.500	1.987	8.500	-9.500	3.000	-2.009	1.010e-01	1.279e+00
0.241	0.500	1.989	8.500	-8.500	1.500	-3.876	9.115e+03	4.968e+06
0.518	0.500	1.989	8.500	-8.500	1.500	-3.421	6.708e+03	2.106e+06
0.711	0.500	1.989	8.500	-8.500	1.500	-2.955	2.148e+03	3.688e+05
0.786	0.500	1.989	8.500	-8.500	1.500	-2.514	2.727e+02	2.157e+04
0.797	0.500	1.989	8.500	-8.500	1.500	-2.027	2.515e+01	6.417e+02
0.619	0.500	1.989	8.500	-8.500	2.000	-3.877	1.090e+04	1.287e+07
0.804	0.500	1.989	8.500	-8.500	2.000	-3.414	5.406e+03	2.750e+06
0.866	0.500	1.989	8.500	-8.500	2.000	-3.020	9.147e+02	2.205e+05
0.884	0.500	1.989	8.500	-8.500	2.000	-2.511	4.993e+01	3.804e+03
0.885	0.500	1.989	8.500	-8.500	2.000	-2.077	3.626e+00	9.715e+01
0.817	0.500	1.989	8.500	-8.500	2.500	-3.931	5.454e+03	7.640e+06
0.903	0.500	1.989	8.500	-8.500	2.500	-3.486	1.062e+03	7.118e+05
0.922	0.500	1.989	8.500	-8.500	2.500	-2.992	3.483e+01	7.919e+03
0.923	0.500	1.989	8.500	-8.500	2.500	-2.525	1.105e+00	8.067e+01
0.923	0.500	1.989	8.500	-8.500	2.500	-2.075	2.427e-01	6.157e+00
0.921	0.500	1.989	8.500	-8.500	3.000	-3.958	1.453e+03	2.035e+06
0.939	0.500	1.989	8.500	-8.500	3.000	-3.488	2.874e+01	1.409e+04
0.939	0.500	1.989	8.500	-8.500	3.000	-3.074	6.652e-01	1.171e+02
0.939	0.500	1.989	8.500	-8.500	3.000	-2.506	1.370e-01	6.293e+00
0.939	0.500	1.989	8.500	-8.500	3.000	-2.094	1.068e-01	1.886e+00
0.000	0.500	2.017	8.500	-7.500	1.500	-3.971	-NaN	-NaN
0.142	0.500	2.017	8.500	-7.500	1.500	-3.421	5.815e+03	3.181e+06
0.366	0.500	2.017	8.500	-7.500	1.500	-2.956	3.998e+03	1.344e+06
0.560	0.500	2.017	8.500	-7.500	1.500	-2.468	8.511e+02	1.524e+05
0.616	0.500	2.017	8.500	-7.500	1.500	-1.997	5.425e+01	3.655e+03
0.110	0.500	2.017	8.500	-7.500	2.000	-3.879	2.544e+04	8.722e+07
0.432	0.500	2.017	8.500	-7.500	2.000	-3.385	1.212e+04	1.404e+07
0.650	0.500	2.017	8.500	-7.500	2.000	-2.959	6.266e+03	3.258e+06
0.751	0.500	2.017	8.500	-7.500	2.000	-2.476	4.675e+02	9.089e+04

0.763	0.500	2.017	8.500	-7.500	2.000	-2.053	3.012e+01	2.095e+03
0.519	0.500	2.017	8.500	-7.500	2.500	-3.874	1.142e+04	3.861e+07
0.777	0.500	2.017	8.500	-7.500	2.500	-3.416	5.765e+03	7.926e+06
0.853	0.500	2.017	8.500	-7.500	2.500	-2.961	3.391e+02	1.800e+05
0.861	0.500	2.017	8.500	-7.500	2.500	-2.555	1.181e+01	2.287e+03
0.861	0.500	2.017	8.500	-7.500	2.500	-2.063	4.482e-01	2.630e+01
0.710	0.500	2.017	8.500	-7.500	3.000	-3.907	1.228e+04	3.359e+07
0.835	0.500	2.017	8.500	-7.500	3.000	-3.488	5.556e+02	6.729e+05
0.849	0.500	2.017	8.500	-7.500	3.000	-3.030	4.732e+00	1.812e+03
0.849	0.500	2.017	8.500	-7.500	3.000	-2.539	1.836e-01	2.110e+01
0.849	0.500	2.017	8.500	-7.500	3.000	-2.070	1.128e-01	4.312e+00
0.427	0.500	1.984	9.000	-9.500	1.500	-3.973	1.412e+03	1.134e+05
0.630	0.500	1.984	9.000	-9.500	1.500	-3.521	5.395e+02	2.815e+04
0.727	0.500	1.984	9.000	-9.500	1.500	-3.047	1.213e+02	3.008e+03
0.743	0.500	1.984	9.000	-9.500	1.500	-2.511	1.594e+01	1.194e+02
0.743	0.500	1.984	9.000	-9.500	1.500	-2.024	3.207e+00	7.708e+00
0.828	0.500	1.984	9.000	-9.500	2.000	-3.969	5.811e+02	1.175e+05
0.875	0.500	1.984	9.000	-9.500	2.000	-3.504	7.937e+01	7.166e+03
0.881	0.500	1.984	9.000	-9.500	2.000	-3.073	1.051e+01	3.532e+02
0.881	0.500	1.984	9.000	-9.500	2.000	-2.565	7.579e-01	7.747e+00
0.881	0.500	1.984	9.000	-9.500	2.000	-2.090	2.888e-01	9.804e-01
0.920	0.500	1.984	9.000	-9.500	2.500	-4.009	1.258e+02	3.673e+04
0.929	0.500	1.984	9.000	-9.500	2.500	-3.517	7.435e+00	7.461e+02
0.929	0.500	1.984	9.000	-9.500	2.500	-3.063	3.889e-01	1.334e+01
0.929	0.500	1.984	9.000	-9.500	2.500	-2.534	1.386e-01	1.393e+00
0.929	0.500	1.984	9.000	-9.500	2.500	-2.045	1.118e-01	3.625e-01
0.931	0.500	1.984	9.000	-9.500	3.000	-4.028	1.625e+01	4.822e+03
0.931	0.500	1.984	9.000	-9.500	3.000	-3.504	2.949e-01	2.494e+01
0.931	0.500	1.984	9.000	-9.500	3.000	-3.022	1.078e-01	2.956e+00
0.931	0.500	1.984	9.000	-9.500	3.000	-2.566	8.673e-02	8.279e-01
0.931	0.500	1.984	9.000	-9.500	3.000	-2.068	8.420e-02	2.547e-01
0.111	0.500	1.992	9.000	-8.500	1.500	-3.930	4.482e+03	6.229e+05
0.284	0.500	1.992	9.000	-8.500	1.500	-3.455	2.145e+03	1.919e+05
0.443	0.500	1.992	9.000	-8.500	1.500	-2.995	5.659e+02	2.890e+04
0.513	0.500	1.992	9.000	-8.500	1.500	-2.519	9.343e+01	1.928e+03
0.518	0.500	1.992	9.000	-8.500	1.500	-2.000	1.019e+01	6.249e+01
0.469	0.500	1.992	9.000	-8.500	2.000	-3.955	2.531e+03	8.147e+05
0.658	0.500	1.992	9.000	-8.500	2.000	-3.473	5.610e+02	9.754e+04
0.721	0.500	1.992	9.000	-8.500	2.000	-3.007	6.220e+01	4.424e+03
0.725	0.500	1.992	9.000	-8.500	2.000	-2.573	6.406e+00	1.633e+02
0.725	0.500	1.992	9.000	-8.500	2.000	-2.062	7.097e-01	5.471e+00
0.755	0.500	1.992	9.000	-8.500	2.500	-3.990	6.827e+02	3.437e+05
0.839	0.500	1.992	9.000	-8.500	2.500	-3.538	8.073e+01	2.010e+04
0.848	0.500	1.992	9.000	-8.500	2.500	-2.996	1.622e+00	1.139e+02
0.848	0.500	1.992	9.000	-8.500	2.500	-2.544	2.173e-01	5.272e+00
0.848	0.500	1.992	9.000	-8.500	2.500	-2.019	1.243e-01	8.908e-01
0.884	0.500	1.992	9.000	-8.500	3.000	-4.000	7.112e+01	4.084e+04
0.889	0.500	1.992	9.000	-8.500	3.000	-3.537	1.274e+00	2.442e+02
0.889	0.500	1.992	9.000	-8.500	3.000	-3.055	1.383e-01	8.480e+00
0.889	0.500	1.992	9.000	-8.500	3.000	-2.500	9.125e-02	1.543e+00
0.889	0.500	1.992	9.000	-8.500	3.000	-2.097	8.691e-02	5.795e-01
0.000	0.500	2.064	9.000	-7.500	1.500	-3.974	1.268e+04	0.000e+00
0.126	0.500	2.064	9.000	-7.500	1.500	-3.398	9.061e+03	3.625e+06
0.316	0.500	2.064	9.000	-7.500	1.500	-2.936	5.602e+03	1.294e+06
0.474	0.500	2.064	9.000	-7.500	1.500	-2.500	1.286e+03	1.608e+05
0.537	0.500	2.064	9.000	-7.500	1.500	-2.049	1.148e+02	5.742e+03
0.141	0.500	2.064	9.000	-7.500	2.000	-3.876	1.250e+04	2.245e+07

0.438	0.500	2.064	9.000	-7.500	2.000	-3.394	8.722e+03	6.464e+06
0.638	0.500	2.064	9.000	-7.500	2.000	-2.941	2.707e+03	9.360e+05
0.712	0.500	2.064	9.000	-7.500	2.000	-2.488	1.834e+02	2.494e+04
0.717	0.500	2.064	9.000	-7.500	2.000	-2.055	1.387e+01	6.572e+02
0.548	0.500	2.064	9.000	-7.500	2.500	-3.892	7.889e+03	1.695e+07
0.766	0.500	2.064	9.000	-7.500	2.500	-3.452	3.085e+03	3.186e+06
0.832	0.500	2.064	9.000	-7.500	2.500	-2.980	1.222e+02	4.736e+04
0.835	0.500	2.064	9.000	-7.500	2.500	-2.566	3.460e+00	4.801e+02
0.835	0.500	2.064	9.000	-7.500	2.500	-2.070	3.215e-01	1.362e+01
0.689	0.500	2.064	9.000	-7.500	3.000	-3.956	6.390e+03	1.345e+07
0.802	0.500	2.064	9.000	-7.500	3.000	-3.524	1.886e+02	1.757e+05
0.810	0.500	2.064	9.000	-7.500	3.000	-3.061	1.165e+00	3.387e+02
0.810	0.500	2.064	9.000	-7.500	3.000	-2.570	1.513e-01	1.350e+01
0.810	0.500	2.064	9.000	-7.500	3.000	-2.005	9.999e-02	2.387e+00
0.000	0.800	1.988	8.000	-9.500	1.500	-3.767	5.765e+06	0.000e+00
0.578	0.800	1.988	8.000	-9.500	1.500	-3.264	2.494e+05	9.234e+08
0.812	0.800	1.988	8.000	-9.500	1.500	-2.811	3.799e+04	3.523e+07
0.905	0.800	1.988	8.000	-9.500	1.500	-2.383	1.723e+04	5.509e+06
0.942	0.800	1.988	8.000	-9.500	1.500	-1.962	8.570e+03	1.201e+06
0.598	0.800	1.988	8.000	-9.500	2.000	-3.752	2.587e+05	3.496e+09
0.821	0.800	1.988	8.000	-9.500	2.000	-3.337	4.873e+04	1.858e+08
0.915	0.800	1.988	8.000	-9.500	2.000	-2.924	1.765e+04	2.215e+07
0.951	0.800	1.988	8.000	-9.500	2.000	-2.485	4.709e+03	2.371e+06
0.963	0.800	1.988	8.000	-9.500	2.000	-2.042	4.822e+02	9.715e+04
0.681	0.800	1.988	8.000	-9.500	2.500	-3.801	5.233e+04	4.758e+08
0.868	0.800	1.988	8.000	-9.500	2.500	-3.376	1.671e+04	5.205e+07
0.923	0.800	1.988	8.000	-9.500	2.500	-3.010	3.244e+03	4.925e+06
0.944	0.800	1.988	8.000	-9.500	2.500	-2.541	1.522e+02	8.555e+04
0.945	0.800	1.988	8.000	-9.500	2.500	-2.079	7.234e+00	1.325e+03
0.656	0.800	1.988	8.000	-9.500	3.000	-3.859	3.157e+04	1.760e+08
0.835	0.800	1.988	8.000	-9.500	3.000	-3.482	3.968e+03	1.168e+07
0.890	0.800	1.988	8.000	-9.500	3.000	-3.018	8.328e+01	9.822e+04
0.892	0.800	1.988	8.000	-9.500	3.000	-2.513	7.472e-01	2.533e+02
0.892	0.800	1.988	8.000	-9.500	3.000	-2.031	1.018e-01	1.104e+01
0.100	0.800	1.989	8.000	-8.500	1.500	-3.809	4.097e+05	4.276e+09
0.505	0.800	1.989	8.000	-8.500	1.500	-3.300	7.207e+04	2.441e+08
0.743	0.800	1.989	8.000	-8.500	1.500	-2.874	2.549e+04	2.946e+07
0.856	0.800	1.989	8.000	-8.500	1.500	-2.471	1.263e+04	6.199e+06
0.906	0.800	1.989	8.000	-8.500	1.500	-2.032	3.041e+03	6.423e+05
0.362	0.800	1.989	8.000	-8.500	2.000	-3.809	1.688e+05	2.232e+09
0.724	0.800	1.989	8.000	-8.500	2.000	-3.328	3.829e+04	1.388e+08
0.863	0.800	1.989	8.000	-8.500	2.000	-2.935	1.608e+04	2.251e+07
0.921	0.800	1.989	8.000	-8.500	2.000	-2.488	3.909e+03	2.231e+06
0.940	0.800	1.989	8.000	-8.500	2.000	-1.997	2.598e+02	5.296e+04
0.627	0.800	1.989	8.000	-8.500	2.500	-3.800	5.522e+04	5.306e+08
0.839	0.800	1.989	8.000	-8.500	2.500	-3.374	1.750e+04	5.605e+07
0.913	0.800	1.989	8.000	-8.500	2.500	-2.939	2.349e+03	3.180e+06
0.931	0.800	1.989	8.000	-8.500	2.500	-2.542	1.616e+02	9.327e+04
0.932	0.800	1.989	8.000	-8.500	2.500	-2.080	7.550e+00	1.421e+03
0.679	0.800	1.989	8.000	-8.500	3.000	-3.856	3.259e+04	1.898e+08
0.849	0.800	1.989	8.000	-8.500	3.000	-3.481	4.321e+03	1.295e+07
0.900	0.800	1.989	8.000	-8.500	3.000	-3.019	8.887e+01	1.069e+05
0.902	0.800	1.989	8.000	-8.500	3.000	-2.514	7.835e-01	2.708e+02
0.902	0.800	1.989	8.000	-8.500	3.000	-2.033	1.132e-01	1.250e+01
0.000	0.800	1.999	8.000	-7.500	1.500	-3.756	-NaN	-NaN
0.049	0.800	1.999	8.000	-7.500	1.500	-3.351	9.108e+04	3.540e+08
0.285	0.800	1.999	8.000	-7.500	1.500	-2.829	2.836e+04	3.437e+07

0.512	0.800	1.999	8.000	-7.500	1.500	-2.410	1.720e+04	9.197e+06
0.671	0.800	1.999	8.000	-7.500	1.500	-1.961	6.519e+03	1.562e+06
0.042	0.800	1.999	8.000	-7.500	2.000	-3.873	2.226e+05	4.457e+09
0.407	0.800	1.999	8.000	-7.500	2.000	-3.338	4.459e+04	2.198e+08
0.684	0.800	1.999	8.000	-7.500	2.000	-2.880	1.763e+04	2.956e+07
0.801	0.800	1.999	8.000	-7.500	2.000	-2.495	5.898e+03	4.619e+06
0.854	0.800	1.999	8.000	-7.500	2.000	-1.987	3.481e+02	9.504e+04
0.440	0.800	1.999	8.000	-7.500	2.500	-3.807	6.185e+04	7.828e+08
0.741	0.800	1.999	8.000	-7.500	2.500	-3.387	2.567e+04	1.103e+08
0.878	0.800	1.999	8.000	-7.500	2.500	-2.930	3.866e+03	6.823e+06
0.909	0.800	1.999	8.000	-7.500	2.500	-2.513	2.132e+02	1.562e+05
0.912	0.800	1.999	8.000	-7.500	2.500	-1.999	5.172e+00	1.081e+03
0.613	0.800	1.999	8.000	-7.500	3.000	-3.835	4.849e+04	3.556e+08
0.817	0.800	1.999	8.000	-7.500	3.000	-3.460	7.295e+03	2.500e+07
0.886	0.800	1.999	8.000	-7.500	3.000	-3.000	1.486e+02	2.068e+05
0.889	0.800	1.999	8.000	-7.500	3.000	-2.494	1.294e+00	5.124e+02
0.889	0.800	1.999	8.000	-7.500	3.000	-2.009	1.255e-01	1.569e+01
0.632	0.800	1.987	8.500	-9.500	1.500	-3.871	1.561e+04	1.595e+07
0.831	0.800	1.987	8.500	-9.500	1.500	-3.402	1.129e+04	5.516e+06
0.901	0.800	1.987	8.500	-9.500	1.500	-3.008	5.046e+03	1.347e+06
0.937	0.800	1.987	8.500	-9.500	1.500	-2.502	7.667e+02	8.722e+04
0.946	0.800	1.987	8.500	-9.500	1.500	-2.069	1.283e+02	5.968e+03
0.788	0.800	1.987	8.500	-9.500	2.000	-3.912	8.566e+03	1.222e+07
0.901	0.800	1.987	8.500	-9.500	2.000	-3.460	4.404e+03	3.339e+06
0.939	0.800	1.987	8.500	-9.500	2.000	-3.033	8.823e+02	3.396e+05
0.952	0.800	1.987	8.500	-9.500	2.000	-2.491	6.386e+01	8.197e+03
0.952	0.800	1.987	8.500	-9.500	2.000	-2.038	8.783e+00	3.879e+02
0.922	0.800	1.987	8.500	-9.500	2.500	-3.947	5.707e+03	1.158e+07
0.956	0.800	1.987	8.500	-9.500	2.500	-3.489	7.788e+02	7.525e+05
0.966	0.800	1.987	8.500	-9.500	2.500	-2.994	4.607e+01	1.623e+04
0.966	0.800	1.987	8.500	-9.500	2.500	-2.521	3.049e+00	3.502e+02
0.966	0.800	1.987	8.500	-9.500	2.500	-2.006	2.498e-01	8.625e+00
0.913	0.800	1.987	8.500	-9.500	3.000	-4.013	1.484e+03	3.126e+06
0.943	0.800	1.987	8.500	-9.500	3.000	-3.525	5.316e+01	4.807e+04
0.945	0.800	1.987	8.500	-9.500	3.000	-3.010	1.071e+00	2.857e+02
0.945	0.800	1.987	8.500	-9.500	3.000	-2.526	1.073e-01	9.187e+00
0.945	0.800	1.987	8.500	-9.500	3.000	-2.003	6.932e-02	1.772e+00
0.188	0.800	1.989	8.500	-8.500	1.500	-3.862	1.461e+04	1.392e+07
0.439	0.800	1.989	8.500	-8.500	1.500	-3.412	1.032e+04	5.266e+06
0.631	0.800	1.989	8.500	-8.500	1.500	-2.988	5.752e+03	1.657e+06
0.753	0.800	1.989	8.500	-8.500	1.500	-2.486	1.029e+03	1.354e+05
0.791	0.800	1.989	8.500	-8.500	1.500	-2.014	1.358e+02	6.932e+03
0.583	0.800	1.989	8.500	-8.500	2.000	-3.900	1.014e+04	1.743e+07
0.778	0.800	1.989	8.500	-8.500	2.000	-3.453	5.545e+03	4.932e+06
0.857	0.800	1.989	8.500	-8.500	2.000	-3.031	1.207e+03	5.462e+05
0.888	0.800	1.989	8.500	-8.500	2.000	-2.492	8.225e+01	1.268e+04
0.890	0.800	1.989	8.500	-8.500	2.000	-2.040	1.080e+01	5.745e+02
0.800	0.800	1.989	8.500	-8.500	2.500	-3.957	5.329e+03	1.135e+07
0.904	0.800	1.989	8.500	-8.500	2.500	-3.483	9.774e+02	1.147e+06
0.930	0.800	1.989	8.500	-8.500	2.500	-3.031	6.852e+01	3.477e+04
0.931	0.800	1.989	8.500	-8.500	2.500	-2.554	2.945e+00	4.842e+02
0.931	0.800	1.989	8.500	-8.500	2.500	-2.001	1.836e-01	8.275e+00
0.898	0.800	1.989	8.500	-8.500	3.000	-4.000	2.078e+03	4.895e+06
0.936	0.800	1.989	8.500	-8.500	3.000	-3.515	7.355e+01	7.526e+04
0.938	0.800	1.989	8.500	-8.500	3.000	-3.000	1.322e+00	3.993e+02
0.938	0.800	1.989	8.500	-8.500	3.000	-2.514	1.178e-01	1.135e+01
0.938	0.800	1.989	8.500	-8.500	3.000	-2.098	7.394e-02	2.715e+00

0.000	0.800	2.017	8.500	-7.500	1.500	-3.774	-NaN	-NaN
0.061	0.800	2.017	8.500	-7.500	1.500	-3.395	1.526e+04	1.431e+07
0.239	0.800	2.017	8.500	-7.500	1.500	-2.913	1.116e+04	5.280e+06
0.419	0.800	2.017	8.500	-7.500	1.500	-2.495	6.297e+03	1.746e+06
0.565	0.800	2.017	8.500	-7.500	1.500	-1.980	9.086e+02	1.114e+05
0.101	0.800	2.017	8.500	-7.500	2.000	-3.903	1.497e+04	6.098e+07
0.419	0.800	2.017	8.500	-7.500	2.000	-3.391	9.828e+03	1.616e+07
0.631	0.800	2.017	8.500	-7.500	2.000	-2.978	5.252e+03	4.785e+06
0.744	0.800	2.017	8.500	-7.500	2.000	-2.526	7.491e+02	3.191e+05
0.772	0.800	2.017	8.500	-7.500	2.000	-2.012	3.857e+01	5.282e+03
0.465	0.800	2.017	8.500	-7.500	2.500	-3.877	1.471e+04	5.765e+07
0.741	0.800	2.017	8.500	-7.500	2.500	-3.430	5.646e+03	1.200e+07
0.840	0.800	2.017	8.500	-7.500	2.500	-3.001	6.245e+02	6.700e+05
0.861	0.800	2.017	8.500	-7.500	2.500	-2.504	1.869e+01	6.624e+03
0.861	0.800	2.017	8.500	-7.500	2.500	-2.078	6.578e-01	8.404e+01
0.623	0.800	2.017	8.500	-7.500	3.000	-3.923	1.340e+04	4.851e+07
0.806	0.800	2.017	8.500	-7.500	3.000	-3.473	6.976e+02	1.386e+06
0.838	0.800	2.017	8.500	-7.500	3.000	-2.986	9.829e+00	6.662e+03
0.838	0.800	2.017	8.500	-7.500	3.000	-2.563	2.487e-01	6.048e+01
0.838	0.800	2.017	8.500	-7.500	3.000	-2.088	8.034e-02	6.411e+00
0.390	0.800	1.984	9.000	-9.500	1.500	-3.978	1.787e+03	2.614e+05
0.606	0.800	1.984	9.000	-9.500	1.500	-3.492	6.348e+02	5.909e+04
0.711	0.800	1.984	9.000	-9.500	1.500	-3.029	1.565e+02	7.400e+03
0.740	0.800	1.984	9.000	-9.500	1.500	-2.523	3.187e+01	5.215e+02
0.740	0.800	1.984	9.000	-9.500	1.500	-2.008	4.758e+00	2.352e+01
0.808	0.800	1.984	9.000	-9.500	2.000	-3.994	6.412e+02	2.434e+05
0.871	0.800	1.984	9.000	-9.500	2.000	-3.497	1.004e+02	1.764e+04
0.882	0.800	1.984	9.000	-9.500	2.000	-3.037	1.593e+01	1.035e+03
0.882	0.800	1.984	9.000	-9.500	2.000	-2.502	1.132e+00	2.111e+01
0.882	0.800	1.984	9.000	-9.500	2.000	-2.008	2.967e-01	1.762e+00
0.912	0.800	1.984	9.000	-9.500	2.500	-3.990	1.136e+02	6.133e+04
0.927	0.800	1.984	9.000	-9.500	2.500	-3.536	1.202e+01	2.626e+03
0.927	0.800	1.984	9.000	-9.500	2.500	-3.066	8.089e-01	5.874e+01
0.927	0.800	1.984	9.000	-9.500	2.500	-2.522	1.220e-01	2.510e+00
0.927	0.800	1.984	9.000	-9.500	2.500	-2.023	7.977e-02	5.185e-01
0.913	0.800	1.984	9.000	-9.500	3.000	-4.025	1.783e+01	9.640e+03
0.915	0.800	1.984	9.000	-9.500	3.000	-3.556	7.203e-01	1.299e+02
0.915	0.800	1.984	9.000	-9.500	3.000	-3.072	8.569e-02	4.988e+00
0.915	0.800	1.984	9.000	-9.500	3.000	-2.517	5.622e-02	9.063e-01
0.915	0.800	1.984	9.000	-9.500	3.000	-2.010	5.388e-02	2.699e-01
0.097	0.800	1.992	9.000	-8.500	1.500	-3.959	3.942e+03	9.652e+05
0.260	0.800	1.992	9.000	-8.500	1.500	-3.472	1.806e+03	3.000e+05
0.425	0.800	1.992	9.000	-8.500	1.500	-2.989	5.033e+02	4.887e+04
0.502	0.800	1.992	9.000	-8.500	1.500	-2.555	1.076e+02	4.920e+03
0.515	0.800	1.992	9.000	-8.500	1.500	-2.022	1.429e+01	1.954e+02
0.436	0.800	1.992	9.000	-8.500	2.000	-3.983	1.807e+03	1.073e+06
0.639	0.800	1.992	9.000	-8.500	2.000	-3.483	4.506e+02	1.534e+05
0.717	0.800	1.992	9.000	-8.500	2.000	-2.996	5.699e+01	8.305e+03
0.724	0.800	1.992	9.000	-8.500	2.000	-2.545	7.242e+00	3.741e+02
0.724	0.800	1.992	9.000	-8.500	2.000	-2.020	4.886e-01	7.418e+00
0.683	0.800	1.992	9.000	-8.500	2.500	-4.010	4.973e+02	4.539e+05
0.801	0.800	1.992	9.000	-8.500	2.500	-3.544	7.496e+01	3.715e+04
0.818	0.800	1.992	9.000	-8.500	2.500	-3.053	4.236e+00	7.117e+02
0.818	0.800	1.992	9.000	-8.500	2.500	-2.517	1.719e-01	8.218e+00
0.818	0.800	1.992	9.000	-8.500	2.500	-2.073	8.903e-02	1.521e+00
0.830	0.800	1.992	9.000	-8.500	3.000	-4.044	1.192e+02	1.303e+05
0.851	0.800	1.992	9.000	-8.500	3.000	-3.495	2.051e+00	6.846e+02

0.851	0.800	1.992	9.000	-8.500	3.000	-3.080	1.481e-01	1.863e+01
0.851	0.800	1.992	9.000	-8.500	3.000	-2.517	6.383e-02	2.177e+00
0.851	0.800	1.992	9.000	-8.500	3.000	-2.005	5.660e-02	5.918e-01
0.000	0.800	2.064	9.000	-7.500	1.500	-3.821	-NaN	-NaN
0.064	0.800	2.064	9.000	-7.500	1.500	-3.420	1.088e+04	6.475e+06
0.219	0.800	2.064	9.000	-7.500	1.500	-2.952	7.104e+03	2.460e+06
0.401	0.800	2.064	9.000	-7.500	1.500	-2.471	2.819e+03	5.486e+05
0.510	0.800	2.064	9.000	-7.500	1.500	-1.997	3.923e+02	3.479e+04
0.128	0.800	2.064	9.000	-7.500	2.000	-3.911	8.415e+03	1.987e+07
0.410	0.800	2.064	9.000	-7.500	2.000	-3.436	6.685e+03	8.200e+06
0.626	0.800	2.064	9.000	-7.500	2.000	-2.962	2.214e+03	1.457e+06
0.717	0.800	2.064	9.000	-7.500	2.000	-2.486	2.066e+02	5.822e+04
0.727	0.800	2.064	9.000	-7.500	2.000	-2.037	1.660e+01	1.649e+03
0.470	0.800	2.064	9.000	-7.500	2.500	-3.928	9.154e+03	2.638e+07
0.731	0.800	2.064	9.000	-7.500	2.500	-3.470	2.791e+03	4.776e+06
0.820	0.800	2.064	9.000	-7.500	2.500	-3.033	2.434e+02	2.043e+05
0.833	0.800	2.064	9.000	-7.500	2.500	-2.534	6.984e+00	1.858e+03
0.833	0.800	2.064	9.000	-7.500	2.500	-2.018	2.228e-01	1.753e+01
0.629	0.800	2.064	9.000	-7.500	3.000	-3.963	6.695e+03	1.955e+07
0.792	0.800	2.064	9.000	-7.500	3.000	-3.496	2.523e+02	3.933e+05
0.811	0.800	2.064	9.000	-7.500	3.000	-2.999	3.241e+00	1.602e+03
0.811	0.800	2.064	9.000	-7.500	3.000	-2.573	1.411e-01	2.521e+01
0.811	0.800	2.064	9.000	-7.500	3.000	-2.096	7.167e-02	4.214e+00
0.000	1.100	1.988	8.000	-9.500	1.500	-3.782	3.726e+06	0.000e+00
0.592	1.100	1.988	8.000	-9.500	1.500	-3.267	2.135e+05	7.724e+08
0.825	1.100	1.988	8.000	-9.500	1.500	-2.807	3.991e+04	4.085e+07
0.905	1.100	1.988	8.000	-9.500	1.500	-2.441	2.084e+04	9.711e+06
0.946	1.100	1.988	8.000	-9.500	1.500	-2.014	1.174e+04	2.585e+06
0.545	1.100	1.988	8.000	-9.500	2.000	-3.779	2.660e+05	3.826e+09
0.820	1.100	1.988	8.000	-9.500	2.000	-3.309	4.991e+04	1.913e+08
0.909	1.100	1.988	8.000	-9.500	2.000	-2.941	2.034e+04	3.428e+07
0.951	1.100	1.988	8.000	-9.500	2.000	-2.486	5.568e+03	4.156e+06
0.965	1.100	1.988	8.000	-9.500	2.000	-2.031	7.432e+02	2.383e+05
0.386	1.100	1.988	8.000	-9.500	2.500	-3.860	4.094e+04	3.366e+08
0.710	1.100	1.988	8.000	-9.500	2.500	-3.411	1.689e+04	6.527e+07
0.854	1.100	1.988	8.000	-9.500	2.500	-2.984	2.803e+03	6.092e+06
0.897	1.100	1.988	8.000	-9.500	2.500	-2.558	2.191e+02	2.224e+05
0.902	1.100	1.988	8.000	-9.500	2.500	-2.040	9.005e+00	2.733e+03
0.320	1.100	1.988	8.000	-9.500	3.000	-3.918	3.018e+04	1.619e+08
0.647	1.100	1.988	8.000	-9.500	3.000	-3.454	4.244e+03	1.473e+07
0.787	1.100	1.988	8.000	-9.500	3.000	-2.998	1.235e+02	2.220e+05
0.796	1.100	1.988	8.000	-9.500	3.000	-2.548	3.708e+00	2.274e+03
0.796	1.100	1.988	8.000	-9.500	3.000	-2.013	8.040e-02	1.388e+01
0.000	1.100	1.989	8.000	-8.500	1.500	-3.804	2.982e+06	0.000e+00
0.432	1.100	1.989	8.000	-8.500	1.500	-3.274	1.673e+05	6.290e+08
0.704	1.100	1.989	8.000	-8.500	1.500	-2.835	3.925e+04	4.656e+07
0.835	1.100	1.989	8.000	-8.500	1.500	-2.447	1.972e+04	1.039e+07
0.906	1.100	1.989	8.000	-8.500	1.500	-1.969	8.929e+03	2.055e+06
0.374	1.100	1.989	8.000	-8.500	2.000	-3.804	1.552e+05	2.017e+09
0.730	1.100	1.989	8.000	-8.500	2.000	-3.318	4.180e+04	1.635e+08
0.871	1.100	1.989	8.000	-8.500	2.000	-2.901	1.655e+04	2.823e+07
0.924	1.100	1.989	8.000	-8.500	2.000	-2.492	4.775e+03	4.052e+06
0.947	1.100	1.989	8.000	-8.500	2.000	-1.986	4.244e+02	1.386e+05
0.437	1.100	1.989	8.000	-8.500	2.500	-3.854	4.402e+04	3.896e+08
0.754	1.100	1.989	8.000	-8.500	2.500	-3.400	1.796e+04	7.085e+07
0.880	1.100	1.989	8.000	-8.500	2.500	-2.970	2.976e+03	6.447e+06
0.916	1.100	1.989	8.000	-8.500	2.500	-2.539	2.301e+02	2.298e+05

0.921	1.100	1.989	8.000	-8.500	2.500	-2.017	9.393e+00	2.776e+03
0.536	1.100	1.989	8.000	-8.500	3.000	-3.883	3.620e+04	2.541e+08
0.791	1.100	1.989	8.000	-8.500	3.000	-3.437	3.842e+03	1.422e+07
0.868	1.100	1.989	8.000	-8.500	3.000	-3.029	1.806e+02	3.417e+05
0.876	1.100	1.989	8.000	-8.500	3.000	-2.518	4.567e+00	2.570e+03
0.876	1.100	1.989	8.000	-8.500	3.000	-2.032	1.051e-01	1.868e+01
0.000	1.100	1.999	8.000	-7.500	1.500	-3.950	-NaN	-NaN
0.102	1.100	1.999	8.000	-7.500	1.500	-3.314	1.385e+05	6.459e+08
0.321	1.100	1.999	8.000	-7.500	1.500	-2.862	4.125e+04	6.752e+07
0.554	1.100	1.999	8.000	-7.500	1.500	-2.421	1.896e+04	1.311e+07
0.709	1.100	1.999	8.000	-7.500	1.500	-1.964	8.899e+03	2.856e+06
0.064	1.100	1.999	8.000	-7.500	2.000	-3.873	1.804e+05	3.392e+09
0.449	1.100	1.999	8.000	-7.500	2.000	-3.338	4.820e+04	2.461e+08
0.708	1.100	1.999	8.000	-7.500	2.000	-2.910	2.080e+04	4.542e+07
0.828	1.100	1.999	8.000	-7.500	2.000	-2.506	6.750e+03	7.509e+06
0.880	1.100	1.999	8.000	-7.500	2.000	-2.059	8.679e+02	4.299e+05
0.347	1.100	1.999	8.000	-7.500	2.500	-3.838	7.540e+04	9.731e+08
0.693	1.100	1.999	8.000	-7.500	2.500	-3.367	2.654e+04	1.252e+08
0.851	1.100	1.999	8.000	-7.500	2.500	-2.936	4.604e+03	1.111e+07
0.899	1.100	1.999	8.000	-7.500	2.500	-2.502	3.589e+02	3.961e+05
0.907	1.100	1.999	8.000	-7.500	2.500	-2.067	2.147e+01	8.689e+03
0.512	1.100	1.999	8.000	-7.500	3.000	-3.867	5.499e+04	4.503e+08
0.784	1.100	1.999	8.000	-7.500	3.000	-3.407	5.950e+03	2.508e+07
0.870	1.100	1.999	8.000	-7.500	3.000	-3.004	2.841e+02	6.050e+05
0.881	1.100	1.999	8.000	-7.500	3.000	-2.492	5.546e+00	3.496e+03
0.881	1.100	1.999	8.000	-7.500	3.000	-2.003	1.143e-01	2.243e+01
0.647	1.100	1.987	8.500	-9.500	1.500	-3.861	2.160e+04	2.759e+07
0.839	1.100	1.987	8.500	-9.500	1.500	-3.398	1.344e+04	8.042e+06
0.912	1.100	1.987	8.500	-9.500	1.500	-2.961	7.555e+03	2.357e+06
0.945	1.100	1.987	8.500	-9.500	1.500	-2.491	1.812e+03	2.711e+05
0.958	1.100	1.987	8.500	-9.500	1.500	-2.034	3.307e+02	2.157e+04
0.792	1.100	1.987	8.500	-9.500	2.000	-3.914	8.971e+03	1.675e+07
0.899	1.100	1.987	8.500	-9.500	2.000	-3.489	4.513e+03	5.042e+06
0.940	1.100	1.987	8.500	-9.500	2.000	-3.047	1.042e+03	6.205e+05
0.957	1.100	1.987	8.500	-9.500	2.000	-2.491	8.735e+01	1.844e+04
0.958	1.100	1.987	8.500	-9.500	2.000	-2.029	1.430e+01	1.039e+03
0.925	1.100	1.987	8.500	-9.500	2.500	-3.964	6.191e+03	1.646e+07
0.962	1.100	1.987	8.500	-9.500	2.500	-3.485	9.308e+02	1.295e+06
0.972	1.100	1.987	8.500	-9.500	2.500	-3.065	1.159e+02	7.650e+04
0.974	1.100	1.987	8.500	-9.500	2.500	-2.590	1.081e+01	2.442e+03
0.974	1.100	1.987	8.500	-9.500	2.500	-2.074	5.134e-01	3.476e+01
0.903	1.100	1.987	8.500	-9.500	3.000	-3.968	1.247e+03	3.348e+06
0.939	1.100	1.987	8.500	-9.500	3.000	-3.536	8.828e+01	1.251e+05
0.944	1.100	1.987	8.500	-9.500	3.000	-3.015	3.419e+00	1.481e+03
0.944	1.100	1.987	8.500	-9.500	3.000	-2.525	1.169e-01	1.608e+01
0.944	1.100	1.987	8.500	-9.500	3.000	-1.999	5.723e-02	2.329e+00
0.212	1.100	1.989	8.500	-8.500	1.500	-3.887	1.677e+04	2.120e+07
0.488	1.100	1.989	8.500	-8.500	1.500	-3.422	1.190e+04	7.988e+06
0.686	1.100	1.989	8.500	-8.500	1.500	-2.964	6.959e+03	2.576e+06
0.793	1.100	1.989	8.500	-8.500	1.500	-2.491	1.700e+03	3.149e+05
0.840	1.100	1.989	8.500	-8.500	1.500	-1.994	2.457e+02	1.846e+04
0.646	1.100	1.989	8.500	-8.500	2.000	-3.901	1.099e+04	2.353e+07
0.813	1.100	1.989	8.500	-8.500	2.000	-3.477	5.575e+03	6.986e+06
0.887	1.100	1.989	8.500	-8.500	2.000	-3.036	1.372e+03	9.137e+05
0.917	1.100	1.989	8.500	-8.500	2.000	-2.564	1.716e+02	4.922e+04
0.921	1.100	1.989	8.500	-8.500	2.000	-2.014	1.735e+01	1.428e+03
0.773	1.100	1.989	8.500	-8.500	2.500	-3.957	4.999e+03	1.315e+07

0.891	1.100	1.989	8.500	-8.500	2.500	-3.516	1.062e+03	1.814e+06
0.927	1.100	1.989	8.500	-8.500	2.500	-3.056	9.982e+01	8.172e+04
0.931	1.100	1.989	8.500	-8.500	2.500	-2.571	6.914e+00	1.888e+03
0.931	1.100	1.989	8.500	-8.500	2.500	-2.013	1.920e-01	1.423e+01
0.876	1.100	1.989	8.500	-8.500	3.000	-3.959	1.688e+03	4.913e+06
0.924	1.100	1.989	8.500	-8.500	3.000	-3.531	1.181e+02	1.853e+05
0.931	1.100	1.989	8.500	-8.500	3.000	-3.009	4.075e+00	1.977e+03
0.931	1.100	1.989	8.500	-8.500	3.000	-2.519	1.247e-01	1.913e+01
0.931	1.100	1.989	8.500	-8.500	3.000	-2.100	6.296e-02	3.658e+00
0.000	1.100	2.017	8.500	-7.500	1.500	-3.968	-NaN	-NaN
0.113	1.100	2.017	8.500	-7.500	1.500	-3.389	1.596e+04	1.949e+07
0.304	1.100	2.017	8.500	-7.500	1.500	-2.937	1.194e+04	8.154e+06
0.490	1.100	2.017	8.500	-7.500	1.500	-2.492	6.419e+03	2.472e+06
0.614	1.100	2.017	8.500	-7.500	1.500	-2.032	1.327e+03	2.518e+05
0.120	1.100	2.017	8.500	-7.500	2.000	-3.917	1.345e+04	5.471e+07
0.440	1.100	2.017	8.500	-7.500	2.000	-3.443	9.826e+03	2.055e+07
0.679	1.100	2.017	8.500	-7.500	2.000	-2.972	4.173e+03	5.033e+06
0.787	1.100	2.017	8.500	-7.500	2.000	-2.492	6.051e+02	3.504e+05
0.813	1.100	2.017	8.500	-7.500	2.000	-2.037	5.344e+01	1.199e+04
0.392	1.100	2.017	8.500	-7.500	2.500	-3.899	1.452e+04	5.748e+07
0.674	1.100	2.017	8.500	-7.500	2.500	-3.482	5.337e+03	1.439e+07
0.819	1.100	2.017	8.500	-7.500	2.500	-2.983	4.938e+02	7.050e+05
0.846	1.100	2.017	8.500	-7.500	2.500	-2.547	2.979e+01	1.737e+04
0.846	1.100	2.017	8.500	-7.500	2.500	-2.029	9.530e-01	1.628e+02
0.551	1.100	2.017	8.500	-7.500	3.000	-3.912	1.020e+04	4.192e+07
0.756	1.100	2.017	8.500	-7.500	3.000	-3.502	8.846e+02	2.357e+06
0.817	1.100	2.017	8.500	-7.500	3.000	-3.011	1.892e+01	1.975e+04
0.818	1.100	2.017	8.500	-7.500	3.000	-2.493	2.397e-01	7.199e+01
0.818	1.100	2.017	8.500	-7.500	3.000	-2.006	6.450e-02	6.215e+00
0.484	1.100	1.984	9.000	-9.500	1.500	-3.976	1.569e+03	3.409e+05
0.680	1.100	1.984	9.000	-9.500	1.500	-3.524	6.269e+02	9.127e+04
0.781	1.100	1.984	9.000	-9.500	1.500	-3.052	1.689e+02	1.293e+04
0.811	1.100	1.984	9.000	-9.500	1.500	-2.536	3.671e+01	9.938e+02
0.811	1.100	1.984	9.000	-9.500	1.500	-2.014	6.423e+00	5.186e+01
0.842	1.100	1.984	9.000	-9.500	2.000	-4.019	6.462e+02	3.758e+05
0.900	1.100	1.984	9.000	-9.500	2.000	-3.508	1.143e+02	3.178e+04
0.913	1.100	1.984	9.000	-9.500	2.000	-3.036	2.006e+01	2.106e+03
0.913	1.100	1.984	9.000	-9.500	2.000	-2.586	4.200e+00	1.551e+02
0.913	1.100	1.984	9.000	-9.500	2.000	-2.092	3.743e-01	4.410e+00
0.915	1.100	1.984	9.000	-9.500	2.500	-4.025	1.177e+02	1.003e+05
0.934	1.100	1.984	9.000	-9.500	2.500	-3.495	1.088e+01	3.415e+03
0.935	1.100	1.984	9.000	-9.500	2.500	-3.010	1.061e+00	1.075e+02
0.935	1.100	1.984	9.000	-9.500	2.500	-2.550	1.098e-01	3.833e+00
0.935	1.100	1.984	9.000	-9.500	2.500	-2.049	6.170e-02	6.781e-01
0.902	1.100	1.984	9.000	-9.500	3.000	-3.997	1.678e+01	1.229e+04
0.905	1.100	1.984	9.000	-9.500	3.000	-3.511	9.889e-01	2.355e+02
0.905	1.100	1.984	9.000	-9.500	3.000	-3.012	6.628e-02	4.932e+00
0.905	1.100	1.984	9.000	-9.500	3.000	-2.542	4.373e-02	1.099e+00
0.905	1.100	1.984	9.000	-9.500	3.000	-2.033	3.996e-02	3.109e-01
0.126	1.100	1.993	9.000	-8.500	1.500	-3.968	3.326e+03	1.110e+06
0.304	1.100	1.993	9.000	-8.500	1.500	-3.508	1.641e+03	3.913e+05
0.485	1.100	1.993	9.000	-8.500	1.500	-3.014	4.996e+02	7.091e+04
0.580	1.100	1.993	9.000	-8.500	1.500	-2.497	8.977e+01	5.328e+03
0.591	1.100	1.993	9.000	-8.500	1.500	-2.022	2.177e+01	4.444e+02
0.498	1.100	1.993	9.000	-8.500	2.000	-3.985	1.296e+03	1.067e+06
0.685	1.100	1.993	9.000	-8.500	2.000	-3.520	4.076e+02	2.087e+05
0.768	1.100	1.993	9.000	-8.500	2.000	-3.027	6.264e+01	1.453e+04

0.777	1.100	1.993	9.000	-8.500	2.000	-2.572	9.866e+00	8.238e+02
0.777	1.100	1.993	9.000	-8.500	2.000	-2.042	6.537e-01	1.593e+01
0.684	1.100	1.993	9.000	-8.500	2.500	-4.011	3.386e+02	4.160e+05
0.810	1.100	1.993	9.000	-8.500	2.500	-3.534	5.665e+01	3.949e+04
0.828	1.100	1.993	9.000	-8.500	2.500	-3.031	4.254e+00	9.996e+02
0.828	1.100	1.993	9.000	-8.500	2.500	-2.569	2.506e-01	1.996e+01
0.828	1.100	1.993	9.000	-8.500	2.500	-2.034	6.518e-02	1.504e+00
0.827	1.100	1.993	9.000	-8.500	3.000	-4.020	9.569e+01	1.317e+05
0.853	1.100	1.993	9.000	-8.500	3.000	-3.528	3.862e+00	1.956e+03
0.853	1.100	1.993	9.000	-8.500	3.000	-3.022	1.310e-01	2.025e+01
0.853	1.100	1.993	9.000	-8.500	3.000	-2.546	5.028e-02	2.586e+00
0.853	1.100	1.993	9.000	-8.500	3.000	-2.033	4.174e-02	6.565e-01
0.000	1.100	2.076	9.000	-7.500	1.500	-3.971	5.988e+04	0.000e+00
0.119	1.100	2.076	9.000	-7.500	1.500	-3.422	1.046e+04	8.508e+06
0.302	1.100	2.076	9.000	-7.500	1.500	-2.948	7.939e+03	3.910e+06
0.473	1.100	2.076	9.000	-7.500	1.500	-2.481	2.632e+03	7.241e+05
0.574	1.100	2.076	9.000	-7.500	1.500	-2.005	3.983e+02	4.992e+04
0.158	1.100	2.076	9.000	-7.500	2.000	-3.922	7.339e+03	1.815e+07
0.449	1.100	2.076	9.000	-7.500	2.000	-3.463	5.364e+03	8.314e+06
0.653	1.100	2.076	9.000	-7.500	2.000	-3.019	1.952e+03	1.856e+06
0.752	1.100	2.076	9.000	-7.500	2.000	-2.538	2.364e+02	1.045e+05
0.768	1.100	2.076	9.000	-7.500	2.000	-2.002	1.598e+01	2.132e+03
0.409	1.100	2.076	9.000	-7.500	2.500	-3.958	8.065e+03	2.491e+07
0.697	1.100	2.076	9.000	-7.500	2.500	-3.478	1.993e+03	4.201e+06
0.803	1.100	2.076	9.000	-7.500	2.500	-3.018	1.867e+02	2.049e+05
0.819	1.100	2.076	9.000	-7.500	2.500	-2.499	7.770e+00	2.677e+03
0.819	1.100	2.076	9.000	-7.500	2.500	-2.063	2.755e-01	3.404e+01
0.557	1.100	2.076	9.000	-7.500	3.000	-3.972	4.845e+03	1.568e+07
0.758	1.100	2.076	9.000	-7.500	3.000	-3.479	2.017e+02	3.870e+05
0.784	1.100	2.076	9.000	-7.500	3.000	-3.042	7.012e+00	5.215e+03
0.784	1.100	2.076	9.000	-7.500	3.000	-2.521	1.127e-01	2.437e+01
0.784	1.100	2.076	9.000	-7.500	3.000	-2.034	5.439e-02	3.792e+00

Table A.1: We present the numerical results from the simulated star forming regions using the full multi-phase interface.

Appendix B

Appendix B

B.1 Herschel PACS and IRAM reduced spectra

Below we present the available Herschel and IRAM data we have assembled for each of the 24 xCOLD-GASS galaxies, similar to Figure 4.2.

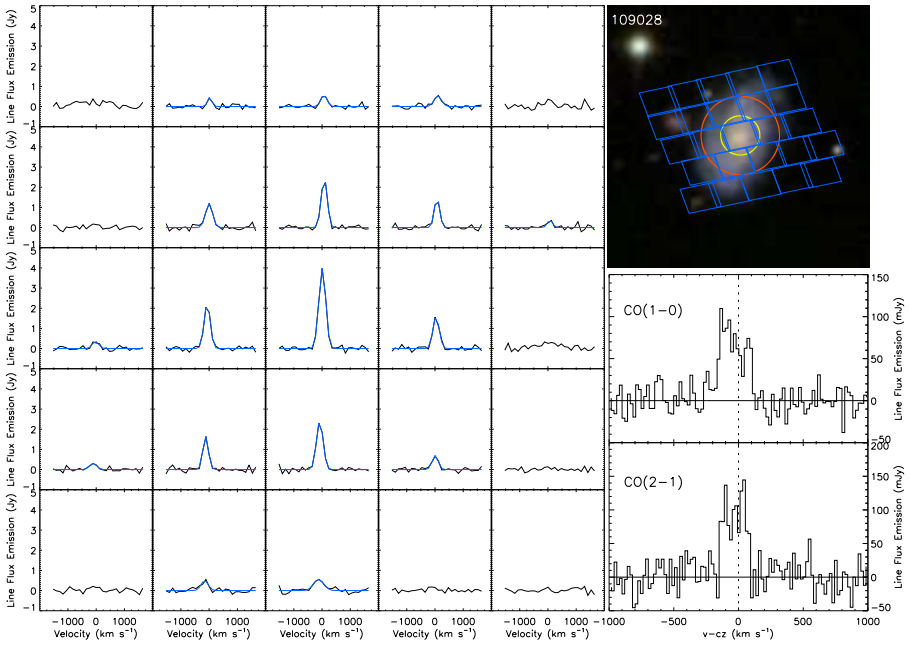

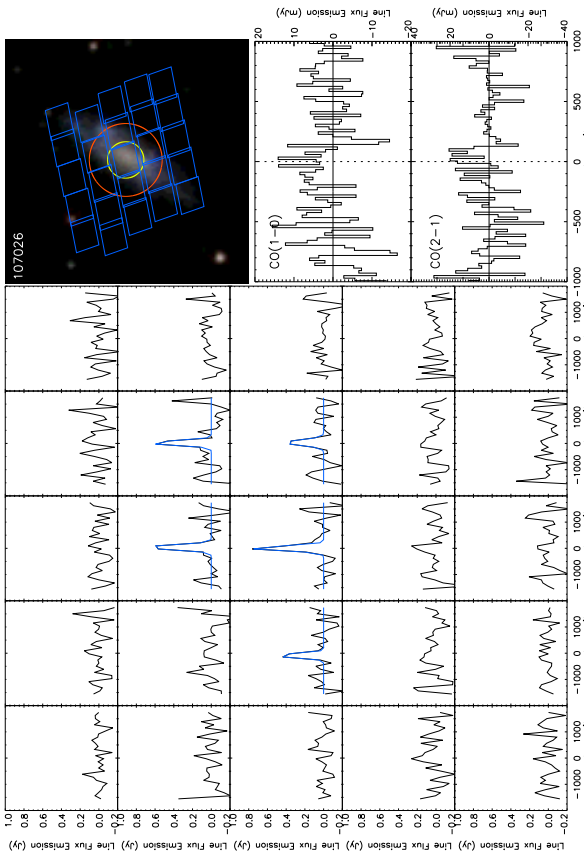
107026
CO(1−0)
CO(2−1)
v−cz (km s⁻¹)
Line Flux Emission (mJy)
Velocity (km s⁻¹)
Line Flux Emission (Jy)

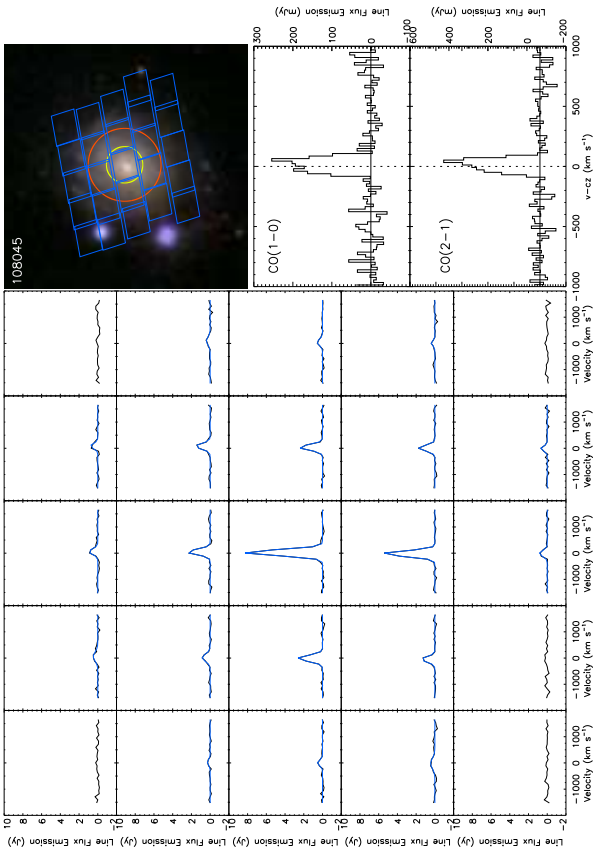
108045
CO(1−0)
CO(2−1)
v−cz (km s⁻¹)
Line Flux Emission (mJy)
Velocity (km s⁻¹)
Line Flux Emission (Jy)

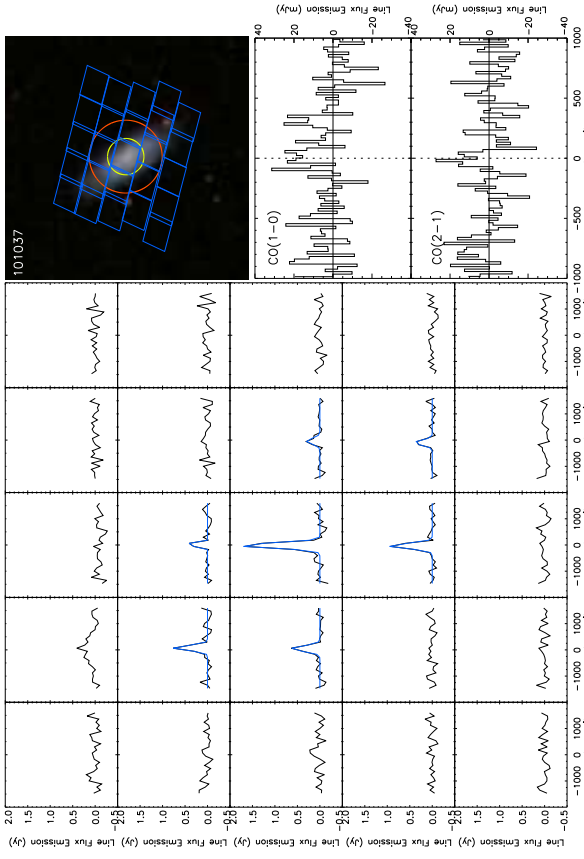
101037
CO(1−0)
CO(2−1)
v−cz (km s⁻¹)
Line Flux Emission (mJy)
Velocity (km s⁻¹)
Line Flux Emission (Jy)

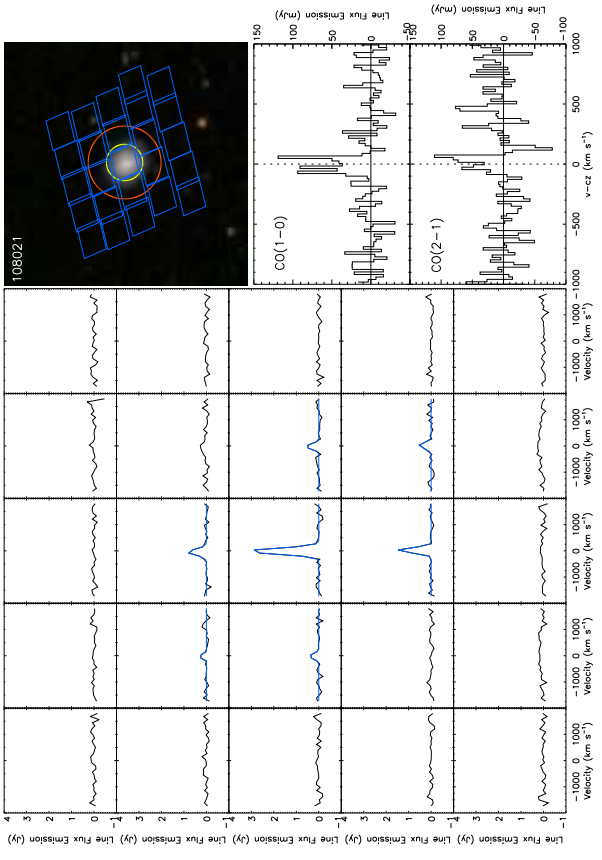
108021
CO(1−0)
CO(2−1)
v−cz (km s⁻¹)
Line Flux Emission (mJy)
Velocity (km s⁻¹)
Line Flux Emission (Jy)

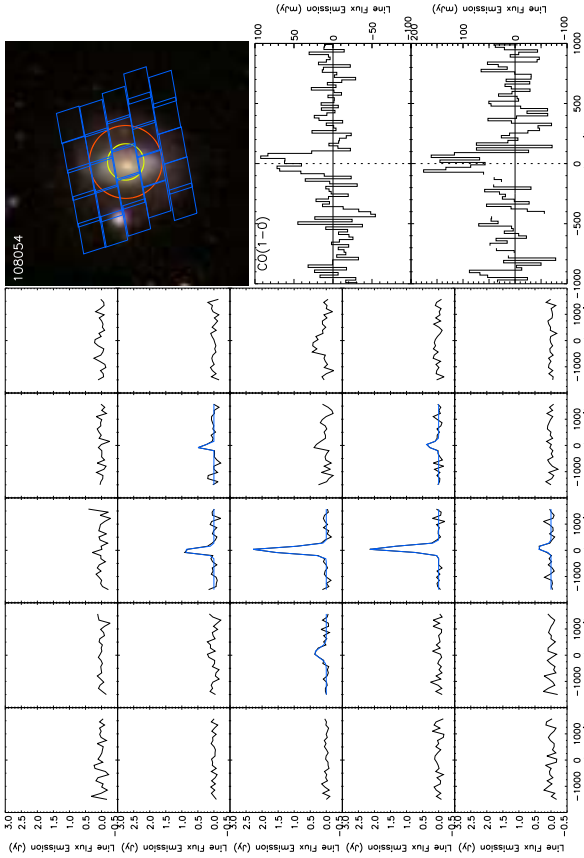
108054
CO(1−0)
CO(2−1)
v−cz (km s⁻¹)
Line Flux Emission (mJy)
Velocity (km s⁻¹)
Line Flux Emission (Jy)

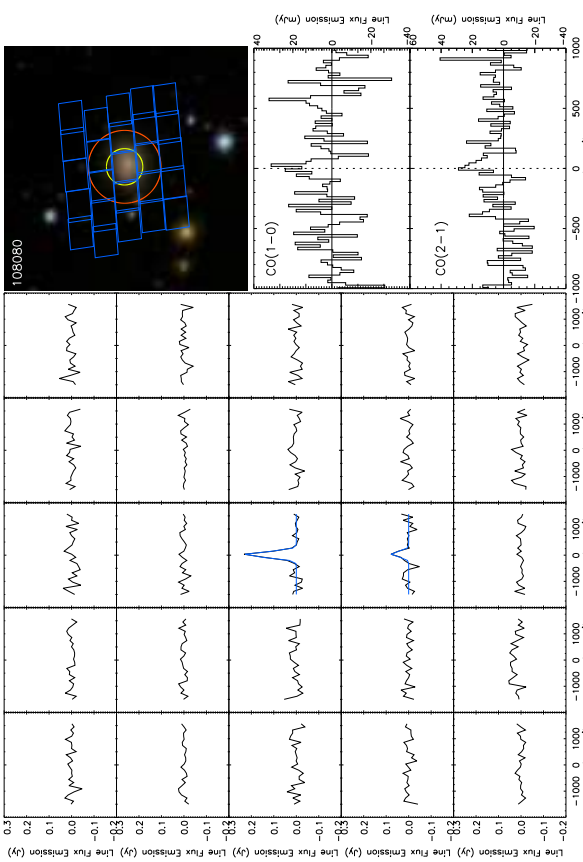
108080
CO(1−0)
CO(2−1)
v−cz (km s⁻¹)
Line Flux Emission (mJy)
Velocity (km s⁻¹)
Line Flux Emission (Jy)

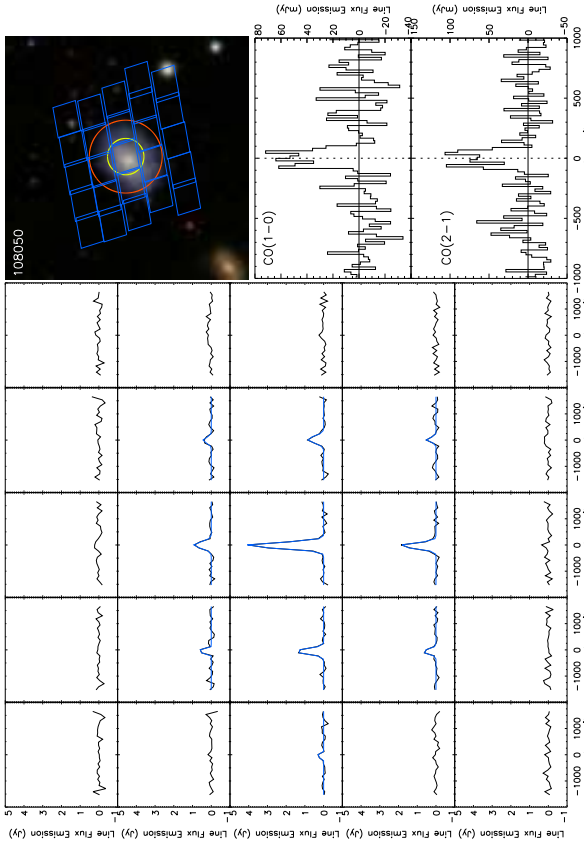
108050
CO(1−0)
CO(2−1)
v−cz (km s⁻¹)
Line Flux Emission (mJy)
Velocity (km s⁻¹)
Line Flux Emission (Jy)

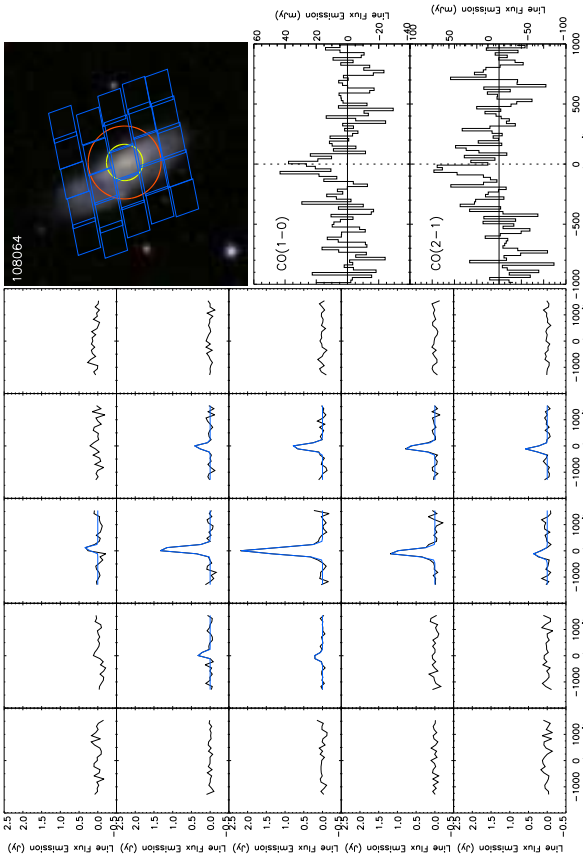
108064
CO(1−0)
CO(2−1)
v−cz (km s⁻¹)
Line Flux Emission (mJy)
Velocity (km s⁻¹)
Line Flux Emission (Jy)

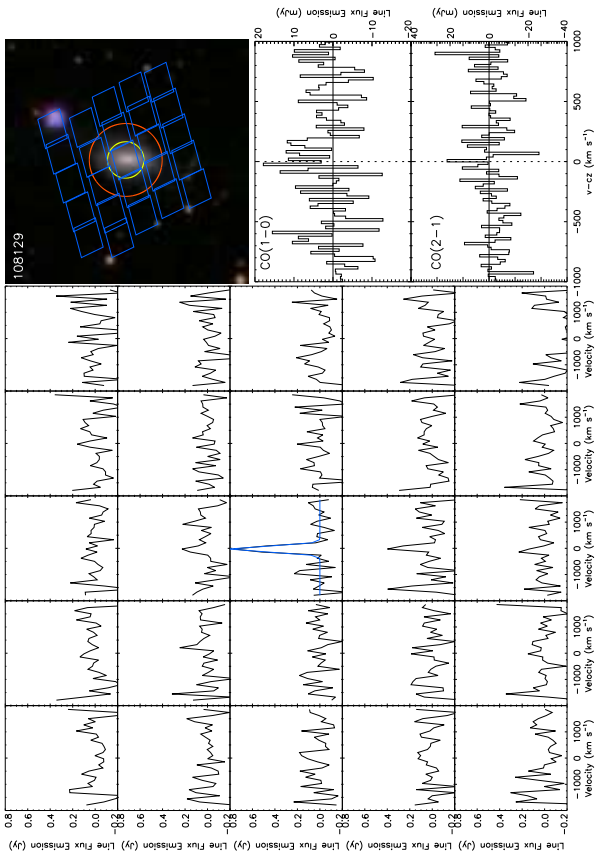
108129
CO(1−0)
CO(2−1)
Line Flux Emission (mJy)
v−cz (km s⁻¹)
Line Flux Emission (Jy)
Velocity (km s⁻¹)

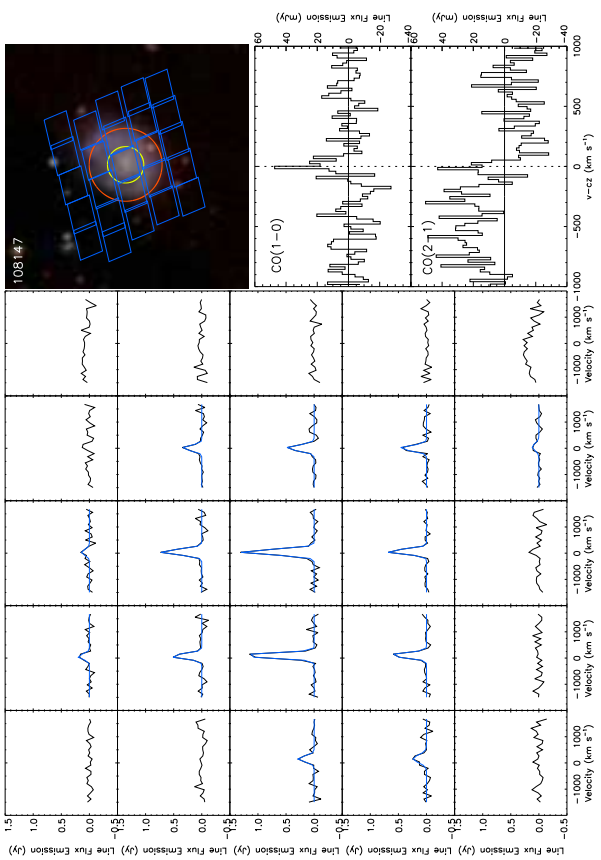
108147
CO(1−0)
CO(2−1)
Line Flux Emission (mJy)
v−cz (km s⁻¹)
Line Flux Emission (Jy)
Velocity (km s⁻¹)

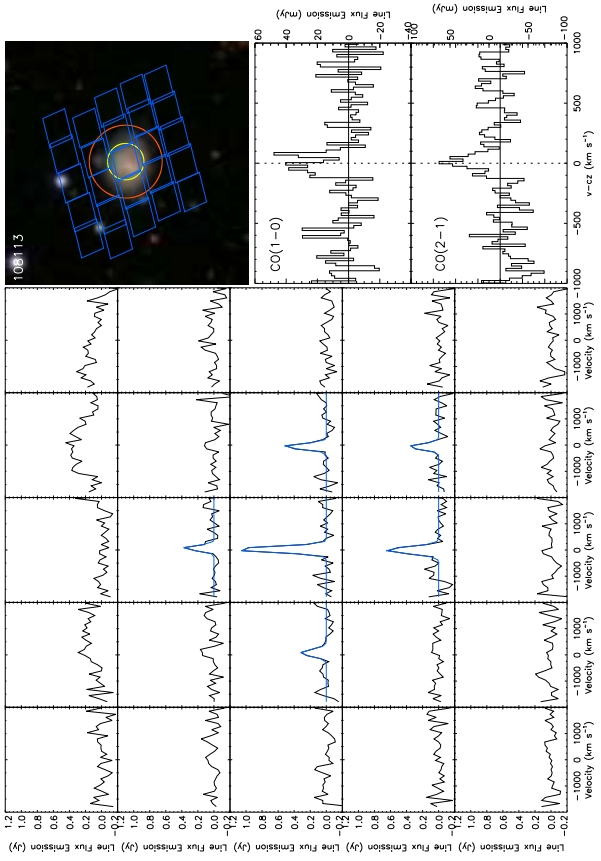
108113
CO(1−0)
CO(2−1)
Line Flux Emission (mJy)
v−cz (km s⁻¹)
Line Flux Emission (Jy)
Velocity (km s⁻¹)

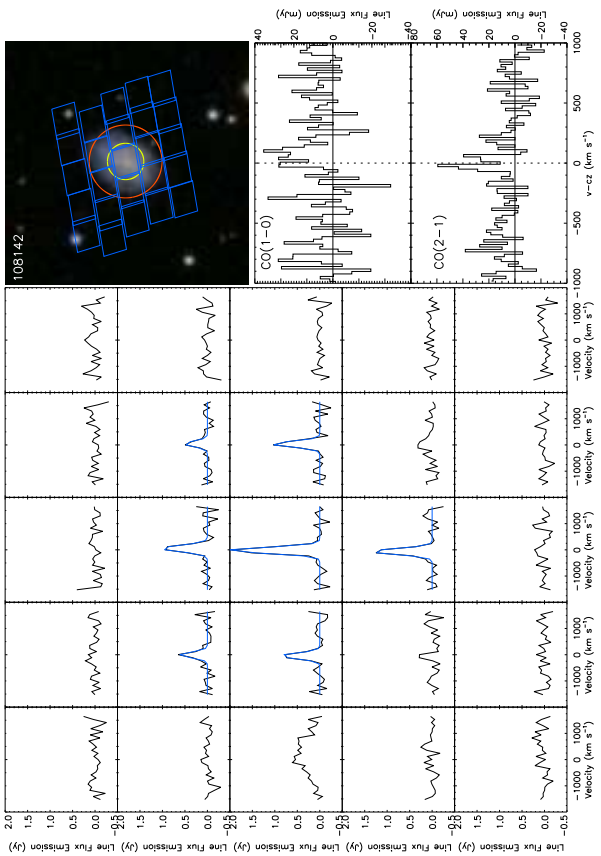
108142
CO(1−0)
CO(2−1)
Line Flux Emission (mJy)
v−cz (km s⁻¹)
Line Flux Emission (Jy)
Velocity (km s⁻¹)

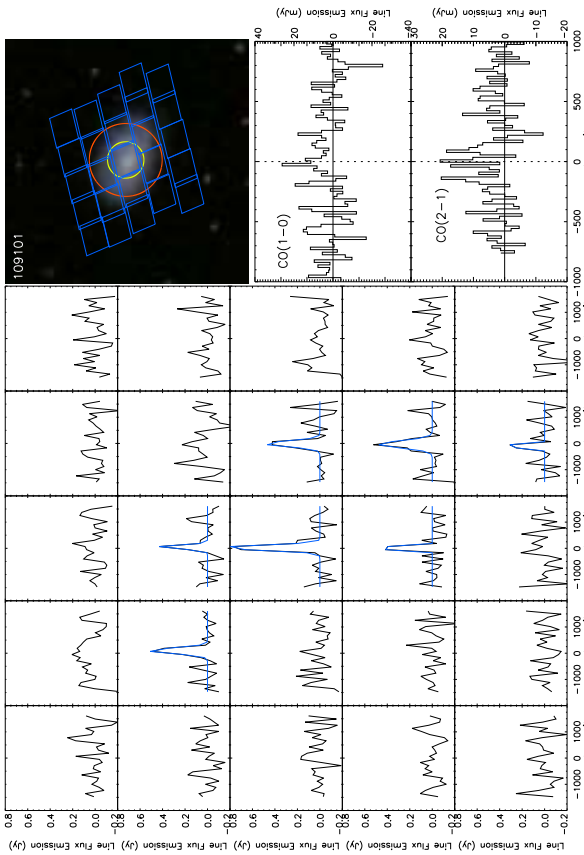
109101
CO(1−0)
CO(2−1)
Line Flux Emission (mJy)
v−cz (km s⁻¹)
Line Flux Emission (Jy)
Velocity (km s⁻¹)

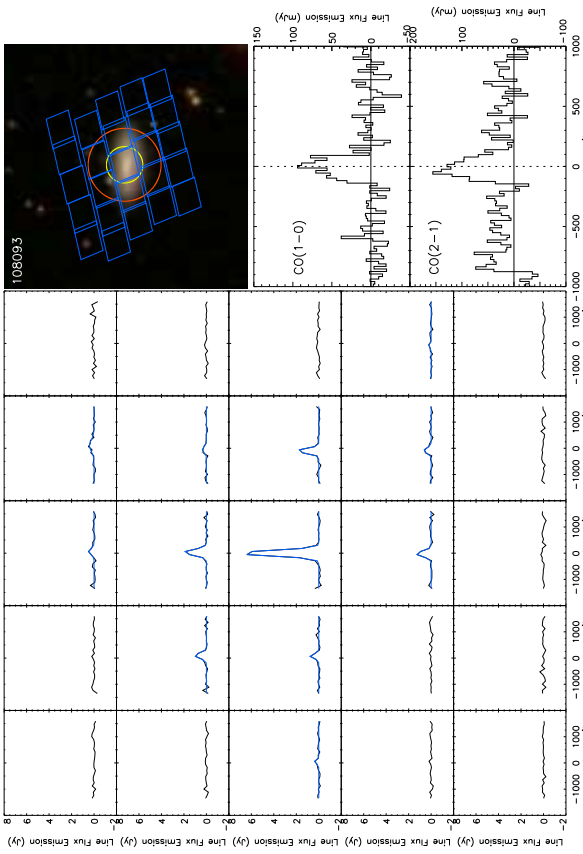
108093
CO(1−0)
CO(2−1)
Line Flux Emission (mJy)
v−cz (km s⁻¹)
Line Flux Emission (Jy)
Velocity (km s⁻¹)

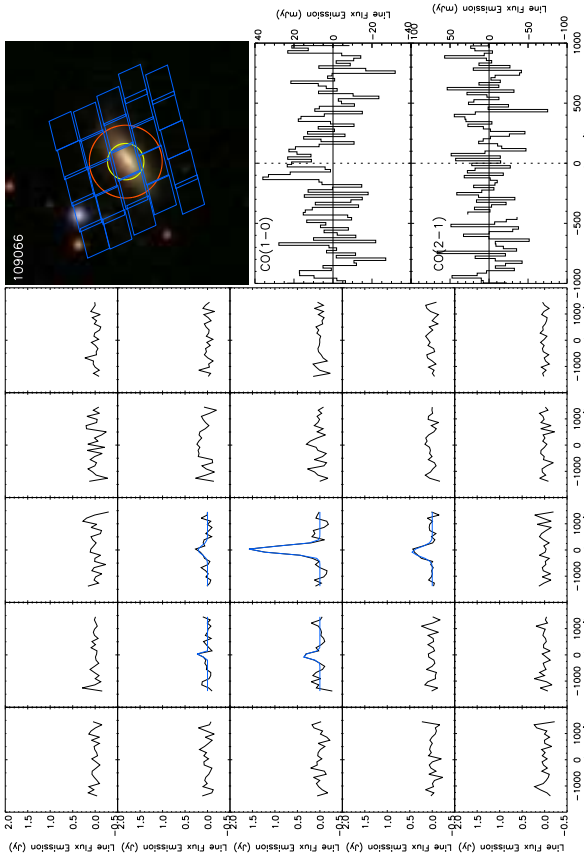
109066
CO(1−0)
CO(2−1)
Line Flux Emission (mJy)
v−cz (km s⁻¹)
Line Flux Emission (Jy)
Velocity (km s⁻¹)

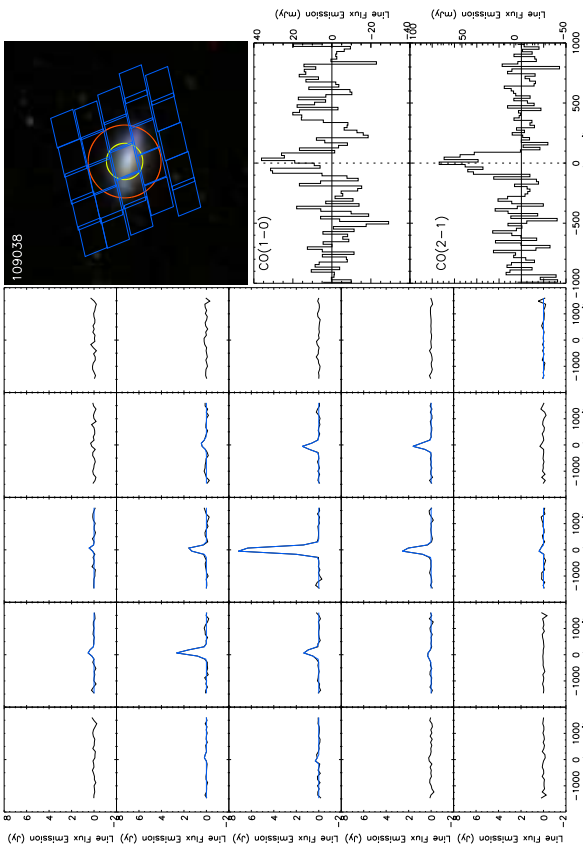
109038
CO(1−0)
CO(2−1)
Line Flux Emission (mJy)
v−cz (km s⁻¹)
Line Flux Emission (Jy)
Velocity (km s⁻¹)

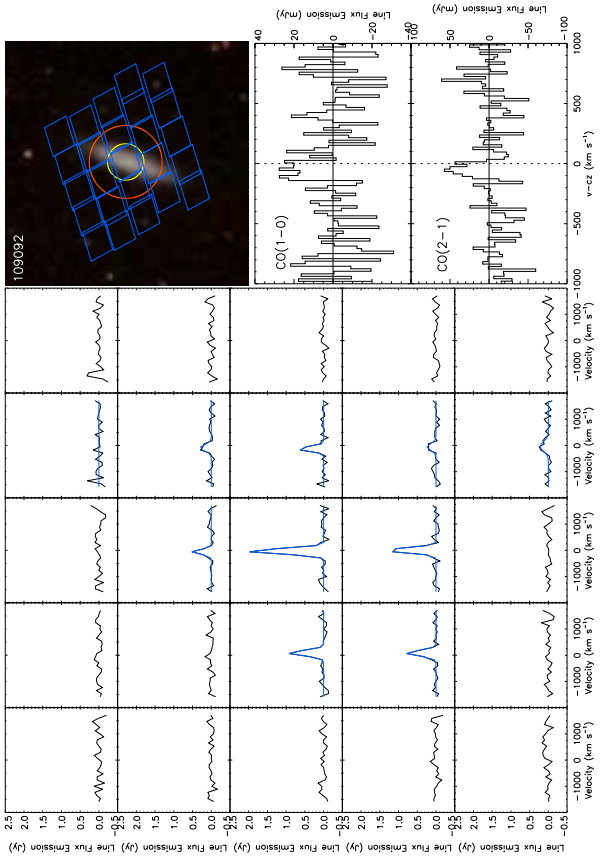
109092
CO(1−0)
CO(2−1)
Line Flux Emission (mJy)
v−cz (km s⁻¹)
Line Flux Emission (Jy)
Velocity (km s⁻¹)

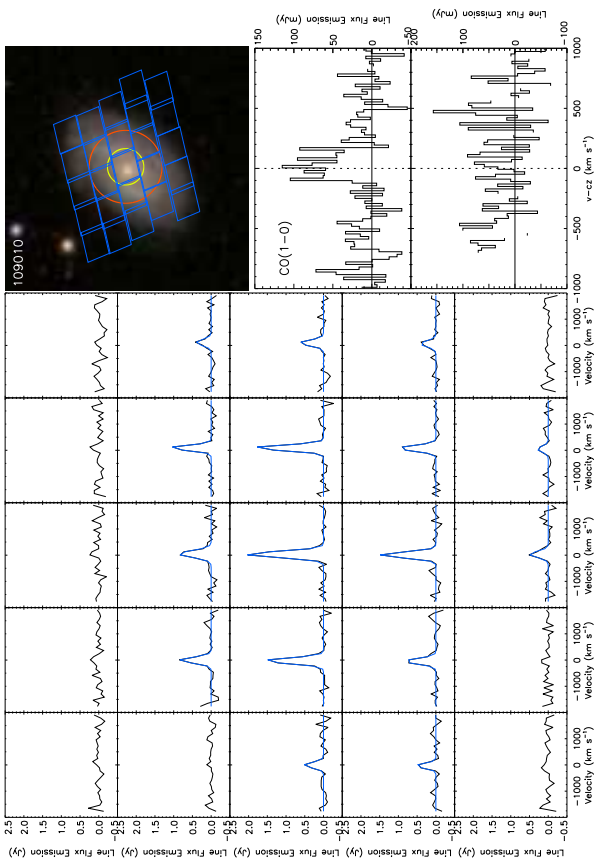
109010
CO(1−0)
Line Flux Emission (mJy)
v−cz (km s⁻¹)
Line Flux Emission (Jy)
Velocity (km s⁻¹)

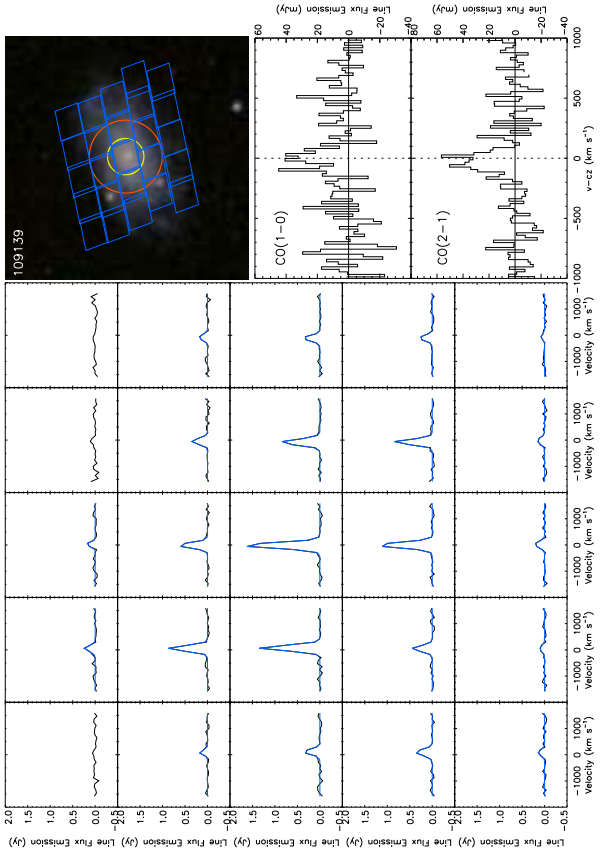
109139
CO(1−0)
CO(2−1)
Line Flux Emission (mJy)
v−cz (km s⁻¹)
Line Flux Emission (Jy)
Velocity (km s⁻¹)

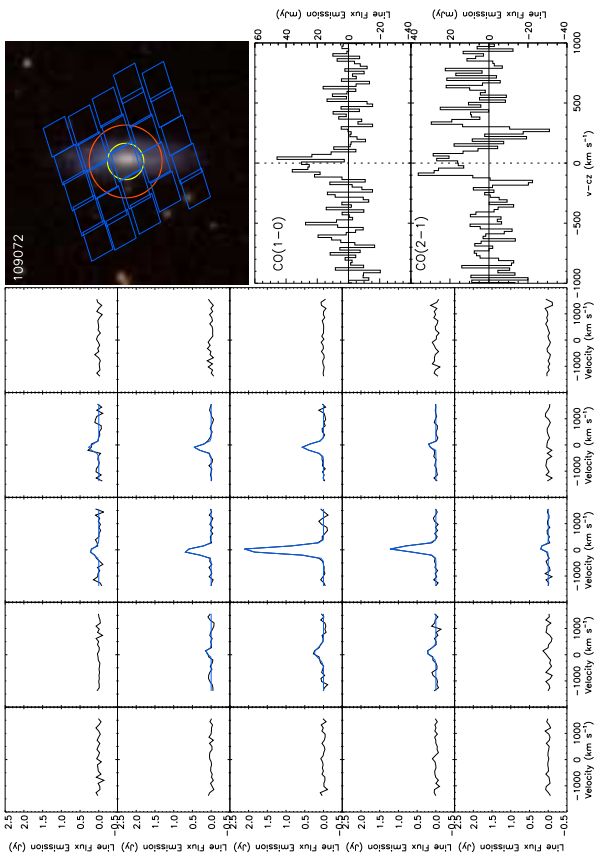
109072
CO(1−0)
CO(2−1)
Line Flux Emission (mJy)
v−cz (km s⁻¹)
Line Flux Emission (Jy)
Velocity (km s⁻¹)

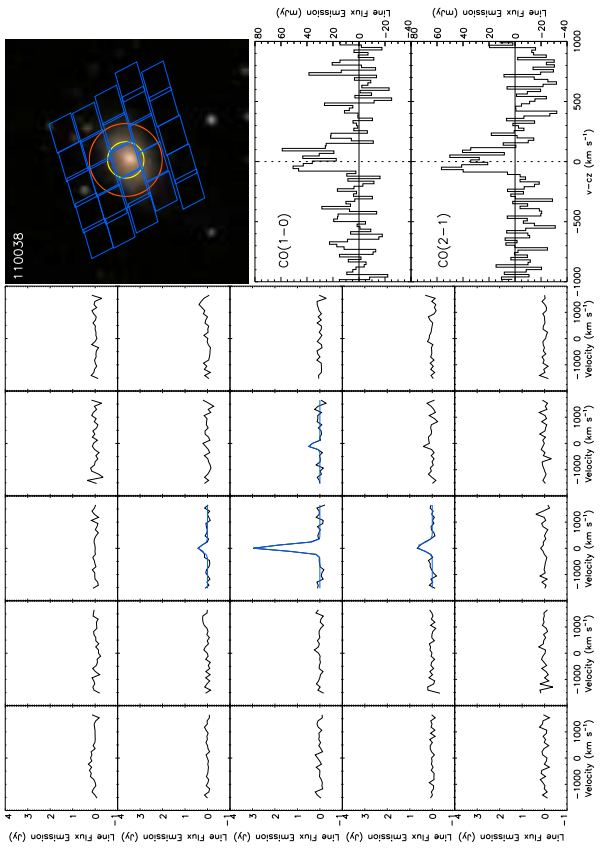
110038
CO(1−0)
CO(2−1)
Line Flux Emission (mJy)
v−cz (km s⁻¹)
Line Flux Emission (Jy)
Velocity (km s⁻¹)

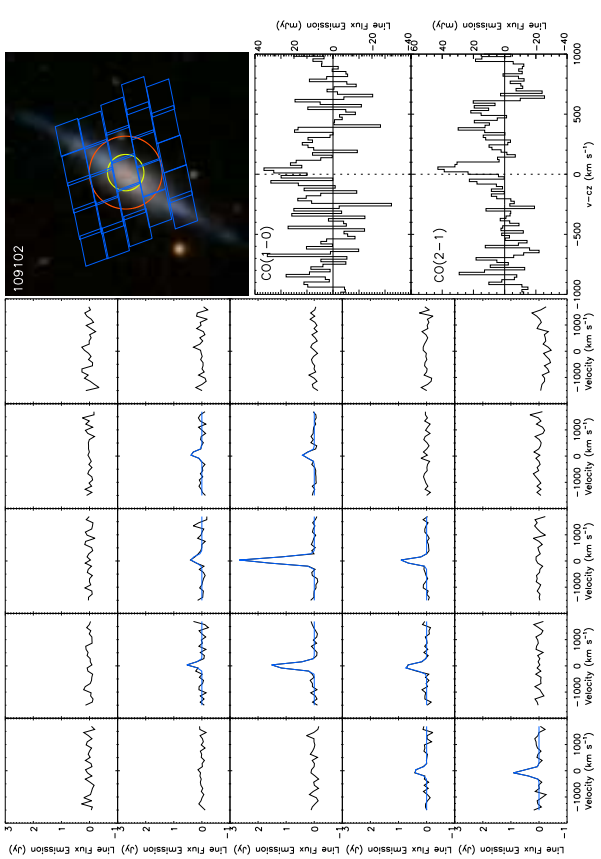
109102
CO(1−0)
CO(2−1)
Line Flux Emission (mJy)
v−cz (km s⁻¹)
Line Flux Emission (Jy)
Velocity (km s⁻¹)

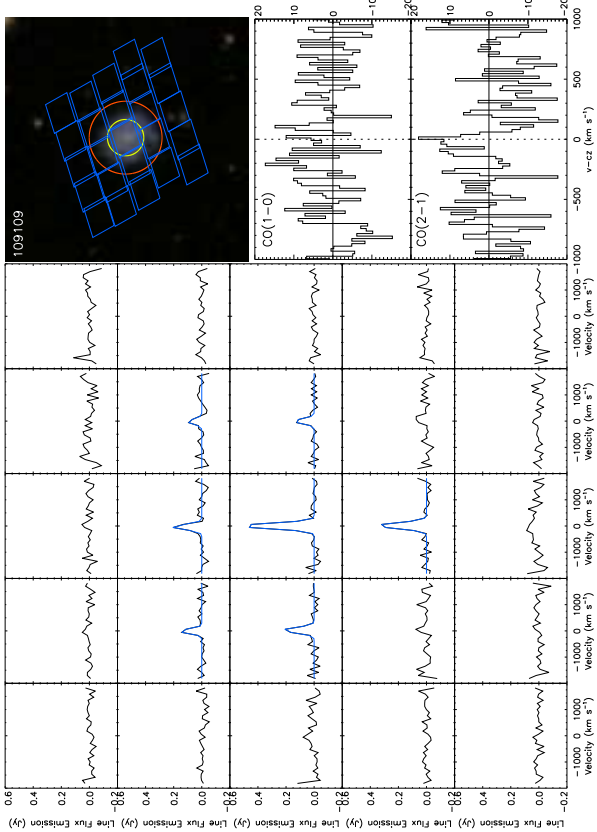
109109
CO(1−0)
CO(2−1)
Line Flux Emission (mJy)
v−cz (km s⁻¹)
Line Flux Emission (Jy)
Velocity (km s⁻¹)

Bibliography

Abazajian, K. N., Adelman-McCarthy, J. K., Agüeros, M. A., Allam, S. S., Allende Prieto, C., An, D., Anderson, K. S. J., Anderson, S. F., Annis, J., Bahcall, N. A. & et al., 2009, *ApJSS*, **182**, 543

Abdo, A. A., Ackermann, M., Ajello, M., Baldini, L., Ballet, J., Barbiellini, G. & Fermi/LAT Collaboration, 2010, *ApJ*, **710**, 133

Abel, N. P., Ferland, G. J., Shaw, G. & van Hoof, P. A. M., 2005, *ApJSS*, **161**, 65

Accurso, G., Saintonge, A., Bisbas, T. G. & Viti, S., 2016, *ArXiv e-prints*

Akaike, H., 1981, *Journal of Econometrics*, **16**(1), 3
URL: *http://EconPapers.repec.org/RePEc:eee:econom:v:16:y:1981:i:1:p:3-14*

Arimoto, N., Sofue, Y. & Tsujimoto, T., 1996, *PASJ*, **48**, 275

Asplund, M., Grevesse, N., Sauval, A. J. & Scott, P., 2009, *Ann. Rev. Astr. Astrophys.*, **47**, 481

Bell, T. A., Roueff, E., Viti, S. & Williams, D. A., 2006, *MNRAS*, **371**, 1865

Bendo, G. J., Dale, D. A., Draine, B. T., Engelbracht, C. W., Kennicutt, Jr., R. C., Calzetti, D., Gordon, K. D., Helou, G., Hollenbach, D., Li, A., Murphy, E. J., Prescott, M. K. M. & Smith, J.-D. T., 2006, *ApJ*, **652**, 283

Bendo, G. J., Wilson, C. D., Pohlen, M., Sauvage, M., Auld, R., Baes, M., Barlow, M. J., Bock, J. J., Boselli, A., Bradford, M., Buat, V., Castro-Rodriguez, N., Chanial, P., Charlot, S., Ciesla, L., Clements, D. L., Cooray, A., Cormier, D., Cortese, L., Davies, J. I., Dwek, E., Eales, S. A., Elbaz, D., Galametz, M., Galliano, F., Gear, W. K., Glenn, J., Gomez, H. L., Griffin, M., Hony, S., Isaak, K. G., Levenson, L. R., Lu, N., Madden,

S., O'Halloran, B., Okumura, K., Oliver, S., Page, M. J., Panuzzo, P., Papageorgiou, A., Parkin, T. J., Perez-Fournon, I., Rangwala, N., Rigby, E. E., Roussel, H., Rykala, A., Sacchi, N., Schulz, B., Schirm, M. R. P., Smith, M. W. L., Spinoglio, L., Stevens, J. A., Sundar, S., Symeonidis, M., Trichas, M., Vaccari, M., Vigroux, L., Wozniak, H., Wright, G. S. & Zeilinger, W. W., 2010, *A&A*, **518**, L65

Bianchi, S., 2008, *A&A*, **490**, 461

Bisbas, T. G., Bell, T. A., Viti, S., Barlow, M. J., Yates, J. & Vasta, M., 2014, *MNRAS*, **443**, 111

Bisbas, T. G., Bell, T. A., Viti, S., Yates, J. & Barlow, M. J., 2012, *MNRAS*, **427**, 2100

Bisbas, T. G., Haworth, T. J., Barlow, M. J., Viti, S., Harries, T. J., Bell, T. & Yates, J. A., 2015*a*, *MNRAS*, **454**, 2828

Bisbas, T. G., Papadopoulos, P. P. & Viti, S., 2015*b*, *ApJ*, **803**, 37

Bolatto, A. D., Wolfire, M. & Leroy, A. K., 2013, *Ann. Rev. Astr. Astrophys.*, **51**, 207

Boselli, A., Eales, S., Cortese, L., Bendo, G., Chanial, P., Buat, V., Davies, J., Auld, R., Rigby, E., Baes, M. & Barlow, M., 2010, *PASP*, **122**, 261

Boselli, A., Fossati, M., Gavazzi, G., Ciesla, L., Buat, V., Boissier, S. & Hughes, T. M., 2015, *A&A*, **579**, A102

Boselli, A., Hughes, T. M., Cortese, L., Gavazzi, G. & Buat, V., 2013, *A&A*, **550**, A114

Boselli, A., Lequeux, J. & Gavazzi, G., 2002, *A&A*, **384**, 33

Bothwell, M. S., Maiolino, R., Kennicutt, R., Cresci, G., Mannucci, F., Marconi, A. & Cicone, C., 2013, *MNRAS*, **433**, 1425

Bouché, N., Dekel, A., Genzel, R., Genel, S., Cresci, G., Förster Schreiber, N. M., Shapiro, K. L., Davies, R. I. & Tacconi, L., 2010, *ApJ*, **718**, 1001

Bourne, N., Maddox, S. J., Dunne, L., Auld, R., Baes, M., Baldry, I. K., Bonfield, D. G., Cooray, A., Croom, S. M., Dariush, A., de Zotti, G., Driver, S. P., Dye, S., Eales, S., Gomez, H. L., González-Nuevo, J., Hopkins, A. M., Ibar, E., Jarvis, M. J., Lapi, A., Madore, B., Michałowski, M. J., Pohlen, M., Popescu, C. C., Rigby, E. E., Seibert, M.,

Smith, D. J. B., Tuffs, R. J., van der Werf, P., Brough, S., Buttiglione, S., Cava, A., Clements, D. L., Conselice, C. J., Fritz, J., Hopwood, R., Ivison, R. J., Jones, D. H., Kelvin, L. S., Liske, J., Loveday, J., Norberg, P., Robotham, A. S. G., Rodighiero, G. & Temi, P., 2012, *MNRAS*, **421**, 3027

Breiman, L., 2006, *Machine Learning*, **45**(1), 5
URL: *http://dx.doi.org/10.1023/A:1010933404324*

Brinchmann, J., Charlot, S., White, S. D. M., Tremonti, C., Kauffmann, G., Heckman, T. & Brinkmann, J., 2004, *MNRAS*, **351**, 1151

Brooks, A. M., Governato, F., Booth, C. M., Willman, B., Gardner, J. P., Wadsley, J., Stinson, G. & Quinn, T., 2007, *ApJL*, **655**, L17

Brown, T., Catinella, B., Cortese, L., Kilborn, V., Haynes, M. P. & Giovanelli, R., 2015, *MNRAS*, **452**, 2479

Buat, V., Giovannoli, E., Takeuchi, T. T., Heinis, S., Yuan, F.-T., Burgarella, D., Noll, S. & Iglesias-Páramo, J., 2011, *A&A*, **529**, A22

Carliles, S., Budavári, T., Heinis, S., Priebe, C. & Szalay, A. S., 2010, *ApJ*, **712**, 511

Carral, P., Hollenbach, D. J., Lord, S. D., Colgan, S. W. J., Haas, M. R., Rubin, R. H. & Erickson, E. F., 1994, *ApJ*, **423**, 223

Carrasco, D., Barrientos, L. F., Pichara, K., Anguita, T., Murphy, D. N. A., Gilbank, D. G., Gladders, M. D., Yee, H. K. C., Hsieh, B. C. & López, S., 2015, *A&A*, **584**, A44

Carter, M., Lazareff, B., Maier, D., Chenu, J.-Y., Fontana, A.-L., Bortolotti, Y., Boucher, C., Navarrini, A., Blanchet, S., Greve, A., John, D., Kramer, C., Morel, F., Navarro, S., Peñalver, J., Schuster, K. F. & Thum, C., 2012, *A&A*, **538**, A89

Caruana, R. & Niculescu-Mizil, A., 2006, in *Proceedings of the 23rd International Conference on Machine Learning* (ACM, New York, NY, USA), ICML '06, pp. 161–168
URL: *http://doi.acm.org/10.1145/1143844.1143865*

Catinella, B., Schiminovich, D., Cortese, L., Fabello, S., Hummels, C. B., Moran, S. M., Lemonias, J. J., Cooper, A. P., Wu, R., Heckman, T. M. & Wang, J., 2013, *MNRAS*, **436**, 34

Catinella, B., Schiminovich, D., Kauffmann, G., Fabello, S. & Wang, J., 2010, *MNRAS*, **403**, 683

Cazaux, S. & Tielens, A. G. G. M., 2004, *ApJ*, **604**, 222

Ceverino, D., Arribas, S., Colina, L., Rodríguez Del Pino, B., Dekel, A. & Primack, J., 2016, *MNRAS*, **460**, 2731

Chabrier, G., 2003, *PASP*, **115**, 763

Chen, Y.-M., Tremonti, C. A., Heckman, T. M., Kauffmann, G., Weiner, B. J., Brinchmann, J. & Wang, J., 2010, *AJ*, **140**, 445

Clark, C. J. R., Dunne, L., Gomez, H. L., Maddox, S., De Vis, P., Smith, M. W. L., Eales, S. A., Baes, M., Bendo, G. J., Bourne, N., Driver, S. P., Dye, S., Furlanetto, C., Grootes, M. W., Ivison, R. J., Schofield, S. P., Robotham, A. S. G., Rowlands, K., Valiante, E., Vlahakis, C., van der Werf, P., Wright, A. H. & de Zotti, G., 2015, *MNRAS*, **452**, 397

Clark, P. C. & Glover, S. C. O., 2015, *MNRAS*, **452**, 2057

Colombo, D., Hughes, A., Schinnerer, E., Meidt, S. E., Leroy, A. K., Pety, J., Dobbs, C. L., García-Burillo, S., Dumas, G., Thompson, T. A., Schuster, K. F. & Kramer, C., 2014, *ApJ*, **784**, 3

Conroy, C., 2013, *Ann. Rev. Astr. Astrophys.*, **51**, 393

Cormier, D., Lebouteiller, V., Madden, S. C., Abel, N., Hony, S., Galliano, F., Baes, M., Barlow, M. J., Cooray, A., De Looze, I., Galametz, M., Karczewski, O. Ł., Parkin, T. J., Rémy, A., Sauvage, M., Spinoglio, L., Wilson, C. D. & Wu, R., 2012, *A&A*, **548**, A20

Cormier, D., Madden, S. C., Lebouteiller, V., Abel, N., Hony, S., Galliano, F., Rémy-Ruyer, A., Bigiel, F., Baes, M., Boselli, A., Chevance, M., Cooray, A., De Looze, I., Doublier, V., Galametz, M., Hughes, T., Karczewski, O. Ł., Lee, M.-Y., Lu, N. & Spinoglio, L., 2015, *A&A*, **578**, A53

Cormier, D., Madden, S. C., Lebouteiller, V., Hony, S., Aalto, S., Costagliola, F., Hughes, A., Rémy-Ruyer, A., Abel, N., Bayet, E., Bigiel, F., Cannon, J. M., Cumming, R. J., Galametz, M., Galliano, F., Viti, S. & Wu, R., 2014, *A&A*, **564**, A121

Cortese, L., Ciesla, L., Boselli, A., Bianchi, S., Gomez, H., Smith, M. W. L., Bendo, G. J., Eales, S., Pohlen, M. & Baes, 2012, *A&A*, **540**, A52

Cortese, L., Fritz, J., Bianchi, S., Boselli, A., Ciesla, L., Bendo, G. J., Boquien, M., Roussel, H., Baes, M. & Buat, V., 2014, *MNRAS*, **440**, 942

Cox, N. L. J., Pilleri, P., Berné, O., Cernicharo, J. & Joblin, C., 2016, *MNRAS*, **456**, L89

Cummings, A., 2015, *Proceedings of Science*

da Cunha, E., Charlot, S. & Elbaz, D., 2008, *MNRAS*, **388**, 1595

da Cunha, E., Groves, B., Walter, F., Decarli, R., Weiss, A., Bertoldi, F., Carilli, C., Daddi, E., Elbaz, D., Ivison, R., Maiolino, R., Riechers, D., Rix, H.-W., Sargent, M. & Smail, I., 2013, *ApJ*, **766**, 13

Daddi, E., Bournaud, F., Walter, F., Dannerbauer, H., Carilli, C. L., Dickinson, M., Elbaz, D., Morrison, G. E., Riechers, D., Onodera, M., Salmi, F., Krips, M. & Stern, D., 2010, *ApJ*, **713**, 686

Daddi, E., Dickinson, M., Morrison, G., Chary, R., Cimatti, A., Elbaz, D., Frayer, D., Renzini, A., Pope, A., Alexander, D. M., Bauer, F. E., Giavalisco, M., Huynh, M., Kurk, J. & Mignoli, M., 2007, *ApJ*, **670**, 156

Dalgarno, A., 2006, *Proceedings of the National Academy of Science*, **103**, 12269

Davé, R., Finlator, K. & Oppenheimer, B. D., 2011*a*, *MNRAS*, **416**, 1354

Davé, R., Finlator, K. & Oppenheimer, B. D., 2012, *MNRAS*, **421**, 98

Davé, R., Oppenheimer, B. D. & Finlator, K., 2011*b*, *MNRAS*, **415**, 11

Davis, T. A., Young, L. M., Crocker, A. F., Bureau, M., Blitz, L., Alatalo, K., Emsellem, E., Naab, T., Bayet, E., Bois, M., Bournaud, F., Cappellari, M., Davies, R. L., de Zeeuw, P. T., Duc, P.-A., Khochfar, S., Krajnović, D., Kuntschner, H., McDermid, R. M., Morganti, R., Oosterloo, T., Sarzi, M., Scott, N., Serra, P. & Weijmans, A.-M., 2014, *MNRAS*, **444**, 3427

de Jong, T., Boland, W. & Dalgarno, A., 1980, *A&A*, **91**, 68

de Looze, I., Baes, M., Bendo, G. J., Cortese, L. & Fritz, J., 2011, *MNRAS*, **416**, 2712

Dekel, A., Birnboim, Y., Engel, G., Freundlich, J., Goerdt, T., Mumcuoglu, M., Neistein, E., Pichon, C., Teyssier, R. & Zinger, E., 2009, *Nature*, **457**, 451

Dickman, R. L., Snell, R. L. & Schloerb, F. P., 1986, *ApJ*, **309**, 326

Domínguez, A., Siana, B., Brooks, A. M., Christensen, C. R., Bruzual, G., Stark, D. P. & Alavi, A., 2015, *MNRAS*, **451**, 839

Drabek, E., Hatchell, J., Friberg, P., Richer, J., Graves, S., Buckle, J. V., Nutter, D., Johnstone, D. & Di Francesco, J., 2012, *MNRAS*, **426**, 23

Draine, B. T., 1978, *ApJSS*, **36**, 595

Draine, B. T., Aniano, G., Krause, O., Groves, B., Sandstrom, K., Braun, R., Leroy, A., Klaas, U., Linz, H., Rix, H.-W., Schinnerer, E., Schmiedeke, A. & Walter, F., 2014, *ApJ*, **780**, 172

Draine, B. T. & Lee, H. M., 1984, *ApJ*, **285**, 89

Draine, B. T. & Li, A., 2007, *ApJ*, **657**, 810

Dunne, L., Eales, S., Edmunds, M., Ivison, R., Alexander, P. & Clements, D. L., 2000, *MNRAS*, **315**, 115

Dunne, L., Gomez, H. L., da Cunha, E., Charlot, S., Dye, S., Eales, S., Maddox, S. J., Rowlands, K., Smith, D. J. B., Auld, R., Baes, M., Bonfield, D. G., Bourne, N., Buttiglione, S., Cava, A., Clements, D. L., Coppin, K. E. K., Cooray, A., Dariush, A., de Zotti, G., Driver, S., Fritz, J., Geach, J., Hopwood, R., Ibar, E., Ivison, R. J., Jarvis, M. J., Kelvin, L., Pascale, E., Pohlen, M., Popescu, C., Rigby, E. E., Robotham, A., Rodighiero, G., Sansom, A. E., Serjeant, S., Temi, P., Thompson, M., Tuffs, R., van der Werf, P. & Vlahakis, C., 2011, *MNRAS*, **417**, 1510

Eales, S., Dunne, L., Clements, D., Cooray, A., De Zotti, G., Dye, S., Ivison, R., Jarvis, M., Lagache, G., Maddox, S., Negrello, M., Serjeant, S., Thompson, M. A., Van Kampen, E., Amblard, A., Andreani, P., Baes, M., Beelen, A., Bendo, G. J., Benford, D., Bertoldi, F., Bock, J., Bonfield, D., Boselli, A., Bridge, C., Buat, V., Burgarella, D., Carlberg, R., Cava, A., Chanial, P., Charlot, S., Christopher, N., Coles, P., Cortese, L., Dariush, A., da Cunha, E., Dalton, G., Danese, L., Dannerbauer, H., Driver, S., Dunlop, J., Fan, L., Farrah, D., Frayer, D., Frenk, C., Geach, J., Gardner, J., Gomez, H., González-Nuevo,

J., González-Solares, E., Griffin, M., Hardcastle, M., Hatziminaoglou, E., Herranz, D., Hughes, D., Ibar, E., Jeong, W.-S., Lacey, C., Lapi, A., Lawrence, A., Lee, M., Leeuw, L., Liske, J., López-Caniego, M., Müller, T., Nandra, K., Panuzzo, P., Papageorgiou, A., Patanchon, G., Peacock, J., Pearson, C., Phillipps, S., Pohlen, M., Popescu, C., Rawlings, S., Rigby, E., Rigopoulou, M., Robotham, A., Rodighiero, G., Sansom, A., Schulz, B., Scott, D., Smith, D. J. B., Sibthorpe, B., Smail, I., Stevens, J., Sutherland, W., Takeuchi, T., Tedds, J., Temi, P., Tuffs, R., Trichas, M., Vaccari, M., Valtchanov, I., van der Werf, P., Verma, A., Vieria, J., Vlahakis, C. & White, G. J., 2010, *PASP*, **122**, 499

Eales, S., Smith, M. W. L., Auld, R., Baes, M., Bendo, G. J., Bianchi, S., Boselli, A., Ciesla, L., Clements, D., Cooray, A., Cortese, L., Davies, J., De Looze, I., Galametz, M., Gear, W., Gentile, G., Gomez, H., Fritz, J., Hughes, T., Madden, S., Magrini, L., Pohlen, M., Spinoglio, L., Verstappen, J., Vlahakis, C. & Wilson, C. D., 2012, *ApJ*, **761**, 168

Elbaz, D., Daddi, E., Le Borgne, D., Dickinson, M., Alexander, D. M., Chary, R.-R., Starck, J.-L., Brandt, W. N., Kitzbichler, M., MacDonald, E., Nonino, M., Popesso, P., Stern, D. & Vanzella, E., 2007, *A&A*, **468**, 33

Erb, D. K., Shapley, A. E., Pettini, M., Steidel, C. C., Reddy, N. A. & Adelberger, K. L., 2006, *ApJ*, **644**, 813

Ercolano, B., Barlow, M. J. & Storey, P. J., 2005, *MNRAS*, **362**, 1038

Ercolano, B., Barlow, M. J., Storey, P. J. & Liu, X.-W., 2003, *MNRAS*, **340**, 1136

Ercolano, B., Dale, J. E., Gritschneder, M. & Westmoquette, M., 2012, *MNRAS*, **420**, 141

Faber, S. M. & Jackson, R. E., 1976, *ApJ*, **204**, 668

Fagotto, F., Bressan, A., Bertelli, G. & Chiosi, C., 1994, *A&AS*, **105**, 29

Farrell, S. A., Murphy, T. & Lo, K. K., 2015, *ApJ*, **813**, 28

Feldmann, R., 2015, *MNRAS*, **449**, 3274

Ferland, G. J., Porter, R. L., van Hoof, P. A. M., Williams, R. J. R., Abel, N. P., Lykins, M. L., Shaw, G., Henney, W. J. & Stancil, P. C., 2013, *Rev. Mex. Astron. Astrofis.*, **49**, 137

Feruglio, C., Maiolino, R., Piconcelli, E., Menci, N., Aussel, H., Lamastra, A. & Fiore, F., 2010, *A&A*, **518**, L155

Flower, D. R., 1968, in D. E. Osterbrock & C. R. O'dell (eds.), *Planetary Nebulae*, volume 34 of *IAU Symposium*, p. 205

Foster, J. B., Mandel, K. S., Pineda, J. E., Covey, K. R., Arce, H. G. & Goodman, A. A., 2013, *MNRAS*, **428**, 1606

Freedman, D. & Diaconis, P., 1981, *ZWVG*, **57**(4), 453
URL: *http://dx.doi.org/10.1007/BF01025868*

Frosch, R. A. & Foley, H. M., 1952, *Physical Review*, **88**, 1337

Galametz, M., Madden, S. C., Galliano, F., Hony, S., Sauvage, M., Pohlen, M., Bendo, G. J., Auld, R., Baes, M., Barlow, M. J., Bock, J. J., Boselli, A., Bradford, M., Buat, V., Castro-Rodríguez, N., Chanial, P., Charlot, S., Ciesla, L., Clements, D. L., Cooray, A., Cormier, D., Cortese, L., Davies, J. I., Dwek, E., Eales, S. A., Elbaz, D., Gear, W. K., Glenn, J., Gomez, H. L., Griffin, M., Isaak, K. G., Levenson, L. R., Lu, N., O'Halloran, B., Okumura, K., Oliver, S., Page, M. J., Panuzzo, P., Papageorgiou, A., Parkin, T. J., Pérez-Fournon, I., Rangwala, N., Rigby, E. E., Roussel, H., Rykala, A., Sacchi, N., Schulz, B., Schirm, M. R. P., Smith, M. W. L., Spinoglio, L., Stevens, J. A., Sundar, S., Symeonidis, M., Trichas, M., Vaccari, M., Vigroux, L., Wilson, C. D., Wozniak, H., Wright, G. S. & Zeilinger, W. W., 2010, *A&A*, **518**, L55

Galliano, F., Madden, S. C., Jones, A. P., Wilson, C. D., Bernard, J.-P. & Le Peintre, F., 2003, *A&A*, **407**, 159

Genzel, R., Tacconi, L. J., Combes, F., Bolatto, A., Neri, R., Sternberg, A., Cooper, M. C., Bouché, N., Bournaud, F., Burkert, A., Comerford, J., Cox, P., Davis, M., Förster Schreiber, N. M., Garcia-Burillo, S., Gracia-Carpio, J., Lutz, D., Naab, T., Newman, S., Saintonge, A., Shapiro, K., Shapley, A. & Weiner, B., 2012, *ApJ*, **746**, 69

Genzel, R., Tacconi, L. J., Lutz, D., Saintonge, A., Berta, S., Magnelli, B., Combes, F., García-Burillo, S., Neri, R., Bolatto, A., Contini, T., Lilly, S., Boissier, J., Boone, F., Bouché, N., Bournaud, F., Burkert, A., Carollo, M., Colina, L., Cooper, M. C., Cox, P., Feruglio, C., Förster Schreiber, N. M., Freundlich, J., Gracia-Carpio, J., Juneau,

S., Kovac, K., Lippa, M., Naab, T., Salome, P., Renzini, A., Sternberg, A., Walter, F., Weiner, B., Weiss, A. & Wuyts, S., 2015, *ApJ*, **800**, 20

Giovanelli, R., Haynes, M. P., Kent, B. R., Perillat, P., Saintonge, A., Brosch, N., Catinella, B., Hoffman, G. L., Stierwalt, S., Spekkens, K., Lerner, M. S., Masters, K. L., Momjian, E., Rosenberg, J. L., Springob, C. M., Boselli, A., Charmandaris, V., Darling, J. K., Davies, J., Garcia Lambas, D., Gavazzi, G., Giovanardi, C., Hardy, E., Hunt, L. K., Iovino, A., Karachentsev, I. D., Karachentseva, V. E., Koopmann, R. A., Marinoni, C., Minchin, R., Muller, E., Putman, M., Pantoja, C., Salzer, J. J., Scodeggio, M., Skillman, E., Solanes, J. M., Valotto, C., van Driel, W. & van Zee, L., 2005, *AJ*, **130**, 2598

Goldsmith, P. F., Langer, W. D., Pineda, J. L. & Velusamy, T., 2012, *ApJSS*, **203**, 13

Gomez, H. L., Baes, M., Cortese, L., Smith, M. W. L., Boselli, A., Ciesla, L., Bendo, G. J., Pohlen, M., di Serego Alighieri, S., Auld, R., Barlow, M. J., Bock, J. J., Bradford, M., Buat, V., Castro-Rodriguez, N., Chanial, P., Charlot, S., Clements, D. L., Cooray, A., Cormier, D., Davies, J. I., Dwek, E., Eales, S., Elbaz, D., Galametz, M., Galliano, F., Gear, W. K., Glenn, J., Griffin, M., Hony, S., Isaak, K. G., Levenson, L. R., Lu, N., Madden, S., O'Halloran, B., Okumura, K., Oliver, S., Page, M. J., Panuzzo, P., Papageorgiou, A., Parkin, T. J., Perez-Fournon, I., Rangwala, N., Rigby, E. E., Roussel, H., Rykala, A., Sacchi, N., Sauvage, M., Schirm, M. R. P., Schulz, B., Spinoglio, L., Srinivasan, S., Stevens, J. A., Symeonidis, M., Trichas, M., Vaccari, M., Vigroux, L., Wilson, C. D., Wozniak, H., Wright, G. S. & Zeilinger, W. W., 2010, *A&A*, **518**, L45

Goodman, J. & Weare, J., 2010, *Comm. App. Math. and Comp. Sci.*, **5**(1)

Gordon, K. D., Roman-Duval, J., Bot, C., Meixner, M., Babler, B., Bernard, J.-P., Bolatto, A., Boyer, M. L., Clayton, G. C., Engelbracht, C., Fukui, Y., Galametz, M., Galliano, F., Hony, S., Hughes, A., Indebetouw, R., Israel, F. P., Jameson, K., Kawamura, A., Lebouteiller, V., Li, A., Madden, S. C., Matsuura, M., Misselt, K., Montiel, E., Okumura, K., Onishi, T., Panuzzo, P., Paradis, D., Rubio, M., Sandstrom, K., Sauvage, M., Seale, J., Sewiło, M., Tchernyshyov, K. & Skibba, R., 2014, *ApJ*, **797**, 85

Górski, K. M., Hivon, E., Banday, A. J., Wandelt, B. D., Hansen, F. K., Reinecke, M. & Bartelmann, M., 2005, *ApJ*, **622**, 759

Grenier, I. A., Casandjian, J.-M. & Terrier, R., 2005, *Science*, **307**, 1292

Griffin, M. J., Abergel, A., Abreu, A., Ade, P. A. R., André, P., Augueres, J.-L., Babbedge, T., Bae, Y., Baillie, T., Baluteau, J.-P., Barlow, M. J., Bendo, G., Benielli, D., Bock, J. J., Bonhomme, P., Brisbin, D., Brockley-Blatt, C., Caldwell, M., Cara, C., Castro-Rodriguez, N., Cerulli, R., Chanial, P., Chen, S., Clark, E., Clements, D. L., Clerc, L., Coker, J., Communal, D., Conversi, L., Cox, P., Crumb, D., Cunningham, C., Daly, F., Davis, G. R., de Antoni, P., Delderfield, J., Devin, N., di Giorgio, A., Didschuns, I., Dohlen, K., Donati, M., Dowell, A., Dowell, C. D., Duband, L., Dumaye, L., Emery, R. J., Ferlet, M., Ferrand, D., Fontignie, J., Fox, M., Franceschini, A., Frerking, M., Fulton, T., Garcia, J., Gastaud, R., Gear, W. K., Glenn, J., Goizel, A., Griffin, D. K., Grundy, T., Guest, S., Guillemet, L., Hargrave, P. C., Harwit, M., Hastings, P., Hatziminaoglou, E., Herman, M., Hinde, B., Hristov, V., Huang, M., Imhof, P., Isaak, K. J., Israelsson, U., Ivison, R. J., Jennings, D., Kiernan, B., King, K. J., Lange, A. E., Latter, W., Laurent, G., Laurent, P., Leeks, S. J., Lellouch, E., Levenson, L., Li, B., Li, J., Lilienthal, J., Lim, T., Liu, S. J., Lu, N., Madden, S., Mainetti, G., Marliani, P., McKay, D., Mercier, K., Molinari, S., Morris, H., Moseley, H., Mulder, J., Mur, M., Naylor, D. A., Nguyen, H., O'Halloran, B., Oliver, S., Olofsson, G., Olofsson, H.-G., Orfei, R., Page, M. J., Pain, I., Panuzzo, P., Papageorgiou, A., Parks, G., Parr-Burman, P., Pearce, A., Pearson, C., Pérez-Fournon, I., Pinsard, F., Pisano, G., Podosek, J., Pohlen, M., Polehampton, E. T., Pouliquen, D., Rigopoulou, D., Rizzo, D., Roseboom, I. G., Roussel, H., Rowan-Robinson, M., Rownd, B., Saraceno, P., Sauvage, M., Savage, R., Savini, G., Sawyer, E., Scharmberg, C., Schmitt, D., Schneider, N., Schulz, B., Schwartz, A., Shafer, R., Shupe, D. L., Sibthorpe, B., Sidher, S., Smith, A., Smith, A. J., Smith, D., Spencer, L., Stobie, B., Sudiwala, R., Sukhatme, K., Surace, C., Stevens, J. A., Swinyard, B. M., Trichas, M., Tourette, T., Triou, H., Tseng, S., Tucker, C., Turner, A., Vaccari, M., Valtchanov, I., Vigroux, L., Virique, E., Voellmer, G., Walker, H., Ward, R., Waskett, T., Weilert, M., Wesson, R., White, G. J., Whitehouse, N., Wilson, C. D., Winter, B., Woodcraft, A. L., Wright, G. S., Xu, C. K., Zavagno, A., Zemcov, M., Zhang, L. & Zonca, E., 2010, *A&A*, **518**, L3

Grossi, M., Corbelli, E., Bizzocchi, L., Giovanardi, C., Bomans, D., Coelho, B., De Looze, I., Gonçalves, T. S., Hunt, L. K., Leonardo, E., Madden, S., Menéndez-Delmestre, K., Pappalardo, C. & Riguccini, L., 2016, *ArXiv e-prints*

Guo, K., Zheng, X. Z., Wang, T. & Fu, H., 2015, *ApJL*, **808**, L49

Gusev, A. S., Sakhibov, F., Piskunov, A. E., Kharchenko, N. V., Bruevich, V. V., Ezhkova, O. V., Guslyakova, S. A., Lang, V., Shimanovskaya, E. V. & Efremov, Y. N., 2016, *MNRAS*

Guseva, N. G., Izotov, Y. I., Stasińska, G., Fricke, K. J., Henkel, C. & Papaderos, P., 2011, *A&A*, **529**, A149

Hao, C.-N., Kennicutt, R. C., Johnson, B. D., Calzetti, D., Dale, D. A. & Moustakas, J., 2011, *ApJ*, **741**, 124

Harries, T. J. & Howarth, I. D., 1997, *A&AS*, **121**, 15

Harris, A. I., Baker, A. J., Zonak, S. G., Sharon, C. E., Genzel, R., Rauch, K., Watts, G. & Creager, R., 2010, *ApJ*, **723**, 1139

Haynes, K., Cannon, J. M., Skillman, E. D., Jackson, D. C. & Gehrz, R., 2010, *ApJ*, **724**, 215

Heiles et al., C., 1994, *ApJ*, **436**, 720

Henney, W. J., Arthur, S. J., Williams, R. J. R. & Ferland, G. J., 2005, *ApJ*, **621**, 328

Hildebrand, R. H., 1983, *QJRAS*, **24**, 267

Ho, I.-T., Kewley, L. J., Dopita, M. A., Medling, A. M., Allen, J. T., Bland-Hawthorn, J., Bloom, J. V., Bryant, J. J., Croom, S. M., Fogarty, L. M. R., Goodwin, M., Green, A. W., Konstantopoulos, I. S., Lawrence, J. S., López-Sánchez, Á. R., Owers, M. S., Richards, S. & Sharp, R., 2014, *MNRAS*, **444**, 3894

Ho, I.-T., Kudritzki, R.-P., Kewley, L. J., Zahid, H. J., Dopita, M. A., Bresolin, F. & Rupke, D. S. N., 2015, *MNRAS*, **448**, 2030

Holland, W. S., Bintley, D., Chapin, E. L., Chrysostomou, A., Davis, G. R., Dempsey, J. T., Duncan, W. D., Fich, M., Friberg, P., Halpern, M., Irwin, K. D., Jenness, T., Kelly, B. D., MacIntosh, M. J., Robson, E. I., Scott, D., Ade, P. A. R., Atad-Ettedgui, E., Berry, D. S., Craig, S. C., Gao, X., Gibb, A. G., Hilton, G. C., Hollister, M. I., Kycia, J. B., Lunney, D. W., McGregor, H., Montgomery, D., Parkes, W., Tilanus, R. P. J., Ullom, J. N., Walther, C. A., Walton, A. J., Woodcraft, A. L., Amiri, M., Atkinson,

D., Burger, B., Chuter, T., Coulson, I. M., Doriese, W. B., Dunare, C., Economou, F., Niemack, M. D., Parsons, H. A. L., Reintsema, C. D., Sibthorpe, B., Smail, I., Sudiwala, R. & Thomas, H. S., 2013, *MNRAS*, **430**, 2513

Hollenbach, D. & McKee, C. F., 1979, *ApJSS*, **41**, 555

Hollenbach, D. J., Takahashi, T. & Tielens, A. G. G. M., 1991, *ApJ*, **377**, 192

Huang, M.-L. & Kauffmann, G., 2014, *MNRAS*, **443**, 1329

Hughes, A., Meidt, S. E., Colombo, D., Schinnerer, E., Pety, J., Leroy, A. K., Dobbs, C. L., García-Burillo, S., Thompson, T. A., Dumas, G., Schuster, K. F. & Kramer, C., 2013, *ApJ*, **779**, 46

Hughes, T. M., Foyle, K., Schirm, M. R. P., Parkin, T. J., De Looze, I., Wilson, C. D., Bendo, G. J., Baes, M., Fritz, J., Boselli, A., Cooray, A., Cormier, D., Karczewski, O. Ł., Lebouteiller, V., Lu, N., Madden, S. C., Spinoglio, L. & Viaene, S., 2015, *A&A*, **575**, A17

Hunt, L. K., García-Burillo, S., Casasola, V., Caselli, P., Combes, F., Henkel, C., Lundgren, A., Maiolino, R., Menten, K. M., Testi, L. & Weiss, A., 2015, *A&A*, **583**, A114

Hunt, L. K. & Hirashita, H., 2009, *A&A*, **507**, 1327

Israel, F. P., 1997, *A&A*, **328**, 471

Israel, F. P. & Baas, F., 2003, *A&A*, **404**, 495

James, A., Dunne, L., Eales, S. & Edmunds, M. G., 2002, *MNRAS*, **335**, 753

Jarrett, T. H., Masci, F., Tsai, C. W., Petty, S., Cluver, M. E., Assef, R. J., Benford, D., Blain, A., Bridge, C., Donoso, E., Eisenhardt, P., Koribalski, B., Lake, S., Neill, J. D., Seibert, M., Sheth, K., Stanford, S. & Wright, E., 2013, *AJ*, **145**, 6

Jimmy, Tran, K.-V., Saintonge, A., Accurso, G., Brough, S. & Oliva-Altamirano, P., 2015, *ApJ*, **812**, 98

Jones, A. P., 2014, *Planetary and Space Science*, **100**, 26

Kamp, I. & Bertoldi, F., 2000, *A&A*, **353**, 276

Karczewski, O. Ł., Barlow, M. J., Page, M. J., Kuin, N. P. M., Ferreras, I., Baes, M., Bendo, G. J., Boselli, A., Cooray, A., Cormier, D. & De Looze, I., 2013, *MNRAS*, **431**, 2493

Karim, A., Schinnerer, E., Martínez-Sansigre, A., Sargent, M. T., van der Wel, A., Rix, H.-W., Ilbert, O., Smolčić, V., Carilli, C., Pannella, M., Koekemoer, A. M., Bell, E. F. & Salvato, M., 2011, *ApJ*, **730**, 61

Kauffmann, G., Heckman, T. M., Tremonti, C., Brinchmann, J., Charlot, S., White, S. D. M., Ridgway, S. E., Brinkmann, J., Fukugita, M., Hall, P. B., Ivezić, Ž., Richards, G. T. & Schneider, D. P., 2003*a*, *MNRAS*, **346**, 1055

Kauffmann, G., Heckman, T. M., White, S. D. M., Charlot, S., Tremonti, C., Brinchmann, J., Bruzual, G., Peng, E. W., Seibert, M., Bernardi, M., Blanton, M., Brinkmann, J., Castander, F., Csábai, I., Fukugita, M., Ivezic, Z., Munn, J. A., Nichol, R. C., Padmanabhan, N., Thakar, A. R., Weinberg, D. H. & York, D., 2003*b*, *MNRAS*, **341**, 33

Kaufman, M. J., Wolfire, M. G., Hollenbach, D. J. & Luhman, M. L., 1999, *ApJ*, **527**, 795

Kaviraj, S., Cohen, S., Windhorst, R. A., Silk, J., O'Connell, R. W., Dopita, M. A., Dekel, A., Hathi, N. P., Straughn, A. & Rutkowski, M., 2013, *MNRAS*, **429**, L40

Kelly, B. C., 2007, *ApJ*, **665**, 1489

Kelly, G., Viti, S., Bayet, E., Aladro, R. & Yates, J., 2015, *A&A*, **578**, A70

Kennicutt, R. C. & Evans, N. J., 2012, *Ann. Rev. Astr. Astrophys.*, **50**, 531

Kennicutt, Jr., R. C., 1998, *ApJ*, **498**, 541

Kereš, D., Katz, N., Weinberg, D. H. & Davé, R., 2005, *MNRAS*, **363**, 2

Kewley, L. J. & Ellison, S. L., 2008, *ApJ*, **681**, 1183

Kirkpatrick, A., Calzetti, D., Kennicutt, R., Galametz, M., Gordon, K., Groves, B., Hunt, L., Dale, D., Hinz, J. & Tabatabaei, F., 2014, *ApJ*, **789**, 130

Krumholz, M. R., McKee, C. F. & Tumlinson, J., 2008, *ApJ*, **689**, 865

Krumholz, M. R., McKee, C. F. & Tumlinson, J., 2009, *ApJ*, **693**, 216

Langer, W. D., Velusamy, T., Pineda, J. L., Goldsmith, P. F., Li, D. & Yorke, H. W., 2010, *A&A*, **521**, L17

Langer, W. D., Velusamy, T., Pineda, J. L., Willacy, K. & Goldsmith, P. F., 2014, *A&A*, **561**, A122

Lee, C., Leroy, A. K., Schnee, S., Wong, T., Bolatto, A. D., Indebetouw, R. & Rubio, M., 2015, *MNRAS*, **450**, 2708

Lee, H.-H., Herbst, E., Pineau des Forets, G., Roueff, E. & Le Bourlot, J., 1996, *A&A*, **311**, 690

Leitherer, C., Ortiz Otálvaro, P. A., Bresolin, F., Kudritzki, R.-P., Lo Faro, B., Pauldrach, A. W. A., Pettini, M. & Rix, S. A., 2010, *ApJSS*, **189**, 309

Leitherer, C., Schaerer, D., Goldader, J. D., Delgado, R. M. G., Robert, C., Kune, D. F., de Mello, D. F., Devost, D. & Heckman, T. M., 1999, *ApJSS*, **123**, 3

Leroy, A. K., Bolatto, A., Gordon, K., Sandstrom, K., Gratier, P., Rosolowsky, E., Engelbracht, C. W., Mizuno, N., Corbelli, E., Fukui, Y. & Kawamura, A., 2011, *ApJ*, **737**, 12

Leroy, A. K., Walter, F., Bigiel, F., Usero, A., Weiss, A., Brinks, E., de Blok, W. J. G., Kennicutt, R. C., Schuster, K.-F., Kramer, C., Wiesemeyer, H. W. & Roussel, H., 2009, *AJ*, **137**, 4670

Leroy, A. K., Walter, F., Brinks, E., Bigiel, F., de Blok, W. J. G., Madore, B. & Thornley, M. D., 2008, *AJ*, **136**, 2782

Licquia, T. & Newman, J., 2014, in *American Astronomical Society Meeting Abstracts #223*, volume 223 of *American Astronomical Society Meeting Abstracts*, p. 336.04

Lilly, S. J., Carollo, C. M., Pipino, A., Renzini, A. & Peng, Y., 2013, *ApJ*, **772**, 119

Liseau, R., Justtanont, K. & Tielens, A. G. G. M., 2006, *A&A*, **446**, 561

Lisenfeld, U., Israel, F. P., Stil, J. M. & Sievers, A., 2002, *A&A*, **382**, 860

Louppe, G., 2014, *ArXiv e-prints*

Lu, Z., Mo, H. J. & Lu, Y., 2015, *MNRAS*, **450**, 606

Lucy, L. B., 1999, *A&A*, **344**, 282

Madden, S. C., Poglitsch, A., Geis, N., Stacey, G. J. & Townes, C. H., 1997, *ApJ*, **483**, 200

Madden, S. C., Rémy-Ruyer, A., Galametz, M., Cormier, D., Lebouteiller, V., Galliano, F., Hony, S., Bendo, G. J., Smith, M. W. L., Pohlen, M., Roussel, H., Sauvage, M., Wu, R., Sturm, E., Poglitsch, A., Contursi, A., Doublier, V., Baes, M., Barlow, M. J., Boselli, A., Boquien, M., Carlson, L. R., Ciesla, L., Cooray, A., Cortese, L., de Looze, I., Irwin, J. A., Isaak, K., Kamenetzky, J., Karczewski, O. Ł., Lu, N., MacHattie, J. A., O'Halloran, B., Parkin, T. J., Rangwala, N., Schirm, M. R. P., Schulz, B., Spinoglio, L., Vaccari, M., Wilson, C. D. & Wozniak, H., 2013, *PASP*, **125**, 600

Magdis, G. E., Daddi, E., Béthermin, M., Sargent, M., Elbaz, D., Pannella, M., Dickinson, M., Dannerbauer, H., da Cunha, E., Walter, F., Rigopoulou, D., Charmandaris, V., Hwang, H. S. & Kartaltepe, J., 2012, *ApJ*, **760**, 6

Magdis, G. E., Daddi, E., Elbaz, D., Sargent, M., Dickinson, M., Dannerbauer, H., Aussel, H., Walter, F., Hwang, H. S., Charmandaris, V., Hodge, J., Riechers, D., Rigopoulou, D., Carilli, C., Pannella, M., Mullaney, J., Leiton, R. & Scott, D., 2011, *ApJL*, **740**, L15

Magnelli, B., Saintonge, A., Lutz, D., Tacconi, L. J., Berta, S., Bournaud, F., Charmandaris, V., Dannerbauer, H., Elbaz, D., Förster-Schreiber, N. M., Graciá-Carpio, J., Ivison, R., Maiolino, R., Nordon, R., Popesso, P., Rodighiero, G., Santini, P. & Wuyts, S., 2012, *A&A*, **548**, A22

Magorrian, J., Tremaine, S., Richstone, D., Bender, R., Bower, G., Dressler, A., Faber, S. M., Gebhardt, K., Green, R., Grillmair, C., Kormendy, J. & Lauer, T., 1998, *AJ*, **115**, 2285

Magrini, L., Coccato, L., Stanghellini, L., Casasola, V. & Galli, D., 2016, *A&A*, **588**, A91

Maiolino, R., Carniani, S., Fontana, A., Vallini, L., Pentericci, L., Ferrara, A., Vanzella, E., Grazian, A., Gallerani, S., Castellano, M., Cristiani, S., Brammer, G., Santini, P., Wagg, J. & Williams, R., 2015, *MNRAS*, **452**, 54

Makrymallis, A. & Viti, S., 2014, *ApJ*, **794**, 45

Mandel, K. S., Narayan, G. & Kirshner, R. P., 2011, *ApJ*, **731**, 120

Mannucci, F., Cresci, G., Maiolino, R., Marconi, A. & Gnerucci, A., 2010, *MNRAS*, **408**, 2115

Martin, D. C., Fanson, J., Schiminovich, D., Morrissey, P., Friedman, P. G. & Barlow, T. A., 2005, *ApJL*, **619**, L1

Mattsson, L., Gomez, H. L., Andersen, A. C. & Matsuura, M., 2015, *MNRAS*, **449**, 4079

McElroy, D., Walsh, C., Markwick, A. J., Cordiner, M. A., Smith, K. & Millar, T. J., 2013, *A&A*, **550**, A36

Messenger, S., Amari, S., Gao, X., Walker, R. M., Clemett, S. J., Chillier, X. D. F., Zare, R. N. & Lewis, R. S., 1998, *ApJ*, **502**, 284

Mookerjea, B., Israel, F., Kramer, C., Nikola, T., Braine, J., Ossenkopf, V., Röllig, M., Henkel, C., van der Werf, P., van der Tak, F. & Wiedner, M. C., 2016, *A&A*, **586**, A37

Mookerjea, B., Kramer, C., Buchbender, C., Boquien, M., Verley, S., Relaño, M., Quintana-Lacaci, G., Aalto, S. & Braine, J., 2011, *A&A*, **532**, A152

Narayanan, D., Krumholz, M. R., Ostriker, E. C. & Hernquist, L., 2012, *MNRAS*, **421**, 3127

Noeske, K. G., Weiner, B. J., Faber, S. M., Papovich, C., Koo, D. C., Somerville, R. S. & Bundy, K., 2007, *ApJL*, **660**, L43

Nuth, J. A., 1985, *Nature*, **318**, 166

Oberst, T. E., Parshley, S. C., Stacey, G. J., Nikola, T., Löhr, A., Harnett, J. I., Tothill, N. F. H., Lane, A. P., Stark, A. A. & Tucker, C. E., 2006, *ApJL*, **652**, L125

Obreschkow, D. & Rawlings, S., 2009, *MNRAS*, **394**, 1857

Offner, S. S. R., Bisbas, T. G., Bell, T. A. & Viti, S., 2014, *MNRAS*, **440**, L81

Okada, Y., Pilleri, P., Berné, O., Ossenkopf, V., Fuente, A., Goicoechea, J. R., Joblin, C., Kramer, C., Röllig, M., Teyssier, D. & van der Tak, F. F. S., 2013, *A&A*, **553**, A2

Oke, J. B., 1990, *AJ*, **99**, 1621

Olsen, K. P., Greve, T. R., Narayanan, D., Thompson, R., Toft, S. & Brinch, C., 2015, *ApJ*, **814**, 76

Oppenheimer, B. D. & Davé, R., 2008, *MNRAS*, **387**, 577

Oppenheimer, B. D., Davé, R., Kereš, D., Fardal, M., Katz, N., Kollmeier, J. A. & Weinberg, D. H., 2010, *MNRAS*, **406**, 2325

Ota, K., Walter, F., Ohta, K., Hatsukade, B., Carilli, C. L., da Cunha, E., González-López, J., Decarli, R., Hodge, J. A., Nagai, H., Egami, E., Jiang, L., Iye, M., Kashikawa, N., Riechers, D. A., Bertoldi, F., Cox, P., Neri, R. & Weiss, A., 2014, *ApJ*, **792**, 34

Ott, S., 2010, in Y. Mizumoto, K.-I. Morita & M. Ohishi (eds.), *Astronomical Data Analysis Software and Systems XIX*, volume 434 of *Astronomical Society of the Pacific Conference Series*, p. 139

Papadopoulos, P. P., 2010, *ApJ*, **720**, 226

Parkin, T. J., Wilson, C. D., Foyle, K., Baes, M., Bendo, G. J., Boselli, A., Boquien, M., Cooray, A., Cormier, D., Davies, J. I., Eales, S. A., Galametz, M., Gomez, H. L., Lebouteiller, V., Madden, S., Mentuch, E., Page, M. J., Pohlen, M., Remy, A., Roussel, H., Sauvage, M., Smith, M. W. L. & Spinoglio, L., 2012, *MNRAS*, **422**, 2291

Pedregosa, F., Varoquaux, G., Gramfort, A., Michel, V., Thirion, B., Grisel, O., Blondel, M., Prettenhofer, P., Weiss, R., Dubourg, V., Vanderplas, J. & Passos, A., 2012, *ArXiv e-prints*

Peng, Y.-j., Lilly, S. J., Kovač, K., Bolzonella, M., Pozzetti, L., Renzini, A., Zamorani, G., Ilbert, O. & Knobel, C., 2010, *ApJ*, **721**, 193

Pettini, M. & Pagel, B. E. J., 2004, *MNRAS*, **348**, L59

Pettini, M., Zych, B. J., Steidel, C. C. & Chaffee, F. H., 2008, *MNRAS*, **385**, 2011

Pierce-Price, D., Richer, J. S., Greaves, J. S., Holland, W. S., Jenness, T., Lasenby, A. N., White, G. J., Matthews, H. E., Ward-Thompson, D., Dent, W. R. F., Zylka, R., Mezger, P., Hasegawa, T., Oka, T., Omont, A. & Gilmore, G., 2000, *ApJL*, **545**, L121

Pilbratt, G. L., Riedinger, J. R., Passvogel, T., Crone, G., Doyle, D. & Gageur, U., 2010, *A&A*, **518**, L1

Pineda, J. L., Langer, W. D., Velusamy, T. & Goldsmith, P. F., 2013, *A&A*, **554**, A103

Planck Collaboration, Ade, P. A. R., Aghanim, N., Arnaud, M., Ashdown, M., Aumont, J., Baccigalupi, C., Balbi, A., Banday, A. J., Barreiro, R. B. & et al., 2011, *A&A*, **536**, A22

Poglitsch, A., Krabbe, A., Madden, S. C., Nikola, T., Geis, N., Johansson, L. E. B., Stacey, G. J. & Sternberg, A., 1995, *ApJ*, **454**, 293

Poglitsch, A., Waelkens, C., Geis, N., Feuchtgruber, H., Vandenbussche, B., Rodriguez, L. & Krause, O., 2010, *A&A*, **518**, L2

Quinlan, J. R., 1986, *Machine Learning*, **1**(1), 81
URL: *http://dx.doi.org/10.1007/BF00116251*

Reddy, N. A., Pettini, M., Steidel, C. C., Shapley, A. E., Erb, D. K. & Law, D. R., 2012, *ApJ*, **754**, 25

Rémy-Ruyer, A., Madden, S. C., Galliano, F., Galametz, M., Takeuchi, T. T. & Asano, R. S., 2014, *A&A*, **563**, A31

Rémy-Ruyer, A., Madden, S. C., Galliano, F., Hony, S., Sauvage, M., Bendo, G. J., Roussel, H., Pohlen, M., Smith, M. W. L., Galametz, M., Cormier, D., Lebouteiller, V., Wu, R., Baes, M., Barlow, M. J., Boquien, M., Boselli, A., Ciesla, L., De Looze, I., Karczewski, O. Ł., Panuzzo, P., Spinoglio, L., Vaccari, M. & Wilson, C. D., 2013, *A&A*, **557**, A95

Rémy-Ruyer, A., Madden, S. C., Galliano, F., Lebouteiller, V., Baes, M., Bendo, G. J., Boselli, A., Ciesla, L., Cormier, D., Cooray, A., Cortese, L., De Looze, I., Doublier-Pritchard, V., Galametz, M., Jones, A. P., Karczewski, O. Ł., Lu, N. & Spinoglio, L., 2015, *A&A*, **582**, A121

Richards, J. W., Starr, D. L., Butler, N. R., Bloom, J. S., Brewer, J. M., Crellin-Quick, A., Higgins, J., Kennedy, R. & Rischard, M., 2011, *ApJ*, **733**, 10

Riechers, D. A., Carilli, C. L., Capak, P. L., Scoville, N. Z., Smolčić, V., Schinnerer, E., Yun, M., Cox, P., Bertoldi, F., Karim, A. & Yan, L., 2014, *ApJ*, **796**, 84

Robaina, A. R., Bell, E. F., Skelton, R. E., McIntosh, D. H., Somerville, R. S., Zheng, X., Rix, H.-W., Bacon, D., Balogh, M., Barazza, F. D., Barden, M., Böhm, A., Caldwell,

J. A. R., Gallazzi, A., Gray, M. E., Häussler, B., Heymans, C., Jahnke, K., Jogee, S., van Kampen, E., Lane, K., Meisenheimer, K., Papovich, C., Peng, C. Y., Sánchez, S. F., Skibba, R., Taylor, A., Wisotzki, L. & Wolf, C., 2009, *ApJ*, **704**, 324

Rodighiero, G., Daddi, E., Baronchelli, I., Cimatti, A., Renzini, A., Aussel, H., Popesso, P., Lutz, D., Andreani, P., Berta, S., Cava, A., Elbaz, D., Feltre, A., Fontana, A., Förster Schreiber, N. M., Franceschini, A., Genzel, R., Grazian, A., Gruppioni, C., Ilbert, O., Le Floch, E., Magdis, G., Magliocchetti, M., Magnelli, B., Maiolino, R., McCracken, H., Nordon, R., Poglitsch, A., Santini, P., Pozzi, F., Riguccini, L., Tacconi, L. J., Wuyts, S. & Zamorani, G., 2011, *ApJL*, **739**, L40

Röllig, M., Ossenkopf, V., Jeyakumar, S., Stutzki, J. & Sternberg, A., 2006, *A&A*, **451**, 917

Romano, P., Guidorzi, C., Segreto, A., Ducci, L. & Vercellone, S., 2014, *A&A*, **572**, A97

Rowlands, K., Dunne, L., Dye, S., Aragón-Salamanca, A., Maddox, S., da Cunha, E., Smith, D. J. B., Bourne, N., Eales, S., Gomez, H. L., Smail, I., Alpaslan, M., Clark, C. J. R., Driver, S., Ibar, E., Ivison, R. J., Robotham, A., Smith, M. W. L. & Valiante, E., 2014, *MNRAS*, **441**, 1017

Saintonge, A., Catinella, B., Cortese, L., Genzel, R., Giovanelli, R., Haynes, M. P., Janowiecki, S., Kramer, C., Lutz, K. A., Schiminovich, D., Tacconi, L. J., Wuyts, S. & Accurso, G., 2016, *ArXiv e-prints*

Saintonge, A., Kauffmann, G., Kramer, C., Tacconi, L. J., Buchbender, C., Catinella, B., Fabello, S., Graciá-Carpio, J., Wang, J., Cortese, L., Fu, J., Genzel, R., Giovanelli, R., Guo, Q., Haynes, M. P., Heckman, T. M., Krumholz, M. R., Lemonias, J., Li, C., Moran, S., Rodriguez-Fernandez, N., Schiminovich, D., Schuster, K. & Sievers, A., 2011*a*, *MNRAS*, **415**, 32

Saintonge, A., Kauffmann, G., Wang, J., Kramer, C., Tacconi, L. J., Buchbender, C., Catinella, B., Graciá-Carpio, J., Cortese, L., Fabello, S., Fu, J., Genzel, R., Giovanelli, R., Guo, Q., Haynes, M. P., Heckman, T. M., Krumholz, M. R., Lemonias, J., Li, C., Moran, S., Rodriguez-Fernandez, N., Schiminovich, D., Schuster, K. & Sievers, A., 2011*b*, *MNRAS*, **415**, 61

Saintonge, A., Lutz, D., Genzel, R., Magnelli, B., Nordon, R., Tacconi, L. J., Baker, A. J., Bandara, K., Berta, S., Förster Schreiber, N. M., Poglitsch, A., Sturm, E., Wuyts, E. & Wuyts, S., 2013, *ApJ*, **778**, 2

Saintonge, A., Tacconi, L. J., Fabello, S., Wang, J., Catinella, B., Genzel, R., Graciá-Carpio, J., Kramer, C., Moran, S., Heckman, T. M., Schiminovich, D., Schuster, K. & Wuyts, S., 2012, *ApJ*, **758**, 73

Sanders, R. L., Shapley, A. E., Kriek, M., Reddy, N. A., Freeman, W. R., Coil, A. L., Siana, B., Mobasher, B., Shivaei, I., Price, S. H. & de Groot, L., 2016, *ApJ*, **816**, 23

Sandstrom, K. M., Leroy, A. K., Walter, F., Bolatto, A. D., Croxall, K. V., Draine, B. T., Wilson, C. D., Wolfire, M., Calzetti, D. & Kennicutt, R. C., 2013, *ApJ*, **777**, 5

Santini, P., Maiolino, R., Magnelli, B., Lutz, D., Lamastra, A., Li Causi, G., Eales, S., Andreani, P., Berta, S., Buat, V., Cooray, A., Cresci, G., Daddi, E., Farrah, D., Fontana, A., Franceschini, A., Genzel, R., Granato, G., Grazian, A., Le Floc'h, E., Magdis, G., Magliocchetti, M., Mannucci, F., Menci, N., Nordon, R., Oliver, S., Popesso, P., Pozzi, F., Riguccini, L., Rodighiero, G., Rosario, D. J., Salvato, M., Scott, D., Silva, L., Tacconi, L., Viero, M., Wang, L., Wuyts, S. & Xu, K., 2014, *A&A*, **562**, A30

Sargent, M. T., Daddi, E., Béthermin, M., Aussel, H., Magdis, G., Hwang, H. S., Juneau, S., Elbaz, D. & da Cunha, E., 2014, *ApJ*, **793**, 19

Sawicki, M., 2012, *PASP*, **124**, 1208

Schiminovich, D., Wyder, T. K., Martin, D. C., Johnson, B. D., Salim, S. & Seibert, M., 2007, *ApJSS*, **173**, 315

Schmidt, M., 1959, *ApJ*, **129**, 243

Schruba, A., Leroy, A. K., Walter, F., Bigiel, F., Brinks, E., de Blok, W. J. G., Kramer, C., Rosolowsky, E. & Sandstrom, K., 2012, *AJ*, **143**, 138

Schwarz, G., 1978, *Ann. Statist.*, **6**(2), 461
URL: *http://dx.doi.org/10.1214/aos/1176344136*

Scoville, N., Aussel, H., Sheth, K., Scott, K. S., Sanders, D., Ivison, R., Pope, A., Capak, P., Vanden Bout, P., Manohar, S., Kartaltepe, J., Robertson, B. & Lilly, S., 2014, *ApJ*, **783**, 84

Scoville, N. Z., 2013, *Evolution of star formation and gas*, p. 491

Shetty, R., Kelly, B. C. & Bigiel, F., 2013, *MNRAS*, **430**, 288

Smith, M. W. L., Eales, S. A., Gomez, H. L., Roman-Duval, J., Fritz, J., Braun, R., Baes, M., Bendo, G. J., Blommaert, J. A. D. L., Boquien, M., Boselli, A., Clements, D. L., Cooray, A. R., Cortese, L., De Looze, I., Ford, G. P., Gear, W. K., Gentile, G., Gordon, K. D., Kirk, J., Lebouteiller, V., Madden, S., Mentuch, E., O'Halloran, B., Page, M. J., Schulz, B., Spinoglio, L., Verstappen, J., Wilson, C. D. & Thilker, D. A., 2012, *ApJ*, **756**, 40

Solomon, P. M., Downes, D., Radford, S. J. E. & Barrett, J. W., 1997, *ApJ*, **478**, 144

Solomon, P. M., Rivolo, A. R., Barrett, J. & Yahil, A., 1987, *ApJ*, **319**, 730

Springel, V. & Hernquist, L., 2003, *MNRAS*, **339**, 289

Stacey, G. J., Geis, N., Genzel, R., Lugten, J. B., Poglitsch, A., Sternberg, A. & Townes, C. H., 1991, *ApJ*, **373**, 423

Stacey, G. J., Hailey-Dunsheath, S., Ferkinhoff, C., Nikola, T., Parshley, S. C., Benford, D. J., Staguhn, J. G. & Fiolet, N., 2010, *ApJ*, **724**, 957

Sternberg, A. & Dalgarno, A., 1995, *ApJSS*, **99**, 565

Stoughton, C., Lupton, R. H., Bernardi, M., Blanton, M. R., Burles, S., Castander, F. J., Connolly, A. J., Eisenstein, D. J., Frieman, J. A., Hennessy, G. S., Hindsley, R. B., Ivezić, Ž., Kent, S., Kunszt, P. Z., Lee, B. C., Meiksin, A., Munn, J. A., Newberg, H. J., Nichol, R. C., Nicinski, T., Pier, J. R., Richards, G. T., Richmond, M. W., Schlegel, D. J., Smith, J. A., Strauss, M. A., SubbaRao, M., Szalay, A. S., Thakar, A. R., Tucker, D. L., Vanden Berk, D. E., Yanny, B., Adelman, J. K., Anderson, Jr., J. E., Anderson, S. F., Annis, J., Bahcall, N. A., Bakken, J. A., Bartelmann, M., Bastian, S., Bauer, A., Berman, E., Böhringer, H., Boroski, W. N., Bracker, S., Briegel, C., Briggs, J. W., Brinkmann, J., Brunner, R., Carey, L., Carr, M. A., Chen, B., Christian, D., Colestock, P. L., Crocker, J. H., Csabai, I., Czarapata, P. C., Dalcanton, J., Davidsen, A. F., Davis, J. E., Dehnen, W., Dodelson, S., Doi, M., Dombeck, T., Donahue, M., Ellman, N., Elms, B. R., Evans, M. L., Eyer, L., Fan, X., Federwitz, G. R., Friedman, S., Fukugita, M., Gal, R., Gillespie, B., Glazebrook, K., Gray, J., Grebel,

E. K., Greenawalt, B., Greene, G., Gunn, J. E., de Haas, E., Haiman, Z., Haldeman, M., Hall, P. B., Hamabe, M., Hansen, B., Harris, F. H., Harris, H., Harvanek, M., Hawley, S. L., Hayes, J. J. E., Heckman, T. M., Helmi, A., Henden, A., Hogan, C. J., Hogg, D. W., Holmgren, D. J., Holtzman, J., Huang, C.-H., Hull, C., Ichikawa, S.-I., Ichikawa, T., Johnston, D. E., Kauffmann, G., Kim, R. S. J., Kimball, T., Kinney, E., Klaene, M., Kleinman, S. J., Klypin, A., Knapp, G. R., Korienek, J., Krolik, J., Kron, R. G., Krzesiński, J., Lamb, D. Q., Leger, R. F., Limmongkol, S., Lindenmeyer, C., Long, D. C., Loomis, C., Loveday, J., MacKinnon, B., Mannery, E. J., Mantsch, P. M., Margon, B., McGehee, P., McKay, T. A., McLean, B., Menou, K., Merelli, A., Mo, H. J., Monet, D. G., Nakamura, O., Narayanan, V. K., Nash, T., Neilsen, Jr., E. H., Newman, P. R., Nitta, A., Odenkirchen, M., Okada, N., Okamura, S., Ostriker, J. P., Owen, R., Pauls, A. G., Peoples, J., Peterson, R. S., Petravick, D., Pope, A., Pordes, R., Postman, M., Prosapio, A., Quinn, T. R., Rechenmacher, R., Rivetta, C. H., Rix, H.-W., Rockosi, C. M., Rosner, R., Ruthmansdorfer, K., Sandford, D., Schneider, D. P., Scranton, R., Sekiguchi, M., Sergey, G., Sheth, R., Shimasaku, K., Smee, S., Snedden, S. A., Stebbins, A., Stubbs, C., Szapudi, I., Szkody, P., Szokoly, G. P., Tabachnik, S., Tsvetanov, Z., Uomoto, A., Vogeley, M. S., Voges, W., Waddell, P., Walterbos, R., Wang, S.-i., Watanabe, M., Weinberg, D. H., White, R. L., White, S. D. M., Wilhite, B., Wolfe, D., Yasuda, N., York, D. G., Zehavi, I. & Zheng, W., 2002, *AJ*, **123**, 485

Strong, A. W. & Mattox, J. R., 1996, *A&A*, **308**, L21

Sturm, E., González-Alfonso, E., Veilleux, S., Fischer, J., Graciá-Carpio, J., Hailey-Dunsheath, S., Contursi, A., Poglitsch, A., Sternberg, A., Davies, R., Genzel, R., Lutz, D., Tacconi, L., Verma, A., Maiolino, R. & de Jong, J. A., 2011, *ApJL*, **733**, L16

Tacconi, L. J., Genzel, R., Neri, R., Cox, P., Cooper, M. C., Shapiro, K., Bolatto, A., Bouché, N., Bournaud, F., Burkert, A., Combes, F., Comerford, J., Davis, M., Schreiber, N. M. F., Garcia-Burillo, S., Gracia-Carpio, J., Lutz, D., Naab, T., Omont, A., Shapley, A., Sternberg, A. & Weiner, B., 2010, *Nature*, **463**, 781

Tacconi, L. J., Neri, R., Genzel, R., Combes, F., Bolatto, A., Cooper, M. C., Wuyts, S., Bournaud, F., Burkert, A., Comerford, J., Cox, P., Davis, M., Förster Schreiber, N. M., García-Burillo, S., Gracia-Carpio, J., Lutz, D., Naab, T., Newman, S., Omont,

A., Saintonge, A., Shapiro Griffin, K., Shapley, A., Sternberg, A. & Weiner, B., 2013, *ApJ*, **768**, 74

Tielens, A. G. G. M. & Hollenbach, D., 1985, *ApJ*, **291**, 722

Tissera, P. B., Pedrosa, S. E., Sillero, E. & Vilchez, J. M., 2016, *MNRAS*, **456**, 2982

Tremonti, C. A., Heckman, T. M., Kauffmann, G., Brinchmann, J., Charlot, S., White, S. D. M., Seibert, M., Peng, E. W. & Schlegel, D. J., 2004, *ApJ*, **613**, 898

Tully, R. B. & Fisher, J. R., 1977, *A&A*, **54**, 661

Valiante, E., Smith, M. W. L., Eales, S., Maddox, S. J., Ibar, E., Hopwood, R., Dunne, L., Cigan, P. J., Dye, S., Pascale, E., Rigby, E. E., Bourne, N., Furlanetto, C. & Ivison, R. J., 2016, *ArXiv e-prints*

van Dishoeck, E. F. & Black, J. H., 1986, *ApJSS*, **62**, 109

van Dishoeck, E. F. & Black, J. H., 1988, *ApJ*, **334**, 771

Vasta, M., 2010, *UCL (University College London)*
URL: *https://core.ac.uk/display/1688816*

Vasta, M., Barlow, M. J., Viti, S., Yates, J. A. & Bell, T. A., 2010, *Highlights of Astronomy*, **15**, 408

Vázquez, G. A. & Leitherer, C., 2005, *ApJ*, **621**, 695

Velusamy, T., Langer, W. D., Pineda, J. L., Goldsmith, P. F., Li, D. & Yorke, H. W., 2010, *A&A*, **521**, L18

Viti, S., 2013, *UCL_PDR: Time dependent photon-dissociation regions model*, Astrophysics Source Code Library

Vlahakis, C., Dunne, L. & Eales, S., 2005, *MNRAS*, **364**, 1253

Wang, J., Overzier, R., Kauffmann, G., von der Linden, A. & Kong, X., 2010, *MNRAS*, **401**, 433

Whitaker, K. E., van Dokkum, P. G., Brammer, G. & Franx, M., 2012, *ApJL*, **754**, L29

White, S. D. M. & Frenk, C. S., 1991, *ApJ*, **379**, 52

Wilson, C. D., 1995, *ApJL*, **448**, L97

Wilson, C. D., Warren, B. E., Israel, F. P., Serjeant, S., Attewell, D., Bendo, G. J., Butner, H. M., Chanial, P., Clements, D. L., Golding, J., Heesen, V., Irwin, J., Leech, J., Matthews, H. E., Mühle, S., Mortier, A. M. J., Petitpas, G., Sánchez-Gallego, J. R., Sinukoff, E., Shorten, K., Tan, B. K., Tilanus, R. P. J., Usero, A., Vaccari, M., Wiegert, T., Zhu, M., Alexander, D. M., Alexander, P., Azimlu, M., Barmby, P., Brar, R., Bridge, C., Brinks, E., Brooks, S., Coppin, K., Côté, S., Côté, P., Courteau, S., Davies, J., Eales, S., Fich, M., Hudson, M., Hughes, D. H., Ivison, R. J., Knapen, J. H., Page, M., Parkin, T. J., Rigopoulou, D., Rosolowsky, E., Seaquist, E. R., Spekkens, K., Tanvir, N., van der Hulst, J. M., van der Werf, P., Vlahakis, C., Webb, T. M., Weferling, B. & White, G. J., 2012, *MNRAS*, **424**, 3050

Wolfire, M. G., Hollenbach, D. & McKee, C. F., 2010, *ApJ*, **716**, 1191

Wong, T., Hughes, A., Ott, J., Muller, E., Pineda, J. L., Bernard, J.-P., Chu, Y.-H., Fukui, Y., Gruendl, R. A., Henkel, C., Kawamura, A., Klein, U., Looney, L. W., Maddison, S., Mizuno, Y., Paradis, D., Seale, J. & Welty, D. E., 2011, *ApJSS*, **197**, 16

Wood, K., Mathis, J. S. & Ercolano, B., 2004, *MNRAS*, **348**, 1337

Wright, E. L., Eisenhardt, P. R. M., Mainzer, A. K., Ressler, M. E., Cutri, R. M. & Jarrett, T., 2010*a*, *AJ*, **140**, 1868

Wright, N. J., Drake, J. J., Drew, J. E. & Vink, J. S., 2010*b*, *ApJ*, **713**, 871

Wuyts, E., Wisnioski, E., Fossati, M., Förster Schreiber, N. M., Genzel, R., Davies, R., Mendel, J. T., Naab, T., Röttgers, B., Wilman, D. J., Wuyts, S., Bandara, K., Beifiori, A., Belli, S., Bender, R., Brammer, G. B., Burkert, A., Chan, J., Galametz, A., Kulkarni, S. K., Lang, P., Lutz, D., Momcheva, I. G., Nelson, E. J., Rosario, D., Saglia, R. P., Seitz, S., Tacconi, L. J., Tadaki, K.-i., Übler, H. & van Dokkum, P., 2016, *ArXiv e-prints*

Wuyts, S., Förster Schreiber, N. M., Lutz, D., Nordon, R., Berta, S., Altieri, B., Andreani, P., Aussel, H., Bongiovanni, A., Cepa, J., Cimatti, A., Daddi, E., Elbaz, D., Genzel, R., Koekemoer, A. M., Magnelli, B., Maiolino, R., McGrath, E. J., Pérez García, A., Poglitsch, A., Popesso, P., Pozzi, F., Sanchez-Portal, M., Sturm, E., Tacconi, L. & Valtchanov, I., 2011, *ApJ*, **738**, 106

Young, J. S. & Scoville, N. Z., 1991, *Ann. Rev. Astr. Astrophys.*, **29**, 581

Zhang, Z.-Y., Papadopoulos, P. P., Ivison, R. J., Galametz, M., Smith, M. W. L. & Xilouris, E. M., 2016, *Royal Society Open Science*, **3**, 160025

Zubko, V., Dwek, E. & Arendt, R. G., 2004, *ApJSS*, **152**, 211